Novel Oxides and Nitrides in the Nuclear Fuel Cycle

Sarah Elizabeth O'Sullivan

A thesis submitted in partial fulfilment of the requirements for the degree of

Doctor of Philosophy

The University of Sheffield

Faculty of Engineering

Department of Materials Science & Engineering

April 2021

Abstract

The majority of civil nuclear reactors currently in operation are light water reactors using uranium oxide fuel assemblies. However, in the legacy of the Fukushima Dai-ichi nuclear accident, fuel with improved accident tolerance are sought, with uranium nitride UN being one such option. Part of the implementation of nitride nuclear fuel is a full lifecycle and safety case assessment. This includes consideration of fuel synthesis, potential products arising from fuel degradation and disposal of fission products. Currently, fission products in High Level Waste are vitrified into borosilicate glass pending disposal, however ceramic compounds can provide tailored immobilisation hosts for long lived or highly mobile isotopes. The aim of this thesis was to develop an understanding of the synthesis, structure and properties of materials relevant to the deployment of uranium nitride as an accident tolerant nuclear fuel in future advanced fuel cycles, taking a holistic approach. The low temperature nitridation of uranium oxides in $NaNH_2$ molten salt was investigated as a potential route to synthesis of uranium nitrides and oxynitrides. This was supported by elucidation of the mechanism of such reactions by synthesis of $Fe_{2+x}N$ from Fe_3O_4 as a case study. Although uranium nitrides and oxynitrides were not synthesised by reaction with $NaNH_2$, this method did afford a novel reduction of hyperstoichiometric UO_{2+x} to stoichiometric $UO_{2.00}$ at only 200 °C. The potential for uranium oxynitride synthesis was further explored through ammonolysis of $CaUO_4$ and $SrUO_4$; this did not yield the targeted oxynitride compounds, but proved effective in achieving highly reduced oxygen deficient compositions. The family of periodate perovskites A_2NaIO_6 (A = Ba, Sr, Ca) and the technetate pyrochlore $Pb_2Tc_2O_{6.5}$ were investigated as candidate wasteforms for ^{129}I and ^{99}Tc fission products, with the crystal structures determined from neutron diffraction data. $Pb_2Tc_2O_{6.5}$ is the first example of a mixed valent Tc^{4+}/Tc^{5+} oxide.

Acknowledgements

The work in thesis owes a great deal to all the people who have contributed and guided me. Firstly, to my supervisors Prof. Neil Hyatt and Dr. Martin Stennett. Neil, thanks is not enough to express my gratitude for your patience and guidance over the past five years. I certainly could not have done this without your insight and your support as a supervisor, mentor and, at times, general life coach. Martin, thank you for all your help and input, including putting with my many and technically challenging laboratory requests.

I would like to profusely thank Dr. Shi-Kuan Sun for all your help with lab work and data analysis. To Dr. Dan Bailey, thank you for all your advice and help with gathering of data. I appreciate you taking on these experiments after my departure, I know they're in good hands. Special thanks go to Dr. Laura Gardner, Dr. Sam Walling and Dr. Seb Lawson for being my go to people to badger with questions. Thank you to everyone in the ISL for your friendship.

I would also like to thank colleagues who have collaborated from other institutions: Eunja Kim, Eduardo Montoya, Jonathan George and Cameron Kirk at UNLV, Philippe Weck at Sandia National Laboratories, Kevin Knight at UCL, Ram Seshadri and Farnaz Kaboudvand at the University of California Santa Barbara, James Buckley and Ben Spencer at the University of Manchester. Thank you all for taking my structures and producing exciting results for our papers. It is a pleasure to work with such talented scientists.

Finally, thank you Ellis. Since meeting on the NGN CDT five years ago, you've had to put up with far more from me than you ever signed up for. Thank you for supporting me, feeding me, caring for me through life altering illness and major surgery and all while completing your own thesis. I couldn't have done this without someone to complain to.

Publications

S. E. O'Sullivan, S-K. Sun, S. M. Lawson, M. C. Stennett, F. Chen, Y. Masubuchi, C. L. Corkhill and N. C. Hyatt, "Low-Temperature Nitridation of Fe_3O_4 by Reaction with $NaNH_2$," *Inorg. Chem.*, 2021.

S. E. O'Sullivan, E. Montoya, S-K. Sun, J. George, C. Kirk, M. C. Dixon Wilkins, P. F. Weck, E. Kim, K. S. Knight and N. C. Hyatt, "Crystal and Electronic Structures of A_2NaIO_6 Periodate Double Perovskites (A = Sr, Ca, Ba): Candidate Wasteforms for I-129 Immobilization," *Inorg. Chem.*, vol. 59, no. 24, pp. 18407–18419, 2020.

N. B. A. Thompson, S. E. O'Sullivan, R. J. Howell, D. J. Bailey, M. R. Gilbert and N. C. Hyatt, "Objective Colour Analysis from Digital Images as a Nuclear Forensic Tool," *Forensic Sci. Int.*, p. 110678, 2020.

Conference presentations

University Nuclear Technology Forum, Liverpool, April 2017

Royal Society of Chemistry Radiochemistry Group Young Researchers Meeting, Leeds, November 2017

Uranium Science, Bristol, January 2019

49th Journées des Actinides, Sicily, April 2019

International Symposium on Nitride Technology, Barcelona, June 2019

Contents

Chapter 1

Introduction

The civil nuclear energy industry faces two pervasive challenges: the legacy of high profile accidents and the management of radioactive waste. A 2020 survey commissioned by the Institute for Mechanical Engineers in the UK reported accidents and waste as the most cited concerns regarding nuclear power in the public perception [1]. The work presented in this thesis takes a holistic approach to implementation of advanced nuclear fuel cycles, with a focus on accident tolerant uranium nitride fuel synthesis and potential oxynitride products arising from fuel degradation, as well as immobilisation hosts for two problematic long lived fission products, ^{129}I and ^{99}Tc, which will require more robust and tailored immobilisation and disposal strategies in future advanced fuel cycles.

Chapter 2 begins by detailing the underlying context of the work: the principles of nuclear fission and the nuclear fuel cycle, as well as focused discussion of uranium nitrides, iodine wasteforms and technetium wasteforms. This is discussed as a broad overview of topics, as specific literature reviews are contained within the subsequent, corresponding papers. This is followed by examination of the characterisation techniques used throughout the body of work in Chapter 3, considering both the underlying theory and experimental set up. Chapters 4 and 5 consider two synthesis methods in detail that are utilised in the subsequent manuscripts presented for publication. Chapter 4 details the design and commission of an ammonolysis furnace for nitride and oxynitride synthesis investigations. An alternative low temperature nitride synthesis route, using sodium amide, $NaNH_2$, is explored in Chapter 5, using the reaction between Fe_3O_4 and $NaNH_2$ as a case study. This paper developed new understanding of the mechanism of this low temperature nitridation mechanism, and the nature of the nitride and oxynitride products formed. This understanding and the skills developed in handling hazardous $NaNH_2$ in these reactions were carried forward and applied in Chapter 6.

Chapters 6 and 7 contribute to the development of accident tolerant fuels for nuclear reactor use, focused on uranium mononitride as one proposed candidate. In Chapter 6, potential novel synthesis routes to UN by reaction of uranium oxides with $NaNH_2$ and NH_3 are

---

[1] Institution of Mechanical Engineers, "PUBLIC PERCEPTIONS: NUCLEAR POWER.", IMechE, Westminster, 2020.

considered. Chapter 7 considers the possible formation of ternary uranium oxynitrides as potential loss of coolant accident or cladding failure products of nitride based fuels, with these also being of fundamental academic interest as potential novel compounds.

Chapters 8 and 9 consider immobilisation compounds for ^{129}I and ^{99}Tc, respectively, two key long lived fission products from future reprocessing of advanced nuclear fuels. The most widely accepted solution for high level waste (that is, waste streams containing highly radioactive fission products separated from reprocessing of spent fuel or spent fuel itself) is a multibarrier geological disposal concept. A layered approach of engineered barriers is utilised to isolate radionuclides from the environment, on a design basis of 100,000 years, the first layer being chemically incorporating a targeted fission product into a ceramic or glass immobilisation host. In this work, ceramic compounds are proposed for ^{129}I and ^{99}Tc. These papers consider a thorough structural characterisation with a view towards assessment for suitability as immobilisation hosts. The A_2NaIO_6 structures published in Chapter 8 are being considered for deposit in the International Centre for Diffraction Data repository.

The author's contributions to the presented papers (published or in progress) is as follows:

Chapter 5 "Low temperature nitridation of Fe_3O_4 by reaction with $NaNH_2$"; the author contributed: production of samples, X-ray diffraction (XRD) and analysis, analysis of thermogravimetric data (TGA-MS), writing of the manuscript. Scanning electron microscopy (SEM) data was acquired by S-K. Sun. TEM and electron diffraction data were acquired by S. M. Lawson. Mössbauer spectroscopy data was acquired by M. C. Stennett. The author analysed the SEM and Mössbauer data.

Chapter 6 "Investigation of reactions of sodium amide with uranium oxides for potential nitride synthesis"; the author contributed: design and commission of experimental apparatus, production of samples, XRD and analysis, SEM measurement and analysis, colour analysis, writing of the manuscript. XPS measurements were taken at the Photon Science Institute, University of Manchester, by B. Spencer and J. Buckley. X-ray absorption spectroscopy

(XAS) data were acquired by M. C. Stennett. The author analysed the XAS data and XPS data with assistance from C. L. Corkhill.

Chapter 7 “An investigation of the ammonolysis of β-$SrUO_4$ and $CaUO_4$ for ternary uranium oxynitride synthesis”; the author contributed: design and commission of experimental apparatus, production of samples, XRD and analysis, colour measurement, XAS measurement and analysis, EXAFS modelling, TGA-MS measurement and analysis, writing of the manuscript. XPS measurements were taken at the Photon Science Institute, University of Manchester, by B. Spencer and J. Buckley. Analysis of XPS data was performed by the author with assistance from C. L. Corkhill.

Chapter 8 “The crystal and electronic structures of A_2NaIO_6 periodate double perovskites (A = Sr, Ca, Ba): Candidate wasteforms for I-129 immobilisation”; the author contributed: preparation of samples, acquisition of XRD and analysis, analysis of neutron diffraction data, analysis of TGA-MS data, writing of the manuscript. TGA-MS and Raman data were acquired by S-K. Sun and analysed by the author. Raman DFPT calculations were performed by P. F. Weck, Sandia National Laboratory, using the structure models provided by the author. DFT structure modelling was performed by E. Kim, E. Montoya, J. George and C. Kirk, University of Nevada Las Vegas, using the structure model provided by the author. Tilt calculations were provided by K. S. Knight, using the structure model provided by the author.

Chapter 9 “The crystal and electronic structure of $Pb_2Tc_2O_{6.5}$: a vacancy ordered mixed valent pyrochlore”: the author contributed: sample preparation, analysis of neutron diffraction data, writing of the manuscript. XRD and SEM measurements were acquired by D. J. Bailey and analysed by the author. XAS measurements were acquired by D. J. Bailey and M. C. Stennett and analysed by the author. DFT calculations were undertaken by F. Kaboudvand and R. Seshadri, at University of California, Santa Barbara, using the structure model provided by the author.

Chapter 2

Literature review

2.1 Principles of nuclear fission

The isotopic content of a nucleus, that is the number of neutrons, dictates the stability of the nucleus. The strong nuclear force binds neutrons to protons while the electrostatic force causes repulsion between the equally positively charged individual protons, thus the neutrons act to stabilise the balance of forces. Differing neutron numbers within the nucleus result in different isotopes of the same atom, which are not always stable. An unstable nucleus will spontaneously undergo a radioactive decay process in order to mitigate the instability. The three main decay routes are alpha decay (emission of an alpha particle composed of two protons and two neutrons), beta decay (emission of an electron or positron, or electron capture) and gamma decay (emission of high energy photons), which may occur individually or in tandem. Of interest to nuclear power generation is fission, whereby the unstable nucleus splits into two or more daughter nuclei or fission products. This process results in massive energy yields, that can be subsequently harnessed for electricity generation.

The fuel of a nuclear reactor is based around a fissile material, which is one that can undergo the described fission decay route and in doing so, releases neutrons alongside the daughter nuclei. Absorption of neutrons by other fissile nuclei destabilises those nuclei, which prompts their own fission decay events. A fissile material is one where the number of released neutrons in a fission event is on average one or greater and thus the chain of fission events is self-sustaining. Spontaneous fission without prior manipulation is rare even in heavy elements. However, ^{235}U, ^{233}U and ^{239}Pu (the latter being formed by neutron capture induced transmutation of fertile ^{232}Th and ^{238}U nuclei respectively) are fissile isotopes. Providing these isotopes with an initial neutron bombardment results in the chain of fission events required to give huge energy outputs for subsequent electricity generation.

The daughter nuclei from fission are rarely identical, with asymmetry of fission products being favoured as this distributes the nuclei preferentially to form those of magic numbers which show extra stability. This is visualised in Figure 1, with two peaks corresponding to light isotopes around Z = 90 and heavier isotopes around Z = 140.

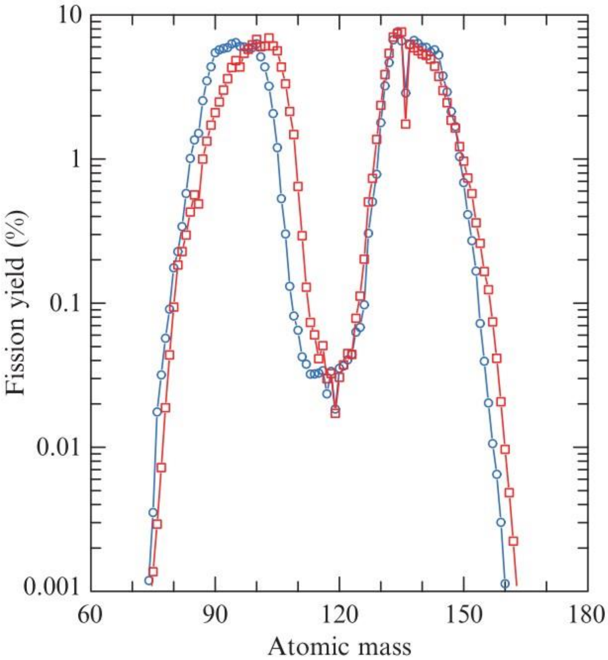

Figure 1. Fission yield from ^{235}U (blue circles) and ^{239}Pu (red squares). Taken from Konings, Wiss and Guéneau (2010) [1].

2.2 Life cycle of nuclear fuels

Of the fissile isotopes, ^{235}U is the most prevalent in various chemical forms in reactors. However, the relative abundance of ^{235}U in natural uranium is extremely low at 0.7%, the remainder being predominantly ^{238}U. Although ^{238}U is fertile, in that it can be transmuted to a fissile isotope, the low proportion of fissile ^{235}U is usually mitigated by enrichment to improve energy yield. Typical enrichment raises the percentage of ^{235}U to 3 - 5% [1]. Most reactors utilise enriched uranium in some format, except for the early generation of Magnox and CANDU reactor designs that use(d) natural uranium metal.

95% of the current operational fleet of nuclear reactors are light water reactors (LWRs) [2], which have only used UO_2 or mixed oxide fuels (MOX) thus far [3]. UO_2 fuel is also prevalent for other reactor designs, such as the Advanced Gas-Cooled Reactor (AGR),

Pressurised Heavy Water Reactor (PHWR) and Reaktor Bolshoy Moshchnosti Kanalniv

(RMBK). MOX fuel combines uranium and plutonium fissile elements in the form $(U,Pu)O_2$, composed of 3 to 5% PuO_2 in either depleted or unenriched UO_2 [4]. The plutonium content for MOX is partitioned from reprocessing of spent nuclear fuel.

Necessary for any chosen chemical composition of fuel is a cladding material. This outer layer to the fuel assembly prevents contact of the fissile material with the coolant. This is to stop release of fission products to the coolant and contamination of the reactor vessel, which would exponentially increase the radioactive waste burden of decommissioning the reactor. However, the cladding must also not interfere with or impede the fission chain reaction, therefore cannot have a high cross section (probability) for neutron absorption. It must also meet the demands of reactor use, such as the operating temperature, being irradiation resistant and chemically inert with respect to the coolant. Most cladding options are zirconium alloys, some of these falling under the Zircaloy umbrella of zirconium and tin alloys [1]. Now defunct Magnox fuel assemblies used magnesium alloy and AGRs use stainless steel cladding [5].

Typical UO_2 fuels reside in a reactor core for 18 months, thereafter it is classified as spent nuclear fuel (SNF). SNF contains a complex mixture of fission products which make up 3 to 4% of the composition [6] and account for the high activity levels of 10^6 GBq MT^{-1} of fuel. Immediately after retrieval from the reactor, SNF is stored in interim cooling ponds to manage the initial decay heat of those fission products. This short term storage also allows for the decay of some of the short lived fission product radioisotopes, such as ^{131}I with a half life (time taken for the radioactivity to drop to half the initial level) of 8 days.

The fate of SNF is dictated by a combination of political atmosphere, availability of reprocessing facilities and the suitability of the existing reactor fleet for reprocessed MOX fuel (including regulatory approval). Direct disposal of SNF is known as an open fuel cycle, whereas reprocessing considers SNF as a resource to be “recycled” in a closed fuel cycle. The aim of reprocessing is to separate or partition Pu and U, while also manipulating other isotopes into forms that are better suited for disposal routes.

Reprocessing of SNF largely utilises aqueous solvent extraction processes, such as PUREX (plutonium uranium reduction extraction) which has been in use for over half a century [7] to recover U and Pu. These processes involve stripping the spent fuel of its claddings, dividing into small pieces, dissolving in acid and adding an organic solvent. For PUREX, these are nitric acid and tri-butyl phosphate (TBP). The majority of fission products preferentially partition to the aqueous acid phase (except volatile species which are recovered from the off gas) while the U and Pu partition to the organic phase. Since the two phases are immiscible, they can be separated, with the U and Pu recovered for MOX fuel fabrication. The aqueous phase, or raffinate, can then be processed to remove further targeted isotopes by ion exchange or flocculation techniques.

Once fission products are separated, it is necessary to manipulate them into a wasteform suitable for disposal. A wasteform is the stable solid product of conditioning (e.g. vitrification, cement encapsulation) of the wastes that is insoluble and prevents migration of radionuclides to the disposal environment. Fission product waste streams are categorised as high level waste (HLW) due to the inherent heat generation and activity concentration. Accepted wasteforms for HLW are broadly glasses, ceramics and glass-ceramics as these immobilise the problematic isotopes within the chemistry of the wasteform. Immobilisation is required for long lived isotopes, such as ^{129}I or ^{99}Tc which have half-lives of 15.74 x 10^6 and 2.13 x 10^5 years respectively and also show high mobility in the environment [8], [9]. Glasses are an amorphous network with no long range order, while ceramics are crystalline. Glass-ceramics are compositionally glass formations but contain a high percentage of crystalline formation within. Glass wasteforms are fabricated in a process called vitrification. The aqueous raffinate is dried and combined with a borosilicate based glass frit in a high temperature melt. Due to the amorphous silica based network of glasses, they can readily accept a variety of isotopes. This can occur by substitution for Si, becoming covalently bonded network formers, or by forming ionic bonds to oxygen within the silicate as network modifiers. However, certain isotopes, such as those of I (recovered from off gas scrubbing during the initial reprocessing of SNF) and Tc, are extremely volatile under the calcining conditions of vitrification. Ceramic wasteforms, often based around titanate materials, such as Synroc [10] and the constituents thereof like brannerite [11], hollandite and zirconolite

[12], offer tailored immobilisation for specific fission products. In ceramics, radioisotopes are substituted into specific atomic positions within the crystalline structure, or within interstices, constrained by the ion size, charge and the coordination of the site. Substitution may be concurrent with charge compensation by formation of cation or anion vacancies, point defects or changes in the structure type.

Final disposal of the conditioned wasteforms is destined to be in deep geological disposal, as the waste should be isolated from the biosphere for the duration of its hazardous lifetime, which is generally accepted as over 100,000 years. Credible deep geological disposal options are repositories and borehole disposal, with the former favoured by the UK [13]. Geological disposal makes use of the multibarrier concept, where the engineered layers of infrastructure and host geology are used to mitigate migration of radioactive isotopes over the lifetime of the repository. The glass or ceramic wasteforms are packed into cannisters which are loaded into vaults in the region of 250 to 1000 m below ground. The vault space is backfilled with either grout or a bentonite clay and capped off to prevent ingress. The host geology provides the final barrier layer. A geological repository is under licensing and construction at Onkalo, Finland, with an expected operational start in 2023 [14].

2.3 Accident tolerant fuels

A severe nuclear accident is defined as an incident involving reactor core melt and release of fission products [15]. The ubiquitous zirconium alloy clad UO_2 for LWRs has been implicated in the high profile nuclear accidents : Three Mile Island (1979), Chernobyl (1986) and most recently Fukushima Dai-ichi (2011) [15]–[17]. In each of these accidents the UO_2 fuel, which has a comparatively low thermal conductivity, was subject to dangerous over-heating. Large temperature increases were caused by interruptions to the coolant supply (Three Mile Island and Fukushima) or criticality resulting from reactor testing operations (Chernobyl). The superheating of the fuel caused cladding failures, partial reactor core melt along with steam and hydrogen explosions [15] that compromised radiation containment. In light of these events, accident tolerant fuels (ATF) are under continued development.

An ATF assembly should tolerate loss of coolant conditions for longer timescales than the UO_2 zirconium alloy equivalents, whilst also maintaining or improving fuel performance [18], [19]. A loss of coolant accident is categorised as a design basis accident (DBA), which is not an anticipated operational occurrence (AOO) in that it is not expected to occur within the reactor lifetime, however it could feasibly happen. A DBA is mitigated in part by reactor design choices and engineering infrastructure, with ATF being one option.

Proposed ATF fuel compositions include uranium or uranium-plutonium nitrides [20], [21], uranium or uranium-plutonium carbides [12][1] and uranium silicides [22] for ceramic options and a uranium-molybdenum metallic option [18]. These could be combined with improved cladding choices such as oxidation resistant coatings for zirconium cladding [16], SiC claddings [23] or refractory alloys [24]. Improved fuel design instead of the typical pellet assembly considers encapsulated fuel kernels called Fully Ceramic Microencapsulated fuels (FCM) [25], similar to the TRISO concept [26].

The principle advantage to the proposed ATF types is their increased thermal conductivity. For example, the thermal conductivities of UN, U_3Si_2 and U-10Mo (U metal with 10 wt% molybdenum) are 20, 15 and 37 W/m·K respectively, whereas the thermal conductivity of UO_2 is just 4 W/m·K [18]. Increased thermal conductivity allows for the fuel to operate at a lower temperature with a decreased temperature gradient from the centre of the fuel pellet, which reduces the likelihood of pellet cracking from thermal stress and subsequent release of fission products [27]. A corollary of increased thermal conductivity is decreased energy stored per unit mass of the fuel [18]. This confers safety benefits for longer timescale loss of coolant accidents, where the longer term driver for cladding heating is the decay heat of the fuel and contained fission products [28]. Challenges of these proposed ATF compositions include the increased cost of fabrication, understanding of irradiation behaviour and behaviour under loss of coolant accidents [16]. Uranium nitrides are known to oxidise readily [29] and are proposed to form uranium oxynitrides which are currently under represented in the literature [30], [31]. Although uranium silicides offer increased thermal conductivity, the reduced melting temperature compared to that of UO_2 leaves a near identical margin to fuel melt [22]. FCM fuels show challenges in fuel enrichment levels and reactor longevity [18]. Recent

	UO_2	FCM	U-10Mo	UN	U_3Si_2
Thermal conductivity (W/m.K)	4	19 UN kernel	37	20	15
Heat capacity at 500 °C (J/kg.K)	300	230 UN kernel	145	230	250
Melting temperature (°C)	2840	2400 SiC 2762 UN kernel	1150	2762	1665
U density (g/cm^3)	9.6	1-2	16.9	13.5	11.3

Table 1. Thermophysical properties of UO_2, UN and other accident tolerant fuels after Youniou and Sen [18]; FCM denotes fully ceramic microencapsulated fuel.

comprehensive review of the literature identified limited experimental data for the understanding of fission gas release and techno-economic assessment [27], which needs addressing prior to feasible consideration of ATF implementation.

2.4 Uranium nitride as an accident tolerant fuel

Uranium nitride, UN, fuels have been advanced as an accident tolerant alternative to conventional uranium dioxide, UO_2, fuels [16], [18], [32], [33]. Uranium nitride fuels have been successfully tested in the Russian BR10 and US FFTF and EBR-II sodium cooled fast reactors [34], and also thermoelectric nuclear power systems [35]. However, UN fuels have not yet been tested in conventional LWRs, although suitable test pins have been fabricated and an experimental irradiation campaign is planned by Oak Ridge National Laboratory using the High Flux Irradiation Reactor [36], [37].

In this context, the primary advantages of UN fuels include higher thermal conductivity, longer fuel cycle time, as well as higher fissile material density; Table 1 summarises some key properties of accident tolerant fuels, reviewed by Youniou and Sen [18]. The thermal conductivity of UN is five times greater than that of UO_2, which reduces the centreline temperature of the fuel and the stored energy per unit mass, increasing the margin for fuel melting [38]. This clearly offers inherent safety advantages, particularly in a loss of coolant accident. In addition, it has been shown that the reduced fuel temperature reduces the migration of fission products and actinides, along the lower thermal gradient, which reduces fuel swelling [39]. The density of fissile material is 40% greater in UN compared to UO_2, which, combined with improved neutronic characteristics, is estimated to increase the fuel cycle length from 18-months for UO_2 to 25 months for UN, assuming a PWR standard fuel assembly [18]. The reduced number of reactor outages is estimated to afford savings of the order of $5M per year. In comparison with conventional UO_2 fuels, UN fuels are expected to be compatible with PUREX reprocessing technology, which is industrially mature, and compatible with conventional fuel cladding materials, such as Zircaloy [18], [40].

Although UN fuels show considerable promise for application as actinide fuels, they also present some considerable drawbacks, which are the focus of current research. The key challenges for deployment of uranium nitride fuels are the maturity of the fuel manufacture process, the oxidation resistance of the fuel, and the high cost of fuel fabrication. UN is pyrophoric when finely divided necessitating an oxygen free environment during large scale fuel manufacture [12]. UN also undergoes hydrolysis in water and in steam [40]–[42], which poses the main barrier to deployment in LWR systems due to the risk of contamination of the water cooling circuit in the case of fuel pin failure. However, UN is believed to be more compatible with liquid metal coolants used in fast reactor systems [43]. A further challenge to UN fuel manufacture process and cost is the requirement for isotopic enrichment in ^{15}N, to mitigate the formation of ^{14}C by (n, p) reaction on ^{14}N (99.6% natural abundance) [44]. ^{14}C is a moderately long lived nuclide, half life 5,730 years, and is problematic in the context of radioactive waste management and disposal due to its facile transport as a gas (e.g. as methane) resulting in rapid migration to the biosphere from the disposal system, solubility as inorganic carbonate, and potential uptake in organisms [45]. However, the cost of ^{15}N enrichment is significantly offset by reduction in the required level of ^{235}U enrichment due to the improved neutron economy [18].

Consensus on fuel manufacture routes for UN fuels has not yet been reached, this is in no small part due to the absence of convergence on a fuel pellet design, which will clearly govern the manufacture route. Fuel pellet designs have taken different approaches to improving the oxidation resistance of UN, and include [18], [46]–[50]:

- Fabrication of U_2Si_3 – UN composites produced by liquid phase sintering, through which more sensitive UN phase is encapsulated and protected.
- Fabrication of UN – UO_2 composites using spark plasma sintering, to produce a composite which balances the advantageous and disadvantageous thermophysical and oxidation behaviour of the components.
- Alloying of UN with CrN by spark plasma sintering, to produce a solid-solution composite, in which the alloying metal produces an interfacial passivating oxide layer when exposed to hydrolysis conditions.
- Production of coated ceramic fuels, in which a UN kernel is encapsulated by an inert matrix to provide a barrier against oxidation and hydrolysis.

Nevertheless, these routes all require UN as a feed material for which there are multiple synthetic routes, as reviewed below.

2.4.1 Uranium – nitrogen phase diagram

The uranium – nitrogen phase diagram at 1 atm nitrogen pressure was established by Bugl and Bauer in 1964 [51], following that of Rundle *et al.* [52], and, although subsequently reinvestigated and subject to minor amendment, is still regarded as definitive. This is shown in Figure 2. Rundle and Bugl and Bauer unequivocally established the existence of three binary uranium nitrides: the mononitride UN, the sesquinitride U_2N_3, and the dinitride UN_2. Earlier reports had identified nitrides of composition U_3N_4, U_5N_4 and U_5N_2, however, their existence was not subsequently confirmed in these phase diagram studies and these compounds are regarded as discredited [51].

2.4.2 Crystal structure and properties of the uranium nitrides

Uranium mononitride, UN, is isostructural with NaCl (*Fm*-3*m*; a= 4.889 Å), with a density of 11.32 g cm^{-3} [51]–[53]. UN is reported to show low electrical resistivity at room temperature (1.6×10^{-4} Ω cm) and exhibit antiferromagnetic ordering below 52 K [54]. Uranium dinitride, UN_2, is isostructural with CaF_2 (*Fm*-3*m*; a= 5.310 Å), with a density of

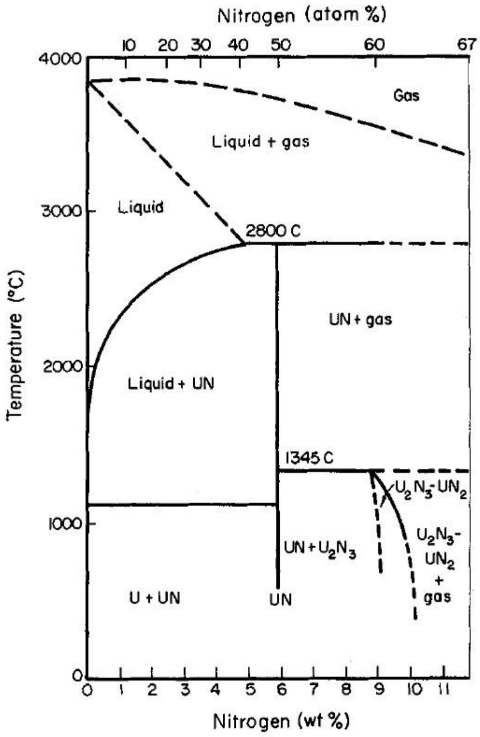

Figure 2: Uranium – nitrogen phase diagram at 1 atm nitrogen, by Bugl and Bauer [51].

11.73 g cm^{-3} [51]–[53]. Uranium sesquinitride, α-U_2N_3, is isostructural with bixbyite Mn_2O_3 (*Ia*-3, a = 10.678 Å), with a density of 11.24 g cm^{-3} [51]–[53]. A continuous solid solution is possible between UN_2 and α-U_2N_3, with the formation of ordered nitrogen vacancies and cation displacements leading to a structural phase transition near a composition $UN_{1.75}$ [55], [56]. Antiferromagnetic behaviour is reported across the solid solution, with the Neel temperature decreasing from 54 K at composition $UN_{1.5}$ to 8 K at composition $UN_{1.8}$ [57]. α-U_2N_3 transforms to β-U_2N_3 with the hexagonal La_2O_3 structure (*P*-3*m*1; a = 3.700 Å, c = 5.825 Å) at 1100 °C under N_2, which can be recovered to room temperature [56]; this material is isostructural with Th_2N_3.

The decomposition sequence of the binary uranium nitrides was investigated by Silva *et al.* and offers one route to the synthesis of lower nitrides from UN_2 [58], through loss of oxygen. Under argon, UN_2 was reported to fully decompose to α-U_2N_3 at 675 °C, partial decomposition of α-U_2N_3 occurred above 975 °C, and was complete at 1100 °C. However, UO_2 was also observed as a contaminant in these decomposition reactions through adventitious oxidation.

2.4.3 Synthesis of uranium nitrides

Several different approaches have been developed for the synthesis of uranium nitride, each of which involves some challenge.

Direct nitridation of uranium metal is reported at 550-900 °C under 1 atm N_2 [59]. The nitride product was formed as reaction film on the surface of the metal, below 750 °C, the product was stated to comprise primarily UN_2 with some α-U_2N_3, whereas above 750 °C a mixture of UN_2, α-U_2N_3 and UN were obtained. The reaction was reported to follow a parabolic rate law, the rate was significantly reduced by oxidation of the metal surface prior to nitridation. This method does not yield single phase uranium nitrides. Arc melting of uranium metal under 20 atm N_2 was reported to yield stoichiometric UN by Bugl and Bauer [51].

Nitridation of uranium hydride, UH_3, using N_2 gas was reported to be more effective for the synthesis of uranium sesquinitride [51], [60]:

$$2UH_3 + \left(\frac{3+x}{2}\right)N_2 \rightarrow U_2N_{3+x} + 3H_2 \quad (1)$$

Uranium metal was first hydrided by reaction with H_2 gas at 300 °C; the hydride product spalls from the surface of the metal as the reaction proceeds due to the increase in molar volume, however the hydride is highly pyrophoric and must be maintained under rigorously anoxic conditions. Reaction of UH_3 with N_2 gas at 1 atm was reported to occur above 300 °C, to yield α-U_2N_{3+x}. Conversion of α-U_2N_{3+x} to UN was achieved by heating to 1150 °C, following the decomposition sequence described by Silva *et al.* [58].

Serizawa reported synthesis of α-U_2N_{3+x} by ammonolysis of U metal or UH_3 at 300 °C. Starting with the metal, some products were observed to contain both UH_3 and α-U_2N_3, implying the reaction involved an initial hydridation step, followed by reaction with N_2 and/or NH_3 [61].

In these reactions, the oxidised surface of the uranium metal must be removed prior to hydridation, nitridation or ammonolysis, by pickling in concentrated HNO_3 and washed with organic solvents to remove the oxidised surface. Handling of pyrophoric U metal, extremely pyrophoric UH_3, and pure H_2 gas is extremely hazardous and this synthetic method therefore requires rigorous risk assessment and stringent anoxic conditions.

Preparation of uranium nitrides from uranium fluorides has been explored to circumvent the hazard of working with U and UH_3. Reaction of UF_4 with NH_3 at 800 °C was reported to yield "U_3N_4", though the actual product is uncertain given the limited characterisation data [62]. Yeamans *et al.* reported the synthesis of uranium nitrides by ammonolysis of $(NH_4)_4UF_8$. This reagent was produced by ball milling of UO_2 with a small excess of NH_4HF_2 for the target stoichiometry, followed by aging of the mixture at room temperature for 50 days [63]. Ammonolysis of $(NH_4)_4UF_8$ at 800 °C yielded UN_2, with the lower nitrides α-U_2N_3 and UN by annealing under argon at 700 °C and 1100 °C, respectively. However, no characterisation data were reported to evidence the purity of the products and later application of this approach was shown to afford products with significant UO_2 contamination, either through incomplete precursor formation or, more likely, by adventitious oxidation [63].

Carbothermic reduction of uranium oxides has been investigated for the synthesis of uranium nitrides and mixed uranium-plutonium nitrides, in particular for the production of microspheres for coated ceramic fuels [64]–[66]. Above 1723 K, carbothermic reduction of UO_2 occurs with excess of C under 1 atm N_2, producing a nitride-carbide $UC_{1\text{-}x}N_x$ intermediate:

$$UO_2 + (2+x)C + \left(\frac{1\text{-}x}{2}\right) N_2 \rightarrow UC_{1\text{-}x}N_x + 2CO \qquad (2)$$

Further heating at 1723 K leads to formation of UN by the slow reaction:

$$UC_{1\text{-}x}N_x + \left(\frac{x}{2}\right) N_2 \rightarrow UN + xC \qquad (3)$$

However, carbothermic reactions are prone to yield products with residual UO_2 due to loss of C and adventitious oxygen, and the nitride products contain significant C impurity carried over from the intermediate phase. A proposed option for removing this impurity is annealing of the product under H_2, to evolve HCN, although with an obvious chemotoxic hazard [67].

Recently, interest has developed in the synthesis of transition metal nitrides, by reaction of the counterpart oxide in $NaNH_2$ molten salt at relatively low temperature of 170 – 300 °C [68]–[71]. Low temperature nitridation reactions have been applied to synthesise InN, $Fe_{2+x}N$, MnN, Cu_3N, from oxide substrates, amongst others, but have not been applied to uranium oxides. In a typical reaction, a transition metal substrate is mixed with an excess of $NaNH_2$, which is transferred to a lidded stainless steel crucible and heated for several hours or days in a closed reaction vessel. Under such conditions, the $NaNH_2$ forms a low melting molten salt eutectic with NaOH, present as a common impurity in commercial grade reagent, or formed by adventitious water. Nitridation takes place within the molten salt, producing NaOH as by product, which is believed to be the thermodynamic driving force for the reaction [70], for example:

$$3Fe_2O_3+7NaNH_2 \rightarrow 2Fe_3N+7NaOH+2N_2+3NH_3 \tag{4}$$

The nitride product is recovered by filtration after soaking the crucible in ethanol to destroy $NaNH_2$, by formation of sodium ethoxide [68]–[71]. Miura *et al.* suggest that the effective concentration of NH_2^- in such molten salt reactions is 500 times that of NH_3 under ammonolysis conditions, making $NaNH_2$ a potent nitriding agent [68]. The reaction is also strongly reducing, as evidenced by reduction of CuO to Cu by reaction with $NaNH_2$ at 190 °C, in contrast to Cu_3N at 170 °C [71]. This synthesis avoids the need for handling of toxic NH_3 gas, however, $NaNH_2$ must itself be stored and manipulated under dry anoxic conditions to avoid hydrolysis the formation of explosive peroxide degradation products [72]. The nitride product produced from counterpart oxides by reaction with $NaNH_2$ are typically nanocrystalline which suggests a dissolution - precipitation reaction mechanism. In addition, XRD data often present considerable diffuse scattering which point to the presence of an amorphous phase. SEM and XPS analysis demonstrate quantitative N incorporation within product materials but also show evidence for the presence of O and OH^-, which may point to the presence of amorphous oxide or oxynitride products, or residual oxides.

Given the apparent efficacy of $NaNH_2$ mediated nitridation of transition metal oxides at low temperature, the potential application of this methodology to synthesis of uranium nitrides from oxide substrates would be worthy of investigation.

2.4.4 Hydrolysis and oxidation of uranium nitrides

The hydrolysis of UN in water vapour / argon gas was investigated by Dell *et al.*, who reported the onset of reaction at 300 °C with rapid reaction above 340 °C [41]. From gravimetric analysis and mass spectroscopy of evolved gas, they proposed the following fundamental reaction:

$$UN + 2H_2O \rightarrow UO_2 + NH_3 + \frac{1}{2}H_2 \tag{5}$$

The NH_3 yield was reported to be 60-100% of that required by this reaction, with the presence of α-U_2N_{3+x} in products for which the NH_3 recovery was <100% determined by X-ray diffraction. Thus, α-U_2N_{3+x} was postulated to be an intermediate in the decomposition reaction, which was proposed to undergo hydrolysis according to the following equation:

$$U_2N_3 + 4H_2O \rightarrow 2UO_2 + \frac{8}{3}NH_3 + \frac{1}{6}H_2 \tag{6}$$

However, in some experiments a weight change consistent with complete hydrolysis of UN to UO_2 was established, but α-U_2N_{3+x} was observed in the product. Evolved gas analysis implied a stoichiometry for the nitride phase of $x = 1.56$, i.e. $UN_{2.28}$, which was, quite reasonably, considered implausible. The authors therefore concluded some fraction of N must therefore be incorporated within the UO_2 lattice, implying the presence of an oxynitride UO_2N_x, with nitrogen present as interstitials. The X-ray diffraction data were reported to exhibit broad and diffuse reflections which could be consistent with this interpretation. Subsequently, Sugihara and Imoto investigated the hydrolysis of UN and α-U_2N_3, their findings were in broad agreement with those of Dell *et al.*, including the fundamental reaction mechanisms, although onset of reaction with water vapour was reported to initiate above 250 °C [73]. Importantly, Sugihara and Imoto also hypothesised the formation of an oxynitride UO_2N_x as a product of UN hydrolysis based on gravimetric and gas chromatography analysis.

Dell *et al.* also investigated the oxidation behaviour of UN, with onset of reaction above 260 °C [74], the reaction sequence was reported to involve first oxidation of UN to yield UO_2N_x and α-U_2N_{3+x}, the N released from UN oxidation reacting with further UN to yield α-U_2N_{3+x}. In the second reaction step α-U_2N_{3+x} and UO_2N_x are oxidised to poorly crystalline and amorphous UO_3N_x ($0.2 < x < 0.4$), with no residual UN or α-U_2N_{3+x}, according to X-ray diffraction and infra-red spectroscopy. The oxynitrides UO_2N_x and UO_3N_x were hypothesised to account for residual N present in the product materials, which was unaccounted for based on gravimetric and gas pressure measurements. The UO_3N_x oxynitride phase was reported to evolve N only gradually above 250 °C, with some retention even to 500 °C. Density measurements suggested that the N was not trapped in interstices within the material as N_2 gas. Additionally, UO_3N_x oxynitride was reported to react vigorously with water at room temperature, with effervescence due to release of N_2 gas.

Rama Rao *et al.* investigated the hydrolysis and oxidation of UN microspheres, with up to 10.9 mol% UO_2 impurities, using thermal analysis and X-ray diffraction [75]. This study confirmed the results of the previous work concerning the fundamental hydrolysis reactions of UN, yielding UO_2. However, Rama Rao *et al.* reported UO_2 to be the product from UN oxidation only in materials with UO_2 impurity. In contrast, U_3O_8 was the reported product from pure UN hydrolysis. They explained this difference in behaviour in terms of the different sequence of layered oxidised products between UN and UN doped with UO_2 and the relative shielding of interface products from further oxidation. This study also reported 17-55% retention of N within the UO_2 product, consistent with the work of Dell *et al.* and Sugihara and Imoto, however, the authors did not rationalise this observation.

More recently, Jolkkonen *et al.* investigated the reaction of UN at 500 °C in 0.5 bar steam / Ar [42]. Hydrolysis of UN was determined to evolve NH_3 gas, verified by mass spectroscopy, and the product was determined by X-ray diffraction to be a mixture of UO_{2+x} and α-U_2N_{3+x}, which is broadly consistent with the work of Dell *et al.* and Sugihara and Imoto. The authors report that at least one fifth of the initial N inventory was retained within the product and acknowledge the formation of an oxynitride phase, in consensus with earlier work. Importantly, these authors undertook inert gas fusion analysis of the residue material to fully evolve O and N, in contrast to earlier studies in which N retention was inferred through mass and pressure balance consideration. Therefore, significant N retention in the product of UN hydrolysis at up to 500 °C has been definitively established, though not necessarily within an oxynitride phase. The Xray diffraction data of hydrolysis residue incorporating 1.11 wt.% N was published by these authors and are in excellent agreement with those of stoichiometric $UO_{2.00.}$ Some weak diffuse scatter is evident in the diffraction data which could be consistent with a second phase. These data imply that any oxynitride phase must be present as an amorphous component.

Hydrolysis of UN at 23 °C and 90 °C was investigated by Sunder *et al.*, which was reported to produce UO_2, plus, at 90 °C, UN_2, α-U_2N_3, U_3O_7, UO_3 [76]. These findings are in broad agreement with the high temperature hydrolysis studies reported above, albeit with lower reaction rates, however, these data are of importance because they suggest that UN fuels are not passively safe in wet storage, should the fuel cladding be compromised. Sunder *et al.* reported X-ray photoelectron spectroscopy data from the surface of UN subject to aqueous corrosion, which could be interpreted as an incomplete film of UO_2 overlying UN; no evidence for oxynitride formation was reported.

2.5 Tailored wasteforms for immobilisation of iodine-129

Iodine-129 is a nuclide of key concern in the safety case for radioactive waste disposal [8], [77]–[79], due to the significant thermal fission yield (0.7%), long half life (1.6 x 10 y), high aqueous solubility and mobility, uptake by living organisms, and concentration in the human thyroid gland. ^{129}I is considered to have unlimited solubility and negligible sorption in performance assessment of geological disposal facilities [80]. Thus, in the long term, ^{129}I is the dominant contributor to the radiological risk to future population from disposed radioactive wastes, although the specific activity is relatively low. The current practice in management of ^{129}I in aqueous effluents is discharge, dilution and dispersal to the marine environment, however, in the context of future advanced fuel cycles, regulatory limits may require capture and immobilisation of ^{129}I for geological disposal [8], [79], [81], [82].

Aqueous reprocessing of spent nuclear fuel, using the PUREX process, evolves 93-99% of the iodine inventory to the Dissolver Off Gas system, as molecular iodine, I_2 [83]–[85], but with a small concentration of inorganic and organic iodide compounds such as HI and CH_3I [86]. The remainder of the iodine is contained within insoluble AgI and PdI_2 [84], or retained within the highly active raffinate as iodide, I^- [83], [84], which is routed to vitrification. Iodine capture from dissolver off gas is conventionally achieved by caustic scrubbing with NaOH, yielding a solution of NaI and $NaIO_3$. Alternatives, as reviewed by Riley *et al.*, include [8]:

- The Mercurex process, which employs a nitric acid solution of $Hg(NO_3)_2$ and affords a dissolved mixture of HgI_2 of $Hg(IO_3)_2$.
- The Iodox process, which uses highly concentrated HNO_3 as a scrubbing medium, affording dissolved iodate, IO_3^- species.
- The electrolytic process, involving a nitric acid solution of Co^{3+}, as an oxidant, which is maintained by electrochemical potential, yielding dissolved periodate, IO_4^-, species.

Thus, future immobilisation of ^{129}I from the dissolver off gas scrubber may proceed from an aqueous solution of iodide I^-, iodate IO_3^-, or periodate IO_4^-, species, which can easily be converted to the counterpart Na or Ag salt.

Riley *et al.* reviewed the solid sorbents utilised to recover iodine from the dissolver off gas [8], which include Ag (or other metal) modified zeolites, ceramics or aerogels, which yield AgI or other metal iodides by capture of iodine from the gas phase. Since these sorbents are already in the solid phase and generally of complex chemical composition, direct immobilisation by incorporation in a glass or ceramic wasteform is the strategy of choice (although considered, cement immobilised sorbents are unlikely to have sufficient chemical durability over the required time frame [87] and are thus not considered further here).

Here, the focus is on the development of tailored wasteforms for ^{129}I from advanced fuel recycle, where there is the opportunity to develop a matrix tailored to the speciation of iodine afforded by the dissolver off gas scrubber. Therefore, potential wasteform options are considered assuming a feed of simple iodide, iodate or periodate salt, since direct immobilisation of solid adsorbents is the most efficient strategy for these wastes, which will not be considered further here. Nevertheless, some wasteform options could be exploitable for solid phase adsorbents such as borosilicate glasses or glass composites.

2.5.1 Vitrified wasteforms

Iodine incorporation has been investigated in several glass systems as an immobilisation medium, including first generation borosilicate glasses, and tailored matrices such as silver iodide and chalcogenide glass systems.

2.5.1.1 Borosilicate glasses

Iodine solubility in borosilicate waste glasses is estimated to be 1-5 mol% [88], [89], which is sufficient for the expected concentration in high level waste feeds, but too low for utilisation as a tailored immobilisation host. Incorporation is limited by volatilisation from the melt rather than solubility in the glass matrix, a comprehensive review by Jubin *et al.* estimated that 80% of the iodine inventory is volatilised under process conditions [85], which is typically recovered in the off gas system by Ag-based adsorbents. Under process conditions, iodine is typically incorporated as the I^- species within the extra-framework cavities of the glass structure, as tetrahedral $(Na,Li)_4I$ clusters, similar to those formed in iodosodalites, according of X-ray absorption spectroscopy studies [88], [90].

2.5.1.2 Silver iodide glasses

$AgI-Ag_2O-M_xO_y$ glass systems have received considerable attention for application as a fast ion conductor, in particular those with $M_xO_y = B_2O_3$, P_2O_5 and TeO_2 [91]–[94], in which the

AgI incorporation may reach 30-60 mol%. X-ray absorption spectroscopy studies established incorporation as iodide species, with no evidence for phase separation of AgI [94]. The AgI-Ag_2O-P_2O_5 system was developed by Fujihara *et al.* [95] as a potential immobilisation matrix, achieving 60 mol% AgI incorporation, with a low melting temperature of 400 °C resulting in negligible volatilisation. The 50(AgI)-30(Ag_2O)-20(P_2O_5) glass composition was reported to exhibit a low forward release rate for iodine of 6×10^{-6} g m^{-2} d^{-1} at 35 °C under reducing conditions. Investigation of the 30(AgI)50(Ag_2O)-20(P_2O_5) composition by Yang *et al.* confirmed iodine incorporation as iodide species by X-ray photoelectron spectroscopy and determined a low leach rate of 1.7×10^{-4} g m^{-2} d^{-1} at 90 °C under air [96]. More recently, Lemesle reported an interesting family of AgI-$AgPO_3$-P_2O_5 glasses, capable of incorporating 35 mol% AgI, with a low melting temperature of 400 °C, precluding I volatilisation [97]. Using multinuclear solid state NMR spectroscopy, they showed that AgI was incorporated by occlusion within cavities in the glass network, and, therefore, polymerisation of the glass was not significantly affected.

2.5.1.3 Chalcogenide glasses

Glasses of the GeS_2-Sb_2S_3 and $GeSe_2$-Sb_2Se_3 system, modified by addition of metal iodides, MI (M = Cs, Rb, Cu, Pb, Zn) have received attention for application as infra-red transmissive windows. Incorporation rates of 10 mol% MI are possible at 800 °C, with quantitative retention of the iodine inventory (albeit melting in a sealed tube) [98]–[100]. The mechanism of incorporation is believed to be the formation of non-bridging Sb-X bonds (X = halogen) which are charge compensated by the M cation. Glasses in the As_2S_3–Sb_2S_3–PbI_2 and As_2S_3–Sb_2S_3–Bi_2S_3–PbI_2 system have also been studied as nonlinear optical materials, incorporating up to 40 mol% PbI_2 [101]. In these applications, such glasses must exhibit high chemical durability, however a systematic study of chalcogenide halide glass dissolution has not been reported.

2.5.1.4 Glass composites

To address the problem of volatilisation of iodine from open glass melts, the fabrication of glass-composites has been explored, in which the objective is to encapsulate an iodine host phase of low solubility, e.g. AgI, within a matrix of a second low solubility binder phase.

Examples include:

- Encapsulation of $BiPbO_2I$ ceramic by PbO-B_2O_3-ZnO glass, by sintering at 540 °C. The composites were reported to have low leach rates of 1.5 g m^{-2} d^{-1} in a bicarbonate ground water simulant and 1 x 10^{-2} g m^{-2} d^{-1} in bentonite $Ca(OH)_2$ saturated solution under reducing conditions at room temperature [102].
- Encapsulation of AgI or AgI-loaded mordenite zeolite by Bi_2O_3-SiO_2-SnO glass, by sintering at 550 °C for 1h, to avoid loss of AgI above 650 °C, which successfully incorporated 20-25 wt.% AgI [103]. Low elemental release rates were reported in dissolution experiments at 90 °C in deionised water but were not quantified as g m^{-2} d^{-1}. The authors reported a tendency for cracking of the encapsulation matrix due to differential thermal expansion.
- A silica encapsulated AgI composite wasteform produced by hot isostatic pressing of a Ag functionalised silica aerogel, proposed as an iodine adsorbent for the dissolver off gas system in reprocessing. The use of hot isostatic pressing ensured full retention of the iodine inventory, producing a well sintered wasteform at 1200 °C, with up to 40 wt.% iodine incorporation [104].

From these studies it is evident that judicious selection of the binder material and control of the sintering regime is important in the successful fabrication of glass composites. A balance is to be found between sufficient temperature and time of sintering to achieve effective encapsulation of the iodine substrate, against potential volatilisation and reaction with the binder phase. Matching of thermal expansion coefficients of substrate and binder phases is also of importance to avoid cracking of the matrix. These challenges mean that glass-composites may be less suitable candidates for iodine immobilisation, with the exception of materials produced by HIP, which assures retention of the iodine inventory and, hence, enables exploitation of higher process temperatures.

2.5.2 Ceramic wasteforms

Iodine incorporation, primarily as iodide, I^-, speciation, has been investigated in several candidate ceramic wasteforms, somewhat less consideration has been directed to immobilisation of iodate, IO_3^-, speciation, whereas immobilisation of periodate, IO_4^-, speciation has not been considered hitherto in a wasteform context.

2.5.2.1 Iodosodalites

Iodosodalite, prototypically $Na_4(SiAlO_4)_3I$, has received considerable attention as a potential ceramic wasteform for iodine immobilisation. The crystal structure of this material comprises an aluminosilicate framework of face sharing cubo-octhedral cages, which encapsulate Na_4I clusters. This material can be conveniently synthesised by hydrothermal reaction at 150 - 200 °C, or by reaction of NaI with zeolite-A at 900 °C [81], [105]–[107]. However, the polycrystalline material requires subsequent consolidation by sintering or hot isostatic pressing to form a ceramic wasteform. Hot isostatically pressed iodosodalite synthesised by hydrothermal reaction demonstrated a low iodine release rate of 0.05 g m^{-2} d^{-1} at 90 °C, in 0.025 M $KHCO_3$ / 0.015 M KOH solution buffered to a pH of 11, to simulate the hyperalkaline plume from a cementitious repository [81], [108]. Of greater technological relevance is direct synthesis of iodosodalites from the reaction of NaI or AgI with nepheline, $NaAlSiO_4$, although full incorporation of the iodide salt was not achieved [108]. Maddrell *et al.* reported the direct conversion of iodine sorbed Ag exchanged or occluded zeolite-A to iodosodalite $(Na_3Ag)(AlSiO_4)_3I$ by hot isostatic pressing at 900 °C [109]. The product achieved almost complete immobilisation of the iodine inventory in the sodalite phase (circa 15 wt.% iodine incorporation), with only trace AgI as an accessory phase. Some significant reaction between iodosodalite and the HIP can was observed, resulting in decomposition and formation of AgI at the can interface [110]. Dissolution experiments performed at 90 °C in deionised water afforded low dissolution rates, however, iodine release was increased by several orders of magnitude under reducing conditions imposed by the addition of Fe powder [110]. Further work is needed to understand the mechanism of iodosodalite $(Na_3Ag)(AlSiO_4)_3I$ under reducing conditions. More recently, ul Hassan *et al.* reported the fabrication of iodosodalite ceramics by cold sintering, in which pre-formed $Na_4(SiAlO_4)_3I$ iodosodalite was sintered in a uniaxial press at 300 °C under and 500 MPa, achieving 91% of theoretical density. Under these conditions, dissolution and re-precipitation at grain interfaces produces an amorphous binder phase which serves to “sinter”, or more accurately "bond" the material. The iodine release rate determined in deionised waster at 90 °C was 7.9 x 10^{-4} g m^{-2} d^{-1}, comparable to materials produced by hot isostatic pressing [111].

2.5.2.2 Iodovanadinite apatites

Lead iodovanadinite, $Pb_5(VO_4)_3I$, has been proposed as a candidate ceramic wasteform for iodine immobilisation by several authors. This compound adopts an apatite related structure, in which corner sharing VO_4, PbO_8 and PbO_9 polyhedra form one dimensional channels, which accommodate the iodide anion [112]. This compound decomposes above 287 °C, releasing iodine [113]. To counter potential iodine volatilisation, fabrication of $Pb_5(VO_4)_3I$ has been achieved by spark plasma sintering, exploiting the rapid kinetics and uniaxial pressure, and hot isostatic pressing [108], [114]. Core-shell ceramic wasteforms have also been proposed, in which $Pb_5(VO_4)_3I$, is formed from a melt reaction of PbI_2 embedded within $Pb_3(VO_4)_2$, with minimal volatilisation of iodine [115].

Recently, Zhang *et al.* have developed a mechanistic understanding of the dissolution behaviour of lead iodovanadinite [116]. Using a semi-dynamic leaching method at 90 °C with dense monolith specimens, involving daily replacement of the deionised water leachant, the initial release of I^- was shown to result from ion exchange by OH^-, controlled by diffusion [116]. Release of Pb and V was via congruent surface controlled process, resulting in an initial preferential release of I relative to Pb and V. This was followed by a parametric study [117], using the same method, to determine the fundamental material dissolution rate dependence on temperature and pH, which suggested that at neutral to high pH long term iodine release is diffusion controlled, whereas at low pH iodine release is controlled by matrix dissolution. At long timescales iodine release in undersaturated conditions the long term maximum dissolution rate was estimated to be 1 x 10^{-2} g m^{-2} d^{-1} at pH 7. Zhang *et al.* further investigated the effect of iodoapatite in high ionic strength solutions of 0.1 mol L^{-1} Na_2SO_4, Na_2CO_3, Na_3PO_4 and NaCl, and showed that the rate of iodine dissolution was enhanced due to the reduced activity co-efficient of dissolved elements [118]. Consequently, the optimal geochemistry for disposal of $Pb_5(VO_4)_3I$ ceramics would be near neutral groundwaters of low ionic strength.

A potential drawback of $Pb_5(VO_4)_3I$ as an immobilisation matrix is the need to utilise PbI_2 as an iodine source which must be formed from AgI or NaI, as which iodine is commonly speciated as undissolved solids in fuel dissolution or by recovery from the dissolver off gas. Thus, the derivative $AgBa_9(VO_4)_6I$ was proposed as an alternate ceramic wasteform, enabling direct synthesis from AgI [119]. This phase has now been discredited, with the phase equilibrium actually comprising a mixture of $Ba_3(VO_4)_2$ and AgI [120]. An attempt to synthesise the analogue $PdPb_9(VO_4)_6I_2$, with the aim of direct immobilisation of PdI_2 present in undissolved solids from fuel dissolution, proved unsuccessful. However, the phase assemblage was a conceptually promising wasteform, comprising cermet of $Pb_5(VO_4)_3I$ and Pd metal, with PdI_2 acting as a "sacrificial" iodine source [121]. Recently Cao *et al.* reported a wet chemical synthesis of $Pb_5(VO_4)_3I$ from AgI, which involves initial stripping by the following stripping reaction at room temperature:

$$2AgI_{(s)}+Na_2S_{(aq)}\rightarrow NaI_{(aq)}+Ag_2S_{(s)} \quad (7)$$

Aqueous NaI was then combined with a solution Na_3VO_4, with addition of $Pb(NO_3)_2$ leading to the precipitation of $Pb_5(VO_4)_3I$ nanoparticles at room temperature [122].

2.5.2.3 Bismuth hydrotalcites

Bismuth hydrotalcites, formulated with general formula $(Bi_2O_2)_nO_n(BiOI)_m$ have been proposed as a potential ceramic immobilisation matrix for ^{129}I, and extensively reviewed [123], [124]. These materials have a complex structure comprising an intergrowth of m BiOI layers with n charge compensated $(Bi_2O_2)^{2+}$ and O^{2-} layers, where n, m = 0, 1, 2... is an integer (i.e. a homologous series). Materials are typically a multi-phase assemblage; Krumhansi and Nenoff report a composition comprising approximately 20 mol% Bi_5O_7 (n=2) and 80% BiOI (n = 0) as showing the lowest I release rate of <4 mg L^{-1} at 25 – 90 °C, in deionised water. These materials are easily prepared by addition of precipitation from an acidified solution of $BiNO_3$ and KI, by addition of NaOH. An interesting functionality of these materials is the potential to replace the O^{2-} or I^- anions by other species such as CO_3^{2-} or IO_3^-, enabling immobilisation of other iodine species. $BiPbO_2I$ noted above has similar layered structure to the end member BiOI [102]. A challenge for deployment of hydrotalcite wasteforms is the fabrication of dense ceramic monoliths from the polycrystalline form produced by precipitation, since Bi_2O_3 has a low melting point of 817 °C and is relatively volatile. Hot isostatic pressing and spark plasma sintering may be suitable candidate manufacturing technologies but have not yet been applied.

2.5.2.4 Titanate ceramic composites

Incorporation of iodine within titanate ceramics by a solid solution mechanism has not yet been realised due to the lack of a suitable host structure with a compatible site to accommodate the large iodide anion. However, titanate ceramic composites have been produced by hot isostatic pressing, in which AgI is encapsulated by titanate ceramic phases, within a variant of the Synroc C wasteform, or simply TiO_2 [108], [125]. However, the normalised iodine release rate in TiO_2 encapsulated AgI was observed to be greater in materials produced at 900 °C compared to 1100 °C, which was suggested to arise from a metastable AgI phase. This issue warrants further investigation, since it may prove a barrier to development of this approach given the need for thermodynamic stability of the wasteform as a result of the long half life of ^{1}I.

2.5.2.5 Iodate apatites

The incorporation of iodate, IO_3^- anions, with I^{5+} speciation, into hydroxyapatite, $(Ca_{10}(PO_4)_6(OH)_{2-2x}(IO_3)_x$, was proposed by Campayo as alternate ceramic wasteform for ^{129}I immobilisation [126]; this system is isostructural with lead iodovanadinite, $Pb_5(VO_4)_3I$. IO_3^- incorporation was achieved by precipitation from a solution of $Ca(NO_3)_2.4H_2O$, $(NH_4)_2HPO_4$ and $NaIO_3$, by addition of NH_4OH, under reflux conditions for 5 h. These compounds were reported to have moderate thermal stability retaining their iodine inventory up to 550 °C in air. The iodate speciation was confirmed by I K and L_3 edge Xray absorption spectroscopy and DFT modelling, which showed the IO_3^- species to be accommodated within the one dimensional tunnels of the apatite structure [127]. Spark plasma sintering was investigated as a potential processing route for ceramic iodate hydroxyapatite wasteforms, however, the maximum density achieved was only 80% theoretical at 300 °C, and strongly dependent on the degree of hydration of the nanoparticulate feed [128]. A recent comprehensive investigation of the dissolution behaviour of iodate hydroxyapatites estimated a forward dissolution rate in pure water of 2 x 10^{-2} g m^{-2} d^{-1} at 50 °C, decreasing to a low residual rate of 10^{-4} g m^{-2} d^{-1}, which is limited by slow ion exchange of IO_3^- for OH^- in solution [129].

2.5.2.5 Periodate perovskites

The archetype cubic perovskite structure ($Pm\text{-}3m$), prototypical composition ABO_3, comprises a three dimensional network of corner sharing BO_6 octahedra, forming cuboctahedral interstices occupied by the A cation [130]. The structure can also be described as a close cubic packed array of ABO_3 layers, with B cations occupying one quarter of the octahedral holes in ordered fashion.

Perovskite compounds incorporating iodine as the I^{7+}, periodate species, formulated A_2MIO_6, were reported by Sleight and Ward in 1964 [131], with A = Ba, M = Na, Ag, synthesised by solid state reaction between BaO and $NaIO_4$ at 400 °C, or by precipitation by addition of $Ba(OH)_2$ to a solution of $NaIO_4$ or $AgIO_4$. This family of compounds was later expanded by de Hair *et al.* to include A = Ba, Sr and M = K, Na, Li, Ag, using similar synthetic methods [132]. The first crystal structure analysis of these compounds was reported by Kubel *et al.* in 2013, for composition of A_2NaIO_6 (A = Ba, Sr, Ca, Pb), by solid state reaction at 650 °C of $A(OH)_2{\cdot}8H_2O$ and $NaIO_4$ (A = Ba, Sr) or AF_2 and an excess of NaI (A = Ba, Sr, Ca); Kubel *et al.* also reported a precipitation route from combination of a solution of $A(NO_3)_2$ and $NaIO_4$ (A = Ba, Sr, Ca, Pb) [133], [134]. Using X-ray diffraction, all compounds were reported to exhibit ordering of Na^+ and I^{7+} on the perovskite B-site; however, whereas Ba_2NaIO_6 was reported to adopt the archetype cubic perovskite structure ($Fm\text{-}3m$), Sr_2NaIO_6 and Ca_2NaIO_6 adopt monoclinic derivatives ($P2_1/c$) due to co-operative tilting of BO_6 octahedra. Nevertheless, neutron diffraction is generally considered essential to ascertain such subtle structure distortions, due to the low sensitivity of X-ray diffraction in determination of O atom positions [135]. The thermal stability of the periodate perovskites and dissolution behaviour were not reported, hitherto.

2.6 Tailored wasteforms for the immobilisation of technetium-99

Technetium-99 is a long lived (half life 2.1 x 10^5 y) fission product, produced in significant yield of 6% from thermal fissions, which translates to 2g per day per 100 MWth in a light water reactor [136]. In the context of geological disposal of radioactive wastes, the predicted radiological risk to future populations depends critically on the speciation of Tc. Whereas Tc^{4+} is relatively insoluble and strongly sorbing, Tc^{7+} as the pertechnetate anion, TcO_4^-, is assumed to have unlimited solubility in ground waters [136]. It is estimated that if Tc were speciated as Tc^{4+} in the anticipated radioactive waste inventory for disposal in the UK, the peak risk could be reduced by three orders of magnitude [136]. As in the case of long lived ^{129}I, it has been argued that future regulation may require immobilisation and disposal of ^{99}Tc in a tailored wasteform to reduce the environmental impact of advanced nuclear fuel cycles, and enhance the safety case for radioactive waste disposal [137]–[140].

In the current PUREX process for nuclear fuel reprocessing, Tc shows complex behaviour but is concentrated in the liquid high level waste (HLW) raffinate of fission products and minor actinides [141]. This HLW raffinate is immobilised in a borosilicate glass, however, retention of Tc is low due to the volatility of Tc_2O_7 and $TcO_3(OH)$, which necessitates off gas capture and recycle to the melter feed [142]–[146]. Deposition of Tc_2O_7 or pertechnetate salts within the off gas systems can be problematic [145] and it is estimated that 2% of the Tc inventory may be lost through discharge to the environment in aqueous effluent [142].

Future advanced flowsheets such as the UREX process, offer the opportunity for Tc coextraction with U, separation of Tc can then be achieved by ion exchange, providing a waste stream for immobilisation in a tailored wasteform [137], [147]. Clearly, it would be advantageous to tailor a wasteform for immobilisation of Tc^{4+} give its lower solubility and sorption to mineral surfaces, relevant to geological disposal. Here, relevant background literature on the consideration of Tc^{4+} wasteforms is considered, where quantitative Tc incorporation is targeted. Thus, wasteforms that consider pertechnetate immobilisation such as the prototypical sodalite $Na_4(AlSiO_4)_3(TcO_4)$ [148], and materials for Tc sequestration from liquid or gaseous effluents, which would typically achieve relatively low Tc incorporation rates by ion exchange and sorption (recently reviewed comprehensively by Pearce *et al.* [149]), are not considered. Issues of Tc recovery from off gas and aqueous effluents, behaviour in melter systems, and some aspects of tailored wasteforms were recently reviewed by Luksic *et al.*, Kim and Kruger, and Pegg [9], [144], [145].

The ground state electronic configuration of Tc^{4+}, $4d^3$, has been reported to give rise to interesting magnetic and electronic properties in ternary oxides such as $SrTcO_3$ and potentially superconductivity in $CaTcO_3$ and $Cd_2Tc_2O_7$ [150]–[152]. Consequently, research on ceramic wasteforms for Tc^{4+} may also afford materials with exploitable physical properties, which, could lead to ^{99}Tc being utilised as a resource rather than a waste. Indeed, Tc alloy superconductors have been suggested to be worthy of exploitation and consideration has been given to safe implementation of such materials given their radioactive hazard [153]. Therefore, in this brief review, the magnetic and electronic properties of Tc^{4+} oxides are also considered where data exist.

2.6.1 Spinel technetates

The archetype spinel structure, with prototypical composition $A^{2+}B^{3+}{}_2O_4$, is cubic (*Fd*-3*m*) and comprises a face centred cubic array of oxygen atoms with the A and B site cations occupying, respectively, in ordered fashion, one eighth of the tetrahedral holes and one half of the octahedral holes [130]. This description applies to “normal spinels” such as $MgAl_2O_4$, general formula $A[B]_2O_4$, in which the A cation occupies the tetrahedral site. Whereas, in “inverse spinels”, general formula $B[AB]O_4$, the A cation occupies the octahedral site and half of the B cations occupy the tetrahedral site; one such example is magnetite, Fe_3O_4, formulated as $Fe^{3+}[Fe^{2+}Fe^{3+}]O_4$. Whether a composition forms a normal or inverse spinel depends on the crystal field stabilisation energy of the component ions.

Muller *et al.* reported a systematic study of M_2TcO_4 spinels prepared from reaction between TcO_2 and counterpart metal oxides at 1100 °C in sealed platinum capsules, leading to the successful synthesis with M = Mg, Mn, Co, $Co_{0.5}Mn_{0.5}$, $Co_{0.5}Ni_{0.5}$, $Ni_{0.5}Mn_{0.5}$, $Ni_{0.5}Zn_{0.5}$, $Co_{0.5}Cd_{0.5}$ [154]; the compositions with M = Mg and $Ni_{0.5}Mn_{0.5}$ were qualitatively determined to be ferromagnetic at 77 K. Tc^{4+} has a $4d^3$ electron configuration and therefore a strong preference for the spinel octahedral site, although detailed characterisation was not reported. Khalil and White reported the synthesis of $Mg_2Ti_{1x}TcO_4$ spinel solid solutions (with $0 < x < 0.2$ and $x = 1.0$), from solid state reactions of the oxides at 1290 °C in sealed platinum tubes, as a candidate ceramic wasteform for ^{99}Tc immobilisation [155]. Tc release was examined in deionised water, using small monolith samples, yielding a dissolved Tc concentration of 0.1 µg L^{-1} after 60 days, corresponding to 0.61% of the initial Tc inventory; the rate of Tc release was initially rapid, but approached a low residual rate after 30 days. In comparison, Tc release was an order of magnitude greater at pH 1.32, but an order of magnitude lower at pH 10.3. Further investigation of the dissolution behaviour in synthetic granite, brine and clay pore waters determined dissolution rates of the order of $10^{-2} – 10^{-3}$ g m^{-2} d^{-1} for the composition $MgTi_{0.5}Tc_{0.5}O_4$, demonstrating the high durability of these materials (although higher dissolution rates were determined for higher Tc incorporation) [156]. Co_2TcO_4 was recently investigated by Thorogood *et al.* and was suggested to incorporate Tc^{3+} according to bond valence sum and Tc K-edge XANES analyses [157].

Liu *et al.*, investigated in the synthesis of $Fe_{3-x}Ti_xO_4$ by addition of NH_4OH to a solution NH_4TcO_4, $FeCl_2$, $FeCl_3$ and $TiCl_4$, spiked with NH_4TcO_4, under anoxic conditions [158]. The titanomagnetite spinel was produced in nanoparticle form, resulting in the coprecipitation of $TcO_2.xH_2O$, through reduction of Tc^{7+} to Tc^{4+} mediated by Fe^{2+}/Fe^{3+} in the spinel phase, as demonstrated by Tc K-edge EXAFS. Thus, Tc^{4+} was not incorporated within the spinel structure through this synthesis [158]. Tc incorporation within $Fe_{3-x-y}M_xTc_yO_4$ (M= Co, Ni, Zn; $x \approx y \approx 0.01$) spinel phases was subsequently achieved by Lee *et al.* [159], using a similar procedure but employing $Fe(OH)_2$ and hydrothermal aging of the solution at 75 °C for 72 hours. Lee *et al.* tuned the redox potential of the magnetite phase through judicious choice of metal dopant, M, which is believed to assist Tc retention of Tc^{4+} during annealing at 700 °C. A similar synthetic procedure with hydrothermal aging of the precipitate at 95 °C for 90 min was utilised by Lukens *et al.* to achieve quantitative incorporation of Tc^{4+} in $Tc_{0.1}M_{1.1}Fe_{1.8}O_4$ (M = Mn, Ni, Co, Fe); in some compositions, for reasons not explained 10-25% of the Tc speciation was as Tc^{5+}, according to Tc K-edge XANES studies [160].

2.6.2 Perovskite technetates

The description of the perovskite structure has been previously summarised above. Several Tc perovskites have been reported and recently reinvestigated, as reviewed below [161]–[169].

Muller *et al.* prepared $SrTcO_3$ at 1225 °C, and reported the compound to adopt a slightly distorted perovskite structure [154]. Rodriguez *et al.* subsequently reinvestigated the structure of $SrTcO_3$ prepared by reaction between $Sr(NO_3)_2$ and NH_4TcO_4 at 700 °C or $SrCO_3$ and TcO_2 at 850 °C, under Ar [161] and confirmed this material to adopt an orthorhombic distortion of the parent perovskite structure (*Pnma*) as a result of cooperative octahedral tilting. Moreover, Rodriguez *et al.* established $SrTcO_3$ to show antiferromagnetic ordering below a Neel temperature of 750 °C, which is unusually high for a 4d transition metal oxide leading to considerable interest in the underlying mechanism [161]. Hartmann *et al.* suggest that $SrTcO_3$ shows superconductivity below 7.8 K [151], however, this result has not been independently verified and, given the weak nature of the magnetic response, and the fact that technetium metal is superconducting below 7.8 K [150], it seems likely that this is present as a trace impurity phase giving rise to the observed weak diamagnetic signal. At high temperature, $SrTcO_3$ undergoes a sequence of phase transitions to higher symmetry $Pnma \rightarrow Imma \rightarrow I4/mcm \rightarrow Pm\text{-}3m$, arising from relaxation of co-operative octahedral tilting [168]. The perovskite $CaTcO_3$ was apparently first reported in 2011 by Avdeev *et al.* [170], synthesised by reaction between $Ca(NO_3)_2.4H_2O$ and NH_4TcO_4 at 700 °C under Ar; although the authors credit Muller *et al.* with discovery in 1964, this compound is, in fact, not mentioned in their work [154]. $CdTcO_3$ was subsequently reported by Rodriguez *et al.*, synthesised by solid state reaction between CdO and TcO_2 at 850 C, under Ar [152]. $CaTcO_3$ and $CdTcO_3$ are isostructural with $SrTcO_3$; it was reported that $CaTcO_3$ is antiferromagnetic below $T_N = 527$ °C, whereas magnetic ordering in $CdTcO_3$ has not been established; however, density functional theory calculations suggest that antiferromagnetic ordering should be stabilised in $CdTcO_3$ at 0 K [152]. Muller *et al.* prepared $BaTcO_3$ at 1225 °C, similar to that of hexagonal $BaTiO_3$, and reported the compound to adopt a hexagonal perovskite structure, with face-sharing TcO_6 octahedra [154]. An attempt to produce $CaTi_{0.5}Tc_{0.5}O_3$ as a ceramic wasteform by hot uniaxial pressing at 900 °C resulted in the formation of a perovskite phase with composition $CaTi_{0.9}Tc_{0.1}O_3$ and Tc metal [171]. However, annealing this material under argon gas at 1500 °C for 1h was reported to yield single phase $CaTi_{0.42}Tc_{0.58}O_3$, albeit with some significant Tc volatilisation.

2.6.3 Pyrochlore technetates

The pyrochlore structure is adopted by compounds with the general formula $A_2B_2O_7$ and is derived from the fluorite structure of CaF_2 (i.e. $A_2B_2O_8$, or AO_2 with A = B), through formation of ordered oxygen vacancies along the (110) direction [130]. The A cations adopt a distorted AO_8 cubic co-ordination, whereas the B cations adopt distorted BO_6 octahedral co-ordination. Writing the composition as $A_2B_2O_6O'$, the pyrochlore structure can also be described as interpenetrating B_2O_6 and A_2O' networks [172]. The B_2O_6 sublattice comprises corner sharing BO_6 octahedra which form a network of interconnecting cages, with the O' atom at the centre, whereas the A_2O' sub lattice comprises a network of corner-sharing O'_4A tetrahedra.

The lanthanide technetate pyrochlores, $Ln_2Tc_2O_7$, with Ln = Sm, Dy, Er, synthesised by reaction of TcO_2 with Ln_2O_3 at 1230 °C in a sealed platinum capsule, were first reported by Muller *et al.* in 1964 [154]. In addition, Muller *et al.* reported the apparently oxygen deficient pyrochlore "$PbTcO_3$" from reaction of PbO and TcO_2 at a relatively low temperature of 890 °C. These compounds were ascertained based on indexed X-ray powder diffraction data. Weck *et al.* subsequently investigated the electronic structures of $Ln_2Tc_2O_7$ pyrochlores [173] using density functional theory. The calculated unit cell parameters were in reasonable agreement with those determined experimentally by Muller *et al.* and subsequently by Hartmann *et al.* (for Ln = Pr, Nd, Gd, Sm, Lu) TcO_2 and Ln_2O_3 or Pr_6O_{11} [174]. The electronic structure calculations established the $Ln_2Tc_2O_7$ pyrochlores to be stable, consistent with the radius ratio r_A/r_B in the range 1.52 (Lu) to 1.77 (Ce) which is within the empirical criterion for pyrochlore formation $1.46 < r_A/r_B < 1.78$ (for A^{3+} and B^{4+} systems) [172]. The density of states at the Fermi level was dominated by hybridised Tc 4d and O 2p states, which were half full, with no gap, leading to prediction of metallic conductivity. The pyrochlore $Bi_2Tc_2O_{7-x}$, and related compound Bi_3TcO_8 with a distorted fluorite structure, were reported by Rodriguez *et al.* [175]. $Bi_2Tc_2O_{7-x}$ was shown to be slightly oxygen deficient from neutron scattering data, x = 0.14, with disordered vacancies occurring on the O' site. The Bi^{3+} cations undergo uncorrelated static displacements from their lattice positions, due to the stereochemically active $6s^2$ lone pair, which also induces similar static displacements of the oxygen anions. The Tc speciation in $Bi_2Tc_2O_{7-x}$ was confirmed to be majority Tc^{4+} by Tc K edge XANES. Density functional theory calculations predicted metallic conductivity, based on the, high density of states at the Fermi energy, arising from Tc 4d and O 2p hybridisation, which are half filled in accordance with the Tc $4d^3$ electron configuration. The compound was reported to show antiferromagnetic ordering below 150 K [152]. The structure of Bi_3TcO_8 is characterised by the presence of tetrahedral TcO_4^- speciation and was thus predicted to be an insulator as a consequence of fully oxidised Tc^{7+} [175]. The pyrochlore $Cd_2Tc_2O_7$ was also reported by Rodriguez *et al.* with Tc^{5+} speciation; electronic structure calculations suggest this material may be metallic with magnetic ordering stabilised at 0 K [152]. The temperature dependence of the magnetic susceptibility is complex, decreasing sharply below 200 K, suggesting antiferromagnetic ordering, with a further decrease below 4 K that was suggested to be a possible signature of superconductivity, though as yet this has not been verified.

2.6.4 Rutile technetate solid solutions

The rutile structure of TiO_2, is tetragonal ($P4_2/mnm$), and comprises infinite chains of edge sharing TiO_6 octahedra, in which each edge shared oxygen is corner shared with the apical oxygen of a neighbouring chain [130]. TcO_2 adopts a distorted rutile structure and, therefore, a significant solid solution is expected [154], [176], [177].

Muller *et al.* prepared the solid solution $Ti_{1-x}Tc_xO_2$ from reaction of TiO_2 with TcO_2 in a sealed platinum capsule at 1200 °C, achieving Tc incorporation up to x = 0.4 [154]. Stewart *et al.* demonstrated conceptual rutile ceramic wasteforms of composition $Tc_{0.9}Tc_{0.1}O_2$, by sintering at 1250 °C; however sintering above 1300 °C led to autoreduction of Tc^{4+} to Tc metal [178]. Carter *et al.* demonstrated the fabrication of a rutile rich wasteform by hot isostatic pressing, producing a phase with composition $Tc_{0.38}Ti_{0.62}O_2$ (together with a hollandite and spinel phase), by hot isostatic pressing at 1150 °C and 30 MPa for 1 h [179], with a low Tc release rate of 0.15g/L in PCT B experiments (deionised water, 90 °C, 7 days).

Kuo examined the $Ti_{1-x}Tc_xO_2$ solid solution theoretically using density functional theory, including the effect of transmutation by replacement of Tc by Ru [180]. Solid solution formation was shown to be thermodynamically stable; binary defect clusters involving TcTc defect pairs (as nearest cation neighbours) were found to be the most stable defects, which was attributed to the formation of metallic bonds due to the short metal-metal distance (similar to those hypothesised in TcO_2 [176]). Transmutation, effected by replacing Tc by Ru, increased the solution energy, signalling reduced stability of the material, and the stable configuration of defect of two Ru atoms was found to be as next nearest neighbours. As a consequence, Kuo *et al.* suggest that a rutile $Ti_{1-x}Tc_xO_2$ solid solution close to the solubility limit, may result in phase separation as transmutation proceeds. More recently, Lukens and Saslow reported the synthesis of $Ti_{1-x}Tc_xO_2$ nanoparticles by reaction of Ti metal with $HTcO_4$ in the presence of NH_4F (which reacts to remove the surface passivating layer of TiO_2 on the metal), under reflux conditions [181]. Tc K-edge EXAFS analysis determined the presence of pairs of edge sharing TcO_6 defect octahedra, which is consistent with the calculations of Kuo *et al.* The release rate of Tc, in deionised water at 90 °C, under anoxic conditions was low, 3×10^{-6} g m^{-2} d^{-1}.

2.6.5 Synroc systems

Hart and Vance investigated the potential for application of the multiphase Synroc ceramic wasteform for immobilisation of Hanford tank wastes with a high inventory of Tc, Cs, Sr and actinide radionuclides [182], [183]. A Synroc C wasteform was investigated for this purpose, doped with 2 wt.% Tc, targeting a phase assemblage of zirconolite ($CaZrTi_2O_7$), perovskite ($CaTiO_3$), hollandite ($Ba(Al,Ti)_2Ti_6O_{16}$) and rutile (TiO_2), and a noble metal alloy phase (incorporating Mo, Ru, Rh, Pd, Ni, Fe). Under the reducing conditions of hot uniaxial pressing, in a graphite die, metallic Tc was produced which partitioned to the noble metal phase.

2.7 Aims and objectives of this thesis

The overarching aim of this thesis, as discussed in Chapter 1, is to develop an understanding of the synthesis, structure and properties of materials relevant to the deployment of uranium nitride as an accident tolerant nuclear fuel in future advanced fuel cycles, taking a holistic approach.

From the literature review presented, several knowledge gaps were identified to be addressed, within this overarching aim. First it is clear that there is opportunity for innovation in the synthesis of uranium nitride, since current methods utilise pyrophoric precursors, such as U or UH_3, and produce materials with significant UO_2 or U(C,N) contamination. Low temperature nitridation using $NaNH_2$ has proven successful in the synthesis of transition metal nitrides and could conceivably be applied to synthesis of uranium nitrides. Nevertheless, the fundamental mechanism of this reaction is poorly understood even for simple transition metal nitride systems. Retention of N within the products of UN hydrolysis in steam and oxidation, is suggested to yield "UO_2N_x" and "UO_3N_x" oxynitrides, however, the evidence to substantiate these compounds is weak, comprising only mass balance considerations and determination of elemental N in the products. Within UN fuels, fission product nitrides may also undergo hydrolysis when the fuel cladding is breached, affording ternary uranium oxynitrides. However, no such ternary uranium oxynitrides have been reported hitherto. Therefore, the synthesis of ternary uranium oxynitrides deserves further consideration and a reasonable starting point would be ternary uranium oxides with U^{6+}, with a known capacity for oxygen vacancies, which could enable N / O substitution, with potential for charge balance by U^{5+}.

Advanced fuel cycles incorporating recycle of accident tolerant nuclear fuels may be subject to more stringent regulatory practice and the need for tailored wasteforms to immobilise particularly long lived fission products such as ^{129}I and ^{99}Tc, where there is evident room for further innovation. These fission products are of key concern in the safety case for radioactive waste disposal; new robust tailored materials for immobilisation could therefore reduce the environmental impact of advanced nuclear fuel cycles and enhance public confidence. Such tailored immobilisation concepts are supported by advanced fuel recycle flowsheets which offer the potential to partition ^{129}I and ^{99}Tc. In the case of ceramic wasteforms for ^{129}I, the reviewed research to date has focused primarily on wasteforms with iodide speciation and, to lesser extent, iodate speciation, however, periodate speciation, which is compatible with advanced scrubber recovery systems for dissolver off gas, has not been considered. The family of periodate perovskites are a potential candidate wasteform but have not been widely investigated hitherto. Finally, in the case of ^{99}Tc, it is clear that speciation as Tc^{4+} is preferable for a tailored immobilisation wasteform, being relatively insoluble and strongly sorbing. However, a review has demonstrated the extent of Tc^{4+} solid state chemistry to be limited, however, the $4d^3$ electron configuration evidently gives rise to interesting, and potentially exploitable, magnetic and electrical properties. One potential candidate host phase is the pyrochlore $PbTcO_3$, which has the apparent advantage of synthesis at relatively low temperature, to assist Tc retention, and avoids the use of lanthanide elements which are considered a critical resource. This compound has been largely ignored since its discovery almost 60 years ago and is worthy of re-investigation.

From this synthesis, within the overarching aim of this thesis, the following objectives were defined:

1. To develop a capability for gas ammonolysis reactions for the synthesis of uranium nitrides and oxynitrides, for comparison with low temperature $NaNH_2$ nitridation. This was addressed through the design, commissioning and operation of an ammonolysis furnace, as described in Chapter 4.
2. To develop a capability for, and understanding of the mechanism of, low temperature nitridation reactions mediated by $NaNH_2$, as a potential route to the synthesis of uranium nitrides. This was addressed by developing expertise in the methodology, which was applied to Fe_3O_4 to develop mechanistic insight, as described in Chapter 5.
3. To investigate the potential low temperature nitridation reactions of uranium oxides, mediated by $NaNH_2$, in comparison with gas phase ammonolysis, as a potential route to the synthesis of uranium oxides and oxynitrides. This work described in Chapter 6, draws on the capability and mechanistic understanding developed in Chapter 4 and 5.

4. To investigate the existence of ternary uranium oxynitrides, as potential degradation products of UN fuels, by identification of rational targets and their synthesis by gas phase ammonolysis. This work, presented in Chapter 7, further develops and applies the understanding and capability developed in Chapters 4 and 6.
5. To investigate the synthesis, structure and properties of the periodate perovskite family, A_2NaIO_6 (A = Ba, Sr, Ca), with determination of accurate crystal structures from neutron diffraction data, as a potential wasteform for ^{129}I immobilisation from advanced fuel cycles. This work is presented in Chapter 8.
6. To investigate the synthesis, structure and properties of the pyrochlore $PbTcO_3$, with determination of accurate crystal structures from neutron diffraction data, as a potential wasteform for ^{99}Tc immobilisation from advanced fuel cycles. This work is presented in Chapter 9.

2.8 References

[1] R. J. M. Konings, T. Wiss, and C. Guéneau, “Nuclear Fuels,” in The Chemistry of the Actinide and Transactinide Elements (Set Vol.1-6), J. J. Katz, L. R. Morss, N. M. Edelstein, and J. Fuger, Eds. Dordrecht: Springer, 2010, pp. 3665–3811.

[2] IAEA, “Advanced Large Water Cooled Reactors,” Adv. React. Inf. Syst., no. September, p. 20, 2015, [Online]. Available: http://www.iaea.org/books%0Ahttps://www.iaea.org/NuclearPower/Downloadable/WCR/IAEA_WRC_Booklet.pdf.

[3] D. Olander, “Nuclear fuels - Present and future,” J. Nucl. Mater., vol. 389, no. 1, pp. 1–22, 2009, doi: 10.1016/j.jnucmat.2009.01.297.

[4] J. J. Carbajo, G. L. Yoder, S. G. Popov, and V. K. Ivanov, “A review of the thermophysical properties of MOX and UO_2 fuels,” J. Nucl. Mater., vol. 299, no. 3, pp. 181–198, 2001, doi: 10.1016/S0022-3115(01)00692-4.

[5] C. R. F. Azevedo, “Selection of fuel cladding material for nuclear fission reactors,” Eng. Fail. Anal., vol. 18, no. 8, pp. 1943–1962, 2011, doi: 10.1016/j.engfailanal.2011.06.010.

[6] R. C. Ewing, “Long-term storage of spent nuclear fuel,” Nat. Mater., vol. 14, no. 3, pp. 252–257, 2015, doi: 10.1038/nmat4226.

[7] A. P. Paiva and P. Malik, “Recent advances on the chemistry of solvent extraction applied to the reprocessing of spent nuclear fuels and radioactive wastes,” J. Radioanal. Nucl. Chem., vol. 261, no. 2, pp. 485–496, 2004, doi: 10.1023/B:JRNC.0000034890.23325.b5.

[8] B. J. Riley, J. D. Vienna, D. M. Strachan, J. S. McCloy, and J. L. Jerden, “Materials and processes for the effective capture and immobilization of radioiodine: A review,” J. Nucl. Mater., vol. 470, pp. 307–326, 2016, doi: https://doi.org/10.1016/j.jnucmat.2015.11.038.

[9] S. A. Luksic, B. J. Riley, M. Schweiger, and P. Hrma, “Incorporating technetium in minerals and other solids: A review,” J. Nucl. Mater., vol. 466, pp. 526–538, 2015, doi: 10.1016/j.jnucmat.2015.08.052.

[10] Y. Zhang et al., “Kinetics of uranium release from Synroc phases,” J. Nucl. Mater., vol. 289, no. 3, pp. 254–262, 2001, doi: http://dx.doi.org/10.1016/S00223115(01)00423-8.

[11] D. J. J. Bailey, M. C. C. Stennett, and N. C. C. Hyatt, “Synthesis and Characterization of Brannerite Wasteforms for the Immobilization of Mixed Oxide Fuel Residues,” Procedia Chem., vol. 21, pp. 371–377, 2016, doi: 10.1016/j.proche.2016.10.052.

[12] W. E. Lee, M. Gilbert, S. T. Murphy, and R. W. Grimes, “Opportunities for advanced ceramics and composites in the nuclear sector,” J. Am. Ceram. Soc., vol. 96, no. 7, pp. 2005–2030, 2013, doi: 10.1111/jace.12406.

[13] Committee on Radioactive Waste Management, “CoRWM Position Paper: Why Geological Disposal?,” no. July 2011, pp. 1–15, 2018, [Online]. Available: https://webarchive.nationalarchives.gov.uk/20081025022110/http://www.defra.gov.uk/environment/radioactivity/publications/co.

[14] World Nuclear Association, "Nuclear Energy in Finland | Finnish Nuclear Power - World Nuclear Association," World Nuclear Association, 2018. http://www.worldnuclear.org/information-library/country-profiles/countries-a-f/finland.aspx (accessed Oct. 14, 2020).

[15] Y. P. Zhang, S. P. Niu, L. T. Zhang, S. Z. Qiu, G. H. Su, and W. X. Tian, "A review on analysis of LWR severe accident," J. Nucl. Eng. Radiat. Sci., vol. 1, no. 4, pp. 1–20, 2015, doi: 10.1115/1.4030364.

[16] S. J. Zinkle, K. A. Terrani, J. C. Gehin, L. J. Ott, and L. L. Snead, "Accident tolerant fuels for LWRs: A perspective," J. Nucl. Mater., vol. 448, no. 1–3, pp. 374– 379, 2014, doi: 10.1016/j.jnucmat.2013.12.005.

[17] P. C. Burns, R. C. Ewing, and A. Navrotsky, "Nuclear fuel in a reactor accident," Science (80-.)., vol. 335, no. 6073, pp. 1184–1188, 2012, doi: 10.1126/science.1211285.

[18] G. J. Youinou and R. S. Sen, "Impact of accident-tolerant fuels and claddings on the overall fuel cycle: A preliminary systems analysis," Nucl. Technol., vol. 188, no. 2, pp. 123–138, 2014, doi: 10.13182/NT14-22.

[19] L. J. Ott, K. R. Robb, and D. Wang, "Preliminary assessment of accident-tolerant fuels on LWR performance during normal operation and under DB and BDB accident conditions," J. Nucl. Mater., vol. 448, no. 1–3, pp. 520–533, 2014, doi: 10.1016/j.jnucmat.2013.09.052.

[20] Y. Arai, "Nitride fuel," in Comprehensive Nuclear Materials, vol. 3, R. Konings, Ed. Oxford: Elsevier Inc., 2012, pp. 41–54.

[21] K. Tanaka, K. Maeda, K. Katsuyama, M. Inoue, T. Iwai, and Y. Arai, "Fission gas release and swelling in uranium-plutonium mixed nitride fuels," J. Nucl. Mater., vol. 327, no. 2–3, pp. 77–87, 2004, doi: 10.1016/j.jnucmat.2004.01.002.

[22] K. Johnson, V. Ström, J. Wallenius, and D. A. Lopes, "Oxidation of accident tolerant fuel candidates," J. Nucl. Sci. Technol., vol. 54, no. 3, pp. 280–286, 2017, doi: 10.1080/00223131.2016.1262297.

[23] K. Yueh and K. A. Terrani, "Silicon carbide composite for light water reactor fuel assembly applications," J. Nucl. Mater., vol. 448, no. 1, pp. 380–388, 2014, doi: https://doi.org/10.1016/j.jnucmat.2013.12.004.

[24] S. J. Zinkle and F. W. Wiffen, "Radiation Effects in Refractory Alloys," AIP Conf. Proc., vol. 699, no. 1, pp. 733–740, Feb. 2004, doi: 10.1063/1.1649637.

[25] K. A. Terrani, L. L. Snead, and J. C. Gehin, "Microencapsulated fuel technology for commercial light water and advanced reactor application," J. Nucl. Mater., vol. 427, no. 1–3, pp. 209–224, 2012, doi: 10.1016/j.jnucmat.2012.05.021.

[26] T. D. Gulden, C. L. Smith, D. P. Harmon, and W. W. Hudritsch, "The Mechanical Design of TRISO-Coated Particle Fuels for the Large HTGR," Nucl. Technol., vol. 16, no. 1, pp. 100–109, Oct. 1972, doi: 10.13182/NT72-A31179.

[27] W. Zhou and W. Zhou, "Enhanced thermal conductivity accident tolerant fuels for improved reactor safety – A comprehensive review," Ann. Nucl. Energy, vol. 119, pp. 66–86, 2018, doi: 10.1016/j.anucene.2018.04.040.

[28] Nuclear Energy Agency, Nuclear fuel behaviour in Loss-of-coolant Accident (LOCA) conditions. State-of-the-art Report, no. 6846. 2009.

[29] M. Streit and F. Ingold, "Nitrides as a nuclear fuel option," J. Eur. Ceram. Soc., vol.

25, no. 12, pp. 2687–2692, 2005, doi: https://doi.org/10.1016/j.jeurceramsoc.2005.03.181.

[30] A. F. Carley, P. Nevitt, and P. Roussel, “The interaction of uranium metal with nitrogen oxides: The formation of an oxynitride surface layer,” J. Alloys Compd., vol. 448, no. 1–2, pp. 355–362, Jan. 2008, doi: 10.1016/j.jallcom.2007.05.028.

[31] M. Eckle and T. Gouder, “Photoemission study of UN_xO_y and UC_xO_y in thin films,” J. Alloys Compd., vol. 374, no. 1–2, pp. 261–264, Jul. 2004, doi: 10.1016/j.jallcom.2003.11.121.

[32] P. Xu, J. Yan, E. J. Lahoda, and S. Ray, Uranium mononitride as a potential commercial LWR fuel. United States: American Nuclear Society - ANS, 2012.

[33] J. Wallenius, “5.03 - Nitride Fuels,” in Comprehensive Nuclear Materials, 2nd Ed., R. J. M. Konings and R. E. B. T.-C. N. M. (Second E. Stoller, Eds. Oxford: Elsevier, 2020, pp. 88–101.

[34] International Atomic Energy Agency, “Status and Trends of Nuclear Fuels Technology for Sodium Cooled Fast Reactors,” IAEA Nucl. Energy Ser., no. NF-T4.1, p. IAEA Nuclear Energy Series No. NF-T-4.1, 2011.

[35] S. B. Ross, M. S. El-Genk, and R. B. Matthews, “Uranium nitride fuel swelling correlation,” J. Nucl. Mater., vol. 170, no. 2, pp. 169–177, 1990, doi: https://doi.org/10.1016/0022-3115(90)90409-G.

[36] K. Johnson and D. A. Lopes, “Fabrication of High Density UN with Enriched N-15 for Test Irradiation,” vol. 10, no. October, pp. 1–6, 2017.

[37] C. M. Petrie, J. R. Burns, R. N. Morris, and K. A. Terrani, “Small-Scale Fuel Irradiation Testing in the High Flux Isotope Reactor,” 2017, [Online]. Available: https://www.osti.gov/biblio/1400191.

[38] S. B. Ross, M. S. El-Genk, and R. B. Matthews, “Thermal conductivity correlation for uranium nitride fuel between 10 and 1923 K,” J. Nucl. Mater., vol. 151, no. 3, pp. 318–326, 1988, doi: https://doi.org/10.1016/0022-3115(88)90026-8.

[39] Y. Arai, A. Maeda, K. Shiozawa, and T. Ohmichi, “Chemical forms of solid fission products in the irradiated uranium—plutonium mixed nitride fuel,” J. Nucl. Mater., vol. 210, no. 1, pp. 161–166, 1994, doi: https://doi.org/10.1016/0022-3115(94)90233X.

[40] E. Renard and B. Rogozkin, “About Applicability of PUREX-Technology to Fast Breeder Reactor Mixed (U-Pu) Monocarbide and Mononitride Fuels Reprocessing,” J. Nucl. Sci. Technol., vol. 39, no. sup3, pp. 753–756, Nov. 2002, doi: 10.1080/00223131.2002.10875576.

[41] R. M. Dell, V. J. Wheeler, and N. J. Bridger, “Hydrolysis of uranium mononitride,” Trans. Faraday Soc., vol. 63, no. 0, pp. 1286–1294, 1967, doi: 10.1039/TF9676301286.

[42] M. Jolkkonen, P. Malkki, K. Johnson, and J. Wallenius, “Uranium nitride fuels in superheated steam,” J. Nucl. Sci. Technol., vol. 54, no. 5, pp. 513–519, 2017, doi: 10.1080/00223131.2017.1291372.

[43] US DOE Nuclear Energy Research Advisory Committee and the Generation IV International Forum, “Generation IV roadmap: R&D scope report for liquid-metalcooled reactor systems,” GIF-005-00, pp. 1–97, 2002.

[44] J. Wallenius and S. Pillon, “N-15 requirement for 2nd stratum ADS nitride fuels.,” in Proceedings of the 2001 ANS topical meeting (AccApp/ADTTA ‘01), Reno, NV, 2002.

[45] Nuclear Decommissioning Authority, “Geological Disposal Carbon-14 Project Phase 2: Overview Report (NDA Report no. NDA/RWM/137),” 2016.

[46] P. A. Lessing, “Oxidation Protection of Uranium Nitride Fuel Using Liquid Phase Sintering.” Idaho National Laboratory, 2012.

[47] B. J. Jaques et al., “Synthesis and sintering of UN-UO_2 fuel composites,” J. Nucl. Mater., vol. 466, pp. 745–754, 2015, doi: http://dx.doi.org/10.1016/j.jnucmat.2015.06.029.

[48] K. S. Chaudri et al., “Coupled analysis for new fuel design using UN and UC for SCWR,” Prog. Nucl. Energy, vol. 63, pp. 57–65, 2013, doi: https://doi.org/10.1016/j.pnucene.2012.11.001.

[49] D. R. Costa, M. Hedberg, S. C. Middleburgh, J. Wallenius, P. Olsson, and D. A. Lopes, “UN microspheres embedded in UO_2 matrix: An innovative accident tolerant fuel,” J. Nucl. Mater., vol. 540, p. 152355, 2020, doi: https://doi.org/10.1016/j.jnucmat.2020.152355.

[50] A. Herman and C. Ekberg, “A Uranium Nitride Doped with Chromium, Nickel or Aluminum as an Accident Tolerant Fuel,” Res. Rev. J. Mater. Sci., vol. 5, no. 4, pp. 83–99, 2017, doi: 10.4172/2321-6212.1000196.

[51] J. Bugl and A. A. Bauer, “Phase Relations in the System Uranium—Nitrogen,” J. Am. Ceram. Soc., vol. 47, no. 9, pp. 425–429, Sep. 1964, doi: https://doi.org/10.1111/j.1151-2916.1964.tb14429.x.

[52] R. A. McDonald, A. S. Wilson, N. C. Baenziger, R. E. Rundle, Ames Laboratory, and U.S. Atomic Energy Commission Technical Information Division, The structures of the carbides, nitrides, and oxides of uranium. Oak Ridge, TN: Atomic Energy Commission, 1947.

[53] P. E. Evans and T. J. Davies, “Uranium nitrides,” J. Nucl. Mater., vol. 10, no. 1, pp. 43–55, 1963, doi: https://doi.org/10.1016/0022-3115(63)90115-6.

[54] N. A. Curry, “An investigation of the magnetic structure of uranium nitride by neutron diffraction,” Proc. Phys. Soc., vol. 86, no. 6, pp. 1193–1198, 1965, doi: 10.1088/0370-1328/86/6/304.

[55] F. Anselin, “Etude des nitrures d’uranium, de plutonium et de leurs solutions solides,” J. Nucl. Mater., vol. 10, no. 4, pp. 301–320, 1963, doi: http://dx.doi.org/10.1016/0022-3115(63)90182-X.

[56] N. Masaki and H. Tagawa, “Diffraction study of α-U_2N_{3+x},” J. Nucl. Mater., vol. 57, no. 2, pp. 187–192, 1975, doi: https://doi.org/10.1016/0022-3115(75)90258-5.

[57] R. Troć, “Magnetic susceptibility of the uranium nitrides,” J. Solid State Chem., vol. 13, no. 1, pp. 14–23, 1975, doi: https://doi.org/10.1016/0022-4596(75)90076-6.

[58] G. W. C. Silva, C. B. Yeamans, A. P. Sattelberger, T. Hartmann, G. S. Cerefice, and K. R. Czerwinski, “Reaction sequence and kinetics of uranium nitride decomposition,” Inorg. Chem., vol. 48, no. 22, pp. 10635–10642, 2009, doi: 10.1021/ic901165j.

[59] M. W. Mallett and A. F. Gerds, “Reaction of Nitrogen with Uranium,” J. Electrochem. Soc., vol. 102, no. 6, p. 292, 1955, doi: 10.1149/1.2430050.

[60] P. Malkki, M. Jolkkonen, T. Hollmer, and J. Wallenius, “Manufacture of fully dense uranium nitride pellets using hydride derived powders with spark plasma sintering,” J. Nucl. Mater., vol. 452, no. 1, pp. 548–551, 2014, doi: https://doi.org/10.1016/j.jnucmat.2014.06.012.

[61] H. Serizawa, K. Fukuda, and M. Katsura, “Study of the formation of α-U_2N_{3+x} using unstable ammonia — reaction sequence and control of nitrogen activity,” J. Alloys Compd., vol. 223, no. 1, pp. 39–44, 1995, doi: https://doi.org/10.1016/09258388(94)01442-6.

[62] H. Funk and H. Böhland, “Zur Darstellung von Metallnitriden aus Ammoniumfluorometallaten und Ammoniak,” Zeitschrift für Anorg. und Allg. Chemie, vol. 334, no. 3-4, pp. 155–162, Dec. 1964, doi: https://doi.org/10.1002/zaac.19643340306.

[63] C. B. Yeamans et al., “Oxidative ammonolysis of uranium(IV) fluorides to uranium(VI) nitride,” J. Nucl. Mater., vol. 374, no. 1–2, pp. 75–78, 2008, doi: 10.1016/j.jnucmat.2007.06.022.

[64] S. K. Mukerjee, J. V Dehadraya, V. N. Vaidya, and D. D. Sood, “Kinetics of the carbothermic synthesis of uranium mononitride microspheres,” J. Nucl. Mater., vol. 185, no. 1, pp. 39–49, 1991, doi: https://doi.org/10.1016/0022-3115(91)90363-C.

[65] T. B. Lindemer, S. L. Voit, C. M. Silva, T. M. Besmann, and R. D. Hunt, “Carbothermic synthesis of 820μm uranium nitride kernels: Literature review, thermodynamics, analysis, and related experiments,” J. Nucl. Mater., vol. 448, no. 1, pp. 404–411, 2014, doi: https://doi.org/10.1016/j.jnucmat.2013.10.036.

[66] Y. Arai and K. Minato, “Fabrication and electrochemical behavior of nitride fuel for future applications,” J. Nucl. Mater., vol. 344, no. 1, pp. 180–185, 2005, doi: https://doi.org/10.1016/j.jnucmat.2005.04.039.

[67] P. Bardelle and D. Warin, “Mechanism and kinetics of the uranium-plutonium mononitride synthesis,” J. Nucl. Mater., vol. 188, pp. 36–42, 1992, doi: https://doi.org/10.1016/0022-3115(92)90451-P.

[68] A. Miura, “Low-temperature synthesis and rational design of nitrides and oxynitrides for novel functional material development,” J. Ceram. Soc. Japan, vol. 125, no. 7, pp. 552–558, 2017, doi: 10.2109/jcersj2.17055.

[69] A. Miura, T. Takei, and N. Kumada, “Synthesis of Wurtzite-Type InN Crystals by Low-Temperature Nitridation of $LiInO_2$ Using $NaNH_2$ Flux,” Cryst. Growth Des., vol. 12, no. 9, pp. 4545–4547, 2012, doi: 10.1021/cg3007266.

[70] A. Miura, T. Takei, and N. Kumada, “Low-Temperature Nitridation of Manganese and Iron Oxides Using $NaNH_2$ Molten Salt,” Inorg. Chem., vol. 52, no. 20, pp. 11787–11791, 2013, doi: 10.1021/ic401951u.

[71] A. Miura, T. Takei, and N. Kumada, “Synthesis of Cu_3N from CuO and $NaNH_2$,” J. Asian Ceram. Soc., vol. 2, no. 4, pp. 326–328, 2014, doi: 10.1016/j.jascer.2014.08.007.

[72] D. E. Clark, “Peroxides and peroxide-forming compounds,” Chem. Health Saf., vol. 8, no. 5, pp. 12–22, 2001, doi: 10.1021/acs.chas.8b08507.

[73] S. Sugihara and S. Imoto, “Hydrolysis of Uranium Nitrides,” vol. 3131, no. 1969, 2012, doi: 10.1080/18811248.1969.9732878.

[74] R. M. Dell, V. J. Wheeler, and E. J. McIver, “Oxidation of uranium mononitride and uranium monocarbide,” Trans. Faraday Soc., vol. 62, no. 0, pp. 3591–3606, 1966, doi:

10.1039/TF9666203591.

[75] G. A. R. Rao, S. K. Mukerjee, V. N. Vaidya, V. Venugopal, and D. D. Sood, “Oxidation and hydrolysis kinetic studies on UN,” J. Nucl. Mater., vol. 185, no. 2, pp. 231–241, 1991, doi: 10.1016/0022-3115(91)90340-D.

[76] S. Sunder and N. H. Miller, “XPS and XRD studies of corrosion of uranium nitride by water,” J. Alloys Compd., vol. 271–273, pp. 568–572, 1998, doi: https://doi.org/10.1016/S0925-8388(98)00157-1.

[77] R. R. Edwards, “Iodine-129: Its Occurrence in Nature and Its Utility as a Tracer,” Science (80-.)., vol. 137, no. 3533, pp. 851–853, Mar. 1962, [Online]. Available: http://www.jstor.org/stable/1710290.

[78] B. Grambow, “Mobile fission and activation products in nuclear waste disposal,” J. Contam. Hydrol., vol. 102, no. 3, pp. 180–186, 2008, doi: https://doi.org/10.1016/j.jconhyd.2008.10.006.

[79] P. Taylor, “A review of methods for immobilizing iodine-129 arising from a nuclear fuel recycle plant, with emphasis on waste-form chemistry (AECL--10163),” Whiteshell Nuclear Research Establishment, Pinawa, MB, Canada, 1990.

[80] D. I. Kaplan et al., “Radioiodine biogeochemistry and prevalence in groundwater,” Crit. Rev. Environ. Sci. Technol., vol. 44, no. 20, pp. 2287–2335, 2014, doi: 10.1080/10643389.2013.828273.

[81] E. Maddrell, A. Gandy, and M. Stennett, “The durability of iodide sodalite,” J. Nucl. Mater., vol. 449, no. 1, pp. 168–172, 2014, doi: https://doi.org/10.1016/j.jnucmat.2014.03.016.

[82] V. (Austria) International Atomic Energy Agency, Treatment, conditioning and disposal of iodine-129. International Atomic Energy Agency (IAEA): IAEA, 1987.

[83] T. Sakurai, A. Takahashi, N. Ishikawa, and Y. Komaki, “The Behavior of Iodine in a Simulated Spent-Fuel Solution,” Nucl. Technol., vol. 85, no. 2, pp. 206–212, May 1989, doi: 10.13182/NT89-A34241.

[84] T. Sakurai, A. Takahashi, N. Ishikawa, Y. Komaki, M. Ohnuki, and T. Adachi, “The Iodine Species and Their Behavior in the Dissolution of Spent-Fuel Specimens,” Nucl. Technol., vol. 99, no. 1, pp. 70–79, Jul. 1992, doi: 10.13182/NT92-A34704.

[85] R. T. Jubin, D. M. Strachan, and N. R. Soelberg, Iodine Pathways and Off- Gas Stream Characteristics for Aqueous Reprocessing Plants – A Literature Survey and Assessment. Idaho National Laboratory, 2013.

[86] D. R. Haefner and T. J. Tranter, “Methods of Gas Phase Capture of Iodine from Fuel Reprocessing Off-Gas : A Literature Survey,” no. February, 2007.

[87] R. D. Scheele, C. F. Wend, W. C. Buchmiller, A. E. Kozelisky, and R. L. Sell, “Preliminary Evaluation of Spent Silver Mordenite Disposal Forms Resulting from Gaseous Radioiodine Control at Hanford’s Waste Treatment Plant,” 2002.

[88] M. R. Cicconi et al., “Iodine solubility and speciation in glasses,” Sci. Rep., vol. 9, no. 1, p. 7758, 2019, doi: 10.1038/s41598-019-44274-4.

[89] B. J. Riley et al., “Iodine solubility in a low-activity waste borosilicate glass at 1000°C,” J. Nucl. Mater., vol. 452, no. 1, pp. 178–188, 2014, doi: https://doi.org/10.1016/j.jnucmat.2014.04.027.

[90] D. A. McKeown, I. S. Muller, and I. L. Pegg, “Iodine valence and local environments in borosilicate waste glasses using X-ray absorption spectroscopy,” J. Nucl. Mater., vol. 456, pp. 182–191, 2015, doi: https://doi.org/10.1016/j.jnucmat.2014.09.033.

[91] S. Rossignol, J. M. Réau, B. Tanguy, J. J. Videau, and J. Portier, “Glass formation and conductivity in the AgI-$AgO_{0.5}$-TeO_2 system,” J. Non. Cryst. Solids, vol. 155, no. 1, pp. 77–84, 1993, doi: https://doi.org/10.1016/0022-3093(93)90473-B.

[92] J. Dexpert-Ghys et al., “Investigation by raman scattering of the [TeO_2−$RMO_{0.5}$] (M = Ag or Tl) glasses and of the related ionic conductors $[TeO_2–RMO_{0.5}]_{1–x})[AgI]_x$,” J. Non. Cryst. Solids, vol. 170, no. 2, pp. 167–174, 1994, doi: https://doi.org/10.1016/0022-3093(94)90043-4.

[93] J. M. Réau et al., “Conductivity relaxation parameters of some Ag+ conducting tellurite glasses containing AgI or the $(AgI)_{0.75}$ $(T1I)_{0.25}$ eutectic mixture,” Solid State Ionics, vol. 74, no. 1, pp. 65–73, 1994, doi: https://doi.org/10.1016/01672738(94)90438-3.

[94] G. Dalba, P. Fornasini, F. Rocca, and E. Burattini, “XANES IN FAST ION CONDUCTING GLASSES AgI : Ag_2O : B_2O_3,” J. Phys. Colloq., vol. 47, no. C8, pp. C8-749-C8-752., 1986.

[95] H. Fujihara, T. Murase, T. Nishi, K. Noshita, T. Yoshida, and M. Matsuda, “Low Temperature Vitrification of Radioiodine Using AgI-Ag_2O-P_2O_5 Glass System,” MRS Online Proc. Libr., vol. 556, no. 1, p. 375, 1999, doi: 10.1557/PROC-556-375.

[96] J. H. Yang, H.-S. Park, and Y.-Z. Cho, “Silver phosphate glasses for immobilization of radioactive iodine,” Ann. Nucl. Energy, vol. 110, pp. 208–214, 2017, doi: https://doi.org/10.1016/j.anucene.2017.06.042.

[97] T. Lemesle, F. O. Méar, L. Campayo, O. Pinet, B. Revel, and L. Montagne, “Immobilization of radioactive iodine in silver aluminophosphate glasses,” J. Hazard. Mater., vol. 264, pp. 117–126, 2014, doi: https://doi.org/10.1016/j.jhazmat.2013.11.019.

[98] X. H. Zhang et al., “Infrared transmitting glasses and glass-ceramics,” J. Non. Cryst. Solids, vol. 352, no. 23, pp. 2411–2415, 2006, doi: https://doi.org/10.1016/j.jnoncrysol.2006.03.029.

[99] X. Wang et al., “Investigations of Ge–Te–AgI chalcogenide glass for far-infrared application,” Spectrochim. Acta Part A Mol. Biomol. Spectrosc., vol. 86, pp. 586–589, 2012, doi: https://doi.org/10.1016/j.saa.2011.11.018.

[100] V. Q. Nguyen, J. S. Sanghera, J. A. Freitas, I. D. Aggarwal, and I. K. Lloyd, “Structural investigation of chalcogenide and chalcohalide glasses using Raman spectroscopy,” J. Non. Cryst. Solids, vol. 248, no. 2, pp. 103–114, 1999, doi: https://doi.org/10.1016/S0022-3093(99)00303-8.

[101] J. Troles, F. Smektala, G. Boudebs, and A. Monteil, “Third order nonlinear optical characterization of new chalcohalogenide glasses containing lead iodine,” Opt. Mater. (Amst)., vol. 22, no. 4, pp. 335–343, 2003, doi: https://doi.org/10.1016/S09253467(02)00345-2.

[102] H. Tanabe, T. Sakuragi, K. Yamaguchi, T. Sato, and H. Owada, “Development of New Waste Forms to Immobilize Iodine-129 Released from a Spent Fuel Reprocessing Plant,” Adv. Sci. Technol., vol. 73, pp. 158–170, 2010, doi: 10.4028/www.scientific.net/AST.73.158.

[103] T. J. Garino, T. M. Nenoff, J. L. Krumhansl, and D. X. Rademacher, “LowTemperature Sintering Bi–Si–Zn-Oxide Glasses for Use in Either Glass Composite Materials or Core/Shell ^{129}I Waste Forms,” J. Am. Ceram. Soc., vol. 94, no. 8, pp. 2412–2419, 2011, doi: 10.1111/j.1551-2916.2011.04542.x.

[104] J. Matyáš, N. Canfield, S. Sulaiman, and M. Zumhoff, “Silica-based waste form for immobilization of iodine from reprocessing plant off-gas streams,” J. Nucl. Mater., vol. 476, pp. 255–261, 2016, doi: https://doi.org/10.1016/j.jnucmat.2016.04.047.

[105] T. Nakazawa, H. Kato, K. Okada, S. Ueta, and M. Mihara, “Iodine Immobilization by Sodalite Waste Form,” MRS Online Proc. Libr., vol. 663, no. 1, p. 51, 2011, doi: 10.1557/PROC-663-51.

[106] S. Chong, J. Peterson, J. Nam, B. Riley, and J. McCloy, “Synthesis and characterization of iodosodalite,” J. Am. Ceram. Soc., vol. 100, no. 5, pp. 2273–2284, May 2017, doi: https://doi.org/10.1111/jace.14772.

[107] G. P. Sheppard, J. A. Hriljac, E. R. Maddrell, and N. C. Hyatt, “Silver Zeolites: Iodide Occlusion and conversion to Sodalite – a potential ^{129}I waste form?,” MRS Online Proc. Libr., vol. 932, no. 1, p. 361, 2006, doi: 10.1557/PROC-932-36.1.

[108] E. R. Maddrell and P. K. Abraitis, “A Comparison of Wasteforms and Processes for the Immobilisation of Iodine-129,” MRS Online Proc. Libr., vol. 807, no. 1, pp. 565–570, 2003, doi: 10.1557/PROC-807-261.

[109] E. R. Maddrell, E. R. Vance, and D. J. Gregg, “Capture of iodine from the vapour phase and immobilisation as sodalite,” J. Nucl. Mater., vol. 467, pp. 271–279, 2015, doi: https://doi.org/10.1016/j.jnucmat.2015.09.038.

[110] E. R. Maddrell et al., “Silver iodide sodalite – Wasteform / Hip canister interactions and aqueous durability,” J. Nucl. Mater., vol. 517, pp. 71–79, 2019, doi: https://doi.org/10.1016/j.jnucmat.2019.02.002.

[111] M. ul Hassan, S. Venkatesan, and H. J. Ryu, “Non-volatile immobilization of iodine by the cold-sintering of iodosodalite,” J. Hazard. Mater., vol. 386, p. 121646, 2020, doi: https://doi.org/10.1016/j.jhazmat.2019.121646.

[112] F. Audubert, J.-M. Savariault, and J.-L. Lacout, “Pentalead tris(vanadate) iodide, a defect vanadinite-type compound,” Acta Crystallogr. Sect. C, vol. 55, no. 3, pp. 271–273, Mar. 1999, [Online]. Available: https://doi.org/10.1107/S0108270198005034.

[113] S. A. T. Redfern, S. E. Smith, and E. R. Maddrell, “High-temperature breakdown of the synthetic iodine analogue of vanadinite , $Pb_5(VO_4)_3I$: an apatite-related compound for iodine radioisotope immobilization ?,” Mineral. Mag., vol. 76, no. August, pp. 997–1003, 2012, doi: 10.1180/minmag.2012.076.4.15.

[114] S. Le Gallet et al., “Spark plasma sintering of iodine-bearing apatite,” J. Nucl. Mater., vol. 400, no. 3, pp. 251–256, 2010, doi: https://doi.org/10.1016/j.jnucmat.2010.03.011.

[115] F. Audubert, J. Carpena, J. L. Lacout, and F. Tetard, “Elaboration of an iodinebearing apatite Iodine diffusion into a $Pb_3(VO_4)_2$ matrix,” Solid State Ionics, vol. 95, no. 1, pp. 113–119, 1997, doi: https://doi.org/10.1016/S0167-2738(96)00570-X.

[116] Z. Zhang et al., “Mechanism of iodine release from iodoapatite in aqueous solution,” RSC Adv., vol. 8, no. 8, pp. 3951–3957, 2018, doi: 10.1039/C7RA11049A.

[117] Z. Zhang, W. L. Ebert, T. Yao, J. Lian, K. T. Valsaraj, and J. Wang, "Chemical Durability and Dissolution Kinetics of Iodoapatite in Aqueous Solutions," ACS Earth Sp. Chem., vol. 3, no. 3, pp. 452–462, Mar. 2019, doi: 10.1021/acsearthspacechem.8b00162.

[118] Z. Zhang, L. Gustin, W. Xie, J. Lian, K. T. Valsaraj, and J. Wang, "Effect of solution chemistry on the iodine release from iodoapatite in aqueous environments," J. Nucl. Mater., vol. 525, pp. 161–170, 2019, doi: https://doi.org/10.1016/j.jnucmat.2019.07.034.

[119] M. Uno, A. Kosuga, S. Masuo, M. Imamura, and S. Yamanaka, "Thermal and mechanical properties of $AgPb_9(VO_4)_6I$ and $AgBa_9(VO_4)_6I$," J. Alloys Compd., vol. 384, no. 1, pp. 300–302, 2004, doi: https://doi.org/10.1016/j.jallcom.2004.04.094.

[120] E. V. Johnstone, D. J. Bailey, M. C. Stennett, J. Heo, and N. C. Hyatt, "On the existence of $AgM_9(VO_4)6I$ (M = Ba, Pb)," RSC Adv., vol. 7, no. 77, pp. 49004– 49009, 2017, doi: 10.1039/c7ra09313f.

[121] E. V Johnstone et al., "Synthesis and characterization of iodovanadinite using PdI_2, an iodine source for the immobilisation of radioiodine," RSC Adv., vol. 10, no. 42, pp. 25116–25124, 2020, doi: 10.1039/D0RA04114A.

[122] C. Cao, S. Chong, L. Thirion, J. C. Mauro, J. S. Mccloy, and A. Goel, "Wet chemical synthesis of apatite-based waste forms – A novel room temperature method for the immobilization of radioactive iodine †," J. Mater. Chem. A Pap. V, no. 5, pp. 14331–14342, 2017, doi: 10.1039/c7ta00230k.

[123] J. L. Krumhansl and T. M. Nenoff, "Hydrotalcite-like layered bismuth–iodine–oxides as waste forms," Appl. Geochemistry, vol. 26, no. 1, pp. 57–64, 2011, doi: https://doi.org/10.1016/j.apgeochem.2010.11.003.

[124] A. Tesfay Reda, M. Pan, D. Zhang, and X. Xu, "Bismuth-based materials for iodine capture and storage: A review," J. Environ. Chem. Eng., vol. 9, no. 4, p. 105279, 2021, doi: https://doi.org/10.1016/j.jece.2021.105279.

[125] E. R. Vance and J. S. Hartman, "Effects of Halides and Sulphates in Synroc-C," MRS Online Proc. Libr., vol. 556, no. 1, p. 41, 1999, doi: 10.1557/PROC-556-41.

[126] L. Campayo, A. Grandjean, A. Coulon, R. Delorme, D. Vantelon, and D. Laurencin, "Incorporation of iodates into hydroxyapatites: a new approach for the confinement of radioactive iodine," J. Mater. Chem., vol. 21, no. 44, pp. 17609–17611, 2011, doi: 10.1039/C1JM14157K.

[127] D. Laurencin, D. Vantelon, C. Gervais, and A. Coulon, "Investigation of the local environment of iodate in hydroxyapatite by combination of X-ray absorption spectroscopy and DFT modeling †," RSC Adv., vol. 4, pp. 14700–14707, 2014, doi: 10.1039/c3ra47691j.

[128] A. Coulon et al., "Key parameters for spark plasma sintering of wet-precipitated iodate-substituted hydroxyapatite," J. Eur. Ceram. Soc., vol. 36, no. 8, pp. 2009–2016, 2016, doi: https://doi.org/10.1016/j.jeurceramsoc.2016.02.041.

[129] A. Coulon, A. Grandjean, D. Laurencin, P. Jollivet, S. Rossignol, and L. Campayo, "Durability testing of an iodate-substituted hydroxyapatite designed for the conditioning of ^{129}I," J. Nucl. Mater., vol. 484, pp. 324–331, 2017, doi: https://doi.org/10.1016/j.jnucmat.2016.10.047.

[130] A. R. West, Solid State Chemistry and its Applications, 2nd Edition, Student Edition, 2nd Ed. Wiley, 2014.

[131] A. W. Sleight and R. Ward, "Compounds of Post-Transition Elements with the Ordered Perovskite Structure," Inorg. Chem., vol. 3, no. 2, p. 292, 1964, doi: 10.1021/ic50012a042.

[132] J.T.W De Hair, A.F Corsmit and G. Blasse, "Vibrational spectra and force constants of periodates with ordered perovskite structure," J. Inorg. Nucl. Chem., vol. 36, no. 2, pp. 313–315, 1974, doi: https://doi.org/10.1016/0022-1902(74)80015-1.

[133] F. Kubel, N. Wandl, M. Pantazi, V. D'Anna, and H. Hagemann, "The periodatebased double perovskites M_2NaIO_6 (M = Ca, Sr, and Ba)," Zeitschrift fur Anorg. und Allg. Chemie, vol. 639, no. 6, pp. 892–898, 2013, doi: 10.1002/zaac.201200555.

[134] F. Kubel, M. Pantazi, N. Wandl, and H. Hagemann, "Synthesis and crystal structures of a stable, a metastable and a high temperature modification of Pb_2NaIO_6," Zeitschrift fur Anorg. und Allg. Chemie, vol. 640, no. 15, pp. 3184–3189, 2014, doi: 10.1002/zaac.201400208.

[135] C. J. Howard, B. J. Kennedy, and P. M. Woodward, "Ordered double perovskites - a group-theoretical analysis," Acta Crystallogr. Sect. B, vol. 59, no. 4, pp. 463–471, Aug. 2003, doi: 10.1107/S0108768103010073.

[136] United Kingdom Nirex Limited, "Nirex Report Generic Repository Studies Generic post-closure Performance Assessment," Nirex Rep. N/080, 2003.

[137] F. Poineau, E. Mausolf, G. D. Jarvinen, A. P. Sattelberger, and K. R. Czerwinski, "Technetium Chemistry in the Fuel Cycle: Combining Basic and Applied Studies," Inorg. Chem., vol. 52, no. 7, pp. 3573–3578, Apr. 2013, doi: 10.1021/ic3016468.

[138] D. J. Bailey et al., "A new approach to the immobilisation of technetium and transuranics: Co-disposal in a zirconolite ceramic matrix," J. Nucl. Mater., vol. 528, p. 151885, 2020, doi: 10.1016/j.jnucmat.2019.151885.

[139] K. L. Nash and M. Nilsson, "1 - Introduction to the reprocessing and recycling of spent nuclear fuels," in Woodhead Publishing Series in Energy, R. B. T.-R. and R. of S. N. F. Taylor, Ed. Oxford: Woodhead Publishing, 2015, pp. 3–25.

[140] L. G. Williams, "4 - Safety and security issues in the reprocessing and recycling of spent nuclear fuels for advanced fuel cycles," in Woodhead Publishing Series in Energy, R. B. T.-R. and R. of S. N. F. Taylor, Ed. Oxford: Woodhead Publishing, 2015, pp. 63–90.

[141] D. D. Sood and S. K. Patil, "Chemistry of nuclear fuel reprocessing: Current status," J. Radioanal. Nucl. Chem., vol. 203, no. 2, pp. 547–573, 1996, doi: 10.1007/BF02041529.

[142] J. G. Darab and P. A. Smith, "Chemistry of technetium and rhenium species during low-level radioactive waste vitrification," Chem. Mater., vol. 8, no. 5, pp. 1004–1021, 1996, doi: 10.1021/cm950418+.

[143] C. Z. Soderquist, M. J. Schweiger, D.-S. Kim, W. W. Lukens, and J. S. McCloy, "Redox-dependent solubility of technetium in low activity waste glass," J. Nucl. Mater., vol. 449, no. 1, pp. 173–180, 2014, doi: https://doi.org/10.1016/j.jnucmat.2014.03.008. [144] I. L. Pegg, "Behavior of technetium in nuclear waste vitrification processes," J. Radioanal. Nucl. Chem., vol. 305, no. 1, pp. 287–292, 2015, doi: 10.1007/s10967-0143900-9.

[145] D. Kim and A. A. Kruger, “Volatile species of technetium and rhenium during waste vitrification,” J. Non. Cryst. Solids, vol. 481, pp. 41–50, 2018, doi: https://doi.org/10.1016/j.jnoncrysol.2017.10.013.

[146] B. C. Childs, F. Poineau, K. R. Czerwinski, and A. P. Sattelberger, “The nature of the volatile technetium species formed during vitrification of borosilicate glass,” J. Radioanal. Nucl. Chem., vol. 306, no. 2, pp. 417–421, 2015, doi: 10.1007/s10967-0154203-5.

[147] F. Poineau et al., “Uranium/technetium separation for the UREX process – synthesis and characterization of solid reprocessing forms,” Radiochim. Acta, vol. 96, no. 9–11, pp. 527–533, 2008, doi: doi:10.1524/ract.2008.1533.

[148] E. M. Pierce et al., “Structure and Thermochemistry of Perrhenate Sodalite and Mixed Guest Perrhenate/Pertechnetate Sodalite,” Environ. Sci. Technol., vol. 51, no. 2, pp. 997–1006, Jan. 2017, doi: 10.1021/acs.est.6b01879.

[149] C. I. Pearce et al., “Technetium immobilization by materials through sorption and redox-driven processes: A literature review,” 2019, doi: 10.1016/j.scitotenv.2019.06.195.

[150] S. T. Sekula, R. H. Kernohan, and G. R. Love, “Superconducting Properties of Technetium,” Phys. Rev., vol. 155, no. 2, pp. 364–369, Mar. 1967, doi: 10.1103/PhysRev.155.364.

[151] T. Hartmann, A. J. Alaniz, and D. J. Antonio, “Fabrication and Properties of Technetium-bearing Pyrochlores and Perovskites as Potential Waste Forms,” Procedia Chem., vol. 7, pp. 622–628, 2012, doi: 10.1016/j.proche.2012.10.095.

[152] E. E. Rodriguez, F. Poineau, A. Llobet, J. D. Thompson, R. Seshadri, and A. K. Cheetham, “Preparation, magnetism and electronic structures of cadmium technetates,” J. Mater. Chem., vol. 21, no. 5, pp. 1496–1502, 2011, doi: 10.1039/c0jm02470h.

[153] V. B. Compton, E. Corenzwit, J. P. Maita, B. T. Matthias, and F. J. Morin, “Superconductivity of Technetium Alloys and Compounds,” Phys. Rev., vol. 123, no. 5, pp. 1567–1568, Sep. 1961, doi: 10.1103/PhysRev.123.1567.

[154] O. Muller, W. B. White, and R. Roy, “Crystal chemistry of some technetiumcontaining oxides,” J. Inorg. Nucl. Chem., vol. 26, no. 12, pp. 2075–2086, 1964, doi: 10.1016/0022-1902(64)80152-4.

[155] M. Y. Khalil and W. B. White, “Magnesium Titanate Spinel: A Ceramic Phase for Immobilization of Technetium-99 from Radioactive Wastes,” J. Am. Ceram. Soc., vol. 66, no. 10, pp. c197–c198, Oct. 1983, doi: https://doi.org/10.1111/j.11512916.1983.tb10554.x.

[156] M. J. den Exter, S. Neumann, and T. Tomasberger, “Immobilization and Behavior of Technetium in a Magnesium Titanate Matrix for Final Disposal,” MRS Online Proc. Libr., vol. 932, no. 1, p. 621, 2006, doi: 10.1557/PROC-932-62.1.

[157] G. J. Thorogood et al., “Structure and cation ordering in spinel-type $TcCo_2O_4$. An example of a trivalent technetium oxide,” Dalt. Trans., vol. 40, no. 41, pp. 10924–10926, 2011, doi: 10.1039/C1DT10954E.

[158] J. Liu, C. I. Pearce, O. Qafoku, E. Arenholz, S. M. Heald, and K. M. Rosso, “Tc(VII) reduction kinetics by titanomagnetite ($Fe_{3-x}Ti_xO_4$) nanoparticles,” Geochim. Cosmochim. Acta, vol. 92, pp. 67–81, 2012, doi:

https://doi.org/10.1016/j.gca.2012.06.004.

[159] M. S. Lee et al., “Impeding ^{99}Tc(IV) mobility in novel waste forms,” Nat. Commun., vol. 7, no. May, pp. 3–8, 2016, doi: 10.1038/ncomms12067.

[160] W. W. Lukens, N. Magnani, T. Tyliszczak, C. I. Pearce, and D. K. Shuh, “Incorporation of Technetium into Spinel Ferrites,” Environ. Sci. Technol., vol. 50, no. 23, pp. 13160–13168, Dec. 2016, doi: 10.1021/acs.est.6b04209.

[161] E. E. Rodriguez et al., “High temperature magnetic ordering in the 4d perovskite $SrTcO_3$,” Phys. Rev. Lett., vol. 106, no. 6, pp. 1–4, 2011, doi: 10.1103/PhysRevLett.106.067201.

[162] J. Mravlje, M. Aichhorn, and A. Georges, “Origin of the High Neel Temperature in $SrTcO_3$,” Phys. Rev. Lett., vol. 108, no. 19, p. 197202, May 2012, doi: 10.1103/PhysRevLett.108.197202.

[163] E. M. Reynolds et al., “Magneto-structural coupling in $SrTc_xRu_{1-x}O_3$ (x = 0.25,0.5) perovskites,” J. Solid State Chem., vol. 287, p. 121378, 2020, doi: https://doi.org/10.1016/j.jssc.2020.121378.

[164] E. Reynolds et al., “Structure and magnetism in $Sr_{1-x}A_xTcO_3$ perovskites: Importance of the A-site cation,” Phys. Rev. B, vol. 95, no. 5, p. 54430, Feb. 2017, doi: 10.1103/PhysRevB.95.054430.

[165] C.-M. Dai and C.-L. Ma, “Optical band gap of $SrTcO_3$ from first-principles calculations,” Mod. Phys. Lett. B, vol. 28, no. 06, p. 1450049, Mar. 2014, doi: 10.1142/S0217984914500493.

[166] V. S. Borisov et al., “Magnetic exchange interactions and antiferromagnetism of $ATcO_3$(A= Ca, Sr, Ba) studied from first principles,” Phys. Rev. B, vol. 85, no. 13, p. 134410, Apr. 2012, doi: 10.1103/PhysRevB.85.134410.

[167] C.-L. Ma and T. Zhou, “Comparison of the structural and magnetic properties of ground-state $SrTcO_3$ and $CaTcO_3$ from first principles,” Phys. B Condens. Matter, vol. 407, no. 2, pp. 218–221, 2012, doi: https://doi.org/10.1016/j.physb.2011.10.031.

[168] G. J. Thorogood, M. Avdeev, M. L. Carter, B. J. Kennedy, J. Ting, and K. S. Wallwork, “Structural phase transitions and magnetic order in $SrTcO_3$,” Dalt. Trans., vol. 40, no. 27, pp. 7228–7233, 2011, doi: 10.1039/C1DT10445D.

[169] C. Franchini, T. Archer, J. He, X.-Q. Chen, A. Filippetti, and S. Sanvito, “Exceptionally strong magnetism in the 4d perovskites $RTcO_3$ (R= Ca, Sr, Ba),” Phys. Rev. B, vol. 83, no. 22, p. 220402, Jun. 2011, doi: 10.1103/PhysRevB.83.220402.

[170] M. Avdeev et al., “Antiferromagnetism in a technetium oxide. Structure of $CaTcO_3$,” J. Am. Chem. Soc., vol. 133, no. 6, pp. 1654–1657, 2011, doi: 10.1021/ja109431t.

[171] N. P. Laverov, S. V. Yudintsev, and B. I. Omel’yanenko, “Isolation of long-lived technetium-99 in confinement matrices,” Geol. Ore Depos., vol. 51, no. 4, pp. 259–274, 2009, doi: 10.1134/S1075701509040011.

[172] M. A. Subramanian, G. Aravamudan, and G. V Subba Rao, “Oxide pyrochlores — A review,” Prog. Solid State Chem., vol. 15, no. 2, pp. 55–143, 1983, doi: https://doi.org/10.1016/0079-6786(83)90001-8.

[173] P. F. Weck, E. Kim, F. Poineau, E. E. Rodriguez, A. P. Sattelberger, and K. R. Czerwinski, “Structural and electronic trends in rare-earth technetate pyrochlores,” Dalt. Trans., vol. 39, no. 31, pp. 7207–7210, 2010, doi: 10.1039/C0DT00212G.

[174] T. Hartmann et al., "Structure studies on lanthanide technetium pyrochlores as prospective host phases to immobilize ^{99}technetium and fission lanthanides from effluents of reprocessed used nuclear fuels," J. Nucl. Mater., vol. 411, no. 1–3, pp. 60–71, 2011, doi: 10.1016/j.jnucmat.2011.01.033.

[175] E. E. Rodriguez, F. Poineau, A. Llobet, K. Czerwinski, R. Seshadri, and A. K. Cheetham, "Preparation and crystal structures of bismuth technetates: A new metal oxide system," Inorg. Chem., vol. 47, no. 14, pp. 6281–6288, 2008, doi: 10.1021/ic8003273.

[176] E. E. Rodriguez et al., "Structural studies of TcO_2 by neutron powder diffraction and first-principles calculations," J. Am. Chem. Soc., vol. 129, no. 33, pp. 10244–10248, 2007, doi: 10.1021/ja0727363.

[177] D. B. Rogers, R. D. Shannon, A. W. Sleight, and J. L. Gillson, "Crystal chemistry of metal dioxides with rutile-related structures," Inorg. Chem., vol. 8, no. 4, pp. 841–849, Apr. 1969, doi: 10.1021/ic50074a029.

[178] M. W. A. Stewart, E. R. Vance, and R. A. Day, "Titanate Wasteforms for Tc-99 Immobilisation," Proc. Annu. Waste Manag. Symp., no. February 2004, 2004.

[179] M. L. Carter, M. W. A. Stewart, E. R. Vance, B. D. Begg, S. Moricca, and J. Tripp, "HIPed tailored ceramic waste forms for the immobilization of Cs, Sr and Tc," Glob. 2007 Adv. Nucl. Fuel Cycles Syst., pp. 1022–1028, 2007.

[180] E. Y. Kuo, M. J. Qin, G. J. Thorogood, K. R. Whittle, G. R. Lumpkin, and S. C. Middleburgh, "Technetium and ruthenium incorporation into rutile TiO_2," J. Nucl. Mater., vol. 441, no. 1, pp. 380–389, 2013, doi: https://doi.org/10.1016/j.jnucmat.2013.06.022.

[181] W. W. Lukens and S. A. Saslow, "Aqueous Synthesis of Technetium-Doped Titanium Dioxide by Direct Oxidation of Titanium Powder, a Precursor for Ceramic Nuclear Waste Forms," Chem. Mater., vol. 29, no. 24, pp. 10369–10376, Dec. 2017, doi: 10.1021/acs.chemmater.7b03567.

[182] K. P. Hart, E. R. Vance, R. A. Day, B. D. Begg, P. J. Angel, and A. [ANSTO Jostsons Menai, New South Wales (Australia)], Immobilization of separated Tc and Cs/Sr in Synroc. United States: Materials Research Society, Pittsburgh, PA (United States), 1996.

[183] E. R. Vance et al., "Synroc Derivatives for the Hanford Waste Remediation Task," MRS Proc., vol. 465, p. 341, 1996, doi: DOI: 10.1557/PROC-465-341.

Chapter 3

Methods

Within this chapter, the individual characterisation techniques used by the author throughout are broken down into their underlying theory. This is accompanied by any relevant sample preparation techniques, experimental apparatus used and subsequent data analysis protocols. This section is focused on the underpinning background to the experimental techniques applied, with further specific details given in each of the following chapters.

3.1 X-ray diffraction

Powder X-ray diffraction (XRD) formed the initial characterisation technique for the samples produced as this method is excellent for phase analysis of crystalline products [1], [2].

When X-rays are incident on sample and the wavelength of the incident X-rays is smaller than that of the lattice spacing of the sample, scattering and diffraction of the X-rays occurs. XRD patterns indicate the relative intensities of coherently scattered X-rays from a sample, an exploitation of the Bragg equation [3]:

$$n\lambda = 2d_{hkl} \sin\theta \tag{1}$$

where n is any integer, λ is the incident X-ray wavelength, d is the lattice plane distance and θ is the scattering angle. The pattern produced by these peaks is unique to the structure of the sample and is a method of phase identification. The relative sizes and shape profiles of the peaks can also provide information on the properties of the sample microstructure. The data can then be used to calculate cell and lattice parameters. It should be noted that while XRD is a powerful characterisation tool, it affords characterisation of structure and not necessarily composition. The scattering cross section for X-rays increases with atomic number Z and relates to the interaction with electron cloud of the atom. In trying to discern two neighbouring elements in the periodic table, there is minimal distinction between neighbouring scattering cross sections due to similarity of the number of electrons. Moreover, the scattering cross section for light Z elements such as oxygen and nitrogen is small.

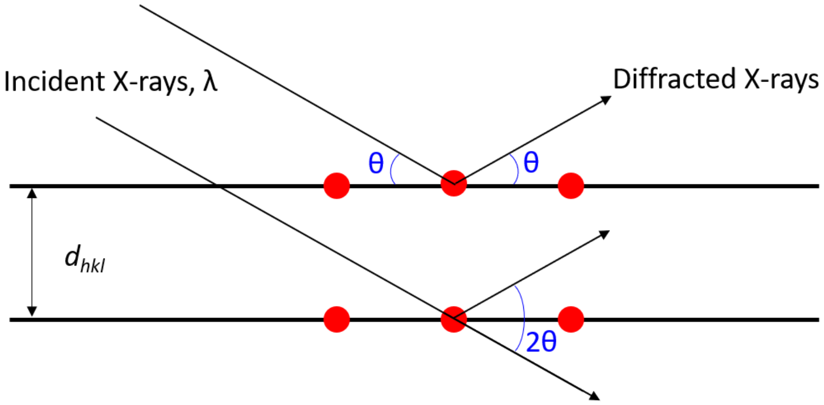

Figure 1. Bragg equation parameters applied to a crystalline solid

However, the structural and microstructural information yielded by XRD still makes this a useful characterisation technique in this study.

Crystalline solids comprise a periodic distribution of atoms in three dimensions, for which the smallest element of a crystal structure that fills all space by suitable translation operations, is termed the unit-cell defined by the dimensions a, b, c and angles α, β, γ [4]. The atomic positions are expressed as fractional co-ordinates (x, y, z) relative to the to the unit cell parameters, a, b, c. In consideration of the diffraction of X-rays and neutrons by crystalline materials, it is useful to define a series of crystal planes, which intersect the unit cell edges. The reciprocal of the plane intercept, normalised to the smallest integral ratio, are denoted as Miller indices, *hkl*; the notation (*hkl*) is used to define a single crystal plane or set of parallel planes. The perpendicular distance between adjacent (*hkl*) planes, the "d-spacing" d_{hkl}, is of significance, and, for an orthogonal cell (α, β, γ, =90°), can be expressed as:

$$\frac{1}{\mathrm{d}_{\mathrm{hkl}}^2} = \frac{\mathrm{h}^2}{\mathrm{a}^2} + \frac{\mathrm{k}^2}{\mathrm{b}^2} + \frac{\mathrm{l}^2}{\mathrm{c}^2} \tag{2}$$

The distance d_{hkl} sets the geometric condition for diffraction to occur. The incident and scattered radiation propagate as waves and diffraction may be considered as reflection of the radiation by the crystal planes (*hkl*), such that the scattered radiation emerges in-phase, leading to constructive interference. Note that the scattering interaction, however, arises from the interaction of the electric field vector of the X-ray and the electron clouds of the composite atom. This in phase criterion is satisfied if the angle of incidence and reflection are equal and the difference in path length, *d*, between the incident and scattered radiation corresponds to an integral number, of wavelengths, λ (see Figure 1); this yields the Bragg equation:

$$\delta=n\lambda=2d_{hkl}\sin\theta \tag{3}$$

The intensity of radiation diffracted by a polycrystalline material, I_{hkl}, may be formulated as:

$$I_{hkl}=F_{hkl}^{2}mL_{hkl}P_{hkl}A \tag{4}$$

where F_{hkl} is the structure factor of a reflection (*hkl*), *m* is the multiplicity factor, *A* an absorption term, L_{hkl} the Lorentz factor and P_{hkl} a polarisation factor. The Lorentz and polarisation terms are geometric factors which account for the fact that the intensity of the diffracted radiation and its polarisation depend on scattering angle.

The structure factor, F_{hkl}, expresses the amplitude and phase of the radiation diffracted by a crystal plane *hkl*. It represents the summation of the amplitude and phase components of the individual waves scattered by each atom, *j*, of the unit cell, with fractional coordinates (x_j, y_j, z_j):

$$F_{hkl}=\sum_j f_j p_j \exp\left[2\pi i\left(x_j h+y_j k+z_j l\right)\right]\exp\left[-\frac{B_j\sin^2\theta}{\lambda^2}\right] \tag{5}$$

With

$$B_j=8\pi^2\langle U_j\rangle^2 \tag{6}$$

Here, f_j is the atomic scattering factor of the *j*th atom and p_j its occupancy factor; B_j accounts for the isotropic thermal vibration, in terms of the root mean squared displacement, $<U_j>$. By modelling the reflection intensity using the Rietveld method, it is possible to determine the fractional co-ordinates of the atoms, site occupancies and thermal vibrations, which define the crystal structure. In the case of X-ray diffraction, the atomic form factor, $f_j = Z_e$,

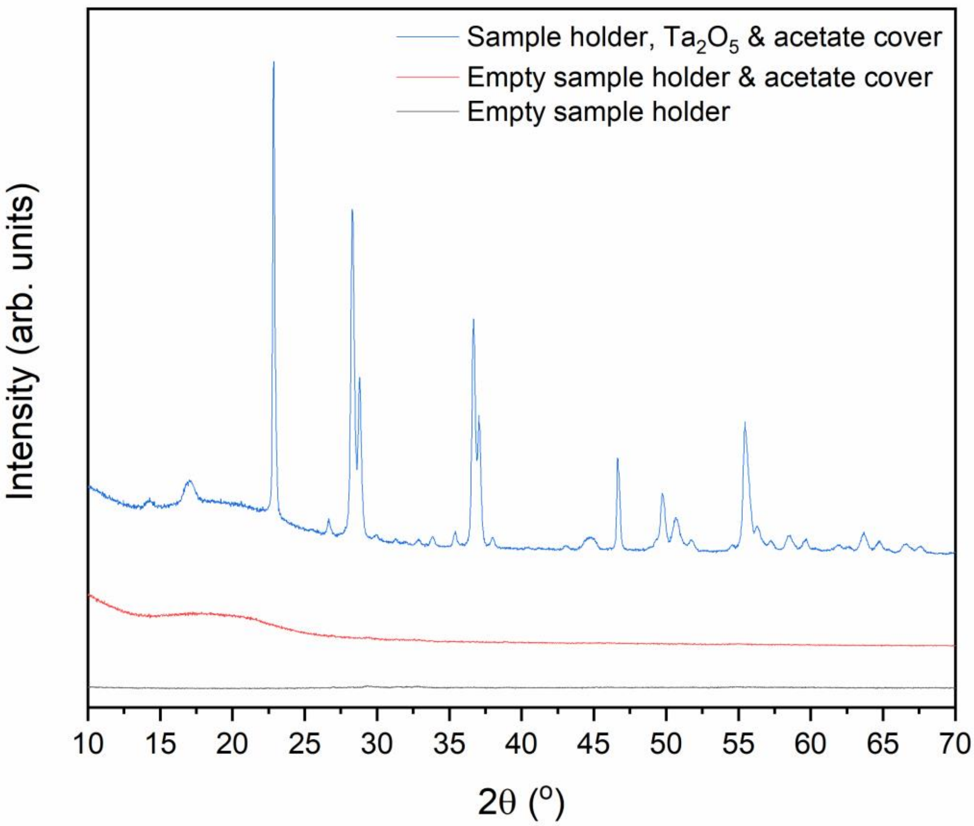

Figure 2. Comparison of XRD patterns obtained from sample holder only, sample holder with applied acetate and sample holder with crystalline Ta_2O_5 sample with applied acetate.

where Z_e is the number of electrons, at $\theta = 0$; however, f_j decreases with increasing sin θ / λ, due to the progressive destructive interference between X-rays scattered by electrons in different parts of the atom, since the X-ray wavelength, λ, is of the atomic size. The latter gives rise to the observed decrease in reflection intensity as a function of scattering angle 2θ in X-ray diffraction.

For the purposes of this research, samples were first prepared by hand grinding in a pestle and mortar before packing into a low background silicon sample holder, with minimal preferred orientation induced during this process. To achieve sealed containment of radioactive powders, the sample surface of approximately 10 mm diameter was occluded and a light spray of 3M ReMount spray adhesive applied. The sample was then exposed and an acetate sheet (provided by STOE and typically used for transmission XRD) was laid taut and flat across the sample and adhesive. This allowed the powders to be contained for use in the diffractometer while also being recoverable in bulk. The use of this acetate sheet and spray adhesive leads to a small contribution in the resultant XRD pattern, visualised as an area of diffuse scattering (non crystallinity) in the low angle region (Figure 2). However, when tested with Ta_2O_5 this was deemed low enough in magnitude to not interfere with analysis of the X-ray diffraction arising from the sample.

XRD data was acquired on a Bruker D2 Phaser diffractometer with Cu K_a radiation of λ =1.54184 Å, collected over an angle range $10 \leq 2\theta \leq 70°$, with incremental steps of 0.2 °2θ with a resultant acquisition time of approximately one hour as standard. The patterns were then analysed for phase using the associated Bruker DIFFRAC.EVA software [5], searching the ICDD PDF 4+ database for phase matching. Preparation of samples for subsequent data analysis using Rietveld refinement was performed as described above but with the addition of approximately 10 to 20 weight percentage of lanthanum hexaboride, LaB_6 (Sigma Aldrich, 99% assay, 10 micron particulate size) to act as an internal standard.

3.2 Neutron diffraction

Neutron diffraction operates on a similar principle to X-ray diffraction, however, relies on different interactions with the target sample. Where X-rays interact with the electron cloud of an atom with a resultant Z dependence, neutrons interact directly with the sample nuclei [6], [7]. This means different isotopes show different magnitudes of nuclear scattering. This property is called the scattering length *b*. Nuclear scattering is isotropic which means that the scattering lengths of isotopes are mostly constant in the wavelength range for thermal neutrons (the exceptions being cadmium, gadolinium and boron, all known neutron absorbers [8]). A corollary of this is that the scattering lengths are therefore isotope specific and do not vary in a simple relationship with atomic number of the scattering nuclei. As a result, this diffraction technique is directly sensitive to nuclei positions within the sample. This is also true at high angles of scattering, as the nuclear scattering is considered a point source and does not suffer from the decrease of scattering power with respect to scattering angle that X-ray diffraction does. This makes neutron diffraction ideal for studying crystallographic structure. Time of flight measurements in neutron diffraction studies also offer the advantage of being able to localise very small distortions in the lattice by way of excellent resolution at these length scales.

Neutron diffraction experiments in this work were performed at the ISIS Neutron and Muon Source at the STFC Rutherford Appleton Laboratory. At this facility, neutrons are produced via spallation where high energy protons are incident on a heavy metal target, forcing neutron release from the target metal atoms. Initially an ion source produces H^- ions, composed of a proton and two electrons. These are stripped of electrons before entering the synchrotron where they are accelerated. An applied radio frequency field bunches the protons into discrete pulses. The accelerated protons are then targeted at a tantalum spallation source, forcing the pulsed release of neutrons, which may be moderated prior to being utilised in the various instruments of the facility.

Neutron diffraction data in this thesis were acquired on the POLARIS diffractometer, which utilises the time of flight principle [9]. The sample is located several metres from the spallation source in an evacuated sample chamber, surrounded by detector banks at fixed angle with respect to the incident beam. The crystallites of the sample are randomly oriented and a fraction will be at the correct Bragg angle, θ, to diffract neutrons of wavelength, λ, present within the pulse spectrum. The distances between source and sample, D_1, and sample and detector, D_2, are known, and the time, t, elapsed between neutron spallation and detection is measured – hence time of flight neutron diffraction. The neutron wavelength can be deduced from the de Broglie equation:

$$\lambda = \frac{\mathrm{ht}}{\mathrm{m_n D}} \tag{7}$$

Where m_n is the neutron rest mass and $\mathrm{D} = \mathrm{D_1} + \mathrm{D_2}$. Since the diffraction angle is known (determined by the fixed detector position), the d-spacing of the diffracting crystal planes is given by the modified Bragg equation:

$$d_{hkl}=\frac{ht}{2m_nD\sin\theta} \tag{8}$$

The constituent equations for neutron diffraction, in terms of the Bragg Law, reflection intensity (I_{hkl}) and structure factor (F_{hkl}) are essentially identical to those for X-ray diffraction, with the substitution of the neutron scattering length b_j, for the atomic scattering factor f_j.

For measurements of time of flight neutron diffraction data, samples were prepared and loaded into vanadium cans provided by ISIS (vanadium having an extremely low scattering length for neutrons). Exact details for individual experiments are given in the relevant chapters.

3.3 Rietveld refinement

Structure analysis and extraction of information contained within diffraction data (XRD or neutron diffraction) was performed using the Rietveld method [10]. Analysis of X-ray diffraction data was performed using the Bruker TOPAS software [11]. Data from neutron diffraction experiments were processed using the General Structure Analysis System (GSAS) package [12] combined with the EXPGUI user interface package [13].

The Rietveld method is used to describe a least squares fitting method applied to powder diffraction data with no requirement to use single crystals of the material of interest. The method requires the initial judicious input of a crystalline structure that makes physical and chemical sense, as well as knowledge of the instrument parameters and a high quality experimental data set. From this starting point, parameters pertaining to the sample and instrument can be refined as needed to fit the model to the experimental data across the entirety of the profile. From careful refinement of the relevant parameters, an array of useful information and characteristics can be modelled. In the scope of this research, the method is used for refinement of structural parameters, e.g. lattice parameters and atomic positions/occupancies, although the method is much more extensive and capable for

Global parameters applied to the model	
Instrument parameters	Parameters pertaining to the specific influence of the instrument on the diffraction pattern, including: zero point, specimen displacement, absorption, preferred orientation, and wavelength or distance of time of flight, Lorentz and polarisation factors.
Background function	All diffraction data are characterised by the presence of a background intensity, which generally varies smoothly as a function of d-spacing. Typically, a linear interpolation function or low order Chebyshev polynomial function was used to fit the background intensity, the latter being better suited to model nonlinear variations in background intensity.
For each phase present	
Scale factor	This parameter allows the calculated intensity at each point to be scaled to approximately match the observed data.
Profile parameters	For X-ray diffraction data, a pseudo-Voigt function was applied, comprising a linear combination of Gaussian and Lorentzian contributions. For time of flight neutron diffraction data, the pseudo Voigt function was convoluted with back-to-back exponentials, to model the time dependence of the neutron pulse intensity (the Ikeda-Carpenter function).
Unit cell dimensions	The unit-cell parameters (a, b, c) and angles (α, β, γ) defined according to the crystal system and space group.
Structure parameters	The atom co-ordinates, site occupancy, and associated thermal parameters, the latter typically modelled assuming isotropic mean squared displacement from the refined position.

Table 1: Summary of key parameters refined in Rietveld method.

modelling of other properties, such as micro-crystalline grain sizes, strains, temperature vibrations and magnetic moments (for neutron diffraction data). Table 1 summarises the key parameters refined by the Rietveld method in this thesis.

The mathematical basis for the Rietveld method is consideration of the diffraction pattern as comprising Bragg reflections, (hkl), which contribute to the observed intensity, y_{oi}, at any point, i [14]. The calculated intensity, y_{ci}, at each point, is the summation of several contributions:

$$y_{ci}=s\sum_{hkl}F_{hkl}^2L_{hkl}P_{hkl}A\varphi(2\theta_i\text{-}2\theta_{hkl})+y_{bi} \tag{9}$$

where, s is the scale factor, F_{hkl} the structure factor, L_{hkl} the combined Lorentz and polarisation terms, P_{hkl} a preferred orientation parameter, A the absorption factor, φ the reflection profile function and y_{bi} the background intensity at the ith point.

The contribution of the crystal structure is made through the structure factor and refinement of the unit cell and structure parameters, which seeks to model the observed position and intensity of the Bragg reflections. The Lorentz and polarisation terms are geometric factors which account for the fact that the intensity of the diffracted radiation and its polarisation depend on scattering angle; these terms are thus specific to the diffractometer and the form is set according to X-ray or neutron diffraction data [14], [15].

The Rietveld method seeks to obtain the best fit to all of the observed intensity points simultaneously, through minimisation of the residual, S_y:

$$S_y=\sum_i w_i\left(y_{oi}\text{-}y_{ci}\right) \tag{10}$$

Where w_i is a weighting factor, equal to the reciprocal of y_{oi}. This process is accomplished by a process of iterative variation of the refinable parameters, to improve the fit of y_{ci} to y_{oi}, utilising a least squares algorithm.

Several metrics are used to assess the goodness of fit achieved by minimisation of the residual, those most frequently and usefully applied are [14], [15]:

$$R_p=\frac{\sum|y_{oi}\text{-}y_{ci}|}{\sum y_{oi}} \tag{11}$$

$$R_{wp}=\left[\frac{\sum w_i\left(y_{oi}\text{-}y_{ci}\right)^2}{\sum w_i y_{oi}{}^2}\right]^{\frac{1}{2}} \tag{12}$$

$$R_{exp}=\left[\frac{\text{N-P+C}}{\sum w_i {y_{oi}}^2}\right]^{\frac{1}{2}} \tag{13}$$

$$\chi^2=\left[\frac{R_{wp}}{R_{exp}}\right]^2 \tag{14}$$

Where N is the number of observables, P, the number of refined parameters and C the number of constraints. The most meaningful of these metrics is R_{wp}, since the residual, S_y, appears in the numerator, and, therefore, R_{wp} is measure of the extent of agreement (or disagreement) between the calculated model and observed data. R_{exp} is effectively the value of R_{wp} that would be expected if only counting statistics are responsible for the residual difference between the calculated model and observed data and thus χ^2 is a useful metric, because it expresses the extent to which deficiencies in the model contribute to the residual. R_p is similar to R_{wp} but excludes the weighting factor, which has the effect of reducing the influence of the background and, therefore, provides perspective on potential deficiencies in the structural model.

3.4 Scanning electron microscopy

Scanning electron microscopy (SEM) is method which exploits the different interactions of electrons with matter to give a high resolution image of the sample topology or provide compositional information [16]–[18]. The sample is loaded into the vacuum chamber of the SEM, where an electron gun directs a beam of incoming electrons onto the sample, which are focused and scanned over a small area of the sample surface. Detection is usually by means of an Everhart-Thornley detector, a device based upon a scintillator and photomultiplier detection system.

The principal detection made using an SEM is that of secondary electrons, which are electrons ejected from the K, L or M shells of atoms by inelastic scattering interactions with the incident beam. These interactions occur only within interaction volume of the incident beam on the order of nanometre depths and are angle dependent (see Figure 3). An increased interaction volume occurs at high angles of incidence between the generated beam and the

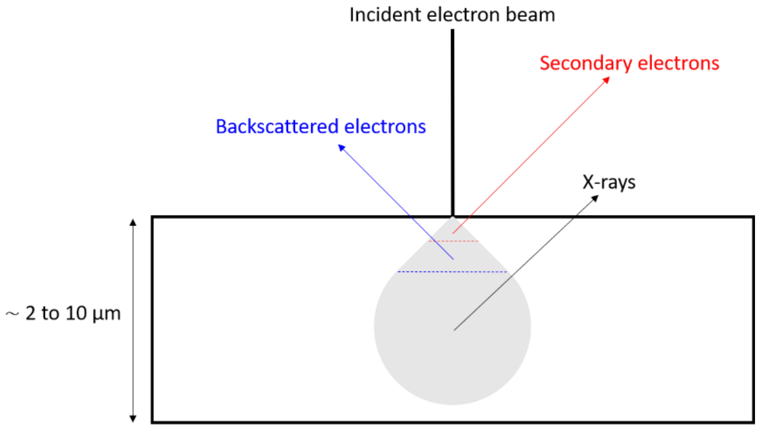

Figure 3. The interaction volume of the incident electron beam in SEM measurement and the origin of detected secondary electrons, backscattered electrons and x-rays.

sample, resulting in more secondary electrons being emitted. This has the effect of appearing brighter on the produced image. Since higher angles of incidence occur when the sample has inclined planes or edges, detection of secondary electrons and the relative brightness of the detections gives a topological image of the sample surface.

The other detected electrons in SEM are backscattered electrons. These result from elastic scattering of the incident beam electrons, originating deeper within the interaction volume and are of higher energies than secondary electrons. The magnitude of the elastic scattering is dependent on the atomic weight of the atoms within the interaction volume; heavier atoms result in greater backscatter of the incident electrons than lighter elements. As a result, backscattered electrons can give compositional contrast of the sample.

For additional compositional spatially resolved chemical analysis, SEM can be combined with energy dispersive X-ray spectroscopy (EDX) that utilises the secondary electron production process. When an incoming electron collision causes ejection of an inner shell electron, this leaves the atom in an excited state. Higher shell electrons drop down into the lower shell vacancy to stabilise the atom. In doing so, the accelerating electron emits X-ray photons of an energy that is inherent and characteristic of that transition in that specific atom. Detection of this X-ray emission gives further compositional analysis of the sample.

To utilise SEM in this study, powder samples were mounted onto a conductive carbon adhesive tab (to prevent charge accumulation within the sample) which was then adhered to an aluminium SEM stub for loading. A Hitachi TM3030 low vacuum desktop SEM unit was used with a 15kV operating voltage. The emission current was 1850 mA and beam current was 31.5 μA. EDX analysis was computed with Bruker Quantax 70 Energy Dispersive X-ray Spectrophotometer software [19].

3.5 X-ray absorption spectroscopy

X-ray absorption spectroscopy is a technique to measure the linear absorption coefficient of a sample, which depends on the atom type, coordination and oxidation state [20]–[22]. The principles of XAS can be further refined into specific regions of measurement- the extended X-ray absorption fine structure (EXAFS) and the X-ray Absorption Near Edge Structure (XANES), which are highlighted in Figure 4.

XAS requires synchrotron X-ray sources for the necessary intensities and tuning of frequency of the X-ray beam using monochromators and slits to define the beam profile. When the beam is incident on a sample it interacts with the electrons of the sample, causing scattering or excitation events. Where the incident beam energy is enough to result in the emission of a photoelectron, a large increase in linear absorption coefficient, known as an absorption edge, is observed. Energies absorbed at these edges correspond to the binding energies of the electrons within the sample and experiments will utilise appropriate X-ray photon energies to achieve the photoelectric ejection from a core shell electron. XAS measurements are either those done in transmission, measuring the relative intensity of the X-ray beam prior to and after the sample interaction, or in fluorescence, which determines the absorption edge energy by measuring the energy of the photoelectron emitted for hole re-compensation after the initial absorption event.

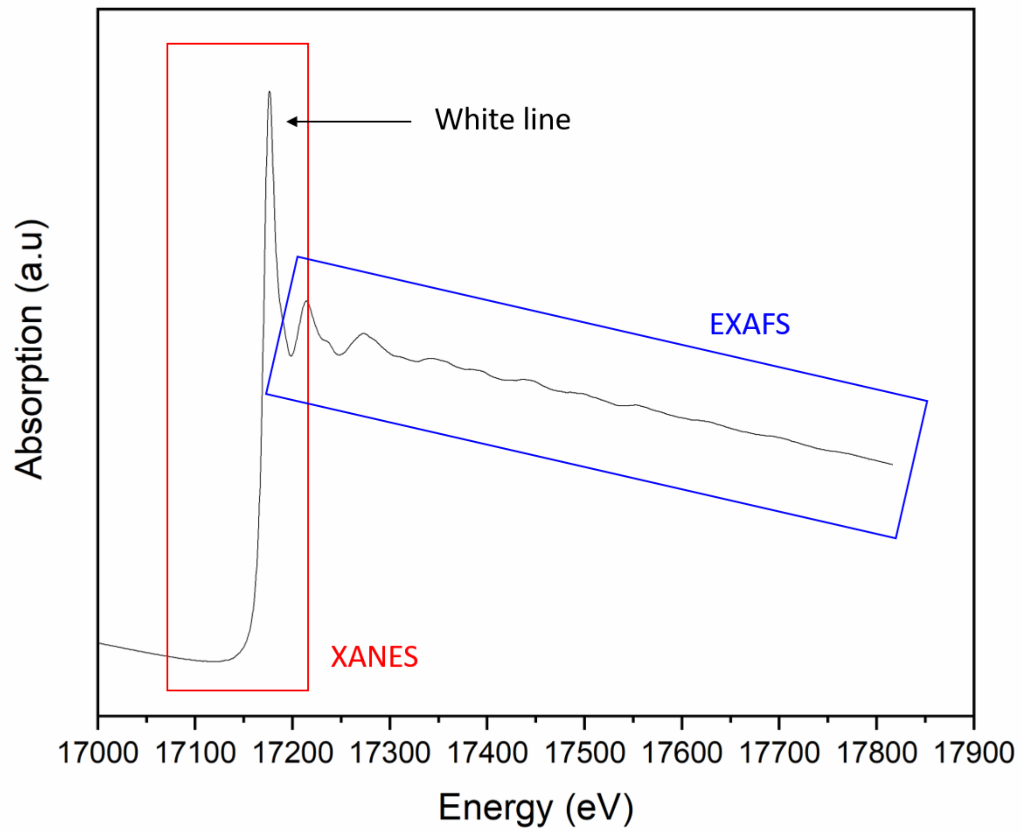

Figure 4. XAS spectrum for UO_2 with XANES, EXAFS and white line regions indicated

For transmission mode measurements, the intensity of X-rays transmitted through the sample, I_t, depends on the incident intensity, I_0, and decreases exponentially with the thickness, x, and mass absorption co-efficient, μ, which is a materials property:

$$I_t = I_0 e^{-\mu x} \tag{15}$$

The absorption coefficient, a(E), in transmission mode is then defined:

$$a(E) = \ln \frac{I_0}{I_t} \tag{16}$$

In the case of measurements in fluorescence mode, the energy of the emitted fluorescent X-rays is equal to the difference in energy between the core-level orbital from which the photoelectron is ejected and the higher energy level, from which an electron transitions to fill the core hole. Since the rate of production of fluorescence X-rays is proportional to the absorption of incident photons, which produce the core-hole, the absorption co-efficient for fluoresce measurements is given by (where *c* is a constant):

$$\mathrm{a(E)=c}\frac{\mathrm{I_f}}{\mathrm{I_0}} \tag{17}$$

Experimental parameters for an XAS investigation are chosen to target the element of interest. For this body of work, uranium samples are measured around the uranium L_3 absorption edge at 17,166 eV and technetium K edge at 21,044 eV. Resolution of the measurements is determined by the step size of the incident X-ray beam over the energy range of interest. The energy range scanned for data presented in this work corresponds to wavenumber (k) range up k=18 $Å^{-1}$, since energy and wavenumber are linked by the following equation:

$$\mathrm{k} = \frac{\mathrm{E}}{\hbar \mathrm{c}} \tag{18}$$

where E is the photon energy, ħ is the reduced Planck constant (1.0546×10^{-34} J.s) and c is the speed of light in a vacuum. Wavenumber therefore represents the spatial frequency of the wave associated with that particular energy.

The XANES region, prior to and close to the edge feature, can indicate oxidation state and local coordinate geometry, while the EXAFS region beyond the edge feature indicates interactions of the X-ray wave front with the nearest neighbours to the atom of interest, which yields information about bond lengths and the local molecular structure. The energy required to form a core-hole depends on the effective nuclear charge, which increases with increasing oxidation state. Therefore, the energy of the absorption edge, E_0, which is typically defined as the energy corresponding to the maximum in the first derivative of $\mu x(E)$ or $\mu x = 0.5$ for normalised spectra, may shift by of the order of a few electron volts per oxidation state unit. This chemical shift in E_0 may thus be used to speciate oxidation states in materials. However, it should be recognised that the local structure of the absorber also contributes to the magnitude of the measured absorption, and, therefore E_0 is not a strict measure of oxidation state. Nevertheless, through calibration of the dependence of E_0 on oxidation state using reference compounds in which the local structure of the absorber is similar to that of an unknown, the influence of local structure may be minimised allowing accurate determination of oxidation sate.

The absorption of X-ray photons by an element at the absorption edge, leads to production of a photoelectron. Above the absorption edge, the photoelectron is excited into the continuum with a kinetic energy E_{KE}, defined by:

$$E_{KE}=E-E_0 \tag{19}$$

Where E is the energy of the incident photon resulting in the excitation and E_0 is the binding energy of the photoelectron. The photoelectron can be described as a spherical wave propagating outward from the absorber, and which are scattered back toward the absorber by the immediate neighbour atoms as shown in Figure 5. On the timescale of the core-hole lifetime, this scattering interaction determines the final electronic state of the photoelectron and thus the probability of X-ray photon absorption, and excitation, between the initial (core) and final state. When the kinetic energy of the photoelectrons is small, corresponding to $E = E_0$, then the outgoing and backscattered photoelectron waves are essentially in phase resulting in maximum absorption in the neighbourhood of the absorption edge – referred to as the white line. Thereafter, as E_K increases, the wavelength of the photoelectron becomes progressively shorter, and the outgoing and backscattered outgoing and backscattered photoelectron waves result in oscillating constructive and destructive interference, and thus modulation in the probability of X-ray absorption, which forms the XANES and EXAFS region. Clearly, the local structure of the absorber atom governs the photo-electron scattering process, in terms of the number, type, distance and disorder of neighbouring atoms. Consequently, modelling of the modulation in X-ray absorption co-efficient, using theory, can retrieve information on this local structure.

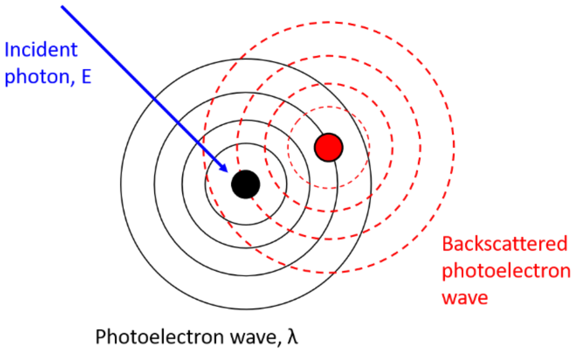

Figure 5. Model of photoelectron wave and backscatter occurring at the absorber atom (black)

The XANES region is typically defined as extending ca. 30-50 eV above the absorption edge and arises from multiple scattering of the photoelectron within the local atomic cluster. Theoretical descriptions of the X-ray scattering process (see below) do not effectively describe the full multiple scattering interactions and, therefore, analysis of XANES is typically made using empirical methods, with quantitative or qualitative comparison of the spectral features against those of reference compounds in which the absorber is in a known similar or dissimilar oxidation state and co-ordination environment. In particular, linear combination analysis is frequently applied to model the XANES data of an unknown by fitting of the contribution of reference data to reconstruct the sample edge feature shapes and oscillations. This allows for an estimate of the oxidation state and coordination of the sample atom to be made based upon the prior knowledge of those properties of the standards.

The EXAFS region is typically defined as extending ca. 50-1000 eV above the absorption edge and arises from both single and multiple scattering of the photoelectron within the local atomic cluster. The amplitude and phase of the sinusoidal oscillating X-ray absorption co-efficient as a function of wavevector k, Eq. 1.2, can be expressed as:

$$\chi(\mathrm{k}) = \frac{\mu(\mathrm{E})-\mu_0(\mathrm{E})}{\mu_0(\mathrm{E})} \tag{20}$$

Where $\mu(E)$ and $\mu_0(E)$ are, respectively, the mass absorption coefficient in the presence and absence of photoelectron scattering. Effectively, $\chi_i(k)$ corresponds to subtraction of the absorption of the photoelectric background, affording only the component arising from photoelectron scattering summed over all (significant) scattering paths, $\chi_i(k)$. Thus:

$$\chi(k)=\Sigma_i \chi_i(k) \tag{21}$$

Each scattering path is represented by the following equation:

$$\chi_i(k) = \frac{\left(N_i S_0^2\right) F_{eff,i}(k)}{kR_i^2} e^{-2\sigma_i^2 k^2} e^{-2R_i/\lambda(k)} \sin\left[2kR_i+\varphi_i(k)\right] \tag{22}$$

With

$$R_i=R_{0,i}+\Delta R_i \tag{23}$$

And

$$k^2=\frac{2m_e(E-E_0+\Delta E_0)}{\hbar} \tag{24}$$

The equation above is one form of the EXAFS equation and comprises an amplitude and phase term which evidently describe the sinusoidal structure of $\chi_i(k)$:

- S_0^2: amplitude reduction factor, accounts for the relaxation of the electrons in the presence of the core hole, typically $0.7 < S_0^2 < 1.0$, to which the backscattered photoelectron returns.
- N_i: amplitude term which, for single scattering interactions, corresponds to the number of atoms co-ordinated to the absorber at a given distance.
- $1/R_i^2$: diminishes the contribution of a shell of atoms at distance R_i, with increasing distance from the absorber.
- $F_{eff,i}(k)$: the effective scattering amplitude, which for a single scattering path is the atomic scattering factor familiar in X-ray diffraction, affording element sensitivity.
- $sin[2kR_i + \varphi_i(k)]$: the phase term, which accounts for the scattering of the photoelectron over a path distance of $2R_i$ (from absorber to neighbouring atom and back to absorber), modified by a phase shift $\varphi_i(k)$. The phase shift term accounts for the photoelectron

wavelength as the electron loses energy with increasing distance from the absorber atom and through the scattering interaction with the neighbouring atoms.

- $e^{-2\sigma_i^2 k^2}$: accounts for the disorder in path length R_i, where σ^2 is the mean square displacement of the interatomic distance between the absorber and neighbour atom, due to dynamic and static disorder.
- $e^{-2R_i/\lambda(k)}$: accounts for the mean free path of the photoelectron in the solid after excitation, $\lambda(k)$, before it is scattered inelastically or the core-hole is filled. This term causes the EXAFS signal to be dominated by scattering contributions within the <10 Å of the absorber, thus the technique is an inherently local probe.
- ΔR_i: accounts for change to the path length relative to that initially defined, R_{0i}, and is refined in model fitting.
- ΔE_0: accounts for the difference between the true and calculated energy scale and is used to align the calculated spectrum to the data, the parameter is a single global factor refined for the model.

The Fourier Transform of the EXAFS signal, $\chi_i(k)$, is useful in analysis of data and is denoted FT [k^w $\chi_i(k)$], where k^w is a weighting factor, generally with w = 1, 2 or 3. Evidently, $\chi_i(k)$ comprises a sum of component sine waves, each with an amplitude and phase term that describes a scattering interaction. The process of Fourier Transform separates the EXAFS waveform into its individual components, each of which contributes a signal with an intensity (often referred to as a peak or shell) at a distance R from the absorber; this distance includes the phase shift and is shorter than the path length by approximately 0.5 Å. The usefulness of the Fourier Transform analysis is that shells of atoms are identifiable at increasing distance from the absorber, similar to a radial distribution function. An example of Fourier Transform analysis of a $\chi_i(k)$ EXAFS signal is given in Figure 6. Finally, the R factor is a metric used to assess the goodness of fit of a model to observed data, defined as:

$$R=\frac{\sum_i (y_{obs,i}-y_{calc,i})^2}{y_{obs,i}^{\ 2}} \tag{25}$$

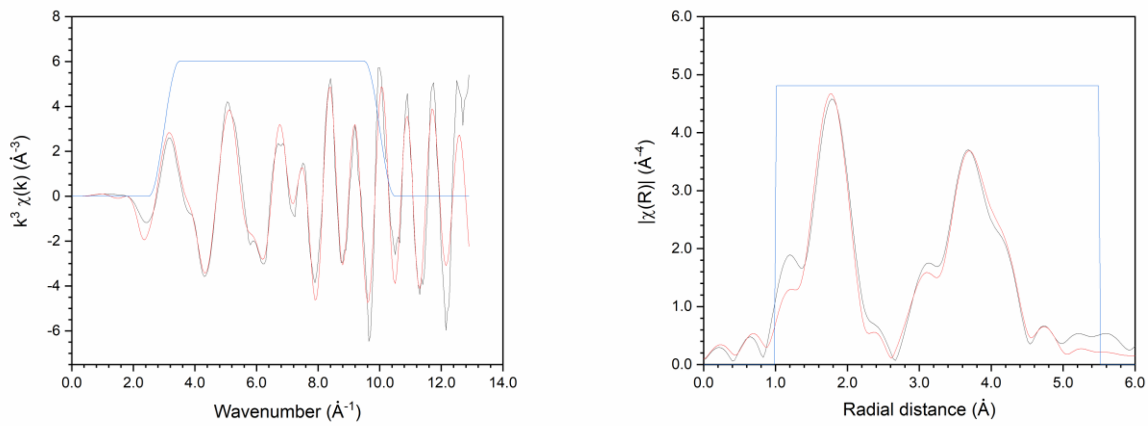

Figure 6. Example EXAFS fit for UO_2. Left is the k^3 weighted signal and right is the magnitude of Fourier transforms. Black line is the observed data, red line is the applied fit and blue line indicates the fitting window.

Where $y_{obs,i}$ and $y_{calc,i}$ are the observed and calculated independent data points.

In this study, both the measured compounds and standards data were taken at the Diamond Light Source (STFC) synchrotron facility on beamline B18 and subsequent data handling and linear combination fitting performed using the ATHENA package of the Demeter suite of analysis programmes [23]. Further analysis of EXAFS data involves fitting various scattering paths defined from crystallographic input files in order to fit the oscillations seen in nearest neighbour scattering, which necessitated the large wavenumber range used. This analysis was performed the ARTEMIS programme of the Demeter package, which employs the FEFF 8 code [23].

3.6 Colour analysis

Humans perceive colour by detection of light incident on retinal cone cells, which respond to photons of wavelengths 390 to 700 nm, corresponding to violet through to red shades in what are called spectral colours (colours which are produced by a single wavelength of light). The wavelength of a photon directly correlates to its energy by the basic equation:

$$\mathrm{E} = \frac{\mathrm{hc}}{\lambda} \tag{26}$$

where E is the photon energy, h is the Planck constant, c is the speed of light and λ is the wavelength of the photon. The colour an object is perceived to have is therefore a result of the reflected visible light photons from the object. When light is incident on an opaque object, that light can be reflected, scattered, or absorbed. In reflection, a mirror like surface is seen. Scattering and absorption result in different colours being perceived. Total absorption of all light results in the absence of reflected light to the retina and therefore appears black. Light scattered from an object but with approximately equal effect on all wavelengths appear white. Preferential scattering of certain wavelengths and the relative absorption of others results in the perception of colour. For example, an object scattering predominantly 560-590 nm photons appears yellow, while one scattering 450-490 nm appears blue.

Absorption of certain wavelengths of light is determined by the band structure of the material and application of the Pauli exclusion principle. Electrons occupy discrete energy states or orbitals, the Pauli exclusion principle means that electrons (or more generally, fermions) cannot simultaneously occupy the same quantum state within a quantum system. For overlapping electron orbitals, this results in the orbital splitting into two energies to satisfy the Pauli exclusion principle by giving the electrons different quantum states to reside in. When scaled up to a bulk substance with a large number of electrons in the same orbital, the splitting is so innumerable that the orbitals appear as a continuum of different energy levels or a band. This effect is more pronounced for the outermost electrons, where the individual orbitals are separated by large forbidden energy gaps and results in a valence band (formed of the outermost electron orbital) and a conduction band (a band partially filled with electrons that are delocalised from the nucleus). The forbidden energy gaps in this band structure is called the band gap and is typically in the order of electron volts. When photons are incident on the material, their energy can be sufficient to excite an electron from the valence band to the conduction band. Insufficient energy photons are not absorbed and instead scattered, resulting in the colour attributed to the object.

As some of the compounds of interest in this study are noted for their vivid and varied colours, a method of measuring and quantifying the colour of compounds to provide additional characterisation was developed, details of which are published elsewhere [24]. This was achieved by first taking high resolution photographs of the samples in a commercially available LED lit light box. Images were taken using a Canon 4000D camera with 18 mm lens and the following optimised settings: shutter speed of 1/640 seconds, lens aperture F6.3 and sensor light sensitivity of ISO 400. This allowed a balance between the three principal camera settings to achieve a clear, detailed image with minimal camera induced artefacts and optimal use of the light available. The samples were photographed alongside a standardised grey card of (R,G,B) value (128,128,128). Post image processing used freely available RawTherapee software to calibrate the input image to the known grey card (R,G,B) value. Images were then transferred to ImageJ to allow for histogram analysis across the entire sample size. From spot analysis, histograms of (R,G,B) value ranges and an average (R,G,B) value was obtained.

3.7 Thermogravimetric mass spectrometry

Thermogravimetric mass spectrometry (TGA-MS) is a combination of thermogravimetric analysis (TGA) coupled with mass spectrometry (MS). TGA is measurement of the mass of a sample as a function of the applied temperature. TGA instrumentation consists of a precision balance held within a furnace to allow for controlled programmes of heating and cooling to be applied while the changing mass of the sample is recorded. An inert purge gas is flowed throughout the measurements to limit sample oxidation or ignition. This technique allows for the identification of temperatures at which key mass losses or gains occur, for example the loss of water from a hydrated compound. This also indicates whether the sample thermal decomposition occurs as one process or in a stepwise nature involving intermediate stable compounds.

The coupled technique of mass spectrometry runs concurrently to the TGA measurements. The evolved off gas from the sample is directed to the spectrometer where the contents are ionised. From there, the varying components are separated by accelerating them through an electric or magnetic field. The relative deflection of the ionised content relies upon the mass to charge ratio of the species involved and is measured as relative abundance. As a result of this, any species with the same mass to charge ratio, albeit with differing masses and charges, will deflect to the same point. However, as the ionisation charge is typically +1, the mass to charge ratio instead collapses to just the mass of the species involved which can then be used to identify the elements or compound found using prior knowledge of the sample contents.

TGA-MS measurements in this work were made using a Netzsch STA 449 F3 *Jupiter* model thermal analyser with a coupled Netzsch QMS 403 *Aëlos Quadro* quadrupole mass spectrometer. As measurement of nitrogen was anticipated, the carrier gas for the experiment was >99.99% purity argon.

3.8 Mössbauer spectroscopy

Mössbauer spectroscopy exploits a recoil free resonant absorption of gamma rays by atomic nuclei, a phenomenon called the Mössbauer effect [25]–[27].

When a photon is incident on a nucleus, it will be absorbed only if the energy of that photon is sufficient to excite that nucleus to a higher energy level. The energy levels available to a nucleus depend on its local electronic and magnetic environments. A nucleus in an excited state resolves this by transitioning back to the ground state, with the loss of excitation energy achieved by emitting another photon. Resonant absorption is the emission and subsequent re-absorption of a photon occurring between two identical nuclei. The nuclei must be identical to ensure the same discrete energy differences between the ground and excited state, which is isotope specific. For resonant absorption to occur, emission and absorption of the photon must occur without any losses to that photons energy. Energy loss would result in a photon with insufficient energy to excite the second nucleus as the excitation energies are quantized values, not continuous.

If a free nucleus were to emit or absorb a gamma ray, a proportion of the energy distribution would be lost to recoil effects as this is required to maintain conservation of momentum. For a nucleus at rest, this can be summarised as:

$$\mathrm{E_{transition}} = \mathrm{E_{photon}} + \mathrm{E_{recoil}} \tag{27}$$

As a result, the energy of the emitted photon is not the total energy of the transition. Furthermore, as the initial excitation event of the first nucleus is a finite time τ, the Heisenberg uncertainty principle dictates that the energy of the emitted photon is not precisely defined. Instead the photon energy follows a Breit-Wigner or Lorentzian distribution which is centred around the absolute value of the energy transition (E_0) and has a full width at half maximum of $\Gamma = \hbar/\tau$, where $\hbar$ is the reduced Planck constant [28]. The magnitude of the recoil energy is large in comparison to the energy distribution. This means that in a free atom, resonant absorption by a second identical nucleus cannot occur due to the discrepancy in energy of the photon in relation to the energy of the excitation.

However, nuclei within a crystal lattice are not free and as such the effective mass of the recoiling nucleus becomes the mass of the system and the recoil energies are vastly reduced. What recoil energy does exist can only occur in phonons, quantised lattice vibrations that occur in integer increments. Where the photon energy is small enough that the recoil energy cannot be transferred as a phonon, i.e. the integer increment of the phonon is zero, the whole system therefore recoils and the magnitude of the recoil energy is negligible. These are recoil free events where resonant absorption is possible and the Mössbauer effect occurs.

For ^{57}Fe Mössbauer spectroscopy, used in this work, a ^{57}Co source is used to generate the initial excitation event. ^{57}Co undergoes radioactive decay by electron capture, absorbing an inner shell electron and converting a proton to a neutron. This change transmutes the atom to ^{57}Fe in an excited state. The excited Fe atom then relaxes to the ground state, emitting a gamma ray photon and instigating the cascade of resonant absorption. Tuning of the energy of the emitted photon is achieved by moving the ^{57}Co source on a driver such that the emitted photon is subject to Doppler shift.

Mössbauer parameters of isomer shift and quadrupole splitting are reported in mm s^{-1}. Isomer shift arises from differences in electronic structure between the source and absorber atoms, electronic structure being related to isotopic composition. Quadrupole splitting arises from asymmetry of the nuclei within the electric field of the lattice, which is indicative of the

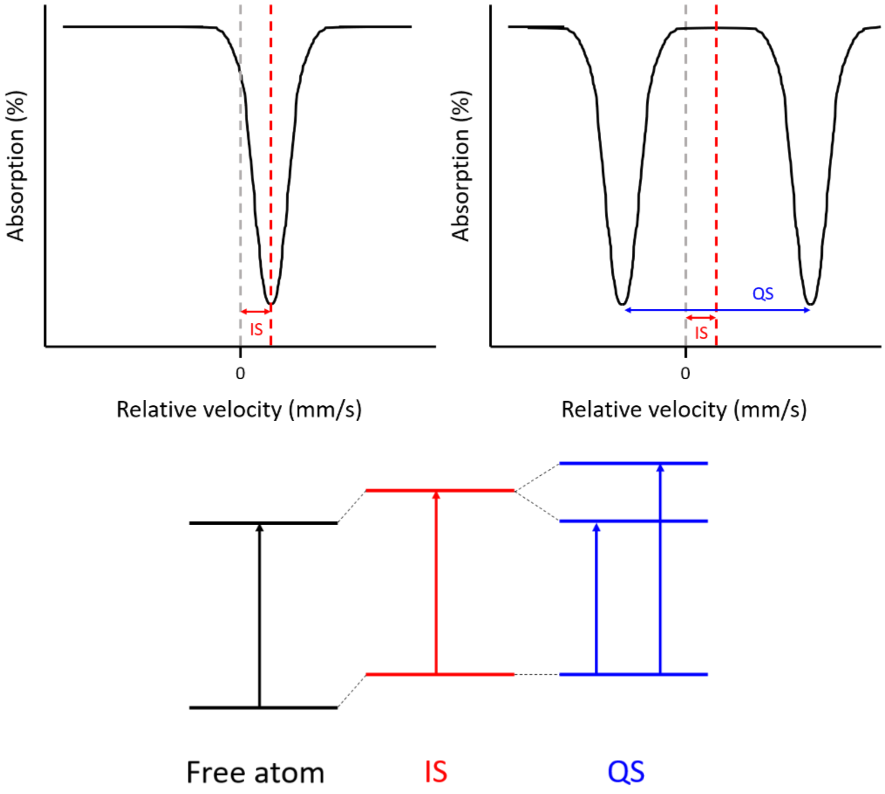

Figure 7. Example Mössbauer spectra (top) with isomer shift (red) and quadrupole splitting (blue) labelled. Bottom shows a diagram of the origin of recoil free transitions that yield IS and QS effects.

chemical environment. Examples of Mössbauer spectra and the recoil free transitions that give rise to isomer shift and quadrupole splitting are shown in Figure 7.

In this work, ^{57}Fe Mössbauer spectroscopy measurements were performed on a Wissel MRG-500 spectrometer in transmission mode. Data were analysed using Recoil software [29].

3.9 X-ray Photoelectron Spectroscopy

X-ray photoelectron spectroscopy (XPS) is a method to measure surface chemistry that utilises the photoelectron effect [16], [17], [30], [31]. When irradiated with high energy X-rays, previously bound state electrons can be ejected from the nucleus. This action is performed under ultra-high vacuum conditions such that the free photoelectrons can be collected, and their kinetic energy measured. If the photoelectron is unimpeded after its ejection from the atom and thus elastically scatters, the previous binding energy of that electron within the atom can be calculated by from its kinetic energy:

$$E_{\mathrm{binding}} = \mathrm{hv} - E_{\mathrm{kinetic}} \tag{28}$$

Elastic scattering is only possible for electrons liberated from small depths from the sample surface, hence the measurement depth of XPS is in the order of 1 to 10 nm. The technique is sensitive to circa 0.1 atomic % concentration of the element of interest. The binding energy of the photoelectron is affected by the valence structure of its environment, which results in slight shifts to the photoelectron peak measured. However, the specificity of binding energies, these being a property of quantised atomic levels, allows for elemental analysis of the sample surfaces.

XPS data in this work were acquired at the Photon Science Institute, University of Manchester. Measurements were performed on an ESCA2SR spectrometer (ScientaOmicron GmbH) using monochromated Al Kα radiation (1486.6 eV, 20 mA emission at 300 W, 1 mm spot size) with a base vacuum pressure of circa 1 x 10^{-9} mbar. Charge neutralisation was achieved using a low energy electron flood source (FS40A, PreVac). Binding energy scale calibration was performed using C-C in the C 1s photoelectron peak at 285 eV. Analysis and curve fitting was performed using Voigt-approximation peaks using CasaXPS [32].

3.10 References

[1] H. P. Klug and L. E. Alexander, *X-Ray Diffraction Procedures: For Polycrystalline and Amorphous Materials*, 2nd Ed. Wiley, 1974.

[2] B. D. Cullity, *Elements of X-ray Diffraction*, 2nd Ed. Addison-Wesley Publishing Company Inc, 1978.

[3] W. L. Bragg, "The Diffraction of Short Electromagnetic Waves by a Crystal," *Proc. Camb. Phil. Soc.*, vol. 17, p. 43, 1913.

[4] C. Hammond, *The Basics of Crystallography and Diffraction.* Oxford: Oxford University Press, 1997.

[5] DIFRRAC.EVA, *V3.* Karlsruhe, Germany: Bruker AXS GmbH, 2013.

[6] G. E. Bacon, *Neutron diffraction.* United Kingdom: Clarendon Press, 1975.

[7] C. G. Windsor, *Pulsed neutron scattering.* United Kingdom: Taylor and Francis Ltd, 1981.

[8] D. S. Sivia, *Elementary Scattering Theory for X-ray and Neutron Users.* Oxford University Press, 2011.

[9] R. I. Smith and S. Hull, "User guide for the POLARIS powder diffractometer at ISIS Report RAL-TR-97-038," 1997.

[10] H. M. Rietveld, "A profile refinement method for nuclear and magnetic structures," *J. Appl. Crystallogr.*, vol. 2, no. 2, pp. 65–71, Jun. 1969, doi: 10.1107/S0021889869006558.

[11] TOPAS, *V4, General profile and structure analysis software for powder diffraction data- User's Manual.* Karlsruhe, Germany: Bruker AXS GmbH, 2008.

[12] A. C. Larson and R. B. Von Dreele, "General Structure Analysis System (GSAS)." 2004.

[13] B. H. Toby, "EXPGUI, a graphical user interface for GSAS," *J. Appl. Crystallogr.*, vol. 34, no. 2, pp. 210–213, Apr. 2001, doi: 10.1107/S0021889801002242.

[14] R. A. Young, Ed., *The Rietveld Method.* Oxford University Press, 1996.

[15] L. B. McCusker, R. B. Von Dreele, D. E. Cox, D. Louër, and P. Scardi, "Rietveld refinement guidelines," *J. Appl. Crystallogr.*, vol. 32, no. 1, pp. 36–50, Feb. 1999, doi: 10.1107/S0021889898009856.

[16] J.-P. Eberhart, *Structural and chemical analysis of materials : X-ray, electron and neutron diffraction, X-ray, electron and ion spectrometry, electron microscopy.* Chichester West Sussex England; New York: Wiley, 1995.

[17] J. P. Sibilia, Ed., *A Guide to Materials Characterisation and Chemical Analysis.* VCH Publishers Inc., 1996.

[18] J. Goldstein *et al.*, *Scanning Electron Microscopy and X-Ray Microanalysis.* New York and London: Plenum press, 1992.

[19] Q. 70, *EDS System for Hitachi Tabletop Microscope TM3000.* Berlin, Germany: Bruker nano GmbH, 2011.

[20] M. Newville, "Fundamentals of XAFS," *Rev. Mineral. Geochemistry*, vol. 78, pp. 33–74, 2014, doi: 10.2138/rmg.2014.78.2.

[21] S. D. Kelly, D. Hesterberg, and B. Ravel, "Analysis of Soils and Minerals Using X-ray Absorption Spectroscopy," *Methods of Soil Analysis Part 5—Mineralogical Methods.* pp. 387–463, Apr. 15, 2008, doi: https://doi.org/10.2136/sssabookser5.5.c14.

[22] S. Calvin, *XAFS for everyone.* Boca Raton, Florida : Boca Raton, Florida , 2013.

[23] B. Ravel and M. Newville, “ATHENA, ARTEMIS, HEPHAESTUS: data analysis for X-ray absorption sepctroscopy using IFEFFIT,” *J. Synchrotron Radiat.*, vol. 12, pp. 537–541, 2005.

[24] N. B. A. Thompson, S. E. O’Sullivan, R. J. Howell, D. J. Bailey, M. R. Gilbert, and N. C. Hyatt, “Objective Colour Analysis from Digital Images as a Nuclear Forensic Tool,” *Forensic Sci. Int.*, p. 110678, 2020, doi: https://doi.org/10.1016/j.forsciint.2020.110678.

[25] R. H. Herber, “Introduction to Mossbauer spectroscopy,” *J. Chem. Educ.*, vol. 42, no. 4, p. 180, Apr. 1965, doi: 10.1021/ed042p180.

[26] Y. Yoshida and G. Langouche, Eds., *Mössbauer Spectroscopy.* Berlin: Springer, 2013.

[27] N. N. Greenwood and T. C. Gibb, *Mössbauer Spectroscopy.* Dordrecht: Springer, 1971.

[28] M. D. Dyar, D. G. Agresti, M. W. Schaefer, C. A. Grant, and E. C. Sklute, “Mössbauer spectroscopy of earth and planetary minerals,” *Annu. Rev. Earth Planet. Sci.*, vol. 34, no. 1, pp. 83–125, 2006.

[29] K. Lagarec and D. G. Rancourt, “Recoil - Mossbauer spectral analysis software for Windows,” Ottawa, ON, Canada, 1998.

[30] F. A. Stevie and C. L. Donley, “Introduction to x-ray photoelectron spectroscopy,” *J. Vac. Sci. Technol. A*, vol. 38, no. 6, p. 63204, Sep. 2020, doi: 10.1116/6.0000412.

[31] P. van der Heide, *X-ray Photoelectron Spectroscopy: An introduction to Principles and Practices.* Wiley, 2011.

[32] N. Fairley, “CasaXPS.” Casa Software Ltd, 2020, [Online]. Available: http://www.casaxps.com/.

Chapter 4

Design and commission of an ammonolysis furnace

4.1 Background

As oxygen and nitrogen share similarities in many properties, such as ionic radii and electronegativity (3.50 and 3.07 for O and N, respectively), substitution of the (N^{3-}) ion for (O^{2-}) ion is attainable in materials, providing the host crystal is capable of charge compensation by way of anion vacancies or cation oxidation state changes, amongst others. Most oxynitride synthesis methods aim to exploit this substitution mechanism.

Ammonolysis describes the splitting of ammonia, NH_3, and the resultant reaction of the split species, including N, NH and NH_2. These species append to the precursor compound of interest, which may lead to nitrogen incorporation, whilst also resulting in the formation of water from residual hydrogen from the split ammonia and oxygen from the lattice. Thermal ammonolysis, exposing a targeted precursor to flowing NH_3 gas at temperatures typically ranging from 600 to 1200 °C, is described as the most common synthesis route for oxynitride formation [1] and is highly prevalent in nitride synthesis [2], [3], particularly uranium nitride synthesis pertinent to this body of work [4]–[8].

Precursors used in ammonolysis reactions are typically of oxide form but the use of finely distributed mixtures of unreacted oxides and carbonates or mixed metal oxides have also been reported [9]. Halides have also been used in ammonolytic nitride synthesis [5], [6], [10], [11]. As the ammonolysis process relies upon gaseous diffusion into a solid precursor, maximisation of the precursor surface area to aid the diffusion mechanics can be beneficial. The Pechini method of “sol -gel” synthesis has been used to produce an ammonolysis precursor to yield a perovskite oxynitride [12]. The method involves forming an aqueous solution of the desired cations in citric acid before stabilising in an organic gel and drying. This prevents the precipitation of the cations from the solution and, once dried, leaves an amorphous mixture of oxides shown to react more readily under the ammonolysis process, requiring lower temperatures and negating the diffusion limitation that usually impede the reaction [1]. Similar complexation and calcination wet routes can also be used, of which the citrate method is predominant [13]. An application of the citrate technique is the formation of amorphous rare earth oxides which otherwise in binary form do not react with transition metal oxides under ammonolysis [9]. The use of amorphous precursors has been shown to give a higher percentage yield when compared to ammonolysis of crystalline equivalents [14]. The oxynitrides yielded from this method have small particle size and large surface area. Similar use of controlled precipitation of cations using a chelating polyol has also been reported [1]. This is commonly used in the synthesis of nanoparticles and offers the same benefits during the ammonolysis process.

The efficacy of the ammonolysis process also depends on the choice of operating temperatures and NH_3 flow rate applied. It is necessary to attain a balance between temperature and gaseous flow rate to ensure a dynamically unstable atmosphere and maximise the breakdown of the NH_3 into component nitriding species, while minimising cracking. Cracking of NH_3 is described by the following:

$$2NH_3 \rightarrow 3H_2 + N_2 \tag{1}$$

This is a hinderance to the desired reaction as the triply bonded N_2 molecule will not act to nitride the precursor and the operating temperatures typical of ammonolysis reactions are not high enough to cause the breaking of this notoriously stable bond to allow for nitriding species. Decomposition of ammonia varies as a function of temperature and flow rate; the percentage decomposition at 700 °C is approximately 10% at 150 cm^3/min flow rates but increases to around 45% at a reduced rate of 50 cm^3/min [15]. The resultant nitrogen content imparted into the oxynitride will also depend on the redox potentials of the cations involved [16]. Another rate limiting step of ammonolysis is the evolution of water from the precursor, which occludes the surface reaction. This can also be minimised by the careful choice of sufficiently vigorous flow rate. Diffusion of nitriding species can also be aided by alkali halide mineralisers introduced to the gas flow which act in a reversible reaction to promote transport of the nitrogen into the precursor lattice, which yields an oxynitride with increased crystallinity [16].

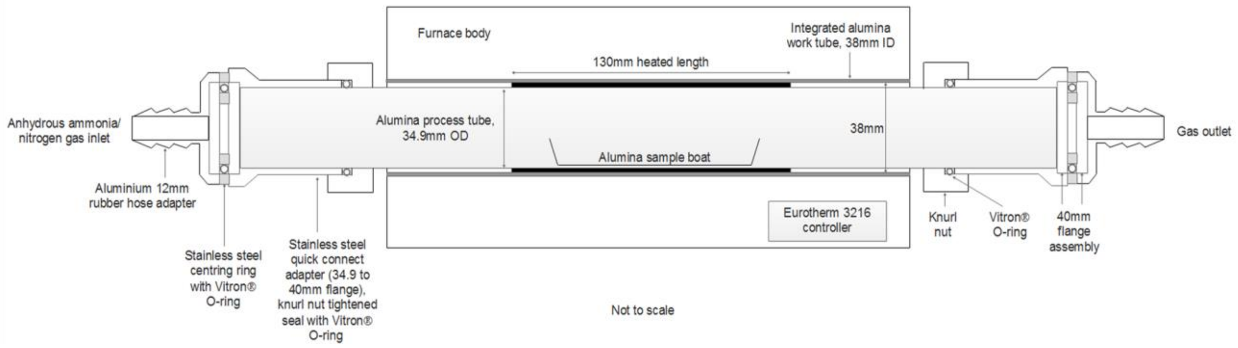

Figure 1: Schematic of central furnace assembly detailing end cap assembly and sample crucible placement

4.2 Furnace design and assembly

Design of the ammonolysis furnace in use throughout this thesis considered both the technical design required to achieve the reaction processes intended as well as the safety implications of such a system. A schematic design on the central furnace assembly is shown in Figure 1, along with a wider assembly diagram in Figure 2.

4.2.1 Central furnace assembly

The ammonolysis furnace was built around a horizontal Elite tube furnace with a central heated zone of 130 mm length, operating temperature up to 1200 °C and internal work tube diameter of 38 mm. The integrated Eurotherm 3216 PID controller was programmed to instigate power increase when a 1 °C difference between the targeted and measured temperatures was detected via the internal furnace feedback. Ramp rates were fixed to 5 °C/minute to minimise thermal stresses on the interior alumina tube during heating and cooling.

A secondary process tube was used for the reactions to prevent contact of ammonia gas with the integrated work tube and any resultant degradation of the material induced by this. This also served to maintain a containment for radioactive materials within the tube. An alumina (Al_2O_3) process tube was used as this material can readily operate in the temperature ranges required without the need for additional cooling, unlike quartz tubes. A standard 34.9 mm internal diameter was chosen, allowing for standard sizes of quick-fit end caps. A tube length of 500 mm was selected to minimise the temperature increase at the site of the end cap. The end cap assembly, supplied by LewVac Components Ltd., and visualised in Figure 1, consisted of a stainless steel Quick Connect adapter with knurl nut fastening, stainless steel centring ring, 12 mm aluminium hose adapter and stainless steel hinged clamp (not shown in Figure 1). Stainless steel was chosen for the components for corrosion resistance under NH_3 exposure. Vitron O rings offered good compression set resistance allowing for prolonged use under compression with recovery when compression is released as well as improved heat resistance to cope with the residual temperature demands on the ends of the process tube.

4.2.2 Gas supplies

The furnace assembly comprised of two gas inputs, one inert purge gas (Argon, 99.998%, BOC) and the reaction gas: either NH_3 required for ammonolysis (99.98%, BOC) or 5% H_2/N_2 for comparison reductions (BOC).

The inert and NH_3 supplies were separately metered with individual cylinder regulators and flowmeters before combining to one line towards the furnace, as indicated in Figure 2, using stainless steel or PTFE components for corrosion resistance. A regulator of 0-6 bar pressure was used for both gas supplies and operated at 1 bar during experiments. The NH_3 flowmeter allowed for flow rates of 50 to 500 ml/min.

gas flows were directed through gas washing bottles prior to and after the furnace process tube. The front gas washing bottle contained inert mineral oil to strip any H_2O contamination. The latter gas washing bottle contained 2M H_2SO_4 to neutralise any remaining NH_3 in the off gas and prevent release of NH_3 to atmosphere. The acid-base reaction produces the ammonium sulphate salt $(NH_4)_2SO_4$ and water which allows for safe dispersal for disposal. Both assemblies consist of a wet bottle and a dry bottle to prevent

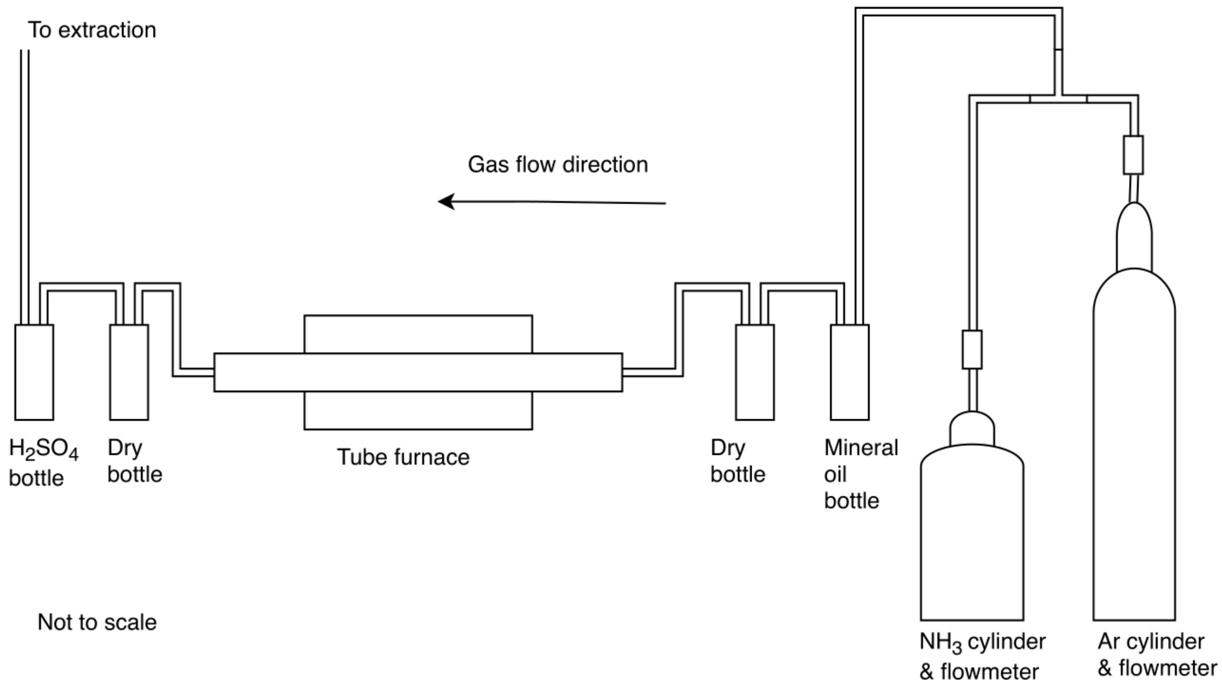

Figure 2: Schematic of wider furnace assembly showing gas supply lines and gas washing bottles in relation to the furnace. Displayed in the physical set up direction for clarity in further discussions.

any liquid suction directly to the reaction tube in the event of low pressures.

4.2.3 Safety considerations

The use of ammonia gas requires careful planning and due consideration to safety. NH_3 poses both an asphyxiant risk from oxygen displacement as per any gas but is also acutely toxic upon inhalation and corrosive. Additionally, at high temperatures, sudden decomposition of NH_3 into N_2 and H_2 poses an explosion risk. A thorough critique of the elements considered in a Control of Substances Hazardous to Health (CoSHH) assessment and risk assessment, along with review from BOC as the gas suppliers, resulted in the implementation of several measures to safely operate the ammonolysis system. This methodology was captured by development of a thorough standard operating procedure.

As well as the choices of materials and assembly used for the gas supply discussed above, additional measures principally focused upon management of any potential NH_3 leaks. The entire assembly was situated in high velocity fume hoods and subjected to regular leak testing using a BW Technologies (by Honeywell) GasAlert Extreme NH_3 model handheld detector. This device provides a digital output of the parts per million measurement of NH_3 present along with associated combined light, sound and vibration alarms for measurements exceeding 25 ppm and 50 ppm. K type respirators were procured for further PPE in the event of an ammonia gas leak that required temporary proximity of personnel.

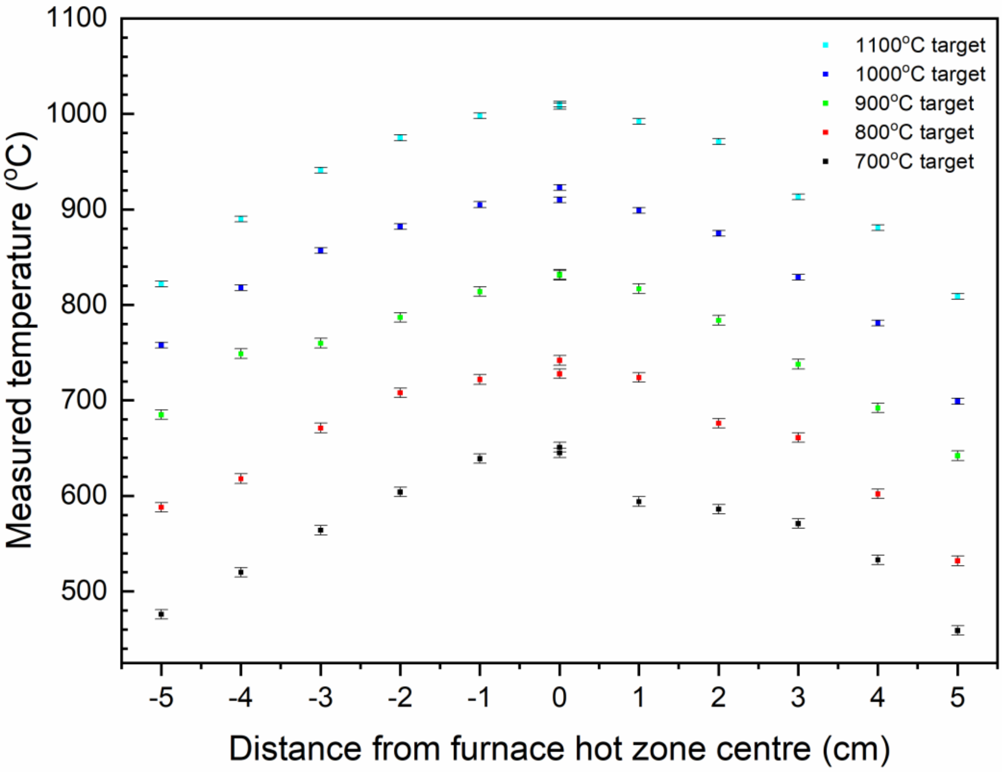

Figure 3: Measured temperatures within the furnace process tube as a function of distance from the centre most point of the heated zone in comparison to the targeted temperature as programmed. Error bars consider the observed fluctuations in temperature during the measurement duration.

4.3 Testing protocol

An initial characterisation of the furnace measured the temperature internal to the process tube across a typical range of operating temperatures. Due to the delays on receiving the

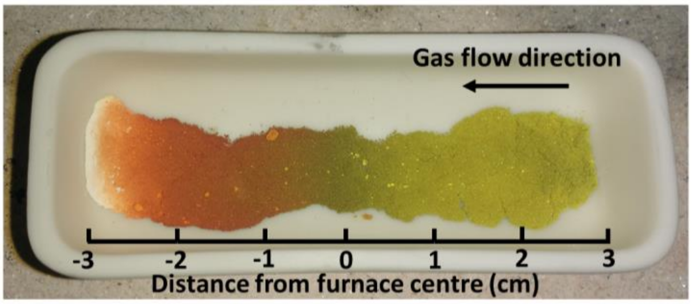

Figure 4: Distribution of colours found after 950 °C 2h 50 ml/min ammonolysis of Ta_2O_5. Gas flow direction from right to left. 0 cm indicates the centre point of the furnace heated zone. Green material (right) is TaON, red material (left) is Ta_3N_5. White material (far left) is retained Ta_2O_5 (see Figure 5 for XRD results).

end cap assemblies, the temperature was measured with the alumina process tube in place but no end caps. The furnace was programmed to reach temperatures of 700 to 1100 °C at 100 °C intervals. After a 30 minute dwell period at each programmed temperature to allow the internal temperature to equilibrate, a thermocouple marked with centimetre increments was inserted into the tube and the temperature recorded after a two minute measurement duration. The observed fluctuations during the measurement were recorded to define the error on the recorded temperature. Measurements were taken across the central 10 cm of the tube, coinciding with the specified furnace hot zone centre of 13 cm. These indicated a typical temperature profile for tube furnaces (Figure 3), with greater deviation from the target temperature further away from the central point of the heated zone, although this should ideally be uniform across the entire heated zone.

Testing the efficacy of the furnace involved replicating an established and facile reaction along with measurement of the temperature profile of the heated zone. The ammonolysis of tantalum oxide, Ta_2O_5, follows a staged reaction:

$$Ta_2O_5+2NH_3 \rightarrow 2TaON+3H_2O \tag{2}$$

$$3TaON+2NH_3 \rightarrow Ta_3N_5+3H_2O \tag{3}$$

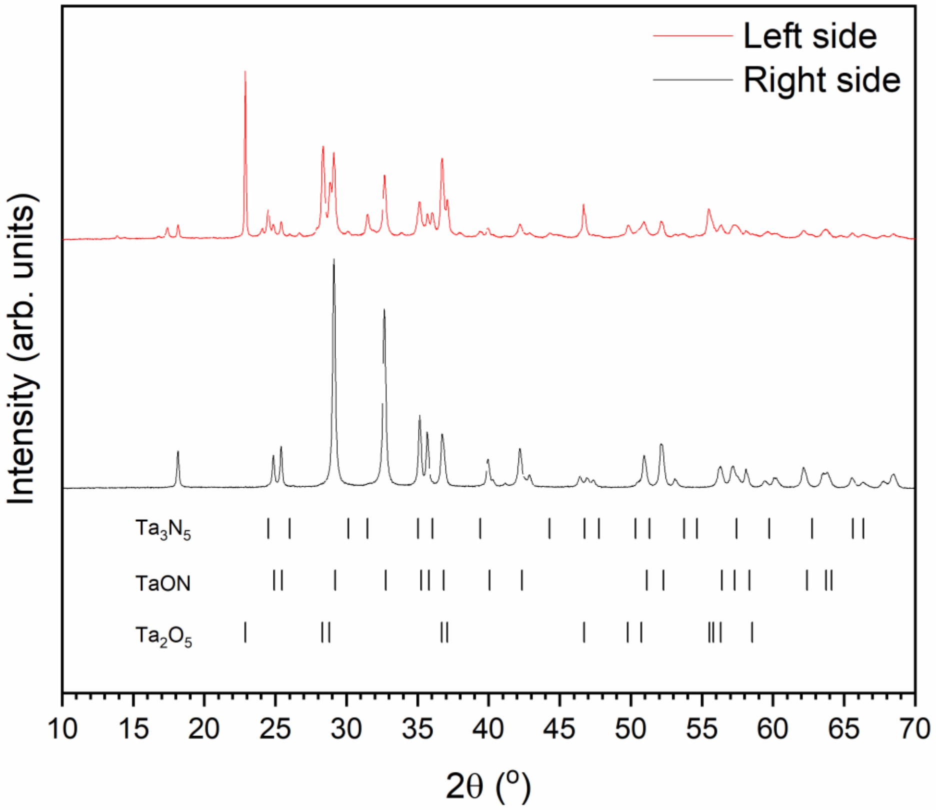

Figure 5: XRD phase identification of Ta_2O_5 subject to 950 °C 50 ml/min NH_3 2h ammonolysis showing different phase distributions between the left and right sides of the crucible – see Figure 4 as a reference. Product was separated into two parts, left (red) and right (black) to analyse the distribution of the products relative to the applied gas flow direction. Tickmarks indicate allowed reflections for Ta_3N_5, TaON and Ta_2O_5.

The tantalum oxynitride and nitride products of these reactions are distinct both x-ray diffraction pattern and colour, with the oxynitride being green [17] and the nitride red [18]. However, these occur at marginally different temperatures of 900 and 950 °C for the oxynitride and nitride respectively. The initial test used a large volume of Ta_2O_5 ramped at 5 °C/min to a target temperature of 950 °C and held at temperature for 2 hours. Ammonia was flowed at 50 ml/min following an initial 20 minute inert gas purge. On recovering the sample, it was evident that two separate phases had formed at either end of the crucible (Figure 4), with the right hand side (leading edge relative to the gas direction defined in

Gas direction	Leading crucible edge	Left side products	Right side products
Right to left	Right	Ta_3N_5, Ta_2O_5	TaON
Left to right	Left	TaON	Ta_3N_5, Ta_2O_5, TaON

Table 1: Phase analysis results from Ta_2O_5 950 °C 50 ml/min NH_3 2h ammonolysis with respect to applied gas direction.

Figure 2) appearing green suggesting incomplete TaON formation, while the left hand side was red suggesting complete nitride formation. XRD phase analysis (Figure 5) verified that the green product was single phase TaON, while the red product contained both Ta_3N_5 as intended and unreacted Ta_2O_5. The distribution of the phases was not in a pattern that would mimic the temperature profile of the furnace but instead was found to be as a result of surface occlusion preventing further reaction, such that the reaction was limited to the intermediate product of equation 2 rather than full completion to the nitride product of equation 3. This was believed to occur as a combination of insufficient gas flow and the larger volume of powder used. Although 50 ml/min NH_3 is published to result in red Ta_3N_5 [18], the reaction duration used differed, resulting in less exposure to nitriding species.

For the asymmetric distribution of products, this implied that for the right hand side of the crucible (leading gas edge) the removal of water evolved from the surface was insufficient and prevented further reaction. This would be compounded by nature of the NH_3 flow over this portion of the crucible. A degree of shielding of the Ta_2O_5 occurs as the gas flows over the rim of the crucible resulting in there being less direct exposure to the NH_3 and less effective removal of evolved H_2O, exacerbated by the comparatively low flow rate. The volume of reactant used was also inappropriately large and hindered full completion of the reaction.

To rectify these issues, subsequent experiments were undertaken to further ascertain the behaviour of the gas flow and any surface occlusion. Firstly, the same experimental parameters were repeated but with the direction of the gas flow reversed, to investigate the

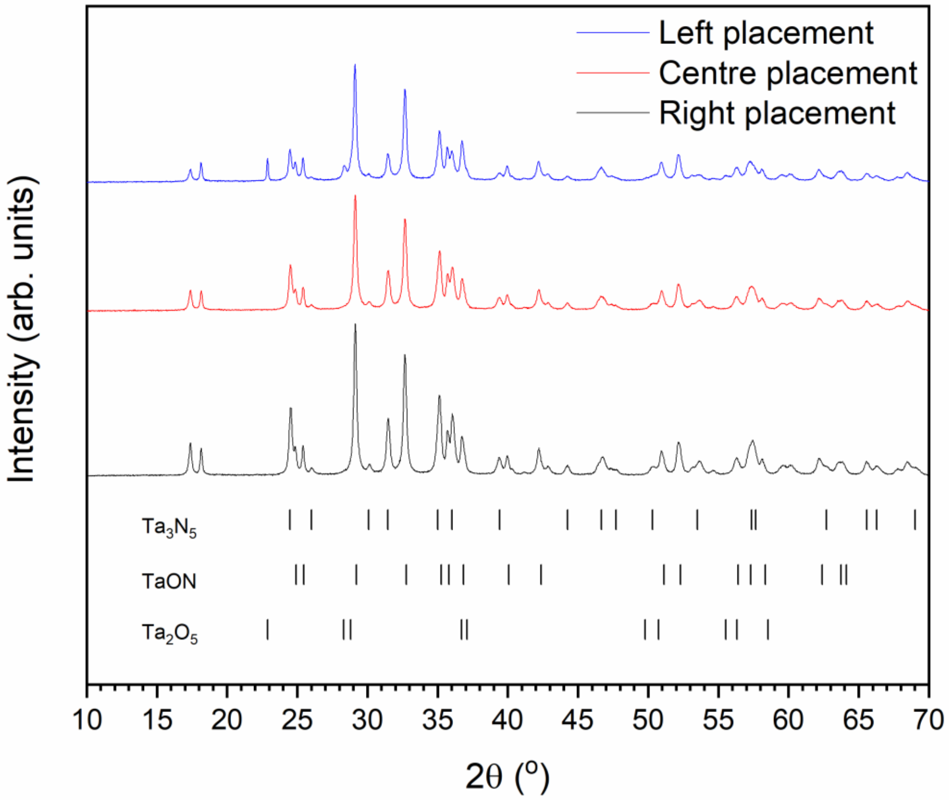

Figure 6: XRD phase identification of left (blue), centre (red) and right (black) crucible placements of Ta_2O_5 subject to 950 °C 75 ml/min NH_3 2h ammonolysis. Tickmarks indicate allowed reflections for Ta_3N_5, TaON and Ta_2O_5.

directional occlusion hypothesis. If the effect were purely as a result of gas flow behaviours, the reversed distribution of products should be attained. This was the case and is summarised in Table 1. To evaluate the insufficient flow rate assertion, the same heating protocol of 950 °C 2h ammonolysis was repeated but using a much increased flow rate of 200 ml/min again using a large volume of Ta_2O_5. The product showed a consistent red colour and phase analysis indicated predominantly Ta_3N_5 but residual TaON, which was attributed to the large volume of powder still in use. From this point, it was decided to use 75 ml/min NH_3 as the minimum flow rate, the efficacy of this verified below.

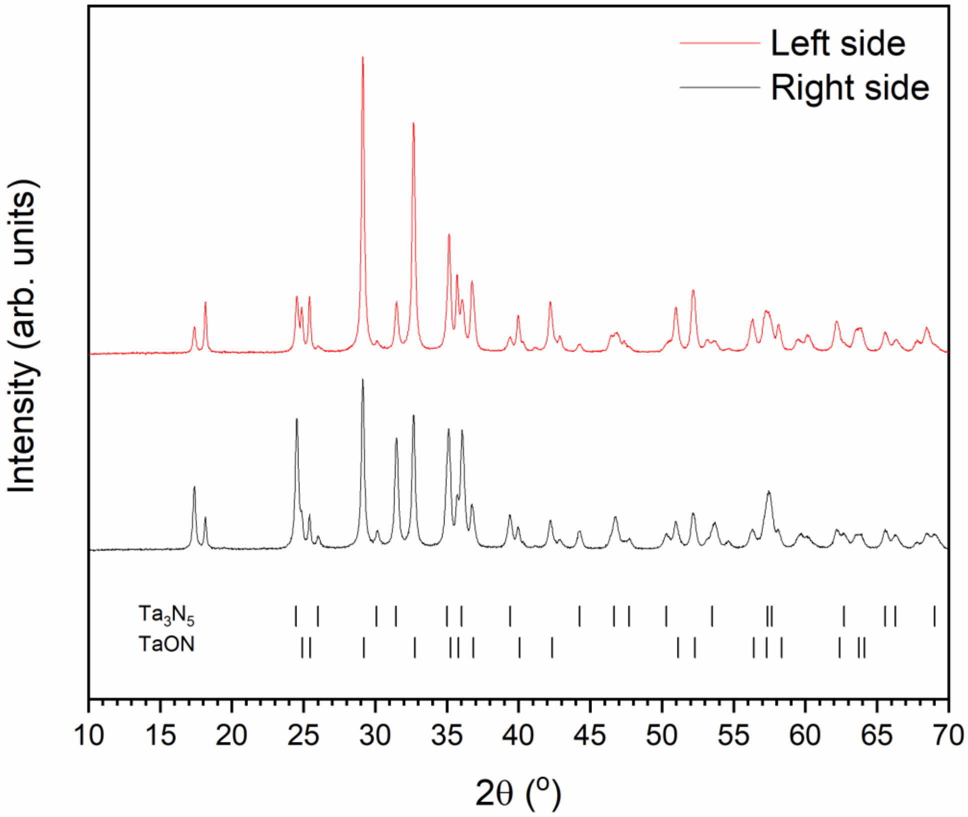

Figure 7: XRD phase identification of Ta_2O_5 subject to 950 °C 50 ml/min NH_3 2h ammonolysis following an inert gas purge at 150 °C for 1h. Product was separated into two parts, left (red) and right (black) to analyse the distribution of the products relative to the applied gas flow direction. Tickmarks indicate allowed reflections for Ta_3N_5, TaON and Ta_2O_5.

In an iterative process, approximately 0.1 g volumes of powder were placed in the left, centre or right of the crucible and subjected to a 950 °C 2 hour 75 ml/min NH_3 reaction protocol. As indicated in Figure 6, phase analysis was consistent between placements, showing the choice of flow rate was sufficient to overcome any shielding effects. However, the clustered nature of the powder placements still indicated mixed phases and therefore incomplete reactions. The volume of powder in use however was suitable for further analysis methods so it was concluded that sample sizes of circa 0.1g would be adequate volume for subsequent characterisation but that this should be spread finely across the crucible to maximise the surface area of the reaction surface.

A final experiment was undertaken to determine an appropriate purge procedure prior to reactions. Using a large volume Ta_2O_5 precursor, an initial purge of 1 hour duration but held at 150 °C was programmed. The use of moderate temperature was to evaporate any residual water within the precursor to ascertain any reaction limiting effects this may have on the end products as compared to the previous body of investigations. A red product was yielded, with phase analysis showing a mixture of Ta_3N_5 and TaON as previously found (Figure 7). From this, it was concluded that the extended purge was not as necessary as careful selection of precursor sample size and so this regime was not included in the final protocol and standard operating procedure. Typical furnace operation used hereafter throughout this body of work therefore utilised 75 ml/min NH_3 flow rates as a minimum. Furnace operation used a 20 minute, room temperature purge before onset of the temperature programme, which used a fixed ramp rate of 5 °C/min and variable reaction durations.

4.4 Precursor selection and preparation

As discussed, ammonolysis typically uses oxide precursors and these form the bulk of precursors used in this thesis. For the formation of ternary (oxy)nitrides via ammonolysis, ternary uranium oxides are chosen as the precursor. However judicious choice of the additional metallic content is required, considering the electropositivity and thermodynamics relating to the metallic species.

Thermodynamic considerations for ternary oxynitrides largely extrapolate from more populated data regarding the ammonolysis of binary oxides to binary nitrides to predict the formation of (oxy)nitride end products. Where the Gibbs free energy of formation for the ternary oxide from its binary is less than the equivalent for the formation of a ternary nitride from its binary, i.e. $\Delta G^{f}_{b}(O) < \Delta G^{f}_{b}(N)$, and/or the free energy of the binary oxide ammonolysis reaction is largely positive (G_b), complete reaction to nitrides is hindered and oxynitrides (or a mixed oxides and nitrides) will form [2]. A corollary of this is that the additional metallic species cannot be too electronegative as the reducing atmosphere of the NH_3 and H_2 resulting from decomposition of the former makes stabilising any oxynitride formed difficult [15]. Electronegative species, e.g. group V elements and the late transition metals, preferentially form ternary nitrides, whereas electropositive elements form oxynitrides under ammonolysis.

Typical sample preparation prior to ammonolysis used hand grinding of the precursor compound before using a minimal mass, sufficient for subsequent XRD and other analysis methods required but small enough to allow for dispersion across the centre of the ammonolysis crucible in a thin layer to maximise surface area for gaseous diffusion. For the purposes of this work, precursors for nitride synthesis of UO_2, UO_3 and U_3O_8 were used (see Chapter 6). Precursors for potential oxynitride synthesis were chosen as $SrUO_4$ and $CaUO_4$ and (see Chapter 7).

4.5 Conclusions

This chapter details the design and ultimate assembly of a tube furnace for the purposes of ammonolysis reactions. The operating behaviour of the furnace was investigated using reaction of a Ta_2O_5 precursor, considering furnace temperature profile, precursor mass and distribution, purge gas duration and temperature and applied NH_3 flow rate. An initial base line of operating conditions was established as using approximately 0.1g of precursor material, distributed finely across the loading crucible to maximise gaseous diffusion, with a 20 minute room temperature purge to evacuate the reaction tube of oxygen prior to applying a minimum of 75 ml/min NH_3 flow rate. Thermodynamic considerations for precursor choice were also discussed.

4.6 References

[1] S. G. Ebbinghaus, H.-P. Abicht, R. Dronskowski, T. Müller, A. Reller, and A. Weidenkaff, "Perovskite related oxynitrides: Recent developments in synthesis, characterisation and investigations of physical properties," *Prog. Solid State Chem.*, vol. 37, no. 2–3, pp. 173–205, 2009, doi: http://dx.doi.org/10.1016/j.progsolidstchem.2009.11.003.

[2] S. H. Elder, F. J. DiSalvo, L. Topor, and A. Navrotsky, "Thermodynamics of ternary nitride formation by ammonolysis: application to lithium molybdenum nitride ($LiMoN_2$), sodium tungsten nitride (Na_3WN_3), and sodium tungsten oxide nitride (Na_3WO_3N)," *Chem. Mater.*, vol. 5, no. 10, pp. 1545–1553, 1993, doi: 10.1021/cm00034a027.

[3] A. Miura, "Low-temperature synthesis and rational design of nitrides and oxynitrides for novel functional material development," *J. Ceram. Soc. Japan*, vol. 125, no. 7, pp. 552–558, 2017, doi: 10.2109/jcersj2.17055.

[4] T. Nakagawa, H. Matsuoka, M. Sawa, M. Hirota, M. Miyake, and M. Katsura, "Formation of uranium and cerium nitrides by the reaction of carbides with NH_3 and N_2/H_2 stream," *J. Nucl. Mater.*, vol. 247, pp. 127–130, 1997, doi: http://dx.doi.org/10.1016/S0022-3115(97)00036-6.

[5] M. Katsura, "A thermodynamic analysis of nitrogen-rich uranium sesquinitride formation by the reaction of uranium with ammonia," *Solid State Ionics*, vol. 49, pp. 225–231, 1991, doi: https://doi.org/10.1016/0167-2738(91)90090-X.

[6] M. Katsura and H. Serizawa, "Formation of a nitrogen-rich α-U_2N_{3+x} phase by the reaction of uranium with a stream of ammonia," *J. Alloys Compd.*, vol. 187, no. 2, pp. 389–399, 1992, doi: https://doi.org/10.1016/0925-8388(92)90444-E.

[7] H. Serizawa, K. Fukuda, Y. Ishii, Y. Morii, and M. Katsura, "Crystallographic study on the phase transition of α-U_2N_3," *J. Nucl. Mater.*, vol. 208, no. 1, pp. 128–134, 1994, doi: https://doi.org/10.1016/0022-3115(94)90204-6.

[8] H. Serizawa, K. Fukuda, and M. Katsura, "Study of the formation of α-U_2N_{3+x} using unstable ammonia - reaction sequence and control of nitrogen activity," *J. Alloys Compd.*, vol. 223, no. 1, pp. 39–44, 1995, doi: https://doi.org/10.1016/0925-8388(94)01442-6.

[9] A. Fuertes, "Synthesis and properties of functional oxynitrides - from photocatalysts to CMR materials," *Dalt. Trans.*, vol. 39, no. 26, pp. 5942–5948, 2010, doi: 10.1039/C000502A.

[10] C. B. Yeamans *et al.*, "Oxidative ammonolysis of uranium(IV) fluorides to uranium(VI) nitride," *J. Nucl. Mater.*, vol. 374, no. 1–2, pp. 75–78, 2008, doi: 10.1016/j.jnucmat.2007.06.022.

[11] G. W. C. Silva, C. B. Yeamans, L. Ma, G. S. Cerefice, K. R. Czerwinski, and A. P. Sattelberger, "Microscopic Characterization of Uranium Nitrides Synthesized by Oxidative Ammonolysis of Uranium Tetrafluoride," *Chem. Mater.*, vol. 20, no. 9, pp. 3076–3084, 2008, doi: 10.1021/cm7033646.

[12] A. Rachel *et al.*, “Tantalum and niobium perovskite oxynitrides: Synthesis and analysis of the thermal behaviour,” *Thermochim. Acta*, vol. 438, no. 1–2, pp. 134–143, 2005, doi: http://dx.doi.org/10.1016/j.tca.2005.08.010.

[13] R. Marchand, Y. Laurent, J. Guyader, P. L’Haridon, and P. Verdier, “Nitrides and oxynitrides: Preparation, crystal chemistry and properties,” *J. Eur. Ceram. Soc.*, vol. 8, no. 4, pp. 197–213, 1991, doi: https://doi.org/10.1016/0955-2219(91)90096-I.

[14] S. J. Clarke, K. A. Hardstone, C. W. Michie, and M. J. Rosseinsky, “High-Temperature Synthesis and Structures of Perovskite and n = 1 Ruddlesden Popper Tantalum Oxynitrides,” *Chem. Mater.*, vol. 14, no. 6, pp. 2664–2669, 2002.

[15] A. Fuertes, “Metal oxynitrides as emerging materials with photocatalytic and electronic properties,” *Mater. Horiz.*, vol. 2, no. 5, pp. 453–461, 2015, doi: 10.1039/C5MH00046G.

[16] A. Fuertes, “Chemistry and applications of oxynitride perovskites,” *J. Mater. Chem.*, vol. 22, no. 8, pp. 3293–3299, 2012, doi: 10.1039/C2JM13182J.

[17] G. Brauer, J. Weidlein, and J. Strähle, “Über das Tantalnitrid {Ta_3N_5} und das Tantaloxidnitrid {TaON},” *Zeitschrift für Anorg. und Allg. Chemie*, vol. 348, no. 5–6, pp. 298–308, 1966, doi: 10.1002/zaac.19663480511.

[18] S.-K. Sun, T. Motohashi, Y. Masubuchi, and S. Kikkawa, “Direct synthesis of $SrTaO_2N$ from $SrCO_3$/Ta_3N_5 involving {CO} evolution,” *J. Eur. Ceram. Soc.*, vol. 34, no. 16, pp. 4451–4455, 2014, doi: http://dx.doi.org/10.1016/j.jeurceramsoc.2014.07.003.

Chapter 5

Low temperature nitridation of Fe_3O_4 by reaction with $NaNH_2$

Inorganic Chemistry

pubs.acs.org/IC
Article

Low-Temperature Nitridation of Fe_3O_4 by Reaction with $NaNH_2$

Sarah E. O'Sullivan, Shi-Kuan Sun,* Sebastian M. Lawson, Martin C. Stennett, Feihong Chen, Yuji Masubuchi, Claire L. Corkhill, and Neil C. Hyatt*

Cite This: Inorg. Chem. 2021, 60, 2553−2562

Read Online

ACCESS | Metrics & More | Article Recommendations | Supporting Information

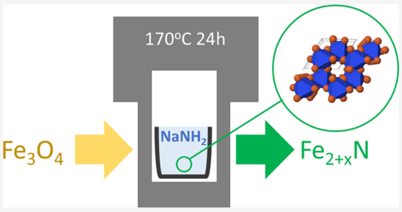

ABSTRACT: Low-temperature soft chemical synthesis routes to transition-metal nitrides are of interest as an alternative to conventional high-temperature ammonolysis reactions involving large volumes of chemotoxic NH_3 gas. One such method is the reaction between metal oxides and $NaNH_2$ at ca. 200 °C to yield the counterpart nitrides; however, there remains uncertainty regarding the reaction mechanism and product phase assemblage (in particular, noncrystalline components). Here, we extend the chemical tool box and mechanistic understanding of such reactions, demonstrating the nitridation of Fe_3O_4 by reaction with $NaNH_2$ at 170−190 °C, via a pseudomorphic reaction. The more reduced Fe_3O_4 precursor enabled nitride formation at lower temperatures than the previously reported equivalent reaction with Fe_2O_3. The product phase assemblage, characterized by X-ray diffraction, thermogravimetric analysis, and ^{57}Fe Mössbauer spectroscopy, comprised 49−59 mol % ε-$Fe_{2+x}N$, accompanied by 29−39 mol % $FeO_{1-x}N_x$ and 8−14 mol % γ''-FeN. The oxynitride phase was apparently noncrystalline in the recovered product but could be crystallized by heating at 180 °C. Although synthesis of transition-metal nitrides is achieved by reaction of the counterpart oxide with $NaNH_2$, it is evident from this investigation that the product phase assemblage may be complex, which could prove a limitation if the objective is to produce a single-phase product with well-defined electrical, magnetic, or other physical properties for applications. However, the significant yield of the $FeO_{1-x}N_x$ oxynitride phase identified in this study opens the possibility for the synthesis of *metastable oxynitride* phases in high yield, by reaction of a metal oxide substrate with $NaNH_2$, with either careful control of H_2O concentration in the system or postsynthetic hydrolysis and crystallization.

■ INTRODUCTION

Transition-metal nitrides have considerable technological potential, with broad applications as functional materials with exploitable physical and chemical properties,[1,2] and advancements in their synthesis have been the focus of considerable interest. Synthesis of a nitride from a readily available oxide precursor is preferential as similarities in ionic radius and electronegativity (3.50 and 3.07 for oxygen and nitrogen, respectively[3]) allow for substitution of nitrogen for oxygen, providing the host compound is capable of charge compensation. However, doing so with gaseous nitrogen is not possible due to unfavorable thermodynamics. The triple N≡N bond has an enthalpy of 941 kJ/mol, whereas the double O═O bond has an enthalpy of only 500 kJ/mol, and thus, nitride formation cannot be achieved.[4] This can be overcome by use of high pressure as well as high temperature to manipulate the thermodynamics to promote nitride stabilization. However, the energy and instrumentation requirements for this can be prohibitive. A detailed discussion and visualization of nitride synthesis methodologies was recently presented by Miura et al.[4]

Typical gaseous nitridation is achieved by using high flow rates of NH_3 gas at high temperatures, in the region of 600−1200 °C[3] acting upon oxide or halide precursors. Although the use of NH_3 has been successfully applied for the synthesis of most known nitride compounds, a large number of diffusion steps and high temperature are essential to activate the diffusion. The high processing temperature may induce the decomposition of NH_3 into N_2 and H_2, which is an undesirable side reaction. In addition, gas exchange between the solid and the ammonia is a limiting factor, sometimes resulting in samples that have reacted at the surface only. Thus, several ammonolysis steps with intermediate regrinding are often required.[3] As such, these reactions demand large volumes of NH_3 gas, which comes with safety and material implications due to the chemotoxic and corrosive nature of NH_3.

Several alternate solid-state nitrogen sources have been developed for nitride synthesis. Urea, $CO(NH_2)_2$, has been used to synthesize a number of nanoparticulate binary nitrides such as TiN, VN, NbN, GaN,[5] and AlN.[6] Ethanol-based solutions of a metal precursor and urea form a gel-like intermediate product, which is then heated to 800 °C or greater under N_2, to yield the nitride. Melamine, $C_3H_6N_6$, decomposes to C_3N_4, which can then be used as a

Received: November 23, 2020
Published: January 25, 2021

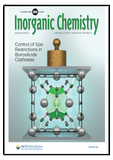

https://dx.doi.org/10.1021/acs.inorgchem.0c03452

carbothermal reducing and nitriding agent.[7,8] Similar to the urea route, the mixed metal precursor and nitriding agent are then heat-treated in the region of 650−800 °C. While these methods offer a more easily implemented nitriding source compared to NH_3 gas, they still require high-temperature processing and are subject to residual carbon impurities in the final product.

A solid-state nitrogen source that does not require high synthesis temperatures is sodium amide, $NaNH_2$. Nitrides synthesized by this method include TiN,[9−11] VN,[12] Cu_3N,[13] InN,[14,15] Si_3N_4,[16][16] BN,[17] Fe_3N_{1+x},[18] and a variety of manganese nitrides.[18−20] These reactions predominantly used oxide precursors, excluding examples of TiN,[9,10] VN,[12] and MnN,[20] which were formed from their respective chlorides, and BN synthesized from liquid BBr_3.[17] All reactions utilized a similar methodology performing reactions in stainless steel autoclaves and the end product being washed with ethanol to destroy and remove excess $NaNH_2$. Typical reaction temperatures range from 170 to 300 °C. Synthesis via $NaNH_2$ therefore offers a route to nitride formation at much lower temperatures than those required for ammonolysis or reactions using other solid-state nitrogen sources and avoids the use of toxic NH_3 gas.

Of interest to this study is the reported formation of $Fe_{2+x}N$ (or, equivalently, Fe_3N_{1+x}),[18] which has broad applications and research potential in corrosion-resistant coatings, magnetic data recording, catalysis, and biomedical uses.[1] Synthesis of $Fe_{2+x}N$ was previously achieved from reaction of Fe_2O_3 with an excess of $NaNH_2$ at 240 °C for 36 h.[18] Previous work indicates that the reactions are highly reducing in nature, with Cu metal being formed from reaction of CuO with $NaNH_2$ at 190 °C for 60 h, compared to Cu_3N being formed at 170 °C for 60 h.[13] As reduction is key to the reaction mechanism, we opted to use Fe_3O_4 as a comparatively reduced counterpart to Fe_2O_3 to explore the potential for synthesis of $Fe_{2+x}N$ under more mild reaction conditions. In this work, we extend the $NaNH_2$ synthetic approach to consider reactions using Fe_3O_4 with lower reaction temperatures of 170−190 °C and variable duration. In particular, we extend the suite of characterization applied to these phases to develop a more complete understanding of the product phase assemblage and reaction mechanism. In all reaction products, we determine a mixture of ε-$Fe_{2+x}N$ and γ''-FeN nitride compositions along with an oxynitride phase $FeO_{1-x}N_x$, demonstrating complexity of the phase assemblage not previously considered.

■ EXPERIMENTAL SECTION

Caution. $NaNH_2$ is a strong base that reacts violently with oxidizing agents and with water (producing ammonia); explosive peroxides may form on atmospheric exposure: use of this reagent must be rigorously risk-assessed; storage and handling under a dry inert atmosphere are advised.[21]

Reagents of Fe_3O_4 and $NaNH_2$ (Sigma-Aldrich, 98% purity) were mixed in a 1:14 molar ratio and hand-ground under a dry nitrogen atmosphere for 5 min. Typically, 1 g of powder was placed in a lidded crucible (5 mL, fabricated from a type 316 stainless steel), which was sealed within a poly(tetrafluoroethylene) (PTFE)-lined stainless steel digestion vessel (45 mL, Parr model 4744); this was performed under a dry nitrogen atmosphere. The vessel was transferred to a temperature-controlled oven (170 or 190 °C, ±1 °C) for the reaction duration (24, 48, or 96 h). Vessels were removed from the oven, cooled at room temperature, and opened in a fume hood, due to the distinctive odor of ammonia evolved from the head space, confirmed by moist universal indicator paper. Inspection of the stainless steel crucible revealed a solid, fused, mass. The product was recovered by soaking in ethanol to dissolve residual $NaNH_2$ forming (soluble) sodium ethoxide and ammonia gas ($NaNH_2 + C_2H_5OH \rightarrow C_2H_5ONa + NH_3$). The product, a black powder, was washed twice in ethanol and recovered by filtration for further analysis.

Characterization of the nitrided powders was carried out by X-ray diffraction (XRD) performed on a Bruker D2 Phaser diffractometer in fluorescence mode with a Ni-filtered Cu Kα radiation of $\lambda = 1.5418$ Å and a Lynxeye position-sensitive detector; the energy discriminator window was adjusted to minimize the acceptance of Fe Kα fluorescence. Scanning electron microscopy coupled with energy-dispersive X-ray analysis (SEM-EDX) was performed first on a Hitachi TM3030 desktop unit with a Bruker Quantax EDX system and subsequently on an FEI Inspect F50 FEG SEM operating at 10 kV. ^{57}Fe Mössbauer spectroscopy measurements were performed with a Wissel MRG-500 spectrometer in transmission mode using a 50 mCi ^{57}Co source; calibration was performed with an α-Fe reference foil. Spectra were measured using a constant acceleration waveform with a velocity range of ±10 mm s^{-1}. Data were analyzed using Recoil software,[22] fitting Lorentzian line shapes. Thermogravimetric analysis mass spectrometry (TG-MS) measurements were made using a Netzsch STA 449 F3 *Jupiter* thermal analyzer coupled with a Netzsch QMS 403 *Aelos Quadro* quadrupole mass spectrometer and using an argon carrier gas.

Samples were prepared for transmission electron microscopy (TEM) using the crushed grain method. Samples were rapidly ground with isopropanol using an agate pestle and mortar and allowed to settle. A small amount of the resultant mixture was siphoned from the top of the solvent line and pipetted onto carbon-holey lined Cu grids (Agar Scientific). TEM was performed using a JEOL F200 operating at 200 keV. Images and electron diffraction patterns were recorded using a Gatan OneView camera under bright-field conditions. EDS was undertaken using dual silicon drift detectors. Electron energy loss spectroscopy (EELS) was recorded using a Gatan Image Filter Quantum ER, with a slit width of 200 eV, a dispersion of 25 eV/channel, and a 5 mm entrance aperture. The energy resolution was 0.8 eV. For each spectral acquisition, 40 frames with an exposure time of 0.5 s were recorded and summed. Conversion of two-dimensional (2D) polycrystalline electron diffraction patterns was achieved by taking several radial grayscale line scans of each pattern using the ImageJ software package,[23] with the undiffracted (000) "reflection" taken as $1/d = 0$. Sample specific line scans were normalized to the most intense reflection, summed to give an average for the whole pattern and inverted to produce a one-dimensional (1D) intensity against the d-spacing pattern.

■ RESULTS AND DISCUSSION

Initial analysis of XRD data (Figure 1) determined all products to be composed of a mixture of crystalline ε-$Fe_{2+x}N$ (space group $P6_322$) and a noncrystalline phase contributing to diffuse scattering most apparent in the regions $20° < 2\theta < 50°$. The relatively broad nature of the reflections associated with the $Fe_{2+x}N$ phase was interpreted as the characteristic of a nanocrystalline material, as later confirmed by TEM observation. Comparison of the XRD data of the ε-$Fe_{2+x}N$ products with reference patterns of ε-Fe_2N (PDF 04−017−2325) and ε-Fe_3N (PDF 01-083-0878) suggested a composition with an intermediate Fe/N ratio ($0 < x < 1$), as shown in Figure 1. The Fe−N phase diagram is known to be complex, but the ε-$Fe_{2+x}N$ solid solution, with $0 < x < 1$, has been reasonably well characterized; the structure, in space group $P6_322$, comprises a hexagonal close-packed array of Fe atoms with N occupying octahedral interstices in an ordered fashion.[24−27] Reaction conditions were systematically varied in an attempt to optimize the crystallinity of the product and control the composition. The yield of $Fe_{2+x}N$ was not improved by increasing the reaction temperature from 170

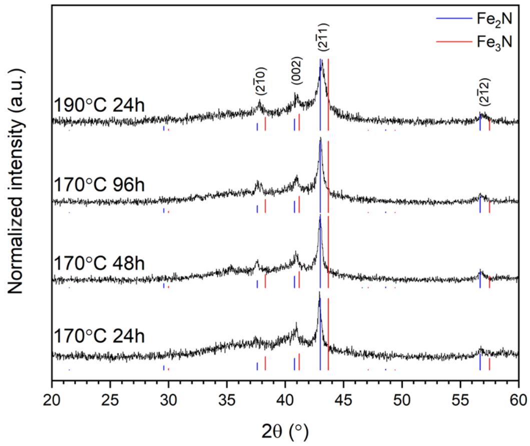

Figure 1. XRD data for the product of reaction of Fe_3O_4 and $NaNH_2$ at 170 °C for (from bottom) 24, 48, and 96 h and at 190 °C for 24 h (top). XRD data are indexed in the space group $P6_322$ structure of ε-$Fe_{2+x}N$. Reference diffraction data for ε-Fe_2N (PDF 04−017−2325) are shown in blue and ε-Fe_3N in red (PDF 01-083-0878).

to 190 °C for 24 h or increasing the reaction time from 24 to 96 h at 170 °C, as shown in Figure 1. However, the reflection full width at half-maximum was observed to increase with reaction temperature and time, indicative of a decrease in crystallite size. To estimate the average composition of the ε-$Fe_{2+x}N$ product phase, the Inorganic Crystal Structure Database[28] was mined to establish a calibration of unit cell volume as a function of x in ε-$Fe_{2+x}N$, assuming a linear dependence in accordance with Vegard's law (see Table S1 and Figure S1 in the Supporting Information). The unit cell parameters of the $Fe_{2+x}N$ products and estimated compositions determined using this linear calibration are reported in Table 1 and establish $x \approx 0.12(2)$, corresponding to an average formal Fe oxidation state of $Fe^{1.42+}$. The refined unit cell parameters show a trend of increasing unit cell volume with reaction time and temperature, as shown in Table 1, implying a small decrease in x, although this is within the estimated uncertainty of the linear calibration. It should be noted that the extracted value of unit cell volume relies upon XRD data with broad reflections and a subsequent calibration of these values to available data and thus represents an estimate of composition only. The trend of increasing cell volume, combined with the increase in full width at half maximum (FWHM) for the XRD data in Figure 1, implies decreased nitridation with increased reaction time and temperature. Miura et al.[18] offer an explanation for this with consideration of the relative excess of $NaNH_2$ present in the reactions. Where reduced concentrations of $NaNH_2$ are present, the reaction is limited, with the formation of H_2O and corresponding positive values for the Gibbs free energy of reaction. In this instance, prolonged reaction times and higher temperatures result in greater dissolution of $NaNH_2$, thus reducing the available reagent at the latter stages of the reaction. Formation of H_2O results in hydrolysis of the nitride content, adding to the amorphous phase and reducing the apparent nitridation of the end product.

Reducing the reaction temperature to 150 °C for 24 h afforded a negligible yield of the ε-$Fe_{2+x}N$ product. The reported melting point of $NaNH_2$ is 200 °C; however, the presence of water (and the formation of NaOH) reduces the melting point to ca. 170 °C.[29] This is consistent with our observation of the product forming a fused mass indicative of the reaction being mediated by a $NaNH_2$−NaOH molten salt and negligible yield realized at 150 °C, below the eutectic melting temperature, where the kinetics of mass transport are limiting.[29]

In an effort to identify the noncrystalline phase contributing to the diffuse scattering apparent in the XRD data of Figure 1, we attempted to crystallize this phase by annealing at 180 °C for 24 h in air. The resulting XRD data exhibited relatively sharp Bragg reflections associated with ε-$Fe_{2+x}N$, with no significant shift in 2θ position but evidently reduced full width at half-maximum (compare to Figure 2), indicative of larger crystallite size and/or narrower distribution of nonstoichiometry about the average of $x \approx 0.12(2)$. Moreover, very broad Bragg reflections were apparent at the location of previously observed diffuse intensity as shown in Figure 2 and a weak unindexed reflection at $2\theta = 36°$ in Figure 1, which could be

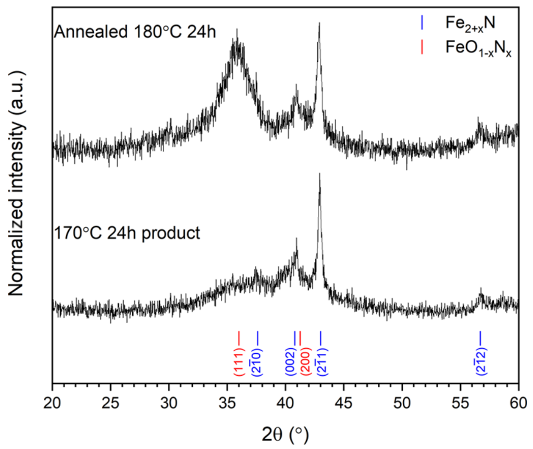

Figure 2. XRD patterns for product from reaction between Fe_3O_4 and $NaNH_2$ at 170 °C/24 h (bottom) and post 180 °C/24 h anneal, showing the onset of broad Bragg reflections associated with a new face-centered cubic $FeO_{1-x}N_x$ phase identified from Mössbauer analysis. Indexed reflections for ε-$Fe_{2+x}N$ (blue) and $FeO_{1-x}N_x$ (red) are shown by tick marks; see the text for details.

Table 1. Unit Cell Dimensions and Inferred Composition for ε-$Fe_{2+x}N$ Reaction Products[a]

sample	a (Å)	c (Å)	volume (Å^3)	x in $Fe_{2+x}N$	estimated composition	avg. Fe oxidation state
170 °C/24 h	4.779(1)	4.418(1)	87.38(1)	0.13(6)	$Fe_{2.13}N$	1.41
170 °C/48 h	4.782(1)	4.416(1)	87.46(1)	0.11(6)	$Fe_{2.11}N$	1.42
170 °C/96 h	4.781(1)	4.420(1)	87.50(1)	0.10(6)	$Fe_{2.10}N$	1.43
190 °C/24 h	4.782(1)	4.418(2)	87.47(1)	0.11(6)	$Fe_{2.11}N$	1.42

[a] Unit cell parameters were calculated using Le Bail fits of XRD data. Estimation of the stoichiometry (x) was made from a calibration of unit cell volume from ICSD data[28] (see Table S1 and Figure S1 in the Supporting Information).

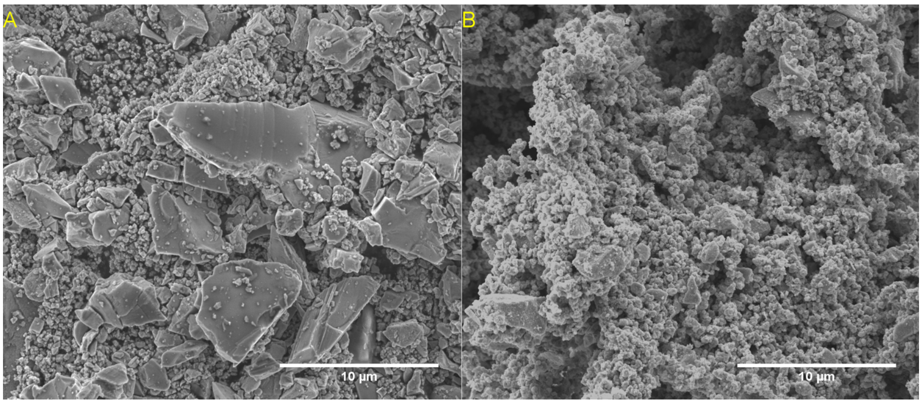

Figure 3. SEM images of untreated Fe_3O_4 (A) and product from reaction with $NaNH_2$ at 190 °C for 24 h (B). Further SEM images of 170 °C reactions can be found in Figure S2 in the Supporting Information.

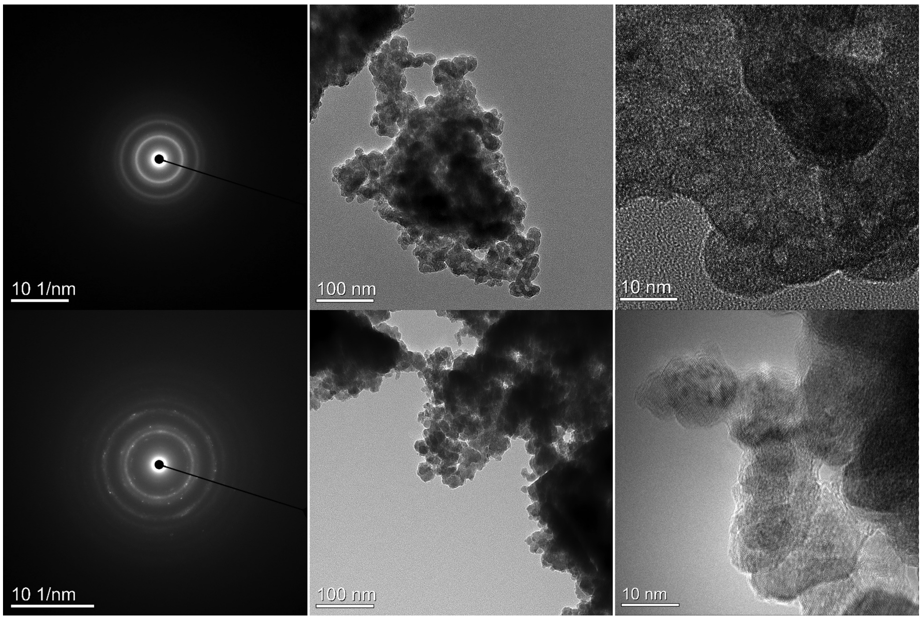

Figure 4. Electron diffraction and TEM images of product from reaction between Fe_3O_4 and $NaNH_2$ reacted at 170 °C/24 h (top) and 190 °C/24 h (bottom).

indexed on a face-centered cubic cell with a = 4.36(1) Å. Analysis of ^{57}Fe Mössbauer data, discussed below, suggested that this phase is in fact an iron oxynitride, in the (wustite-$Fe_{1-x}O)_{1-y}(\gamma'''-FeN)_y$ solid solution, adopting a NaCl-type structure. Indeed, the determined unit cell parameter is intermediate between that of wustite $Fe_{1-x}O$ (a = 4.28−4.31 Å) and γ'''-FeN (a = 4.50 Å),[30−32] consistent with such a solid solution. Hitherto, iron oxynitrides, of the type $FeO_{1-x}N_x$, have been reported only as thin films produced by magnetron sputtering or molecular beam epitaxy and exhibit unstrained unit cell parameters in the range 4.25 Å < a < 4.52 Å depending on composition (with (N + O)/Fe ≈ 1.0 and 0.13 < N/(N + O) < 0.65), consistent with our determined unit cell parameter.[33−38] Analysis of ^{57}Fe Mössbauer data also established the presence of minor γ''-FeN, adopting the zinc blende structure and a = 4.31 Å.[39] This phase would also make a minor contribution to the broad Bragg reflections of the face-centered cubic phase indexed in Figure 2, based on the estimated phase fraction derived from ^{57}Fe Mössbauer data.

SEM observation of the Fe_3O_4 reagent and ε-$Fe_{2+x}N$ product produced at 190 °C/24 h (Figure 3) revealed no significant change in the bimodal primary particle size. However, the ε-$Fe_{2+x}N$ product particles evidenced additional nanoscale texture compared to the reagent, consistent with the occurrence of an interfacial reaction occurring in a molten salt medium. EDX analysis (Figure S3) confirmed the presence of N in the product from the presence of N Kα emission, which was not observed in the reagent. Note that no Na was detected and hence residual $NaNH_2$ is considered to have been removed by the washing procedure. Similar observations were made for the products obtained after reaction at 170 °C and are shown in Figure S2. The relative intensity of the N Kα emission was evidently reduced for ε-$Fe_{2+x}N$ (Figure S3) produced after reaction at 96 h consistent with an increase in the Fe/N ratio inferred from XRD analysis. From these data, we deduce that the synthesis of ε-$Fe_{2+x}N$ from Fe_3O_4 proceeds via a pseudomorphous reaction involving replacement of Fe_3O_4 by ε-$Fe_{2+x}N$ through reaction with $NaNH_2$−NaOH molten salt. However, since the spinel structure of Fe_3O_4 and hexagonal ε-$Fe_{2+x}N$ do not have a three-dimensional correspondence, the reaction mechanism cannot readily be understood as being topotactic in nature.

Further investigation of the product materials was made by transmission electron microscopy, which revealed the primary particles to be composed of nanoparticles of typically 5−20 nm dimension, shown in Figure 4. These nanoparticles exhibited both the presence and absence of fringes characteristic of both nanocrystalline and noncrystalline materials, consistent with XRD data. It is hypothesized that the distribution of amorphous material forms as a shell coating around intact cores of nitride material, as previously seen for amorphous MnO_x layers around crystalline Mn_4N_2 particles.[40] Selected area electron diffraction (SAED) patterns exhibited primarily rings consistent with sampling of many nanocrystalline domains, although the SAED data of the product arising from reaction at 190 °C/24 h also exhibited spots indicative of the presence of some single crystalline domains, consistent with the core−shell structures and inner crystalline SAED findings reported by Walter et al.[40] Integration of the two-dimensional SAED data was performed, yielding one-dimensional diffraction patterns, to assist interpretation, as shown in Figure S4 in the Supporting Information. Consistent with XRD and ^{57}Fe Mössbauer data shown in Figures 1 and 5, the SAED patterns can be interpreted as having contributions from ε-$Fe_{2+x}N$ ($P6_322$) associated with diffraction maxima indexed as $d_{(101)} = 3.02$ Å, $d_{(110)} = 2.39$ Å, $d_{(002)} = 2.21$ Å, $d_{(111)} = 2.10$ Å, and $d_{(112)} = 1.62$ Å, and an iron oxynitride, $FeO_{1-x}N_x$ ($Fm\bar{3}m$, $a = 4.36$ Å), associated with diffraction maxima indexed as $d_{(111)} = 2.52$ Å, $d_{(200)} = 2.18$ Å, $d_{(220)} = 1.52$ Å, and $d_{(311)} = 1.34$ Å.

^{57}Fe Mössbauer spectroscopy analysis of the product materials revealed a paramagnetic doublet feature, with similar spectral envelope and the absence of any magnetic hyperfine splitting, as shown in Figure 5; fitting parameters are detailed in Table 2. Paramagnetic doublets indicate a composition ε-$Fe_{2+x}N$ with $x < 0.4$,[41−45] consistent with XRD analyses. Hyperfine parameters have previously been reported in paramagnetic ε-$Fe_{2+x}N$ phases, characterized by several doublet subspectra contributing to the overall spectral envelope and associated with nitrogen ordering around the unique Fe(II) and Fe(III) sites[44,45] (note that the nomenclature here is used to denote site designation, consistent with the literature, and does not relate to oxidation state). These are labeled D1 and D2 in our assignment in Table 2, represented by solid and dashed gray lines, respectively, in Figure 5. Refinement of the isomer shift and quadrupole shift of these contributions was followed by refinement of the site fractions, the refined parameters being consistent with previously reported values. Comparing the relative spectral area between the two components D1 and D2, the Fe(II) site, with two nearest-neighbor nitrogen atoms, contributes approximately 45% to the total signal for this phase. Based on the analysis of site fraction as a function of nitrogen content by Schaaf,[45] the phase has a composition with 1.26 formula units of nitrogen ε-$Fe_3N_{1.26}$, otherwise expressed as ε-$Fe_{2.38}N$. This is reasonably consistent with the interpretation of XRD data and the estimate of $x = 0.12(2)$, described above. The inferred composition from XRD data relied upon the measurement of unit cell volume of comparatively broad reflections compared to the precision offered by Mössbauer spectroscopy, and, thus, the estimated compositions afforded from the Mössbauer spectroscopy data are preferred.

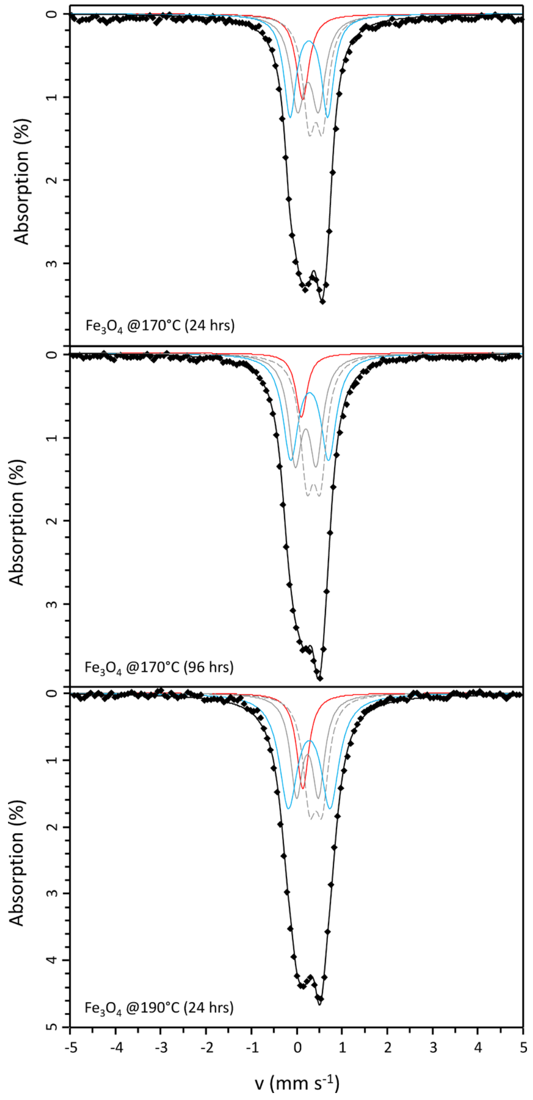

Figure 5. ^{57}Fe Mössbauer data from the product of reaction between Fe_3O_4 and $NaNH_2$ at 170 °C/24 h and 96 h, and 190 °C for 24 h. Data are shown as solid points and the solid black line shows the overall model fit (components shown as blue, red, and gray lines; see the text for details).

On using the analysis from Schaaf, we assume that the recoil-free fractions (f) of the Fe(II) and Fe(III) sites are equal and thus the spectral area is directly proportional to the number of absorbing nuclei. The recoil-free fraction (f) is a measure of the probability of recoil-free emission from the Fe atoms and is influenced by the strength of the interatomic forces between those atoms and the crystal lattice.[46] The fraction therefore depends on the local structure of the surrounding lattice and according to the Debye model has contributions related to temperature, the energy of the γ ray, and the Debye temperature of the crystal.[45] Limited information exists in the literature on the determination of recoil-free fractions in iron nitrides; however, similar Debye temperatures have been reported for ε-Fe_xN ($2 < x < 3$),[47,48] γ-FeN_x,[49] Fe_4N,[50] and FeO_x[51] phases. This suggests that all of the phases assigned in

Table 2. Parameters Obtained from Fitting ^{57}Fe Mössbauer Data of Products from Reaction between Fe_3O_4 and $NaNH_2$[a]

sample	site	δ (mm s^{-1})	Δ (mm s^{-1})	Γ (mm s^{-1})	fraction (%)	assignment	approximate composition	average formal Fe oxidation state
170 °C/24 h	S1	0.13		0.18	14	γ''-FeN	FeN_x	3.00
	D1	0.43	0.30	0.16	30	ε-$Fe_{2+x}N$ Fe(III)	$Fe_{2.38}N$	1.26
	D2	0.25	0.46	0.19	26	ε-$Fe_{2+x}N$ Fe(II)	$Fe_{2.38}N$	
	D3	0.27	0.83	0.17	29	$FeO_{1-x}N_x$	$FeO_{0.20}N_{0.80}$	2.80
170 °C/96 h	S1	0.16		0.14	8	γ''-FeN	FeN_x	3.00
	D1	0.44	0.29	0.18	31	ε-$Fe_{2+x}N$ Fe(III)	$Fe_{2.38}N$	1.26
	D2	0.25	0.46	0.18	28	ε-$Fe_{2+x}N$ Fe(II)	$Fe_{2.38}N$	
	D3	0.28	0.84	0.20	33	$FeO_{1-x}N_x$	$FeO_{0.25}N_{0.75}$	2.75
190 °C/24 h	S1	0.16		0.16	12	γ''-FeN	FeN_x	3.00
	D1	0.45	0.28	0.17	26	ε-$Fe_{2+x}N$ Fe(III)	$Fe_{2.38}N$	1.26
	D2	0.26	0.48	0.17	23	ε-$Fe_{2+x}N$ Fe(II)	$Fe_{2.38}N$	
	D3	0.30	0.92	0.24	39	$FeO_{1-x}N_x$	$FeO_{0.35}N_{0.65}$	2.65

[a] δ − Isomer Shift, Δ − Quadrupole Splitting, Γ − Half-Width Full Max. Δ is given relative to metallic Fe at room temperature. Estimated precision on δ, Δ, and Γ is 0.02 mm s^{-1} and 2% on the site fraction. Site assignment for each spectral component is indicated.

our model (and their individual subspectra) have similar recoil-free fractions and the assumption of $f = 1$, for all of the Fe sites, is reasonable.

The lower weighting of Fe(II) sites to Fe(III) sites is consistent with findings for the ε-Fe_xN ($2 < x < 3$) system measured between 4.2 and 300 K.[44] The compositions of ε-$Fe_{2.47}N$ and ε-$Fe_{2.20}N$ have Fe(II) site fractions of 58 and 27%, respectively, which places our intermediate ε-$Fe_{2.38}N$ product with 45% Fe(II) sites satisfactorily within this region.

The remaining doublet D3 (blue line in Figure 5) is assigned to a paramagnetic iron oxynitride phase, which was identified in both XRD and SAED data, and implied by the relatively wide spectral envelope characteristic of oxynitrides with large quadrupole splitting. ^{57}Fe Mössbauer spectra have previously been reported for iron oxynitrides with additional contributions assigned to ε-$Fe_{2+x}N$ ($0 \leq x \leq 1$) or γ''-FeN suggesting the simultaneous formation and coexistence of these phases.[36,38,43] For iron oxynitride thin films, the relative contribution of the doublet to the total signal increased with increasing oxygen content, which was assigned to a composition $Fe_yO_{1-x}N_x$ with $y \approx 1$.[36,38] Increased measured oxygen content in the films was correlated to the observed increase in isomer shift values. The isomer shift values for the doublets we observed (ca. 0.29 mm s^{-1}) suggest an oxygen content of approximately 15 atom % equivalent to $FeO_{0.32}N_{0.38}$.

The singlet S1 (red line in Figure 5) was assigned to a binary nitride compound FeN_x, for which face-centered cubic γ'''-FeN (NaCl structure) and γ''-FeN (ZnS structure) were considered as candidate species. Previous reports indicate that these can coexist and both present a singlet in Mössbauer measurements. However, the distinction can be made by the values of isomer shift; the isomer shift for γ''-FeN is approximately 0.1 mm s^{-1}, while γ'''-FeN has an isomer shift of 0.6 mm s^{-1}.[52,53] This arises due to a different local geometry of the N environment. Our refined Mössbauer parameters are consistent with the γ''-FeN phase.[42,54,55]

Overall, the Mössbauer analysis confirms a phase assemblage for the reaction products of ε-$Fe_{2+x}N$ ($x \approx 0.38$), $FeO_{1-x}N_x$ ($0.65 \leq x \leq 0.80$), and γ''-FeN in a decreasing order of prevalence based upon refined site fractions. The identified phases are consistent with other characterization data presented here, similarly showing decreased total nitridation with increasing temperature and time. Estimated ε-$Fe_{2+x}N$ compositions of $x \approx 0.12$ were made from XRD data (see Table 1), in comparison to $x \approx 0.38$ implied from Mössbauer analysis, which are preferred as noted above. This corresponds to ε-$Fe_{2+x}N$ with estimated average formal Fe oxidation states in the range 1.43−1.26+.

We note that the analysis of the Mössbauer data may be complicated by the previously determined nanoparticle size. Nanoparticles can inhibit the presence of any ferromagnetic hyperfine splitting due to an absence of long-range magnetic order,[56] as would impurities within those particles. Our analysis also extrapolates findings reported for thin films to the nanoparticulate system evident in the data. Thus, our determination of relative phase fractions and inferred stoichiometries should be interpreted with due caution.

Figure 6 shows the TGA-MS analysis of the product obtained from reaction at 170 °C for 24 h obtained under flowing Ar. These data show two distinctive regions of weight loss. The first region, from 25 to 270 °C, corresponds to a weight loss of 2.5 wt %, which was dominated by the loss of H_2O, as evidenced by the MS signal corresponding to m/z = 18. The product therefore evidently retains both physisorbed water (lost below ca. 100 °C) and chemisorbed water (retained up to 270 °C). The second region, from 270 to 800 °C, corresponds to a further weight loss of 12.9 wt %, which was dominated by the loss of N_2, as evidenced by the

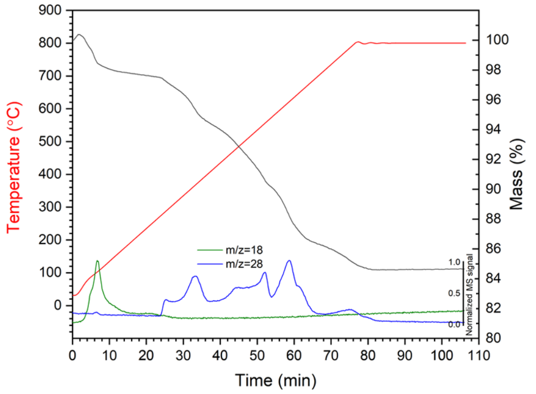

Figure 6. Thermogravimetry (TG, black) curve and mass spectrometry (MS) signals of 170 °C 24 h amide product (mass numbers 18 and 28 represent H_2O and N_2, respectively).

MS signal corresponding to $m/z = 28$. The material recovered after the TGA analysis was found to comprise $Fe_{1-x}O$ and Fe, indicating complete decomposition of the ε-$Fe_{2+x}N$ and $FeO_{1-x}N_x$ phases, with evolution of N_2 as evidenced by the MS data. Combined with the analysis of ^{57}Fe Mössbauer data, assuming the site fractions are directly proportional to the spectral area in determining the initial phase assemblage, the weight loss above 270 °C is attributed to the following (approximate) decomposition reaction

$$0.56\varepsilon\text{-}Fe_{2+x}N + 0.29FeO_{0.2}N_{0.8} + 0.14\gamma''\text{-}FeN \rightarrow (1.55 + 0.56x)Fe + 0.06FeO + 0.47N_2 \quad (1)$$

The expected weight loss for this reaction is between 11.8 wt % ($x = 0.38$, as implied from Mössbauer) and 12.6 wt % ($x = 0.12$, as implied from XRD). This is in reasonable agreement with the experimentally determined weight loss of 13.0 wt %, renormalized for loss of water below 270 °C, given the overall uncertainty in the precise stoichiometry of the component phases. TGA-MS data for the product obtained from reaction at 190 °C for 24 h, obtained under a flowing Ar, is shown in Figure S5 in the Supporting Information and exhibits two similar and distinctive weight loss events attributable to loss of water from 25 to 290 °C and loss of N_2 from 290 to 800 °C. A similar calculation estimated the expected weight loss to be between 11.4 wt % ($x = 0.38$) and 12.2 wt % ($x = 0.11$), which was again in reasonable agreement with the experimentally determined weight loss of 10.7 wt %, renormalized for loss of water.

The TGA-MS data of the product from reaction at 170 °C for 24 h exhibits a staged weight loss in the second region between 270 and 800 °C, with onset at approximately (1) 270 °C, (2) 325 °C, (3) 425 °C, (3) 600 °C, and (4) 725 °C. Considering these events in order, we first attribute the onset of weight loss at 270 °C to the decomposition of the oxynitride $FeO_{1-x}N_x$ phase to $Fe_{1-x}O$ (with the evolution of N_2). This is consistent with the reported synthesis conditions required for $FeO_{1-x}N_x$ oxynitrides, which were stabilized only in the thin film formed at low temperature, by magnetron sputtering with a substrate temperature estimated not to exceed 50 °C,[38] or by molecular beam epitaxy with a substrate temperature of 250 °C.[33,34] The weight loss at approximately 325 °C, associated with N_2 loss, is consistent with the decomposition mechanism for γ''-FeN described by Suzuki et al.[39] In the range of 320−340 °C, under vacuum, γ''-FeN was reported to decompose to ζ-Fe_2N and ε-$Fe_{2+x}N$ with the release of N_2. Decomposition of γ''-FeN was reported to be complete at 365 °C, yielding nearly single-phase ε-$Fe_{2+x}N$. Widenmeyer et al.[57] reported TGA analysis of the decomposition of a phase with composition ε-$Fe_{2.17}N$ under Ar. They established a two-stage mechanism of decomposition, which involves the onset of decomposition to γ'-$Fe_{4+x}N$ above 422 °C (with evolution of N_2) and subsequent onset of decomposition to α-Fe above 622 °C (again, with evolution of N_2), which is complete by 800 °C (these findings are also in general agreement with the findings of Suzuki et al.[39]). Neutron diffraction data has shown that this decomposition also involves the formation of austentite-type γ'-FeN_z (<10 atom % N), which is fully converted to α-Fe at 679 °C. Thus, we attribute the weight losses observed in our data at 425, 600, and 725 °C, each accompanied by loss of N_2 evidenced in the MS signal (Figure 6), to the sequential decomposition of ε-$Fe_{2+x}N \rightarrow \gamma'$-$Fe_{4+x}N \rightarrow \gamma'$-$FeN_z \rightarrow \alpha$-Fe, broadly consistent with the reported literature data for the thermal stability of these phases.

Low-temperature nitridation of metal oxides by reaction with $NaNH_2$ has proven an effective route to synthesis of InN (from $LiInO_2$[15]), ε-$Fe_{2+x}N$ (from Fe_3O_4 as shown here and Fe_2O_3[18]), Mn_6N_{5+x} (from Mn_2O_3[18]), and Cu_3N (from CuO).[13] Consideration of the thermodynamics of this reaction suggested that the driver is the high Gibbs free energy of NaOH combined with the extremely high local concentration of NH_2^-/NH_3 achieved in the melt (with excess $NaNH_2$).[18] NaOH is formed in a metathesis reaction between the iron oxide and sodium amide by exchange of oxide and nitride anions. The formation of NaOH then results in further dissolution of $NaNH_2$ and propagation of the metathesis and nitridation. The $NaNH_2$ reaction is evidently reducing in nature, as exemplified by the reaction of CuO with $NaNH_2$ to form Cu_3N at 170 °C/60 h, but resulting in the formation of Cu at 190 °C/60 h.[13] The more reduced nature of Fe_3O_4 therefore explains the exceptionally mild synthesis conditions required to yield ε-$Fe_{2+x}N$ by reaction with $NaNH_2$ (170 °C/24 h), compared to that of Fe_2O_3 (240 °C/36 h). Hence, the redox character of the metal oxide substrate is recognized and demonstrated to be an important consideration in optimizing the conditions for $NaNH_2$-mediated nitridation reactions. Furthermore, we achieved synthesis of ε-$Fe_{2+x}N$ by reaction between Fe_3O_4 and $NaNH_2$, evidently mediated in a molten salt, although the reaction temperature is below the melting point of pure $NaNH_2$ (210 °C). This suggests that trace water and NaOH byproduct play an important role in reducing the melting point in these reactions, consistent with the observations reported here, yielding a $NaNH_2$−NaOH molten salt with a melting point between 210 °C and 170 °C.[29] Our characterization data confirm the general understanding of a $NaNH_2$ molten salt-mediated dissolution−precipitation reaction, which results in the pseudomorphous replacement of the metal oxide substrate with a nanocrystalline product in a metathesis reaction, consistent with reports of similar reactions.[18] Similar solid-state metathesis reactions have yielded various binary, ternary, and quaternary nitrides, recent examples being Mn_3N_2[58] and $Zn_{1-x}Mn_xSiN_2$.[59] The reaction between Fe_3O_4 and $NaNH_2$ produced ε-$Fe_{2+x}N$ as the major product, but also a noncrystalline phase, as was also observed in the reaction with Fe_2O_3.[18] We successfully crystallized this phase to yield a face-centered iron oxynitride, $FeO_{1-x}N_x$ (and γ''-FeN), as verified using ^{57}Fe Mössbauer spectroscopy. The presence of such an oxynitride phase in the product of reaction between Fe_2O_3 and $NaNH_2$ was hypothesized by Miura et al., according to X-ray photoelectron spectroscopy data, which evidenced a material with an O-rich surface and N-rich interior. Miura et al. suggested that this phase was formed in the reaction workup by hydrolysis of the ε-$Fe_{2+x}N$ phase.[18] This hypothesis is in agreement with a recently published analysis of solution thermochemical data, showing that Fe_2N is stable in strongly alkaline and reducing conditions, otherwise decomposing to yield Fe_2O_3 or Fe_3O_4.[60] However, we cannot exclude the possibility that the $FeO_{1-x}N_x$ is formed, at least in part, by in situ reaction between ε-$Fe_{2+x}N$ and/or γ''-FeN with the NaOH byproduct. The presence of $FeO_{1-x}N_x$ from this synthesis in substantial yield may also prove exploitable for metastable oxynitride synthesis. Substantial data harvesting, application of informatics tools, and subsequent density functional theory analyses have identified many metastable nitrides that are attainable experimentally,[61−63] which the authors suggest is further applicable to oxynitrides.[62] These rely upon "remnant metastability", such that the nitride is synthesized in targeted thermodynamic conditions where it is stable and then kinetically retained when transitioned to metastable conditions,[61] which the pseudomorphic reaction with $NaNH_2$ in a sealed system and careful postreaction workup of the products may be able to achieve.

■ CONCLUSIONS

Reaction of Fe_3O_4 with excess $NaNH_2$ produced ε-$Fe_{2+x}N$ under exceptionally mild conditions of 170 °C for 24 h. The reaction takes place by pseudomorphous replacement of the reagent by the product, mediated by a $NaNH_2$−NaOH molten salt phase, involving dissolution of Fe_3O_4 and precipitation of nanocrystalline product. The recovered product contains an amorphous component, which was crystallized to yield an oxynitride, $FeO_{1-x}N_x$. ^{57}Fe Mössbauer spectra could be fitted with contributions of ε-$Fe_{2+x}N$, $FeO_{1-x}N_x$, and γ''-FeN in agreement with the observed phase assemblage. Interpretation of coupled thermogravimetric and mass spectroscopy data was consistent with this phase assemblage, with the observed mass loss attributed to N_2 in reasonable agreement with that expected based on the relative proportions of phases estimated from ^{57}Mössbauer spectroscopy and decomposition temperatures in reasonable agreement with available data for stepwise decomposition of ε-$Fe_{2+x}N$ to α-Fe. The yield of ε-$Fe_{2+x}N$ in the recovered product was 49−59 mol %, accompanied by 29−39 mol % $FeO_{1-x}N_x$, as determined from refined site fractions from ^{57}Mössbauer spectroscopy. It is not yet clear whether $FeO_{1-x}N_x$ is formed as a primary reaction product or by hydrolysis of ε-$Fe_{2+x}N$ in the reaction workup. Either way, this may pose a limitation to the synthesis of ε-$Fe_{2+x}N$, and other metal nitrides, if the objective is to produce a single-phase product with well-defined electrical, magnetic, or other physical property for applications. On the other hand, the reported $FeO_{1-x}N_x$ oxynitride phase identified in this study is an interesting outcome and opens the possibility for the synthesis of metastable oxynitride phases in high yield, by reaction of a metal oxide substrate with $NaNH_2$, with either careful control of H_2O concentration in the system or postsynthetic hydrolysis and crystallization.

■ ASSOCIATED CONTENT

SI Supporting Information

The Supporting Information is available free of charge at https://pubs.acs.org/doi/10.1021/acs.inorgchem.0c03452.

> ICSD data used for stoichiometry estimation (Table S1); calibration graph of ICSD data for stoichiometry estimation (Figure S1); SEM of 170 °C for 24 and 96 h products (Figure S2); EDX spectra for starting reagent and reaction products (Figure S3); integrated 1d line scans from electron diffraction data (Figure S4); and TGA data for 190 °C/24 h sample (Figure S5) (PDF)

■ AUTHOR INFORMATION

Corresponding Authors

Shi-Kuan Sun − *Department of Materials Science & Engineering, Sir Robert Hadfield Building, Immobilisation Science Laboratory, University of Sheffield, Sheffield S1 3JD, U.K.;* orcid.org/0000-0002-1688-5072; Email: shikuan.sun@sheffield.ac.uk

Neil C. Hyatt − *Department of Materials Science & Engineering, Sir Robert Hadfield Building, Immobilisation Science Laboratory, University of Sheffield, Sheffield S1 3JD, U.K.;* orcid.org/0000-0002-2491-3897; Email: n.c.hyatt@sheffield.ac.uk

Authors

Sarah E. O'Sullivan − *Department of Materials Science & Engineering, Sir Robert Hadfield Building, Immobilisation Science Laboratory, University of Sheffield, Sheffield S1 3JD, U.K.*

Sebastian M. Lawson − *Department of Materials Science & Engineering, Sir Robert Hadfield Building, Immobilisation Science Laboratory, University of Sheffield, Sheffield S1 3JD, U.K.;* orcid.org/0000-0003-4786-6947

Martin C. Stennett − *Department of Materials Science & Engineering, Sir Robert Hadfield Building, Immobilisation Science Laboratory, University of Sheffield, Sheffield S1 3JD, U.K.;* orcid.org/0000-0002-8363-9103

Feihong Chen − *Department of Materials Science & Engineering, Sir Robert Hadfield Building, Immobilisation Science Laboratory, University of Sheffield, Sheffield S1 3JD, U.K.*

Yuji Masubuchi − *Faculty of Engineering, Hokkaido University, Sapporo 060-8628, Japan;* orcid.org/0000-0003-3601-7077

Claire L. Corkhill − *Department of Materials Science & Engineering, Sir Robert Hadfield Building, Immobilisation Science Laboratory, University of Sheffield, Sheffield S1 3JD, U.K.;* orcid.org/0000-0002-7488-3219

Complete contact information is available at: https://pubs.acs.org/10.1021/acs.inorgchem.0c03452

Notes

The authors declare no competing financial interest.

■ ACKNOWLEDGMENTS

This research utilized the HADES/MIDAS facility at the University of Sheffield established with financial support from EPSRC and BEIS, under grant EP/T011424/1.[64] The authors are grateful for financial support from EPSRC under grant numbers EP/L015390/1 (S.E.O., N.C.H.), EP/S011935/1 (S.E.O., S.-K.S., N.C.H.), EP/S01019X/1 and EP/P013600/1 (S.-K.S., N.C.H.), and EP/N017374/1 (S.M.L., C.L.C.). The authors wish to acknowledge the Henry Royce Institute for Advanced Materials, funded through EPSRC grants EP/R00661X/1, EP/S019367/1, EP/P02470X/1, and EP/P025285/1, for JEOL JEM-F200 access at Royce@Sheffield. Y.M. is also supported partly by JSPS Grant-in-Aid for Scientific Research on Innovative Areas "Mixed anion" (Grant Number JP16H06439).

■ REFERENCES

(1) Bhattacharyya, S. Iron Nitride Family at Reduced Dimensions: A Review of Their Synthesis Protocols and Structural and Magnetic Properties. *J. Phys. Chem. A* **2015**, *119*, 1601−1622.

(2) Rasaki, S. A.; Zhang, B.; Anbalgam, K.; Thomas, T.; Yang, M. Synthesis and application of nano-structured metal nitrides and carbides: A review. *Prog. Solid State Chem.* **2018**, *50*, 1−15.

(3) Ebbinghaus, S. G.; Abicht, H.-P.; Dronskowski, R.; Müller, T.; Reller, A.; Weidenkaff, A. Perovskite related oxynitrides recent developments in synthesis, characterisation and investigations of physical properties. *Prog. Solid State Chem.* **2009**, *37*, 173−205.

(4) Miura, A. Low-temperature synthesis and rational design of nitrides and oxynitrides for novel functional material development. *J. Ceram. Soc. Jpn.* **2017**, *125*, 552−558.

(5) Giordano, C.; Erpen, C.; Yao, W.; Milke, B.; Antonietti, M. Metal nitride and metal carbide nanoparticles by a soft urea pathway. *Chem. Mater.* **2009**, *21*, 5136−5144.

(6) Gao, Z.; Wan, Y.; Xiong, G.; Guo, R.; Luo, H. Synthesis of aluminum nitride nanoparticles by a facile urea glass route and influence of urea/metal molar ratio. *Appl. Surf. Sci.* **2013**, *280*, 42−49.

(7) Masubuchi, Y.; Tadaki, M.; Kikkawa, S. Synthesis of the perovskite $SrTaO_2N$ using C_3N_4 for both reduction and nitridation. *Chem. Lett.* **2018**, *47*, 31−33.

(8) Zhao, H.; Lei, M.; Chen, X.; Tang, W. Facile route to metal nitrides through melamine and metal oxides. *J. Mater. Chem.* **2006**, *16*, 4407−4412.

(9) Feng, X.; Bai, Y.-J.; Lu, B.; Wang, C.-G.; Qi, Y.-X.; Liu, Y.-X.; Geng, G.-L.; Li, L. Low Temperature Induced Synthesis of TiN Nanocrystals. *Inorg. Chem.* **2004**, *43*, 3558−3560.

(10) Guo, Q.; Xie, Y.; Wang, X.; Lv, S.; Hou, T.; Bai, C. Synthesis of uniform titanium nitride nanocrystalline powders via a reduction−hydrogenation−dehydrogenation−nitridation route. *J. Am. Ceram. Soc.* **2005**, *88*, 249−251.

(11) Huang, Y.; Gu, Y.; Zheng, M.; Xu, Z.; Zeng, W.; Liu, Y. Synthesis of nanocrystalline titanium nitride by reacting titanium dioxide with sodium amide. *Mater. Lett.* **2007**, *61*, 1056−1059.

(12) Chen, L.; Gu, Y.; Shi, L.; Yang, Z.; Ma, J.; Qian, Y. A room-temperature synthesis of nanocrystalline vanadium nitride. *Solid State Commun.* **2004**, *132*, 343−346.

(13) Miura, A.; Takei, T.; Kumada, N. Synthesis of Cu_3N from CuO and $NaNH_2$. *J. Asian Ceram. Soc.* **2014**, *2*, 326−328.

(14) Barick, B.; Dhar, S. Surface and bulk electronic properties of low temperature synthesized InN microcrystals. *J. Cryst. Growth* **2015**, *416*, 154−158.

(15) Miura, A.; Takei, T.; Kumada, N. Synthesis of Wurtzite-Type InN Crystals by Low Temperature Nitridation of $LiInO_2$ Using NaNH2 Flux. *Cryst. Growth Des.* **2012**, *12*, 4545−4547.

(16) Chen, L.; Huang, T.; Qian, Y.; Zhu, L.; Gu, Y. Nitridation of Silica to an α-Silicon Nitride Nanorod Using $NaNH_2$ in the Autoclave at 700C. *J. Am. Ceram. Soc.* **2007**, *90*, 1243−1245.

(17) Chen, L.; Gu, Y.; Shi, L.; Yang, Z.; Ma, J.; Qian, Y. A room-temperature approach to boron nitride hollow spheres. *Solid State Commun.* **2004**, *130*, 537−540.

(18) Miura, A.; Takei, T.; Kumada, N. Low-Temperature Nitridation of Manganese and Iron Oxides Using $NaNH_2$ Molten Salt. *Inorg. Chem.* **2013**, *52*, 11787−11791.

(19) Laassiri, S.; Zeinalipour-Yazdi, C. D.; Catlow, C. R. A.; Hargreaves, J. S. The potential of manganese nitride based materials as nitrogen transfer reagents for nitrogen chemical looping. *Appl. Catal., B* **2018**, *223*, 60−66.

(20) Chang, F.; Guo, J.; Wu, G.; Wang, P.; Yu, P.; Chen, P. Influence of alkali metal amides on the catalytic activity of manganese nitride for ammonia decomposition. *Catal. Today* **2017**, *286*, 141−146.

(21) Clark, D. E. Peroxides and peroxide-forming compounds. *Chem. Health Safety* **2001**, *8*, 12−22.

(22) Lagarec, K.; Rancourt, D. G. *Recoil—Mössbauer spectral analysis software for Windows, tech. rep.*; Department of Physics, University of Ottawa: Ottawa, ON, Canada, 1998.

(23) Schneider, C.; Rasband, W.; Eliceiri, K. NIH Image to ImageJ: 25 years of image analysis. *Nat. Methods* **2012**, *9*, 671−675.

(24) Bergerhoff, G.; Brown, I. D. Inorganic Crystal Structure Database. *Acta Crystallogr., Sect. A: Found. Crystallogr.* **1981**, *37*, C342.

(25) du Marchie van Voorthuysen, E. H.; Boerma, D. O.; Chechenin, N. Low-temperature extension of the Lehrer diagram and the iron-nitrogen phase diagram. *Metall. Mater. Trans. A* **2002**, *33*, 2593−2598.

(26) Jacobs, H.; Rechenbach, D.; Zachwieja, U. Structure determination of γ'-Fe_4N and ε-Fe_3N. *J. Alloys Compd.* **1995**, *227*, 10−17.

(27) Leineweber, A.; Jacobs, H.; Hüning, F.; Lueken, H.; Kockelmann, W. Nitrogen ordering and ferromagnetic properties of ε-Fe_3N_{1+x} $(0.106 \leq x \leq 60.39)$ and ε-$Fe_3(N_{0.80}C_{0.20})_{1.38}$. *J. Alloys Compd.* **2001**, *316*, 21−38.

(28) Jack, K. H. Binary and Ternary Interstitial Alloys. I. The Iron-Nitrogen System: The Structures of Fe_4N and Fe_2N. *Proc. R. Soc. London, Ser. A* **1948**, *195*, 34−40.

(29) Jepsen, L. H.; Wang, P.; Wu, G.; Xiong, Z.; Besenbacher, F.; Chen, P.; Jensen, T. R. Thermal decomposition of sodium amide, $NaNH_2$, and sodium amide hydroxide composites, $NaNH_2$−NaOH. *Phys. Chem. Chem. Phys.* **2016**, *18*, 25257−25264.

(30) Willis, B. T. M.; Rooksby, H. P. Change of structure of ferrous oxide at low temperature. *Acta Crystallogr.* **1953**, *6*, 827−831.

(31) Yamamoto, A. Modulated structure of wustite ($Fe_{1-x}O$) (three-dimensional modulation). *Acta Crystallogr., Sect. B: Struct. Sci.* **1982**, *38*, 1451−1456.

(32) Jette, E. R.; Foote, F. An X-Ray Study of the Wüstite (FeO) Solid Solutions. *J. Chem. Phys.* **1933**, *1*, 29−36.

(33) Voogt, F. C.; Hibma, T.; Smulders, P.; Iesen, L.; Fujii, T. MBE-Growth of Iron and Iron Oxide Thin Films on MgO(100), Using NO_2, NO, and N_2O as Oxidising Agents. *MRS Proc.* **1997**, *474*, 211−216.

(34) Smulders, P.; Wijnja, G.; Niesen, L.; Fujii, T.; Voogt, F. C.; Smulders, P. J. M.; Wijnja, G. H.; James, M. A.; Hibma, T. NO_2-assisted molecular-beam epitaxy of wustite like and magnetite like Fe oxynitride films on MgO(100). *Phys. Revi.* **2001**, *63*, No. 125409.

(35) Petitjean, C.; Grafouté, M.; Pierson, J. F.; Rousselot, C.; Banakh, O. Structural, optical and electrical properties of reactively sputtered iron oxynitride films. *J. Phys. D: Appl. Phys.* **2006**, *39*, 1894−1898.

(36) Grafouté, M.; Petitjean, C.; Rousselot, C.; Pierson, J.; Grenèche, J. Chemical environment of iron atoms in iron oxynitride films synthesized by reactive magnetron sputtering. *Scr. Mater.* **2007**, *56*, 153−156.

(37) Petitjean, C.; Grafouté, M.; Rousselot, C.; Pierson, J. F. Reactive gas pulsing process: A method to extend the composition range in sputtered iron oxynitride films. *Surf. Coat. Technol.* **2008**, *202*, 4825−4829.

(38) Grafouté, M.; Petitjean, C.; Diama, A.; Pierson, J.; Greneche, J.; Rousselot, C. Structural investigations of iron oxynitride multilayered films obtained by reactive gas pulsing process. *Surf. Coat. Technol.* **2015**, *272*, 158−164.

(39) Suzuki, K.; Morita, H.; Kaneko, T.; Yoshida, H.; Fujimori, H. Crystal structure and magnetic properties of the compound FeN. *J. Alloys Compd.* **1993**, *201*, 11−16.

(40) Walter, C.; Menezes, P. W.; Orthmann, S.; Schuch, J.; Connor, P.; Kaiser, B.; Lerch, M.; Driess, M. A Molecular Approach to Manganese Nitride Acting as a High Performance Electrocatalyst in the Oxygen Evolution Reaction. *Angew. Chem., Int. Ed.* **2018**, *57*, 698−702.

(41) Schaaf, P.; Illgner, C.; Niederdrenk, M.; Lieb, K. Characterization of laser-nitrided iron and sputtered iron nitride films. *Hyperfine Interact.* **1995**, *95*, 199−225.

(42) Prieto, P.; Marco, J. F.; Sanz, J. M. Synthesis and characterization of iron nitrides. An XRD, Mössbauer, RBS and XPS characterization. *Surf. Interface Anal.* **2008**, *40*, 781−785.

(43) Borsa, D.; Boerma, D. Phase identification of iron nitrides and iron oxy-nitrides with Mössbauer spectroscopy. *Hyperfine Interact.* **2003**, *151/152*, 31−48.

(44) Chen, G.; Jaggl, N.; Butt, J.; Yeh, E.; Schwartz, L. Mössbauer and magnetic studies of ε-Fe_xN, $2 < x < 3$. *J. Phys. Chem. A* **1983**, *87*, 5326−5332.

(45) Schaaf, P. Laser nitriding of metals. *Prog. Mater. Sci.* **2002**, *47*, 1−161.

(46) Qaim, S. M. Recoil-free fractions of the 14.4 keV Mössbauer gamma line of ^{57}Fe in various host lattice. *J. Phys. F: Met. Phys.* **1971**, *1*, 320−327.

(47) Kurian, S.; Gajbhiye, N. S. Magnetic and Mössbauer study of ε-Fe_yN ($2 < y < 3$) nanoparticles. *J. Nanopart. Res.* **2010**, *12*, 1197−1209.

(48) Litasov, K. D.; Shatskiy, A.; Ponomarev, D. S.; Gavryushkin, P. N. Equations of state of iron nitrides ε-Fe_3N_x and γ-Fe_4N_y to 30 GPa and 1200 K and implications for nitrogen in the Earth's core. *J. Geophys. Res.:Solid Earth* **2017**, *122*, 3574−3584.

(49) Oda, K.; Umezu, K.; Ino, H. Interaction and arrangement of nitrogen atoms in FCC γ-iron. *J. Phys.: Condens. Matter* **1990**, *2*, 10147−10158.

(50) Imbihl, R.; Behm, R. J.; Ertl, G.; Moritz, W. The structure of atomic nitrogen absorbed on Fe(100). *Surf. Sci.* **1982**, *123*, 129−140.

(51) Fisher, R. A.; Campbell, A. J.; Shofner, G. A.; Lord, O. T.; Dera, P.; Prakapenka, V. B. Equation of state and phase diagram of FeO. *Earth Planet. Sci. Lett.* **2011**, *304*, 496−502.

(52) Rissanen, L.; Neubauer, M.; Lieb, K.; Schaaf, P. The new cubic iron-nitride phase FeN prepared by reactive magnetron sputtering. *J. Alloys Compd.* **1998**, *274*, 74−82.

(53) Rissanen, L.; Schaaf, P.; Neubauer, M.; Lieb, K.-P.; Keinonen, J.; Sajavaara, T. The production of the new cubic FeN phase by reactive magnetron sputtering. *Appl. Surf. Sci.* **1999**, *138−139*, 261−265.

(54) Frątczak, E. Z.; Prieto, J.; Moneta, M. Magnetic study of α'' and γ''-phases of iron nitride thin films. *Acta Phys. Pol., A* **2014**, *126*, 214−215.

(55) Hinomura, T.; Nasu, S. A study of Fe−N alloy systems. *Hyperfine Interact.* **1998**, *111*, 221−226.

(56) Murad, E. Mössbauer spectroscopy of clays, soils and their mineral constituents. *Clay Miner.* **2010**, *45*, 413−430.

(57) Widenmeyer, M.; Hansen, T. C.; Meissner, E.; Niewa, R. Formation and Decomposition of Iron Nitrides Observed by in situ Powder Neutron Diffraction and Thermal Analysis. *Z. anorg. allg. Chem.* **2014**, *640*, 1265−1274.

(58) Rognerud, E. G.; Rom, C. L.; Todd, P. K.; Singstock, N. R.; Bartel, C. J.; Holder, A. M.; Neilson, J. R. Kinetically Controlled Low-Temperature Solid-State Metathesis of Manganese Nitride Mn_3N_2. *Chem. Mater.* **2019**, *31*, 7248−7254.

(59) Zeman, O. E. O.; von Rohr, F. O.; Neudert, L.; Schnick, W. Facile One-step Synthesis of $Zn_{1-x}Mn_xSiN_2$ Nitride Semiconductor Solid Solutions via Solid-state Metathesis Reaction. *Z. anorg. allg. Chem.* **2020**, *646*, 228−233.

(60) Matanovic, I.; Garzon, F. H. Assessing Stability of Transition Metal Nitrides in Aqueous Environments: The Case of Molybdenum, Iron, Vanadium and Nickel Nitride. *J. Electrochem. Soc.* **2020**, *167*, No. 046518.

(61) Sun, W.; Dacek, S. T.; Ong, S. P.; Hautier, G.; Jain, A.; Richards, W. D.; Gamst, A. C.; Persson, K. A.; Ceder, G. The thermodynamic scale of inorganic crystalline metastability. *Sci. Adv.* **2016**, *2*, No. e1600225.

(62) Sun, W.; Holder, A. M.; Orvañanos, B.; Arca, E.; Zakutayev, A.; Lany, S.; Ceder, G. Thermodynamic Routes to Novel Metastable Nitrogen-Rich Nitrides. *Chem. Mater.* **2017**, *29*, 6936−6946.

(63) Sun, W.; Bartel, C. J.; Arca, E.; Bauers, S. R.; Matthews, B.; Orvañanos, B.; Chen, B.-R.; Toney, M. F.; Schelhas, L. T.; Tumas, W.; Tate, J.; Zakutayev, A.; Lany, S.; Holder, A. M.; Ceder, G. A map of the inorganic ternary metal nitrides. *Nat. Mater.* **2019**, *18*, 732−739.

(64) Hyatt, N. C.; Corkhill, C. L.; Stennett, M. C.; Hand, R. J.; Gardner, L. J.; Thorpe, C. L. The HADES facility for high activity decommissioning engineering & science: part of the UK national nuclear user facility. *IOP Conf. Ser.: Mater. Sci. Eng.* **2020**, *818*, No. 012022.

https://dx.doi.org/10.1021/acs.inorgchem.0c03452
Inorg. Chem. 2021, 60, 2553−2562

Supporting information

Low temperature nitridation of Fe_3O_4 by reaction with $NaNH_2$

Sarah E. O'Sullivan[1], Shi-Kuan Sun[1], Sebastian M. Lawson[1], Martin C. Stennett[1], Feihong Chen[1], Yuji Masubuchi[2], Claire L. Corkhill[1], Neil C. Hyatt[1*].*

1. Immobilisation Science Laboratory, University of Sheffield, Department of Materials Science & Engineering, Sir Robert Hadfield Building, Mappin Street, Sheffield, S1 3JD, UK.
2. Faculty of Engineering, Hokkaido University, N13W8, Kita-ku, Sapporo, 060-8628, Japan

*Corresponding author e-mail: shikuan.sun@sheffield.ac.uk ; n.c.hyatt@sheffield.ac.uk

Collection Code	Space Group	Formula	Volume (Å^3)	Temperature (K)	Year	Quality Data	DOI
79982	$P6_322$	Fe_3N	84.24	298	1995	*	10.1016/0925-8388(95)01610-4
79983	$P6_322$	Fe_3N	83.71	295	1995	*	10.1016/0925-8388(95)01610-4
80930	$P6_322$	Fe_3N	83.63	293	1995	*	No DOI
93173	$P6_322$	$Fe_3N_{1.107}$	84.48	293	2001		10.1016/S0925-8388(00)01435-3
93174	$P6_322$	$Fe_3N_{1.239}$	85.69	293	2001		10.1016/S0925-8388(00)01435-3
93175	$P6_322$	$Fe_3N_{1.3}$	86.63	293	2001		10.1016/S0925-8388(00)01435-3
93176	$P6_322$	$Fe_3N_{1.33}$	87.05	293	2001		10.1016/S0925-8388(00)01435-3
93177	$P6_322$	$Fe_3N_{1.39}$	87.60	293	2001		10.1016/S0925-8388(00)01435-3
93183	$P6_322$	$Fe_3N_{1.1}$	84.49	293	2001		10.1016/S0925-8388(00)01435-3
93195	$P6_322$	$Fe_3N_{1.235}$	85.59	293	2001		10.1016/S0925-8388(00)01435-3
162698	$P6_322$	$Fe_3N_{1.2}$	84.77	293	2009		10.1021/cm802721k
163929	$P6_322$	$Fe_3N_{0.97}$	83.00	293	2009	*	10.1016/j.jallcom.2008.09.178
420214	$P6_322$	$Fe_3N_{1.47}$	88.39	293	2009	*	10.1002/ejic.200801222

Table S1: Cell volume and formula data for ε-$Fe_{2+x}N$ mined from the ICSD [28] and used to build the calibration and subsequent stoichiometry estimation shown in Figure S1. Note – quality data highlights with an asterisk data considered to be of highest quality by ICSD.

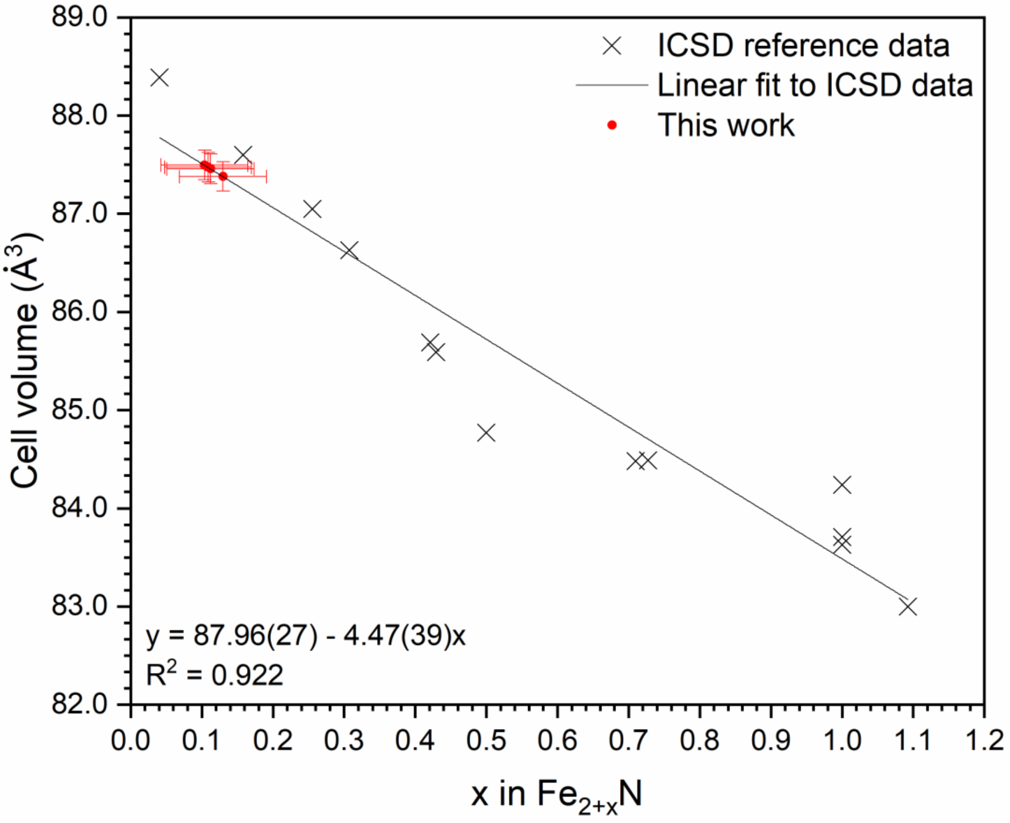

Figure S1: Dependence of unit cell volume on stoichiometry x in ε-$Fe_{2+x}N$ assuming a linear dependence. Black crosses indicate data for $P6_322$ ε-$Fe_{2+x}N$ data sourced from the ICSD (Table S1), normalised to the $Fe_{2+x}N$ composition. The applied linear fit was then used to calculate the estimated x values for the data points in this work shown in red.

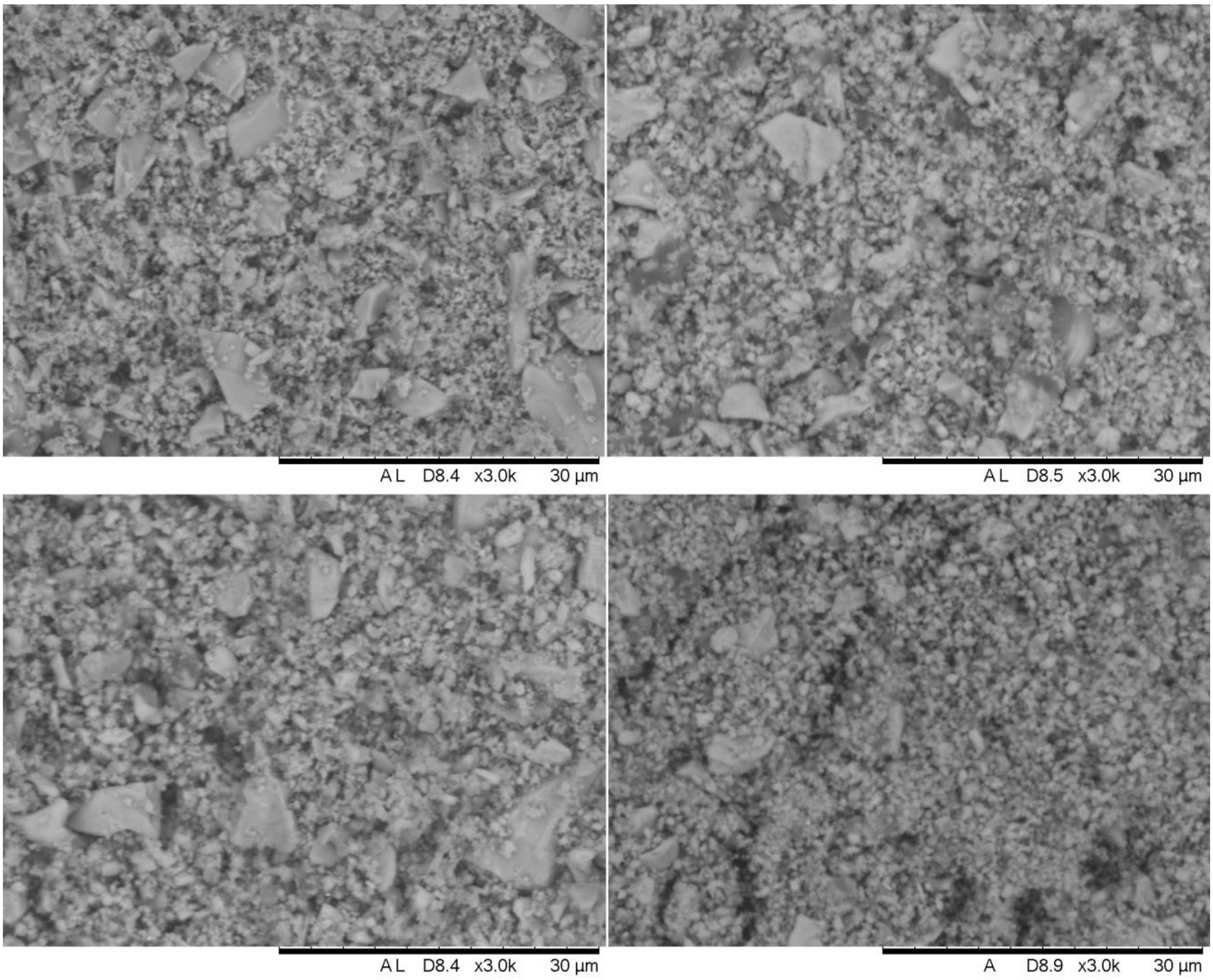

Figure S2: SEM images of raw and Fe_3O_4 powders reacted with $NaNH_2$ at 170 °C for 24, 48 and 96 h. Top row L-R: untreated Fe_3O_4, 24 h product. Bottom row L-R: 48 h product, 96 h product.

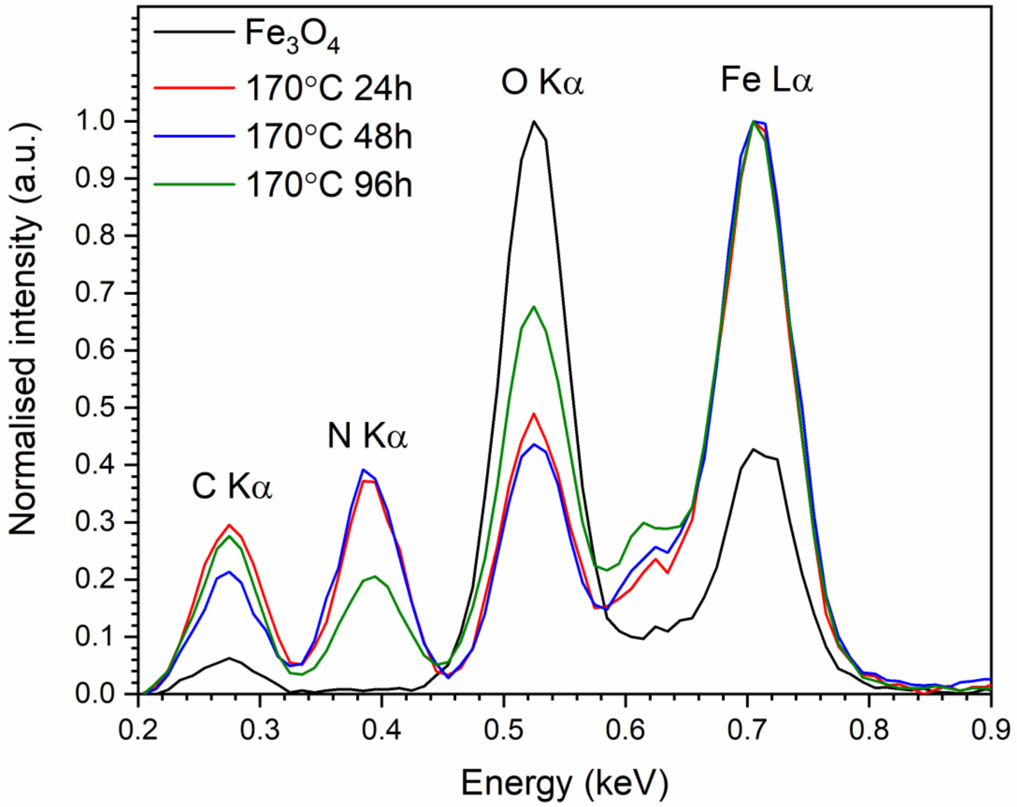

Figure S3: EDX spectra for starting Fe_3O_4 reagent (black) and products of amide reactions at 170 °C for 24/48/96 h (red/blue/green). Note the presence of N K*α* transitions only in the reaction products. C K*α* is attributed to the adhesive tab used for securing the powder during SEM measurement.

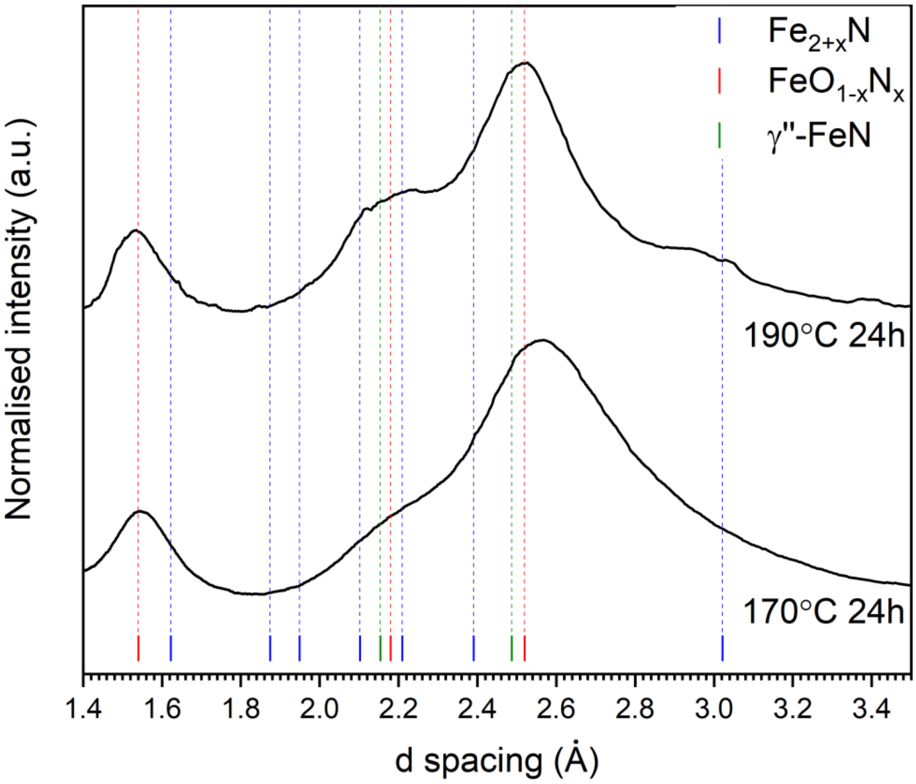

Figure S4: d spacing data integrated from electron diffraction linescans for (bottom) 170 °C 24 h and (top) 190 °C 24 h samples. Indexed are allowed reflections for ε-Fe$_{2+x}$N (blue), FeO$_{1-x}$N$_x$ (red) and γ´´-FeN (green) confirming the findings from recrystallisation data of the presence of the oxynitride and nitride phases.

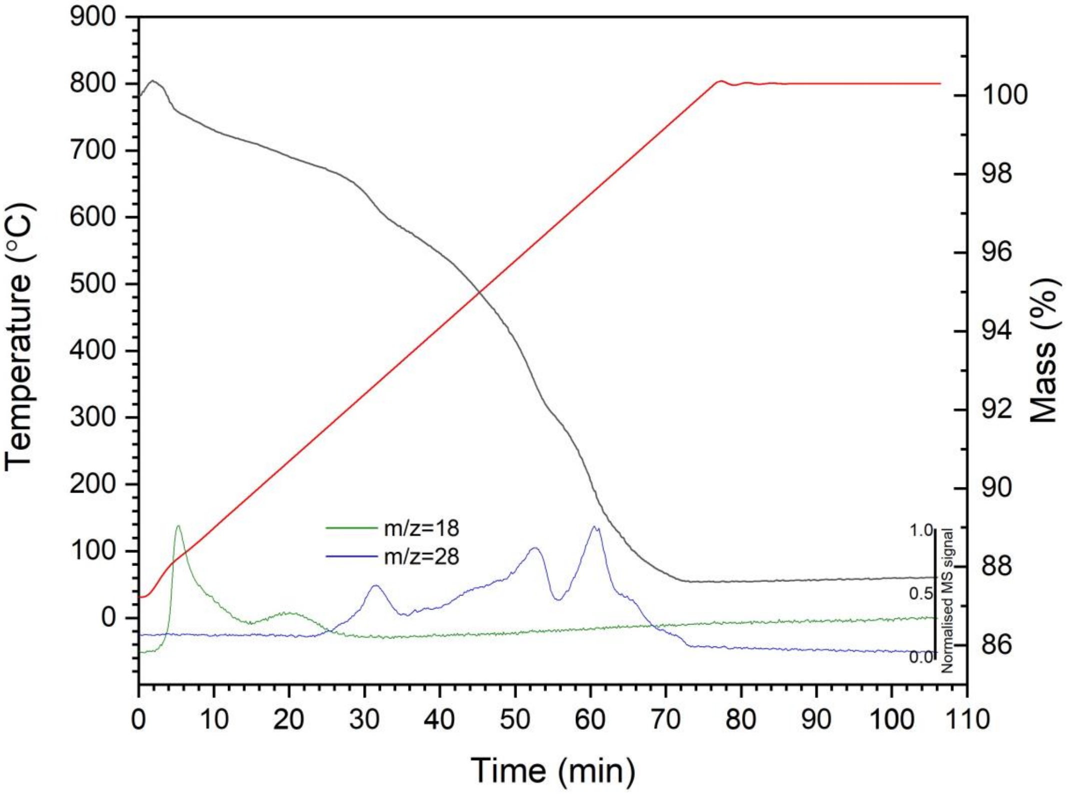

Figure S5: Thermogravimetry (TG, black) curve and mass spectrometry (MS) signals of 190 °C 24 h product (mass numbers 18 and 28 represent H_2O and N_2).

Chapter 6

Investigation of reactions of sodium amide with uranium oxides as a route to the synthesis of uranium nitrides

Investigation of reactions of sodium amide with uranium oxides as a route to the synthesis of uranium nitrides

Sarah E. O'Sullivan[1], Shi-Kuan Sun[1], Claire L. Corkhill[1], Ben F. Spencer[2], James Buckley[3], Martin C. Stennett[1], Neil C. Hyatt[1]*

[1] *Immobilisation Science Laboratory, Department of Materials Science and Engineering, The University of Sheffield, Mappin Street, Sheffield, S1 3JD, UK.*

[2] *Sir Henry Royce Institute, Department of Materials, School of Natural Sciences, The University of Manchester, Manchester M13 9PL, UK.*

[3] *Nuclear Fuel Centre of Excellence, Department of Mechanical, Aerospace and Civil Engineering, The University of Manchester, Sackville Street, Manchester, M13 9PL, UK.*

6.1 Abstract

Reactions of UO_2, U_3O_8 and UO_3 with $NaNH_2$ molten salt were investigated with the intention of novel soft chemical synthesis of uranium (oxy)nitrides. Reaction of UO_{2+x} with $NaNH_2$ afforded stoichiometric $UO_{2.00}$ at a remarkably low reaction temperature of 200°C, with trace $Na_2U_2O_7$ and $Na_4(UO_2)_2(CO_3)_3$ secondary phases. Reactions of U_3O_8 with $NaNH_2$ afforded poorly crystalline perovskite $NaUO_3$, with Na_2UO_4 and $Na_2U_2O_7$, whereas reaction of UO_3 with $NaNH_2$ produced $Na_2U_2O_7$. The phase assemblage was determined to be dependent on the ratio of uranium oxide to $NaNH_2$, reaction time and temperature. The formation of uranyl compounds implies some dissolution of the uranium oxide into the molten salt and precipitation of uranyl phases.

6.2 Introduction

A variety of uranium, plutonium and minor actinide mononitrides are proposed as nuclear fuel options for both new Gen IV reactors, with uranium mononitride also proposed for existing LWR reactors. UN has a higher thermal conductivity and melting temperature compared to traditional UO_2 fuel and thus has increased accident tolerance in the event of loss of coolant accidents [1–3]. In addition to this improved safety case consideration, the higher fissile density of UN allows for either reduced enrichment levels and thus lower fissile inventory for safeguarding purposes or higher burn up [4]. The neutronic properties of UN also allows for a longer period of reactor use, increasing from 18 to 25 months, assuming a burn up of 50 GWd/tU [4][5]. This confers economic and logistical benefits associated with decreased reactor downtime for refuelling. Ceramic UN is additionally compatible with existing cladding options and due to the high solubility in nitric acid, can be reprocessed *via* the established PUREX process. However, the synthesis of UN can be challenging. Investigations of the hydrolysis reactions of UN and U_2N_{3+x} in high temperature steam, in the context of a loss of coolant accident, generally evidenced the formation of UO_2 [6–9]. However, complete evolution of the nitrogen inventory in these UN hydrolysis reactions, and also oxidation of UN, was not conclusively established and, therefore, the formation of oxynitrides "UO_2N_x" and "UO_3N_x" were hypothesised to account for the apparently retained N [6–9]. However, only one study established significant N retention in the product of UN hydrolysis using direct chemical methods [8], although the determination of 1.1 wt% N in the UO_2 product is broadly consistent with earlier investigation using indirect mass or pressure determinations [6, 7]. These studies suggest that such oxynitrides may be important intermediates in the hydrolysis of UN fuels in conditions of a loss of coolant accident, wet storage, or geological disposal. However, such uranium oxynitrides have, hitherto, not been synthesised and their existence remains an open question.

Typical uranium nitride synthesis, forming mononitride UN, dinitride UN_2 and sesquinitride U_2N_3, utilises gaseous reactions of N_2 or NH_3 on uranium metal [10–14] (*via* uranium hydride) or fluoride precursors [15][16] in the range of 300 to 900 °C. UN may also be produced from UC by reaction with NH_3 gas at 900 °C [17][18]. Reaction of UO_2 with NH_3 to yield UN requires higher processing temperatures of 1400-1600 °C along with a carbon reducing agent [16][17], the ratio of carbon to uranium being tailored to the reaction temperature to optimise nitride purity. Common to all these reactions are multiple phases reliant upon gaseous diffusion into a powder precursor, often requiring large volumes of chemotoxic NH_3 gas.

Several recent studies have investigated the use of sodium amide, $NaNH_2$, as a solid state reductant and nitriding agent to avoid the need for NH_3 gas and lower process temperatures for the synthesis of metal nitrides and oxynitrides. In a typical procedure a metal oxide reacts with $NaNH_2$ in sealed pressure vessels in the range of 170 to 300 °C [21, 22, 31, 23–30], to yield a counterpart metal nitride and/or oxynitride. The lower temperature limits particle growth, maximising surface area for enhanced substitution of N for O which occurs in a pseudomorphous reaction. The reactions are understood to be mediated by a $NaNH_2$-NaOH molten salt, the dissolution of $NaNH_2$ into NaOH beginning at 100 °C [32]. As the thermodynamic driver for nitridation in these reactions is the production of NaOH, an excess of $NaNH_2$ is generally employed [27]. At the melting temperature of 200 °C, $NaNH_2$ decomposition yields nascent NH_3 gas at a rate of 0.36 mol NH_3 per mol $NaNH_2$, with greater yield of NH_3 when increasing the proportion of NaOH in the molten salt [32]. Additionally, the effective concentration of NH_2 in molten $NaNH_2$ was found to be circa 500 times greater than the concentration of NH_3 in commercially available gases [33], making molten $NaNH_2$ a potentially more potent nitriding agent. Thus, our interest was drawn to the potential reaction between uranium oxides and $NaNH_2$ as a possible route to the synthesis of uranium nitrides and hypothetical uranium oxynitrides.

The potential for uranium nitride synthesis by reaction between uranium oxides and $NaNH_2$ was explored with the Interface Reactions application hosted by the Materials Project [34] [35]. This tool uses the methodology of Richards *et al.* [34], to calculate the reaction energy of two reagents ($c_{A,B}$) at an interface, to yield the phase equilibrium (c_{eq}) determined from the phase diagram, according to the equation $xc_A + (1-x)c_B \rightarrow c_{eq}$ (where $0 \leq x \leq 1$, is a mixing parameter representing the mole fraction of reagents). For closed systems, the reaction energy of reagents A and B is given by:

$$\Delta E[A, B, x] = E_{pd}[xc_A + (1 - x)c_B] - xEA - (1-x)E_B \tag{1}$$

Where $c_{A,B}$ are the normalised compositions (i.e. composition normalised to 1 atom) for reagents A and B, $E_{A,B}$ are the ground state energies and E_{pd} is the energy on the energy convex hull at composition c. In general, the convex hull corresponds to the set of ground state phases in the composition phase diagram. The lowest energy is achieved by a linear combination of these phases. The ground state energy of each phase is determined from Density Functional Theory, implemented in the Vienna Ab Initio Simulation Package (VASP) [36], using relaxed input structures from the Inorganic Crystal Structure Database (ICSD) [37]; full details are given by Jain *et al.* [38, 39]. In our assessment we assumed a closed system at 0 K and neglected the presence of NaOH. Since the interfacial reaction may in reality consume *arbitrary* amounts of either phase, all reaction products are *possible* phases that *could* be formed at the reaction interface. Therefore, in our application, this tool provides only a qualitative feasibility assessment of the potential to form uranium nitrides from reaction between $NaNH_2$ and UO_2, U_3O_8 or UO_3, the output of which given in Table S1. Likely products identified from the model included UN_2 and U_2N_{3+x} (U_4N_7), although not necessarily as the most thermodynamically favoured reaction. Other predicted products included a range of sodium uranium oxides ($NaUO_3$, Na_2UO_4, $Na_2U_2O_7$, Na_3UO_4 and Na_4UO_5) as well as NaH, NaN_3, NH_4OH, NH_3 and N_2. The potential for uranium nitride, and potentially oxynitride, synthesis indicated by the model predictions afforded a novel and worthwhile opportunity for investigation. Here we investigate reactions of UO_2, UO_3 and U_3O_8 with $NaNH_2$, varying UO_x:$NaNH_2$ ratio, as well as considering reaction temperature. As a counterpart, reactions of those same oxides with NH_3 and 5%H_2/N_2 were also explored as more typical nitridation and reduction methods, as discussed above. Although these endeavours did not yield the uranium nitride phases initially targeted, or uranium oxynitrides, the results nonetheless show the use of $NaNH_2$ allows for a novel low temperature method of reduction of UO_{2+x} to stoichiometric UO_2 and synthesis of $NaUO_3$ from U_3O_8.

6.3 Experimental

6.3.1 Reagents

Reagents with depleted uranium isotopic composition of UO_{2+x}, α-UO_3 and U_3O_8 were used in powder form. UO_{2+x} was used in the hyperstoichiometric state without other preparation. To prepare U_3O_8, ammonium diuranate (ADU) was precipitated from uranyl nitrate using addition of ammonium hydroxide. The precipitated ADU was then calcined in air at 750 °C for 8h to convert to U_3O_8. Crystalline α-UO_3 was prepared by mixture of uranyl nitrate with

15% hydrogen peroxide to yield metastudtite, $UO_4{\cdot}4H_2O$, which was subsequently calcined at 535 °C for 1h, according to the method of Thompson *et al.* [40].

6.3.1 Solid state reductions

Caution: $NaNH_2$ is a strong reducing agent and liberates ammonia on contact with water, explosive peroxides may form on atmospheric exposure; use of this reagent must be rigorously risk assessed, storage and handling under dry inert atmosphere is advised [41]. *Uranium is a radioactive a-emitter and poses a radiotoxic hazard. Exposure to, and ingestion and inhalation of, uranium materials must be prevented. Manipulations should be rigorously risk assessed and carried out with care in monitored fume hoods or gloveboxes in a suitable radiochemical laboratory, with appropriate personal protective equipment.*

Uranium oxides were mixed in 1:48, 1:24 or 1:12 molar ratio with $NaNH_2$ (Sigma Aldrich, 98%) and hand ground under a dry argon atmosphere for 5 minutes. Still under the argon atmosphere, the mixed powder was transferred to a 5 ml lidded 316 stainless steel crucible, which was placed into a PTFE lined stainless steel digestion vessel (45 ml, Parr model 4744). The sealed vessel was transferred to a temperature controlled oven (120, 140, 160, 180, 200 or 240 ± 1 °C) for the reaction duration (24, 48 or 72 hours). After cooling to room temperature, the vessel was opened in a fume hood, allowing for release of NH_3 gas from the head space (confirmed by moist universal indicator paper and NH_3 detector). Inspection of the crucible, post reaction, revealed a solid mass, often with a white upper layer of residual $NaNH_2$. The crucible was soaked in ethanol to destroy the residual $NaNH_2$, by formation of sodium ethoxide, and release the product powder. The product was recovered *via* vacuum filtration of the ethanol solution, washed with further ethanol.

6.3.3 Gas phase reductions

Gas phase reductions were performed on samples of approximately 0.1 g, distributed evenly within a 6 cm long alumina crucible. Reductions were performed in an Elite tube furnace with alumina process tube. An initial Ar purge gas (BOC, 99.98%) was applied to evacuate the tube of oxygen, followed by either NH_3 (BOC, 99.98%) or 5%H_2/N_2 (BOC) for the duration of the reaction, controlled by flowmeter. Preliminary investigations (not presented) ascertained an optimal reaction protocol at 1100 °C for 2 to 16 hours. After cooling, the reaction gas was exchanged for an Ar purge to eliminate any remaining NH_3 before recovery of the product.

6.3.4 Characterisation

Product materials were initially characterised by powder X-ray diffraction (XRD) performed on a Bruker D2 Phaser diffractometer with Cu Kα radiation of $\lambda = 1.541$ Å. Samples were ground in a pestle and mortar before transfer to a sample holder. UO_{2+x} samples were pressed into a 3 mm diameter well in an Si flat plate, low background, sample holder. UO_3 and U_3O_8 samples were pressed into a 10 mm diameter well of a similar low background holder. Containment of the large powder volume was achieved by adhesion of a STOE brand transmission measurement acetate disc. An additional 10 wt% LaB_6 was added as an internal standard for measurements prior to Rietveld analysis, which was performed using TOPAS [42]. Scanning Electron Microscopy (SEM) was first performed on powder samples pressed onto carbon adhesive tabs first on a Hitachi TM3030 with 15 kV operating voltage using Bruker Quantax 70 Energy Dispersive X-ray (EDX) software [43] and subsequently on an FEI Inspect F50 FEG SEM operating at 10 kV. Colour analysis of the samples was performed on digital photographic images taken with a Canon 4000D camera with 18 mm lens and calibrated to a grey card of (R,G,B) (128,128,128). The pixels within such a digital image are composed of red (R), green (G) and blue (B) channels, each set at values between 0–255, formally reported as coordinates. The colour of a given pixel is determined by the contributions of the (R,G,B) components, for example, coordinate (R:0, G:0, B:0) is black and (R:255, G:255, B:255) is white. Development of this methodology is detailed elsewhere [44]. X-ray photoelectron spectroscopy (XPS) was performed using an ESCA2SR spectrometer (ScientaOmicron GmbH) using monochromated Al Kα radiation (1486.6 eV, 20 mA emission at 300 W, 1 mm spot size) with a base vacuum pressure of circa 1×10^{-9} mbar. Charge neutralisation was achieved using a low energy electron flood source (FS40A, PreVac). Binding energy scale calibration was performed relative to the C 1s photoelectron peak at 285 eV. Analysis and curve fitting was performed using Voigt-approximation peaks using CasaXPS [45]. U L_3 X-ray Absorption Near Edge Spectroscopy (XANES) was performed at the Diamond Light Source B18 beamline. Samples were pressed into 6 mm

PEG pellets with the equivalent of 1 absorption length of uranium. Measurement was made in transmission mode around the U L_3 edge at 17166 eV, with data analysis performed in the ATHENA program [46].

6.4 Results and discussion

6.4.1 UO_{2+x}

UO_{2+x} was reacted with $NaNH_2$ in 1:12, 1:24 and 1:48 molar ratios for 24h at 200 °C, with an additional 1:48 experiment for 72h. Inspection of the recovered powder displayed a range of colours, shown in Figure 1 and detailed in Table 1, that are reminiscent of those observed for hydrothermally altered natural uraninites, i.e. *gummites*, which are a complex assemblage of uranium phases, varying from tan brown, through orange, to yellow in appearance [47]. Untreated UO_{2+x} powder displayed the typical black colour with (R,G,B) (27,24,19). The powder product of UO_{2+x} reaction with $NaNH_2$ in 1:12 ratio displayed a light brown shade of (R,G,B) (111,93,62), while the product of 1:48 ratio reacted for 72 hours yielded an orange powder of (R,G,B) (134,97,6). A similar orange powder product with (R,G,B) (163,105,12) was obtained for UO_{2+x} reacted under NH_3 gas, with this colour being localised to particulate surface apparent in Figure 1 (f). As the equivalent 5%H_2/N_2 reduction did not yield an orange product, combined with the surface effect for the NH_3 product due to the gaseous diffusion process of this reaction, it was hypothesised that the orange coloured products were a result of increased efficacy of the reduction for those products.

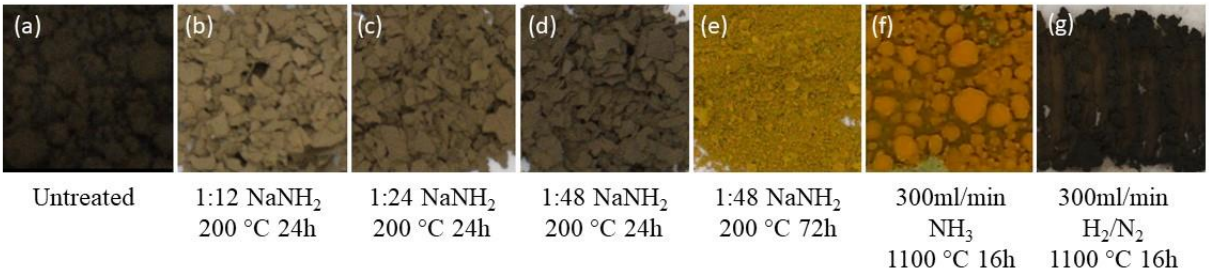

Figure 1. Colours of untreated UO_{2+x} reagent (a), products of reaction with $NaNH_2$ (b,c,d,e) and products of reaction with NH_3 (f) and H_2/N_2 (g). Note the intensity of the orange colour localised to the particulate surfaces compared to the darker bedded material for reaction of UO_2 with NH_3 (f). Images are calibrated to a grey card standard of (R,G,B) (128,128,128) [44].

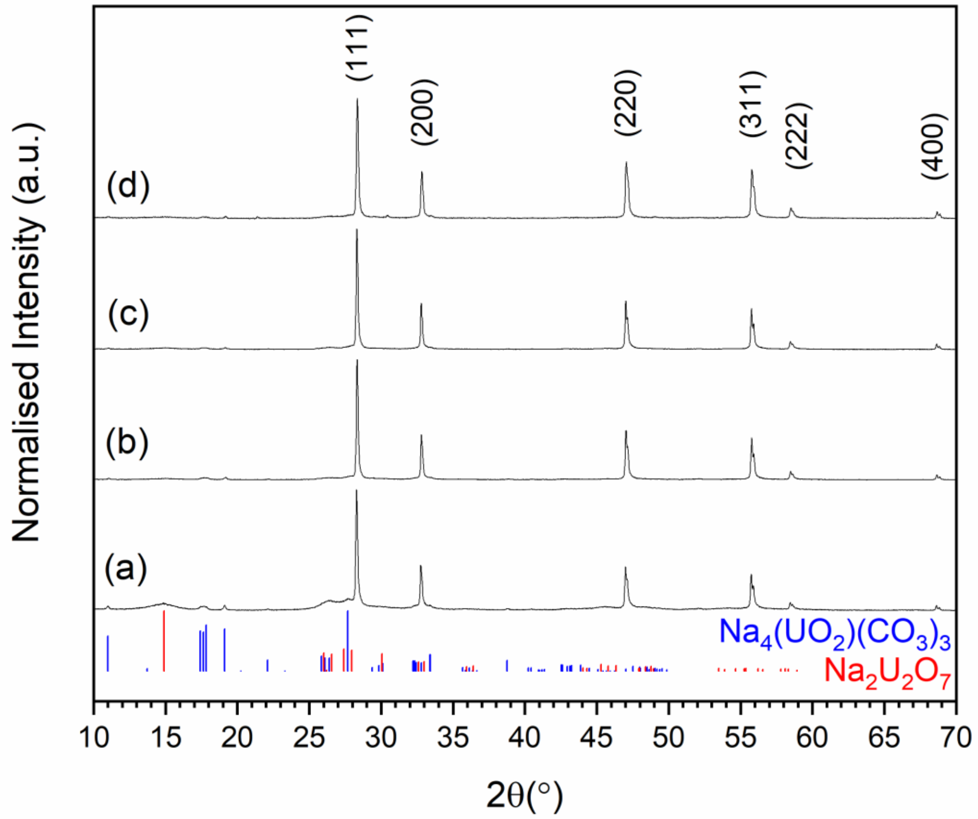

Figure 2. XRD patterns of products of UO_{2+x} reacted with $NaNH_2$ at 200 °C in (a) 1:12, (b) 1:24 and (c) 1:48 molar ratio for 24h and (d) 1:48 molar ratio 72h. UO_2 reflections are indexed. Red tickmarks indicate allowed reflections for $Na_2U_2O_7$ (PDF 01-083-5849). Blue tickmarks indicate allowed reflections for $Na_4(UO_2)_2(CO_3)_3$ (PDF 00-055-0721).

Phase analysis, by XRD, of products from reaction of UO_{2+x} with $NaNH_2$ (Figure 2), and NH_3 or 5%H_2/N_2 gas (Figure S1), showed UO_{2+x} as the primary phase. Unit cell parameters were determined from refinement of data sets containing a LaB_6 internal standard, with results presented in Table 1. In all products, the unit cell parameter was increased compared to the starting UO_{2+x} reagent. For the products of reaction with $NaNH_2$, the magnitude of the cell parameter increase was greater with increasing excess of $NaNH_2$ added, and with increased reaction time at a constant 1:48 UO_{2+x}:$NaNH_2$ ratio. For the products of reaction with NH_3 or 5%H_2/N_2 gas, the magnitude of the unit cell parameter increase was greater for the product from NH_3 annealing than from 5%H_2/N_2 annealing. Of the amide reaction products, the largest refined unit cell parameter of $a = 5.4714(1)$ Å was determined for the product of UO_{2+x} reaction in 1:48 UO_2:$NaNH_2$ ratio for 72h, which was in excellent

Reaction protocol	Phase analysis	Colour (R,G,B)	a (Å)	Estimated x in UO_{2+x}	Estimated stoichiometry
Untreated (Batch 1)	UO_{2+x}	(27,24,19)	5.4607(1)	0.044(4)	$UO_{2.044}$
1:12 $NaNH_2$ 200 °C 24h	UO_{2+x} $Na_2U_2O_7.3H_2O$	(111,93,62)	5.4614(2)	0.041(8)	$UO_{2.041}$
1:24 $NaNH_2$ 200 °C 24h	UO_{2+x} $Na_2U_2O_7.3H_2O$	(86,70,45)	5.4659(8)	0.022(4)	$UO_{2.022}$
1:48 $NaNH_2$ 200 °C 24h	UO_{2+x}	(70,56,38)	5.4679(6)	0.014(3)	$UO_{2.014}$
1:48 $NaNH_2$ 200 °C 72h	UO_{2+x}	(134,97,6)	5.4714(1)	0.000(4)	$UO_{2.000}$
Untreated (Batch 2)	UO_{2+x}	(27,24,19)	5.4691(1)	0.015(5)	$UO_{2.015}$
300ml/min H_2/N_2 1100 °C 16h	UO_{2+x}	(37,31,23)	5.4721(1)	0.003(3)	$UO_{2.003}$
300ml/min NH_3 1100 °C 16h	UO_{2+x}	(163,105,12)	5.4727(3)	0.000(1)	$UO_{2.000}$

Table 1 Refined unit cell parameters, colour analysis data and estimated stoichiometry for UO_{2+x} reactions with $NaNH_2$, NH_3 and H_2/N_2. 1 e.s.d. confidence intervals are given in parentheses.

agreement with that for stoichiometric $UO_{2.000 \pm 0.001}$ of a = 5.47127(8) Å [48]. The change in unit cell parameter of UO_{2+x}, following reaction with $NaNH_2$, NH_3 or 5%H_2/N_2, and subtle change in reflection profile asymmetry (see below), implied a reduction in hyperstoichiometry (x). The estimated hyperstoichiometry was determined using the linear calibration against absolute unit cell parameter developed by Elorrieta *et al.* [49]. The calibration line is shown in Figure 3, with the calculated values of x and the inferred stoichiometry given in Table 1. Note that the product of the reaction of UO_{2+x}:$NaNH_2$ in 1:48 ratio for 72h has a unit cell parameter which is not significantly different from that of stoichiometric $UO_{2.000}$ previously reported [48], which defines the intercept of the calibration line. For comparison, the products of reaction of UO_{2+x} with NH_3 and 5%H_2/N_2 are also plotted onto this calibration

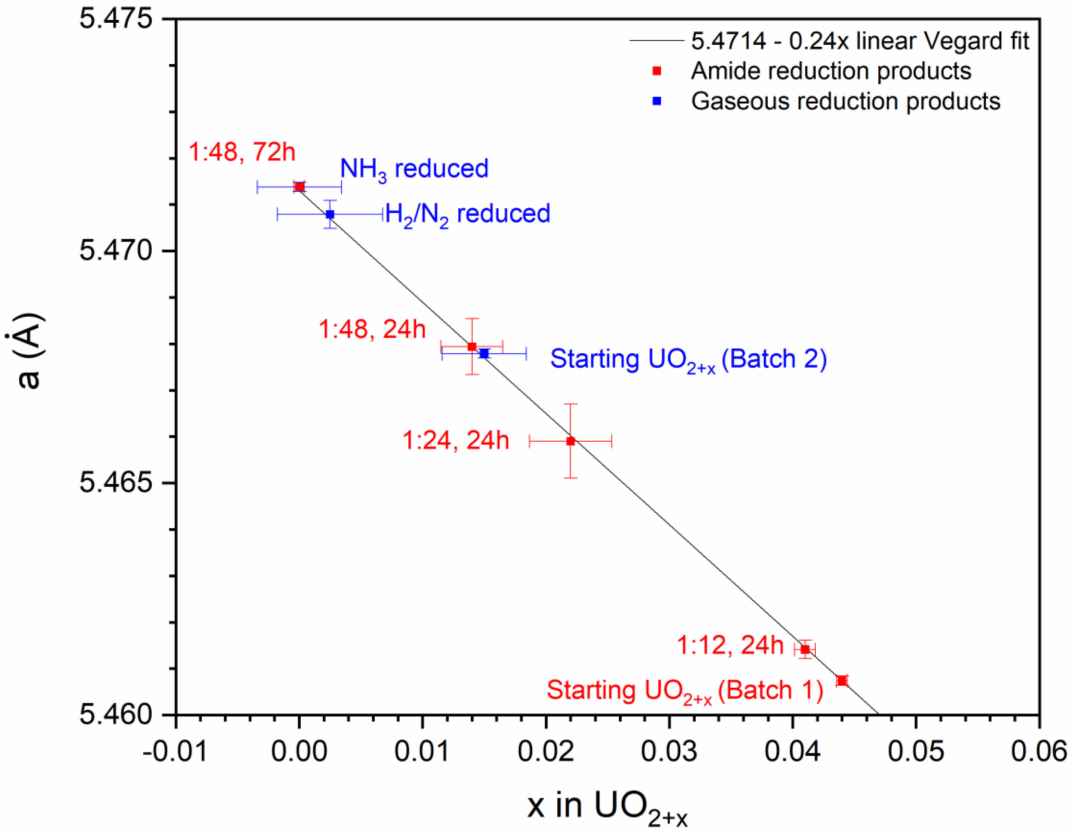

Figure 3. Estimated stoichiometry of reduced UO_{2+x} products assuming a linear dependence between x and unit cell parameter a, according to Elorrieta, *et al.* [49]. Products from reactions with $NaNH_2$ are shown in red, products from reaction with NH_3 and 5%H_2/N_2 in blue. See text for details.

line; it should be noted that these reactions utilised a different batch of UO_{2+x} (Batch 2), with slightly different hyperstoichiometry (x).

For reaction between UO_{2+x} and $NaNH_2$, hyperstoichiometry was reduced with increasing excess of $NaNH_2$ or longer reaction time at fixed 1:48 ratio of UO_{2+x}:$NaNH_2$, comparable to the reduction in hyperstoichiometry achieved by annealing under NH_3 and 5%H_2/N_2 gas. The reduction of hyperstoichiometric $UO_{2.044}$ to stoichiometric $UO_{2.000}$ under relatively mild conditions of 200 °C in $NaNH_2$-NaOH molten salt is remarkable. The mechanism of reduction is assumed to involve nascent NH_3 gas produced *in situ*, that extracts mobile hyperstoichiometric oxygen from UO_{2+x}, which is insoluble in the molten salt medium, to produce N_2 and H_2O, as in the gas phase reaction.

Inspection of XRD data also revealed a change in the reflection profiles of the UO_{2+x} phase post-reaction. The reflections profiles of the UO_{2+x} reagent showed notable high angle asymmetry, consistent with the presence of a gradient of oxygen hyperstoichiometry. The contribution of this reflection asymmetry was observed to decrease with increasing unit cell parameter, consistent with an overall reduction in hyperstoichiometry. Note that this asymmetry was not observed for reflections from the internal LaB_6 standard and therefore is not an instrumental aberration. Examples of reflections from the products and the internal standard are presented in Figure S2.

The XRD data of products from reaction of UO_{2+x} and $NaNH_2$ also evidenced weak and diffuse reflections of uranyl phases $Na_2U_2O_7$ (PDF 01-083-5849) [50] and $Na_4(UO_2)(CO_3)_3$ (PDF 00-055-0721) [51]; these reflections were most evident for the product of the 1:12 UO_{2+x}:$NaNH_2$ ratio. The relative intensity of these reflections was greatly reduced by regrinding of the product prior to measurement, suggesting the product is in fact a reduced UO_{2+x} core within a surface shell of uranyl phases. This implies that some hydrolysis of UO_{2+x} must also take place in the $NaNH_2$-NaOH molten salt, leading to dissolution and precipitation of secondary uranyl phases, incorporating adventitious carbonate (consistent with the behaviour of U(VI) in highly basic solutions [52]). This reaction is more significant for lower UO_{2+x}:$NaNH_2$ ratios because H_2O released from nascent NH_3 mediated reduction of UO_{2+x} will have effectively higher activity. Laboratory synthesis of uranyl carbonates utilises evaporation of solutions containing the relevant species under conditions that emulate those of mineral analogue formation [53] (in [54]). Both $Na_2U_2O_7$ and $Na_4(UO_2)(CO_3)_3$ are associated with a yellow colour typical of uranyl phases [54, 55], which may both contribute to the yellow-brown colour of the recovered UO_{2+x} product shown in Figure 1. SEM imaging with EDX spectra (Figure 4) and element mapping (Figure S3) confirmed the presence of Na in the products of UO_{2+x} reaction with $NaNH_2$ (and absence in the starting material) from detectable Na Kα emission, which was distributed across the product, with no obvious concentration, consistent with the formation of a shell of uranyl

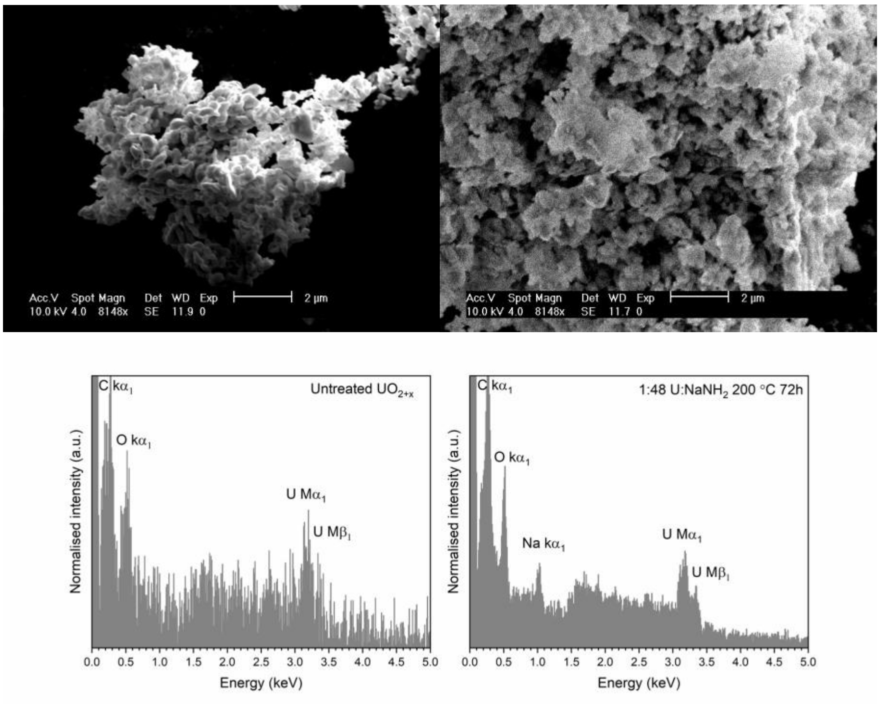

Figure 4. SEM images (top) and EDX spectra (bottom) for untreated UO_2 reagent (left) and UO_2 reacted in 1:48 molar ratio with $NaNH_2$ at 200 °C for 72h (right).

phases around a UO_{2+x} core. No evidence for N Kα emission was observed in EDX analyses, consistent with the absence of any uranium nitride product in XRD data. XPS measurements were performed to further understand the surface chemistry of the UO_{2+x} reagents and products from reaction with $NaNH_2$, NH_3 and $5\%H_2/N_2$, the results of which are presented in Figure 5 and Table 2. Relative to the UO_{2+x} reagent, the U $4f_{7/2}$ emission line is shifted to *higher* binding energy by 1.0 ± 0.1 eV for the products of reaction with $NaNH_2$, consistent with a more oxidised surface post-reaction. The U $4f_{7/2}$ binding energy for our UO_{2+x} reagents (381.0 eV) was slightly higher than that reported for the stoichiometric phase, in the range 379.9-380.4 eV [56], consistent with $x > 0$ and a gradient of hyperstoichiometry inferred from XRD data. The U $4f_{7/2}$ binding energy of the UO_{2+x} products following reaction with $NaNH_2$ (382.0 eV) was higher than that reported for $Na_2U_2O_7$ (380.8 eV) [57], but broadly consistent with that of reported uranyl phases, in particular $UO_2(OH)_2$ (382.3 eV) [56, 58, 59], which could plausibly be present at the surface, given the strongly basic conditions of synthesis and work up. The larger than anticipated FWHM values were attributed to the signal to noise quality of the data as addition of further components (implying secondary chemical environments) did not produce meaningful fits with satisfactory fitting statistics. In contrast, relative to the UO_{2+x} reagent, the U $4f_{7/2}$

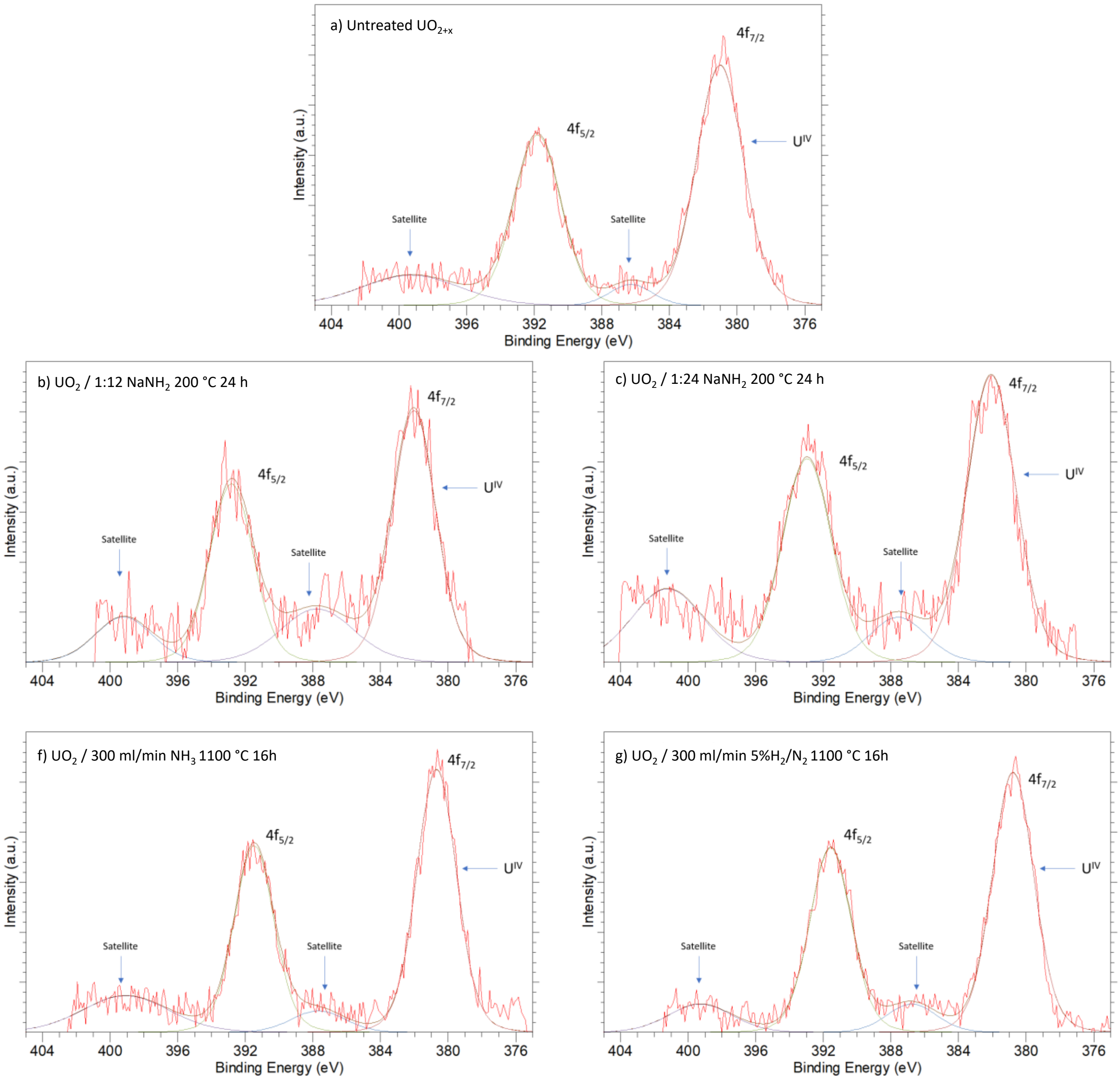

Figure 5. Fitted U 4f XPS spectra: a) untreated UO_{2+x} reagent. b) UO_2 reacted in 1:12 molar ratio with $NaNH_2$ at 200 °C for 24h. c) UO_2 reacted in 1:24 molar ratio with $NaNH_2$ at 200 °C for 24h. f) UO_2 reacted under 300 ml/min NH_3 at 1100 °C for 16h. g) UO_2 reacted under 300 ml/min 5%H_2/N_2 at 1100 °C for 16h. Lettering of products correspond to those as indicated in Figure 1 for consistency.

emission line of the products of reaction with NH_3 or 5%H_2/N_2 were shifted to slightly *lower* binding energy by up to 0.3 ± 0.1 eV, consistent with a more reduced surface post-reaction. For these products, the surface sensitive XPS data are clearly more representative of the bulk material. No N 1s or N Auger peaks were visible in any XPS spectra and the analysis of the U $4f_{7/2}$ emission line, in comparison with published data for thin films of UN_2 and U_2N_3 [60], excluding the possibility of any significant surface nitride or oxynitride formation in the reaction products.

Sample	U $4f_{7/2}$ binding energy (± 0.1 eV)	FWHM (eV)	Elements detected by XPS survey scan
Reagent UO_{2+x}	381.0	3.30	U,O
1:12 $NaNH_2$ 200 °C 24h	382.0	3.14	U, O, Na
1:24 $NaNH_2$ 200 °C 24h	382.1	3.43	U, O, Na
300 ml/min H_2/N_2 1100 °C 16h	380.8	2.89	U,O
300 ml/min NH_3 1100 °C 16h	380.6	2.78	U,O

Table 2. U 4f binding energies fitted from XPS spectra for untreated UO_{2+x} reagent, $NaNH_2$ and products of NH_3 or 5%H/N_2 reduction. Elements identified in the XPS survey scan spectra are listed (excluding adventitious carbon).

In summary, the primary product of reaction between UO_{2+x} and $NaNH_2$ is $UO_{2+x'}$, with $x' < x$, as evidenced by powder XRD data and accurate unit cell parameter determination with an internal LaB_6 standard. This is consistent with the relatively small reaction energy (-15 kJ mol^{-1}) determined from DFT calculations for hypothetical reactions in a closed system (Table S1), which do not suggest a significant thermodynamic driving force, given the typical uncertainty of such calculations (±30 kJ mol^{-1}) for oxides [35, 61]. Initial heating of $NaNH_2$ reagent with NaOH impurities (arising at manufacture or from reaction with trace H_2O) results in formation of a $NaNH_2$-NaOH molten salt [27, 32]. This molten salt has a reduced melting temperature of 160 °C compared to the melting temperatures of $NaNH_2$ and NaOH individually. At 200 °C, nascent NH_3 arises from the thermal decomposition of $NaNH_2$, with the amount of NH_3 released increasing with increasing proportion of NaOH in the melt [32]. The nascent NH_3 evidently results in the reduction of UO_{2+x} towards $UO_{2.000}$, yielding H_2O and N_2. Reaction of UO_2, H_2O and NaOH also occurs, forming $Na_2U_2O_7$ and likely other uranyl phases on the surface of the $UO_{2+x'}$ product, as identified by XRD and consistent with SEM-EDX analysis (evidencing the presence of Na), XPS analysis (demonstrating the product to be oxidised at surface, consistent with a uranyl phase), and visual observation of a yellow-brown colour post-reaction (characteristic of uranyl compounds). The origin of the orange colour of the $UO_{2.000}$ product obtained after annealing under NH_3 gas is unclear. The colour was lost after grinding the product, confirming it must arise from a surface phase, consistent with XRD data. This colour cannot be plausibly attributed to the presence of a surface oxidised phase, which would be contrary to available XPS data and is presumed to arise from a trace impurity colour centre.

While the reaction of UO_{2+x} with $NaNH_2$ did not afford the synthesis of uranium nitrides or oxynitrides, we have demonstrated $NaNH_2$-NaOH molten salt mediated reduction of UO_{2+x} under exceptionally mild conditions (200 °C). This is of significance given the importance of controlling UO_{2+x} stoichiometry relevant to its use as a nuclear fuel. Thermal conductivity was found to be correlated to the relative hyper- or hypostoichiometry of this material [62], and molecular dynamics simulation of UO_{2+x} and (U,Pu)O_{2+x} found that thermal conductivity was lowered with increasing non-stoichiometry [63], driven by point defects formed by occupied O interstitial sites. Decreased thermal conductivity is detrimental to UO_2 nuclear fuels and, as such, the possible application of a solid state reduction process at a remarkably low temperature is an interesting outcome worthy of further investigation.

6.4.2 UO_3

α-UO_3 was reacted with $NaNH_2$ in 1:12, 1:24 and 1:48 molar ratios at 200 °C for 24h, and, for comparison, with NH_3 and 5%H_2/N_2 gas using 300 ml/min gas flows at 1100 °C for 16h. The latter demonstrated complete reduction of UO_3 to UO_{2+x} (Figure S4). The gas phase reductions using NH_3 yielded UO_{2+x} with slightly larger unit cell parameters than those using 5%H_2/N_2, consistent with similar reductions of UO_{2+x} in this work. Refined unit cell parameters were a = 5.4714(1) Å for the of NH_3 reaction and a = 5.4697(1) Å for 5% H_2/N_2 reaction (determined using LaB_6 internal standard). Using the calibration shown in Figure 3, the estimated stoichiometries were $UO_{2.001(1)}$ for the product of NH_3 reaction and $UO_{2.007(1)}$ for the product of 5% H_2/N_2 reaction.

The XRD patterns of the products of UO_3 reaction with $NaNH_2$ are shown in Figure 6, and evidence a poorly crystalline phase assemblage, analysis of which was complicated by the

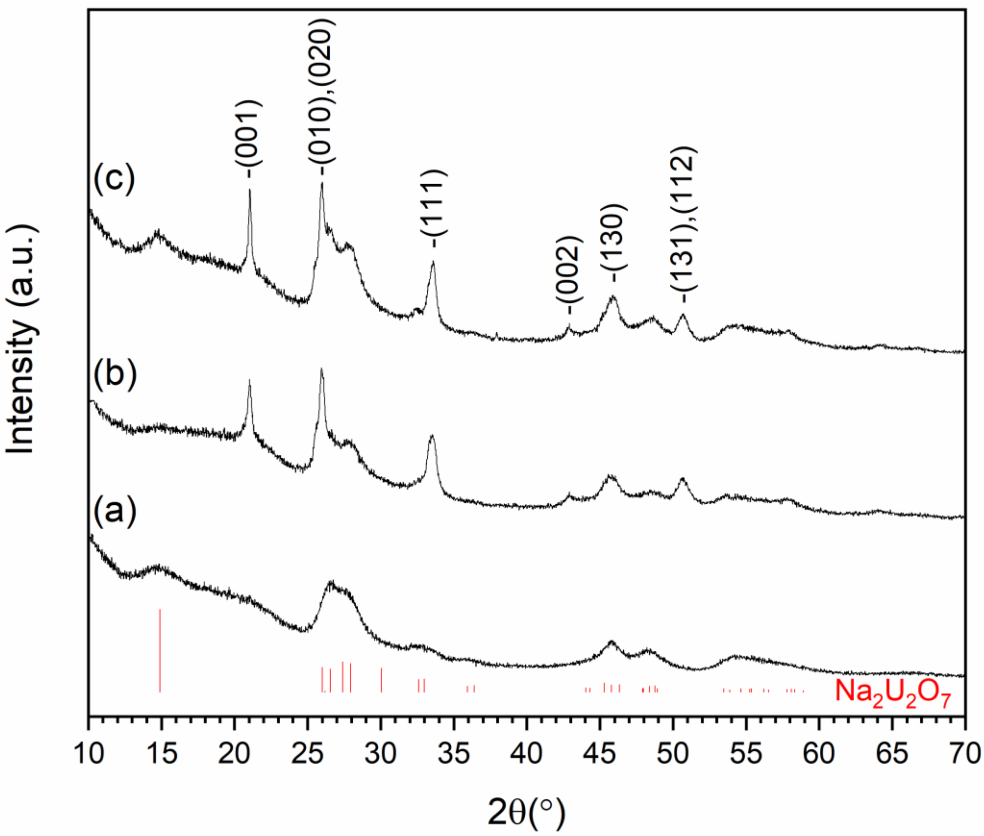

Figure 6. XRD patterns for products from reaction of α-UO_3 in 1:12 (a), 1:24 (b) and 1:48 (c) molar ratios with $NaNH_2$ at 200 °C for 24h. Reflections of α-UO_3 in space group *C*2*mm* (PDF 04-007-1155) are indexed. Tickmarks indicate allowed reflections for $Na_2U_2O_7$ (PDF 01-083-5849).

presence of considerable diffuse scatter associated with the containment used for XRD sample preparation. The XRD pattern of the product of reaction between α-UO_3 and $NaNH_2$ at 1:12 ratio, evidenced the formation of $Na_2U_2O_7$ (PDF 01-083-5849). This is consistent with the reported synthesis of $Na_2U_2O_7.6H_2O$ by hydrothermal reaction of schoepite $UO_3{\cdot}2.25H_2O$ with NaOH at 200 °C (in a Teflon lined autoclave) [55]. The XRD patterns of the products of reaction between α-UO_3 and $NaNH_2$ at 1:24 and 1:48 ratio, also evidenced the formation of $Na_2U_2O_7$, with residual α-UO_3, see Figure 6 and Table 3. The α-UO_3 reagent and products were further characterised by U $4f_{7/2}$ XPS (Figure 7) and U L_3 XANES measurements (Figure 8). The U $4f_{7/2}$ binding energy for both the α-UO_3 reagent and product of reaction with $NaNH_2$ in 1:48 ratio, were in reasonable agreement with the binding energy previously

Sample	a (Å)	b (Å)	c (Å)	Volume (Å^3)	U4f$_{7/2}$ BE (±0.1 eV)	FWHM (±0.1 eV)	XANES estimated oxidation state
α-UO_3	3.971(2)	6.834(3)	4.167(2)	113.06(8)	381.7	2.2	6.0(1)
1:12 $NaNH_2$ 200 °C 24h	*no UO_3 phase evident*				-	-	-
1:24 $NaNH_2$ 200 °C 24h	3.99(1)	6.88(3)	4.26(1)	116.7(6)	-	-	-
1:48 $NaNH_2$ 200 °C 24h	4.01(1)	6.86(1)	4.26(1)	116.9(3)	381.8	2.5	6.0(1)

Table 3 Refined unit cell parameters, XPS fitting parameters and estimated oxidation states from U L_3 XANES of untreated α-UO_3 reagent and products of reaction with $NaNH_2$ at 200 °C for 24h. 1 e.s.d confidence intervals are given in parentheses.

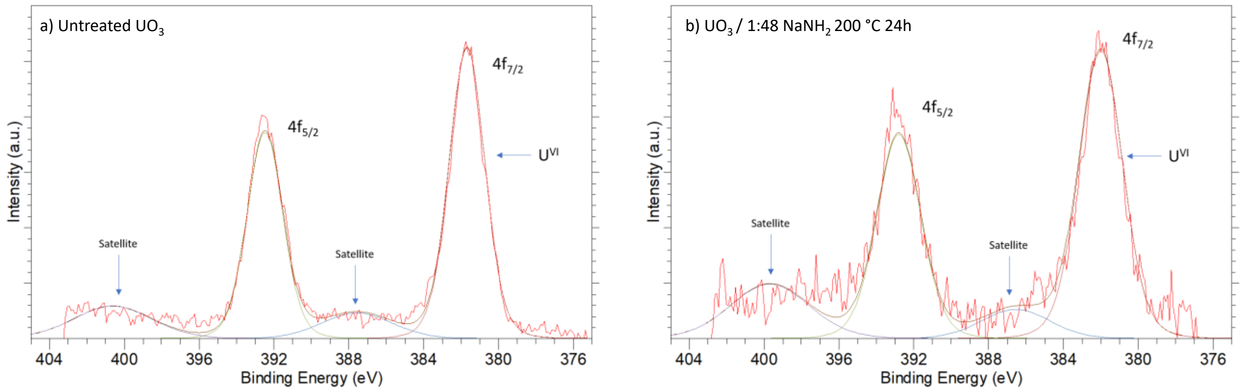

Figure 7. Fitted U 4f XPS spectra for a) untreated UO_3 reagent and b) product of UO_3 reaction with $NaNH_2$ in 1:48 molar ratio at 200 °C for 24 h.

reported for α-UO_3 at 382.1 eV [59], consistent with XRD data. The survey level scan also identified Na in the product of reaction with $NaNH_2$ in 1:48 ratio, consistent with the identification of $Na_2U_2O_7$ in XRD data. No N 1s or N Auger peaks were observable in any XPS spectra and the analysis of the U 4f$_{7/2}$ emission line, in comparison with published data for thin films of UN_2 and U_2N_3 [60], which excludes the possibility of any significant surface nitride or oxynitride formation in the reaction products. The bulk sensitive U L_3 XANES data of the α-UO_3 reagent and product of reaction with $NaNH_2$ in 1:48 ratio are shown in Figure 8. The E_0 (determined as $\mu x(E) = 0.5$) is shifted 0.2 ± 0.1 eV higher in the reaction product relative to α-UO_3, which implies the presence of dominant U(VI) speciation of uranium contribution, characteristic of α-UO_3, plus one or more additional U(VI) environments in the product material. The presence of the post edge shoulder feature located

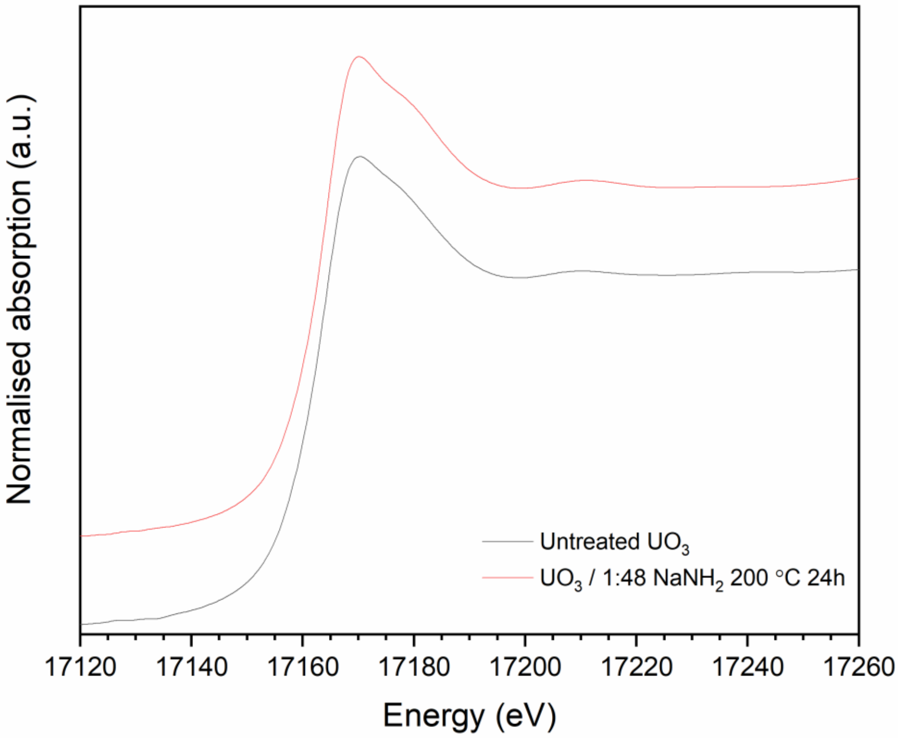

Figure 8. U L_3 XANES data for untreated UO_3 reagent (black) and UO_3 reacted with $NaNH_2$ in 1:48 molar ratio at 200 °C for 24 h.

ca. 15 eV above E_0 is characteristic of the uranyl oxocation [64], and more pronounced in the spectrum of the product. Taken together, the U $4f_{7/2}$ XPS and U L_3 XANES are consistent with XRD data, and evidence the product of α-UO_3 reaction with $NaNH_2$ being either $Na_2U_2O_7$ or a mixture of $Na_2U_2O_7$ and α-UO_3. Overall, these reactions are broadly consistent with the predictions of the DFT calculated reaction energies, which identify sodium uranate phases as potential reaction products, including, $Na_2U_2O_7$ (Table S1). Notably, in reactions predicted to yield $Na_2U_2O_7$ as a product, UN_2 is not favoured, consistent with our findings. The hypothetical reaction energies for interfacial reactions of α-UO_3 and $NaNH_2$ are significantly more negative than those for reactions of UO_2, implying a greater thermodynamic driving force in agreement with our experimental findings.

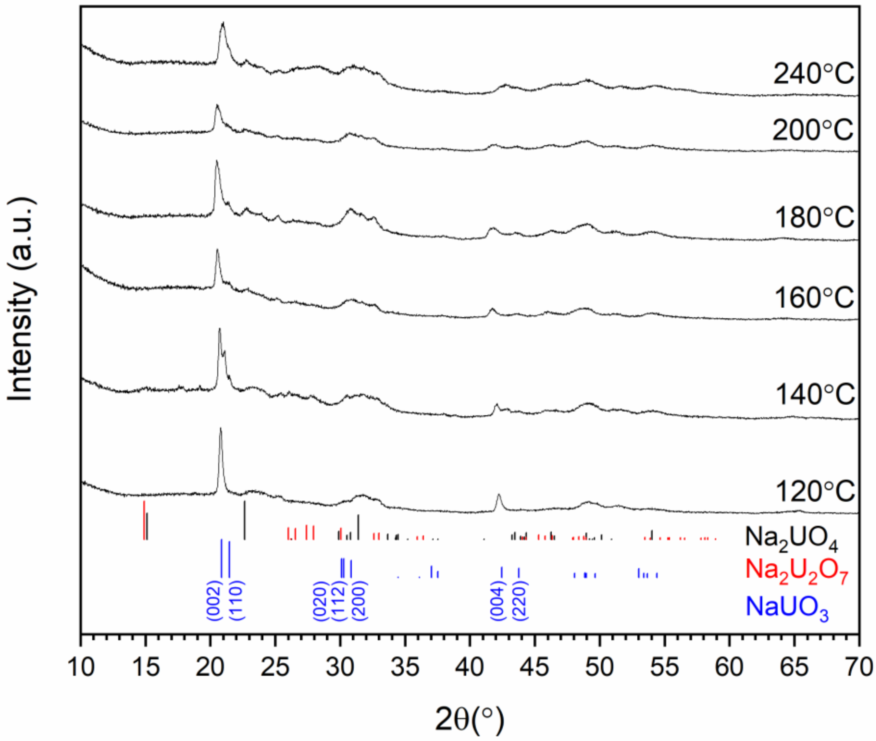

Figure 9. XRD patterns of the product of U_3O_8 reacted with $NaNH_2$ in 1:48 molar ratio, at varying temperature for 24h. Black and red tickmarks indicate allowed reflections for Na_2UO_4 (PDF 00-025-1295), $Na_2U_2O_7$ (PDF 01-083-5849), respectively. Blue tickmarks indicate reflections of $NaUO_3$ with refined unit cell parameters.

6.4.2 U_3O_8

U_3O_8 was reacted with $NaNH_2$ in a 1:48 molar ratio for 24 h at temperatures between 120 - 240 °C, and with NH_3 and 5%H_2/N_2 gas using 300 ml/min gas flows at 1100 °C for 16 h. The latter reactions afforded reduction to $UO_{2.001(1)}$ (see Figure S5), which was anticipated as reduction of U_3O_8 to stoichiometric UO_2 under NH_3 and H_2 was previously reported [65, 66]. Figure 9 shows the XRD patterns of the products of the reaction of U_3O_8 and $NaNH_2$. All diffraction patterns show a similar profile, with broad Bragg reflections of low relative intensity, signifying a similar assemblage of poorly crystalline phases. A search-match analysis of the PDF database identified $NaUO_3$ (*Pbnm*) as a plausible reaction product, accounting for the most intense reflections in the data at $2\theta = 21.5^\circ$ (002) (110), 30.5° (020) (112) (200), and 43.8° (004) (220), with a reasonable ratio of expected intensities [67]. The presence of significant U_3O_8 (*C2mm*)could account for the intense reflection observed at $2\theta = 21.5^\circ$ (100), but expected reflections of significant intensity at $2\theta = 26.1^\circ$ (031) (002) and

Reaction temperature (°C)	a (Å)	b (Å)	c (Å)	Volume (Å^3)
120	5.77(1)	5.91(1)	8.53(2)	291(1)
140	5.79(1)	5.90(1)	8.50(3)	290(1)
160	5.79(1)	5.90(1)	8.50(3)	290(1)
180	5.79(1)	5.90(1)	8.51(3)	291(1)
200	5.78(1)	5.90(2)	8.51(3)	290(1)
240	5.78(1)	5.91(2)	8.49(3)	290(1)
$NaUO_3$ PDF 04-015-2059	5.776	5.910	8.283	282.75

Table 4. Refined unit cell parameters for the *Pbnm* $NaUO_3$ phase apparent in XRD patterns of product from U_3O_8 reacted with 1:48 molar ratio with $NaNH_2$ at varying temperature for 24 h. Unit cell parameters were calculated from Le Bail fits of XRD data with 1 e.s.d confidence intervals given in parentheses. The published parameters from PDF 04-015-2059 are given for comparison.

34.0° (131) (102) were not observed [68]. Although the contribution of U_3O_8 to the product diffraction patterns cannot be ruled out, it is evidently not the major component of the phase assemblage. Refinement of the unit cell parameters for $NaUO_3$, presented in Table 4, showed an increase in cell volume compared to published data, with expansion of the *a* and *c* axis compensated by minor contraction of the *b* axis. However, the precision of the determined unit cell parameters is low, due to the broad associated reflections and reflection overlap. Consideration of other broad low intensity reflections in the diffraction patterns suggested they could be accounted for by contributions from Na_2UO_4 (PDF 00-025-1295) and $Na_2U_2O_7$ (PDF 01-083-5849). Notably, both $NaUO_3$ and Na_4UO_5 were predicted as products of the reaction between U_3O_8 and $NaNH_2$, based on DFT calculated reaction energies, indeed reactions yielding $NaUO_3$ have the most negative calculated reaction energies (Table S1). DFT calculations suggest these reactions could yield UN_2 or U_4N_7 as products, but these phases could not be identified.

Figure 10 shows a comparison of U L_3 edge XANES of the U_3O_8 reagent and the product of reaction with $NaNH_2$ in 1:48 ratio at 200 °C. The absorption edge, E_0, of the product was shifted by 0.2 ± 0.1 eV, compared to that of U_3O_8, implying an average oxidation state close to 5.7+ in the product. The U L_3 edge XANES of the product also showed post edge

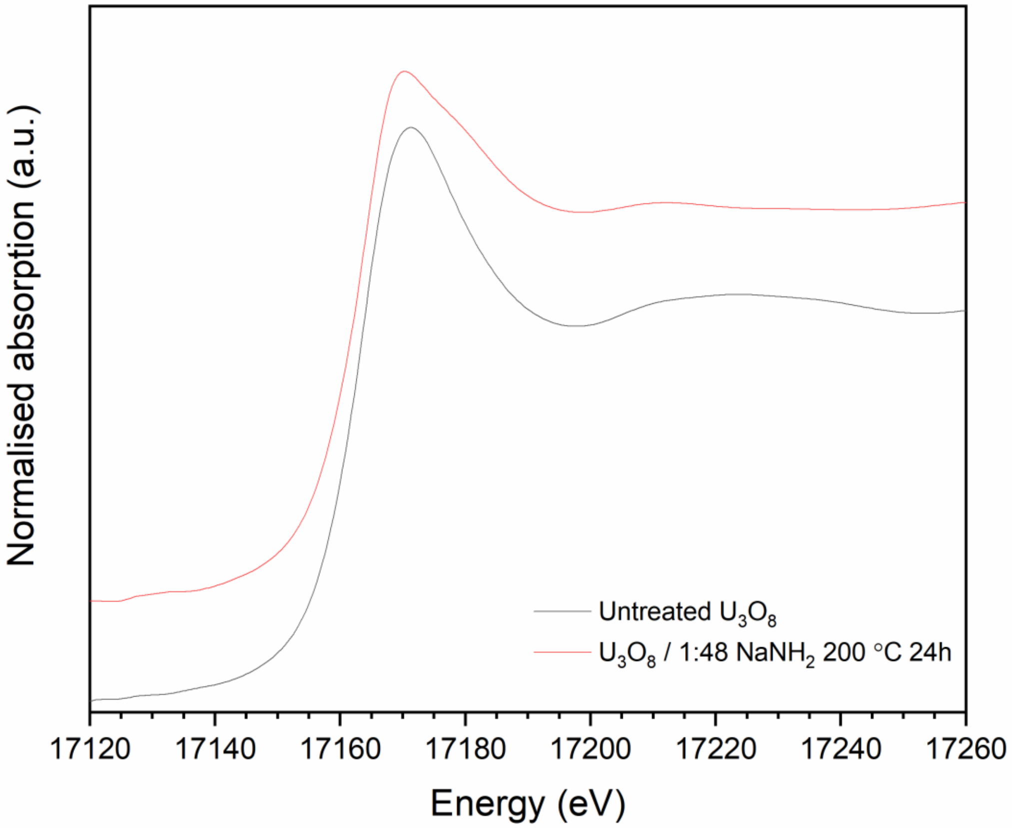

Figure 10. U L_3 XANES data for untreated U_3O_8 reagent (black) and U_3O_8 reacted with $NaNH_2$ in 1:48 molar ratio at 200 °C for 24 h (red).

shoulder feature located ca. 15 eV, characteristic of the uranyl oxocation [64], and that observed in data previously reported for Na_2UO_4 and $Na_2U_2O_7$ [69], and for UO_3 as measured in this work. Thus, U L_3 XANES, which is a probe of bulk speciation demonstrates that the reaction product has both U(V) and U(VI) contributions, consistent with the phase assemblage determined from XRD data.

Further characterisation of the U_3O_8 reagent and product of reaction with $NaNH_2$ in 1:48 ratio at 200 °C, was undertaken by U $4f_{7/2}$ XPS, as shown in Figure 11 with detail in Table 5. The U $4f_{7/2}$ emission of the U_3O_8 reagent presented two components with binding energy 381.1(1) eV and 382.6(1) eV, as expected for the presence of U(V) and U(VI) species, and in reasonable agreement with the determination of Wang *et al.* (380.8 eV and 381.9 eV

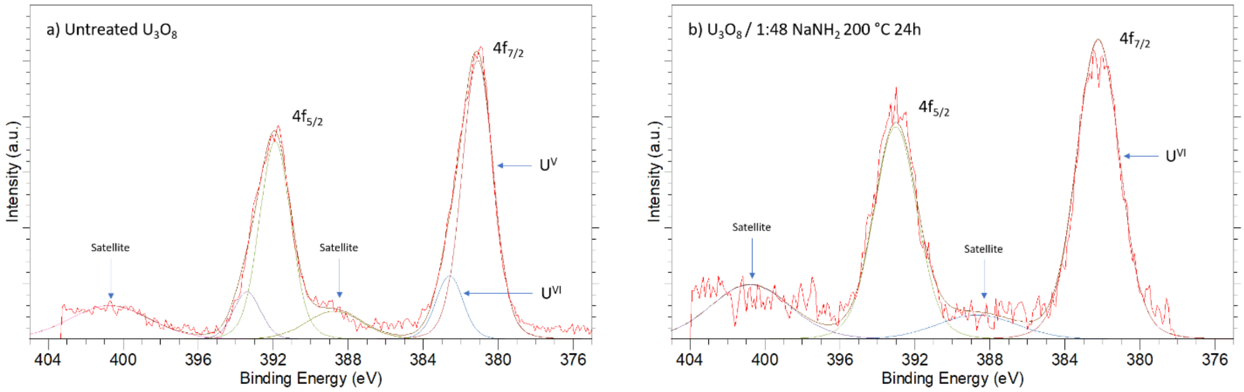

Figure 11. Fitted U 4f XPS spectra for a) untreated U_3O_8 reagent and b) U_3O_8 reacted with $NaNH_2$ in 1:48 molar ratio at 200 °C for 24 h.

	Environment 1		Environment 2		
Sample	U 4f$_{7/2}$ B.E. (±0.1 eV)	FWHM (eV)	U 4f$_{7/2}$ B.E. (±0.1 eV)	FWHM (eV)	XANES estimated oxidation state
Untreated U_3O_8 reagent	381.1	2.0	382.6	1.7	5.7(1)
U_3O_8 reacted with 1:48 $NaNH_2$ 200 °C 24h	382.2	2.5	-	-	5.7(1)

Table 5. U 4f$_{7/2}$ binding energies and estimated oxidation states from U L_3 XANES for untreated U_3O_8 reagent and U_3O_8 reacted with $NaNH_2$ in 1:48 molar ratio at 200 °C for 24 h. 1 e.s.d. uncertainties are given in parentheses

respectively) [70]. The U 4f$_{7/2}$ XPS of the product presented a single component positioned at 382.2 eV. This is higher than that reported for $NaUO_3$ (380.6 eV), Na_2UO_4 (380.7 eV) and $Na_2U_2O_7$ (380.8 eV) [57], but broadly consistent with that of other reported uranyl phases, in particular $UO_2(OH)_2$ (382.3 eV) [56, 58, 59] and demonstrates the surface of the product material to be oxidised relative to the U_3O_8 reagent.

The combination of characterisation modalities leads to the following description of the reaction of U_3O_8 with $NaNH_2$. The dissolution of $NaNH_2$ into NaOH begins at 100 °C [32], forming the molten salt that mediates the formation of $NaUO_3$, Na_2UO_4 and $Na_2U_2O_7$. The latter compounds are reported to be synthesised from mixtures of U_3O_8 and Na_2CO_3 calcined at 700 to 1000 °C [71]. $NaUO_3$ synthesis is typically achieved as a two stage reaction *via* an intermediate Na_2UO_4. Na_2UO_4 and UO_2 are then reacted under inert atmosphere or vacuum to achieve U(V) in $NaUO_3$ [72]. Direct synthesis of $NaUO_3$ from Na_2CO_3 and U_3O_8 at 800

°C under an Ar and H_2 atmosphere is also reported [67]. It is interesting to note that within the sealed reaction vessel we have achieved both U(V) and U(VI) species, analogous to the reactions described above but at a significantly lower temperature afforded by the $NaNH_2$-NaOH molten salt. The partially oxidised nature of the phase assemblage is evident in both the bulk XANES analysis and the surface XPS measurements.

While the targeted uranium nitride and potential oxynitride phases were not achieved, the predicted phases of $NaUO_3$, Na_2UO_4 and $Na_2U_2O_7$ were obtained, although with poor crystallinity. Investigation of reaction temperature did not reveal any definite trends in phase assemblage, although an increased FWHM for reflections from $NaUO_3$ was observed with increasing temperature suggesting a broadening of crystallite size with increasing temperature. In comparison to the reactions with UO_2 and UO_3 presented here, the effect of temperature does not appear to be as significant on the resultant phase assemblage as the relative ratio of $NaNH_2$ used.

6.5 Conclusions

The reaction of UO_{2+x}, UO_3 and U_3O_8 with $NaNH_2$ and NH_3 gas was explored as a route to the synthesis of uranium nitrides and hypothetical uranium oxynitrides. No evidence for N incorporation in the products of reactions was determined from the absence of N 1s and N Auger peaks in XPS data, and N Kα emission in EDX data. Thus, it may be concluded that these reactions are not effective for the synthesis of uranium nitrides or hypothetical oxynitrides. DFT computed reaction energies using the Materials Project interfacial reactions application, at 0 K in a closed system, suggest that uranium nitrides are potential products of such reactions, with negative reaction energies. An explanation for the lack of formation of uranium nitride phases by reaction of uranium oxides with $NaNH_2$ may be *in situ* hydrolysis, contributing to the yield of observed uranyl phases, $Na_2U_2O_7$ and Na_2UO_4, which were predicted reaction products. These phases also likely form from dissolution of the uranium oxide into the $NaNH_2$ molten salt and precipitation of oxidised uranyl phases. Nevertheless, reaction of uranium oxides with $NaNH_2$ molten salt afforded interesting and potentially useful synthetic methods. First, hyperstoichiometric UO_{2+x} was shown to be reduced to stoichiometric $UO_{2.00}$ (x = 0) presumably mediated by abstraction of mobile hyperstoichiometric oxygen by nascent NH_3, as observed in the gas phase reduction. However, reduction in $NaNH_2$ molten salt was achieved at remarkably low temperature of 200 °C. Second, reaction of U_3O_8 produced $NaUO_3$ perovskite under similarly mild conditions, albeit poorly crystalline and with accessory phases. Third, reaction of UO_3 with $NaNH_2$ produced poorly crystalline $Na_2U_2O_7$, consistent with the known synthesis of $Na_2U_2O_7$ by reaction of $UO_3{\cdot}2.25H_2O$ with NaOH under hydrothermal conditions. These reactions are apparently governed by the solubility of the uranium oxide in $NaNH_2$ molten salt. The reflection profiles of UO_{2+x} in XRD data were not observed to be significantly broadened post-reaction and XPS demonstrated the surface of the product to be oxidised to U(VI). This suggests UO_{2+x} has relatively low solubility in $NaNH_2$, and dissolves slowly by adventitious oxidation of the surface of UO_2 particles and precipitation of uranyl phases. In contrast, the diffraction profiles of the products from UO_3 and U_3O_8 reaction with $NaNH_2$ were observed to be broad and of low intensity, consistent with significant dissolution of these oxides and the formation of poorly crystalline product phases.

6.6 Acknowledgements

Components of this research utilised the HADES facility for High Activity Decommissioning Engineering & Science/MIDAS facility at the University of Sheffield established with financial support from the Engineering & Physical Science Research Council (EPSRC) and the Department for Business, Energy and Industrial Strategy, under grant EP/T011424/1 [52]. The authors are grateful for financial support from EPSRC under grant numbers EP/L015390/1 and EP/S01019X/1. XPS measurement was supported by the Henry Royce Institute, funded through EPSRC grants EP/R00661X/1, EP/P025021/1 and EP/P025498/1. We acknowledge Diamond Light Source for time on Beamline B18 under Proposal SP17243 and wish to thank G. Cibin for assistance with data acquisition.

6.7 References

1. Ekberg C, Ribeiro Costa D, Hedberg M, Jolkkonen M (2018) Nitride fuel for Gen IV nuclear power systems. J Radioanal Nucl Chem 318:1713–1725. https://doi.org/10.1007/s10967-018-6316-0
2. Streit M, Ingold F (2005) Nitrides as a nuclear fuel option. J Eur Ceram Soc 25:2687–2692. https://doi.org/https://doi.org/10.1016/j.jeurceramsoc.2005.03.181
3. Arai Y (2012) Nitride fuel. In: Konings R (ed) Comprehensive Nuclear Materials. Elsevier Inc., Oxford, pp 41–54
4. Youinou GJ, Sen RS (2014) Impact of accident-tolerant fuels and claddings on the overall fuel cycle: A preliminary systems analysis. Nucl Technol 188:123–138. https://doi.org/10.13182/NT14-22
5. Zakova J, Wallenius J (2012) Fuel residence time in BWRs with nitride fuels. Ann Nucl Energy 47:182–191. https://doi.org/10.1016/j.anucene.2012.03.033
6. Dell RM, Wheeler VJ, Bridger NJ (1967) Hydrolysis of uranium mononitride. Trans Faraday Soc 63:1286–1294. https://doi.org/10.1039/TF9676301286
7. Dell RM, Wheeler VJ, McIver EJ (1966) Oxidation of uranium mononitride and uranium monocarbide. Trans Faraday Soc 62:3591–3606. https://doi.org/10.1039/TF9666203591
8. Rao GAR, Mukerjee SK, Vaidya VN, et al (1991) Oxidation and hydrolysis kinetic studies on UN. J Nucl Mater 185:231–241. https://doi.org/10.1016/0022-3115(91)90340-D
9. Jolkkonen M, Malkki P, Johnson K, Wallenius J (2017) Uranium nitride fuels in superheated steam. J Nucl Sci Technol 54:513–519. https://doi.org/10.1080/00223131.2017.1291372
10. Katsura M (1991) A thermodynamic analysis of nitrogen-rich uranium sesquinitride formation by the reaction of uranium with ammonia. Solid State Ionics 49:225–231. https://doi.org/10.1016/0167-2738(91)90090-X
11. Katsura M, Serizawa H (1992) Formation of a nitrogen-rich α-U_2N_{3+x} phase by the reaction of uranium with a stream of ammonia. J Alloys Compd 187:389–399. https://doi.org/10.1016/0925-8388(92)90444-E
12. Serizawa H, Fukuda K, Ishii Y, et al (1994) Crystallographic study on the phase transition of α-U_2N_3. J Nucl Mater 208:128–134. https://doi.org/10.1016/0022-3115(94)90204-6
13. Serizawa H, Fukuda K, Katsura M (1995) Study of the formation of α-U_2N_{3+x} using unstable ammonia — reaction sequence and control of nitrogen activity. J Alloys Compd 223:39–44. https://doi.org/10.1016/0925-8388(94)01442-6
14. Katsura M, Hirota M, Miyake M (1994) The role of unstable NH_3 in the formation of nitrogen-rich α-U_2N_{3+x} by the reaction of UC or U with NH_3. J Alloys Compd 213–214:440–443. https://doi.org/10.1016/0925-8388(94)90955-5
15. Silva GWC, Yeamans CB, Ma L, et al (2008) Microscopic Characterization of Uranium Nitrides Synthesized by Oxidative Ammonolysis of Uranium Tetrafluoride. Chem Mater 20:3076–3084. https://doi.org/10.1021/cm7033646
16. Yeamans CB, Silva GWC, Cerefice GS, et al (2008) Oxidative ammonolysis of uranium(IV) fluorides to uranium(VI) nitride. J Nucl Mater 374:75–78. https://doi.org/10.1016/j.jnucmat.2007.06.022

17. Nakagawa T, Matsuoka H, Sawa M, et al (1997) Formation of uranium and cerium nitrides by the reaction of carbides with NH_3 and N_2/H_2 stream. J Nucl Mater 247:127–130. https://doi.org/10.1016/S0022-3115(97)00036-6
18. Nishimaki K, Hirota M, Nakagawa T, et al (1998) Thermodynamics of nitrogen-rich uranium sesquinitride formation by reaction of uranium monocarbide with ammonia. J Alloys Compd 271–273:654–657. https://doi.org/10.1016/S0925-8388(98)00180-7
19. Muromura T, Tagawa H (1977) Formation of uranium mononitride by the reaction of uranium dioxide with carbon in ammonia and a mixture of hydrogen and nitrogen- I synthesis of high purity UN. J Nucl Mater 71:65–72. https://doi.org/10.1016/0022-3115(77)90187-8
20. Muromura T, Tagawa H (1979) Formation of uranium mononitride by the reaction of uranium dioxide with carbon in ammonia and a mixture of hydrogen and nitrogen. II. Reaction rates. J Nucl Mater 80:330–338. https://doi.org/10.1016/0022-3115(79)90196-X
21. Huang Y, Gu Y, Zheng M, et al (2007) Synthesis of nanocrystalline titanium nitride by reacting titanium dioxide with sodium amide. Mater Lett 61:1056–1059. https://doi.org/10.1016/j.matlet.2006.06.048
22. Feng X, Bai Y-J, Lü B, et al (2004) Low Temperature Induced Synthesis of TiN Nanocrystals. Inorg Chem 43:3558–3560. https://doi.org/10.1021/ic049841n
23. Guo Q, Xie Y, Wang X, et al (2005) Synthesis of Uniform Titanium Nitride Nanocrystalline Powders via a Reduction–Hydrogenation–Dehydrogenation–Nitridation Route. J Am Ceram Soc 88:249–251. https://doi.org/10.1111/j.1551-2916.2004.00050.x
24. Chang F, Guo J, Wu G, et al (2017) Influence of alkali metal amides on the catalytic activity of manganese nitride for ammonia decomposition. Catal Today 286:141–146. https://doi.org/10.1016/j.cattod.2016.09.010
25. Miura A, Takei T, Kumada N (2014) Synthesis of Cu_3N from CuO and $NaNH_2$. J Asian Ceram Soc 2:326–328. https://doi.org/10.1016/j.jascer.2014.08.007
26. Chen L, Gu Y, Shi L, et al (2004) A room-temperature synthesis of nanocrystalline vanadium nitride. Solid State Commun 132:343–346. https://doi.org/10.1016/j.ssc.2004.07.041
27. Miura A, Takei T, Kumada N (2013) Low-Temperature Nitridation of Manganese and Iron Oxides Using $NaNH_2$ Molten Salt. Inorg Chem 52:11787–11791. https://doi.org/10.1021/ic401951u
28. Laassiri S, Zeinalipour-Yazdi CD, Catlow CRA, Hargreaves JSJJ (2018) The potential of manganese nitride based materials as nitrogen transfer reagents for nitrogen chemical looping. Appl Catal B Environ 223:60–66. https://doi.org/10.1016/j.apcatb.2017.04.073
29. Barick BK, Dhar S (2015) Surface and bulk electronic properties of low temperature synthesized InN microcrystals. J Cryst Growth 416:154–158. https://doi.org/10.1016/j.jcrysgro.2015.01.010
30. Miura A, Takei T, Kumada N (2012) Synthesis of Wurtzite-Type InN Crystals by Low-Temperature Nitridation of $LiInO_2$ Using $NaNH_2$ Flux. Cryst Growth Des 12:4545–4547. https://doi.org/10.1021/cg3007266
31. O'Sullivan SE, Sun S-K, Lawson SM, et al (2021) Low-Temperature Nitridation of Fe_3O_4 by Reaction with $NaNH_2$. Inorg Chem.

https://doi.org/10.1021/acs.inorgchem.0c03452

32. Jepsen LH, Wang P, Wu G, et al (2016) Thermal decomposition of sodium amide, $NaNH_2$, and sodium amide hydroxide composites, $NaNH_2$-NaOH. Phys Chem Chem Phys 18:25257–25264. https://doi.org/10.1039/c6cp01604a
33. Miura A (2017) Low-temperature synthesis and rational design of nitrides and oxynitrides for novel functional material development. J Ceram Soc Japan 125:552–558. https://doi.org/10.2109/jcersj2.17055
34. Richards WD, Miara LJ, Wang Y, et al (2016) Interface Stability in Solid-State Batteries. Chem Mater 28:266–273. https://doi.org/10.1021/acs.chemmater.5b04082
35. Jain A, Ong SP, Hautier G, et al (2013) Commentary: The Materials Project: A materials genome approach to accelerating materials innovation. APL Mater 1:11002. https://doi.org/10.1063/1.4812323
36. Kresse G, Furthmüller J (1996) Efficient iterative schemes for ab initio total-energy calculations using a plane-wave basis set. Phys Rev B 54:11169–11186. https://doi.org/10.1103/PhysRevB.54.11169
37. Bergerhoff G, Brown ID (1981) Inorganic Crystal Structure Database. Acta Crystallogr Sect A 37:C342. https://doi.org/10.1107/S0108767381089411
38. Jain A, Hautier G, Moore CJ, et al (2011) A high-throughput infrastructure for density functional theory calculations. Comput Mater Sci 50:2295–2310. https://doi.org/10.1016/j.commatsci.2011.02.023
39. Jain A, Hautier G, Ong SP, et al (2011) Formation enthalpies by mixing GGA and GGA + U calculations. Phys Rev B 84:45115. https://doi.org/10.1103/PhysRevB.84.045115
40. Thompson NBA, Gilbert MR, Hyatt NC (2021) Nuclear forensic signatures of studtite and α-UO_3 from a matrix of solution processing parameters. J Nucl Mater 544:152713. https://doi.org/10.1016/j.jnucmat.2020.152713
41. Clark DE (2001) Peroxides and peroxide-forming compounds. Chem Health Saf 8:12–22. https://doi.org/10.1021/acs.chas.8b08507
42. TOPAS (2008) V4, General profile and structure analysis software for powder diffraction data- User's Manual. Bruker AXS GmbH, Karlsruhe, Germany
43. Bruker (2011) QUANTAX 70 EDS System for Hitachi Tabletop Microscope TM3000. Bruker nano GmbH, Berlin, Germany
44. Thompson NBA, O'Sullivan SE, Howell RJ, et al (2020) Objective Colour Analysis from Digital Images as a Nuclear Forensic Tool. Forensic Sci Int 110678. https://doi.org/10.1016/j.forsciint.2020.110678
45. Fairley N (2020) CasaXPS
46. Ravel B, Newville M (2005) ATHENA, ARTEMIS, HEPHAESTUS: data analysis for X-ray absorption sepctroscopy using IFEFFIT. J Synchrotron Radiat 12:537–541
47. Frondel C (1956) Mineral composition of gummite. Am Mineral 41:539–568
48. Leinders G, Cardinaels T, Binnemans K, Verwerft M (2015) Accurate lattice parameter measurements of stoichiometric uranium dioxide. J Nucl Mater 459:135–142. https://doi.org/10.1016/j.jnucmat.2015.01.029
49. Elorrieta JM, Bonales LJ, Rodríguez-Villagra N, et al (2016) A detailed Raman and X-ray study of UO_{2+x} oxides and related structure transitions. Phys Chem Chem Phys 18:28209–28216. https://doi.org/10.1039/c6cp03800j
50. Ijdo DJW, Akerboom S, Bontenbal A (2015) Crystal structure of α- And β-$Na_2U_2O_7$:

From Rietveld refinement using powder neutron diffraction data. J Solid State Chem 221:1–4. https://doi.org/10.1016/j.jssc.2014.09.011

51. Ondrus P, Skála R, Veselovsky F, et al (2003) Cejkaite, the triclinic polymorph of $Na_4(UO_2)(CO_3)_3$—a new mineral from Jáchymov, Czech Republic. Am Mineral 88:686–693. https://doi.org/10.2138/am-2003-0422
52. Kitamura A, Yamamura T, Fukui A, Moriyama H (1998) Studies of U(VI) in highly basic solutions. In: Kyoto Daigaku Genshiro Jikkensho Gakujutsu Koenkai Hobunshu. Japan, pp 107–112
53. Williams PA (1990) Oxide Zone Geochemistry. NY, Ellis Horwood
54. Čejka J, Sejkora J, Plášil J, et al (2010) Raman spectroscopic study of the uranyl carbonate mineral čejkaite and its comparison with synthetic trigonal $Na_4[UO_2(CO_3)_3]$. J Raman Spectrosc 41:459–464. https://doi.org/10.1002/jrs.2349
55. Chernorukov NG, Nipruk O V., Kostrova EL (2016) Synthesis and study of sodium uranate $Na_2U_2O_7{\cdot}6H_2O$ and of products of its dehydration and thermal decomposition. Radiochemistry 58:124–127. https://doi.org/10.1134/S106636221602003X
56. Schindler M, Hawthorne FC, Freund MS, Burns PC (2009) XPS spectra of uranyl minerals and synthetic uranyl compounds. I: The U 4f spectrum. Geochim Cosmochim Acta 73:2471–2487. https://doi.org/10.1016/j.gca.2008.10.042
57. Ilton ES, Bagus PS (2011) XPS determination of uranium oxidation states. Surf Interface Anal 43:1549–1560. https://doi.org/10.1002/sia.3836
58. Dacheux N, Brandel V, Genet M, et al (1996) Solid solutions of uranium and thorium phosphates: synthesis, characterization and X-ray photoelectron spectroscopy. New J Chem 20:301–310
59. Allen GC, Holmes NR (1987) Surface characterisation of α-, β-, γ-, and δ-UO_3 using X-ray photoelectron spectroscopy. J Chem Soc Dalt Trans 3009–3015. https://doi.org/10.1039/DT9870003009
60. Lawrence Bright E, Rennie S, Cattelan M, et al (2018) Epitaxial UN and α-U_2N_3 thin films. Thin Solid Films 661:71–77. https://doi.org/10.1016/j.tsf.2018.07.018
61. Wang L, Maxisch T, Ceder G (2006) Oxidation energies of transition metal oxides within the GGA + U framework. Phys Rev B 73:195107. https://doi.org/10.1103/PhysRevB.73.195107
62. Fink JK (2000) Thermophysical properties of uranium dioxide. J Nucl Mater 279:1–18. https://doi.org/10.1016/S0022-3115(99)00273-1
63. Maxwell CI, Pencer J (2019) Molecular dynamics modelling of the thermal conductivity of off-stoichiometric $UO_{2\pm x}$ and $(U_yPu_{1-y})O_{2\pm x}$ using equilibrium molecular dynamics. Ann Nucl Energy 131:317–324. https://doi.org/10.1016/j.anucene.2019.03.029
64. Den Auwer C, Simoni E, Conradson S, Madic C (2003) Investigating Actinyl Oxo Cations by X-ray Absorption Spectroscopy. Eur J Inorg Chem 3843–3859. https://doi.org/10.1002/ejic.200300093
65. Valdivieso F, Pijolat M, Soustelle M, Jourde J (2001) Reduction of uranium oxide U_3O_8 into uranium dioxide UO_2 by ammonia. Solid State Ionics 141–142:117–122. https://doi.org/10.1016/S0167-2738(01)00730-5
66. Pijolat M, Brun C, Valdivieso F, Soustelle M (1997) Reduction of uranium oxide U_3O_8 to UO_2 by hydrogen. Solid State Ionics 101–103:931–935. https://doi.org/10.1016/s0167-2738(97)00385-8

67. Van Den Berghe S, Leenaers A, Ritter C (2004) Antiferromagnetism in MUO_3 (M=Na,K,Rb) studied by neutron diffraction. J Solid State Chem 177:2231–2236. https://doi.org/10.1016/j.jssc.2004.02.021
68. Loopstra BO (1977) On the crystal structure of α-U_3O_8. J Inorg Nucl Chem 39:1713–1714. https://doi.org/10.1016/0022-1902(77)80137-1
69. Smith AL, Raison PE, Martel L, et al (2014) A ^{23}Na Magic Angle Spinning Nuclear Magnetic Resonance, XANES, and High-Temperature X-ray Diffraction Study of $NaUO_3$, Na_4UO_5, and $Na_2U_2O_7$. Inorg Chem 53:375–382. https://doi.org/10.1021/ic402306c
70. Wang X, Fu Y, Xie R (1997) Effect of CO on surface behaviour of U_3O_8. J Radioanal Nucl Chem 218:243–245. https://doi.org/10.1007/BF02039343
71. Cordfunke EHP, Loopstra BO (1971) Sodium uranates: Preparation and thermochemical properties. J Inorg Nucl Chem 33:2427–2436. https://doi.org/10.1016/0022-1902(71)80217-8
72. Bartram SF, Fryxell RE (1970) Preparation and crystal structure of $NaUO_3$ and $Na_{11}U_5O_{16}$. J Inorg Nucl Chem 32:3701–3706. https://doi.org/10.1016/0022-1902(70)80187-7

6.8 Supporting information

Reagents (normalised molar fractions)	Predicted products	E_{rxn} (kJ/mol)
0.704 $NaNH_2$ + 0.296 UO_2	0.119 Na_4UO_5 + 0.393 NH_3 + 0.044 U_4N_7	-14.74
0.673 $NaNH_2$ + 0.327 UO_2	0.163 Na_3UO_4 + 0.184 NaH + 0.388 NH_3 + 0.041 U_4N_7	-16.12
0.547 $NaNH_2$ + 0.453 UO_2	0.302 $NaUO_3$ + 0.245 NaH + 0.283 NH_3 + 0.038 U_4N_7	-14.63
0.706 $NaNH_2$ + 0.294 UO_3	0.176 Na_4UO_5 + 0.471 NH_3 + 0.118 UN_2	-57.58
0.600 $NaNH_2$ + 0.400 UO_3	0.300 Na_2UO_4 + 0.400 NH_3 + 0.100 UN_2	-64.43
0.529 $NaNH_2$ + 0.471 UO_3	0.471 $NaUO_3$ + 0.059 NaN_3 + 0.353 NH_3	-66.29
0.500 $NaNH_2$ + 0.500 UO_3	0.500 $NaUO_3$ + 0.333 NH_3 + 0.083 N_2	-65.03
0.286 $NaNH_2$ + 0.714 UO_3	0.143 U_3O_8 + 0.143 $Na_2U_2O_7$ + 0.190 NH_3 + 0.048 N_2	-45.04
0.213 $NaNH_2$ + 0.787 UO_3	0.085 NH_4OH + 0.191 U_3O_8 + 0.106 $Na_2U_2O_7$ + 0.064 N_2	-34.76
0.154 $NaNH_2$ + 0.846 UO_3	0.231 U_3O_8 + 0.077 $Na_2U_2O_7$ + 0.154 H_2O + 0.077 N_2	-26.19
0.873 $NaNH_2$ + 0.127 U_3O_8	0.203 Na_4UO_5 + 0.06 NaH + 0.562 NH_3 + 0.044 U_4N_7	-48.87
0.861 $NaNH_2$ + 0.139 U_3O_8	0.156 Na_3UO_4 + 0.098 Na_4UO_5 + 0.574 NH_3 + 0.041 U_4N_7	-53.30
0.818 $NaNH_2$ + 0.182 U_3O_8	0.143 Na_4UO_5 + 0.247 $NaUO_3$ + 0.545 NH_3 + 0.039 U_4N_7	-63.51
0.783 $NaNH_2$ + 0.217 U_3O_8	0.087 Na_4UO_5 + 0.435 $NaUO_3$ + 0.522 NH_3 + 0.13 UN_2	-71.64
0.750 $NaNH_2$ + 0.250 U_3O_8	0.125 Na_2UO_4 + 0.5 $NaUO_3$ + 0.5 NH_3 + 0.125 UN_2	-76.61
0.733 $NaNH_2$ + 0.267 U_3O_8	0.711 $NaUO_3$ + 0.022 NaN_3 + 0.489 NH_3 + 0.089 UN_2	-78.12
0.727 $NaNH_2$ + 0.273 U_3O_8	0.727 $NaUO_3$ + 0.485 NH_3 + 0.03 N_2 + 0.091 UN_2	-77.93

Table S1. Example outputs from the Interface Reactions application [34] hosted by the Materials Project [35] for UO_2, UO_3 and U_3O_8 reacted with $NaNH_2$. Reactions shown are modelled in closed systems.

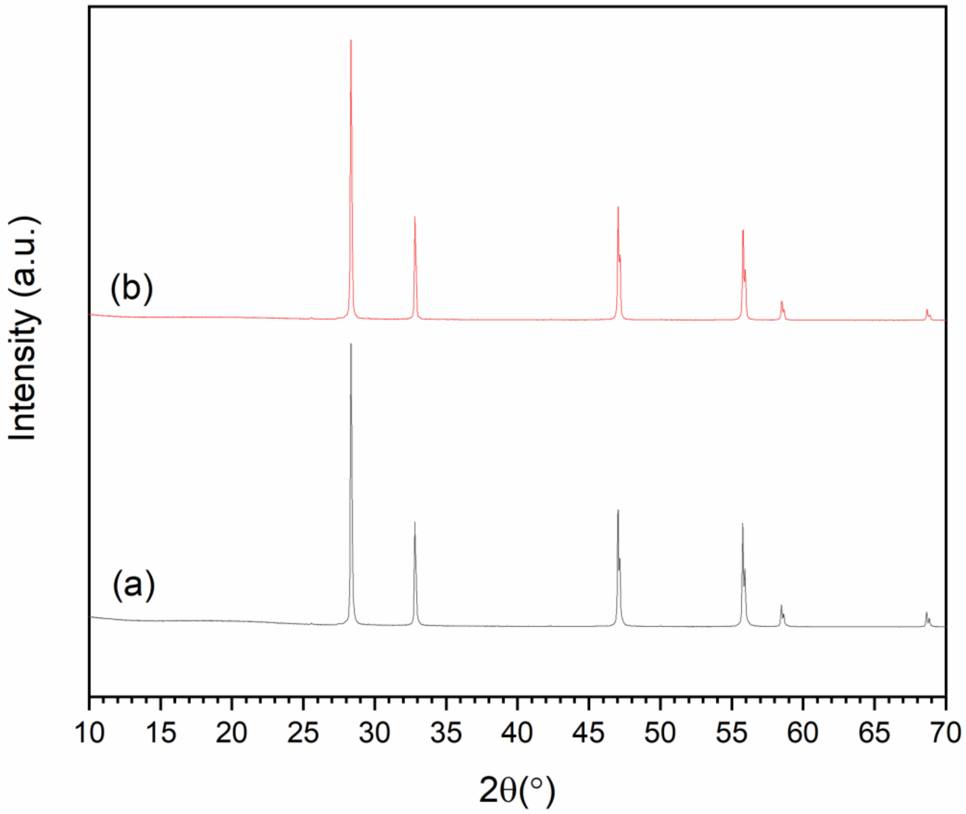

Figure S1. XRD patterns of products of UO_2 after gaseous reductions. (a) 300ml/min NH_3 at 1100 °C for 16h, refined UO_2 lattice parameter a = 5.4727(3) Å . (b) 300ml/min H_2/N_2 at 1100 °C for 16h, refined UO_2 lattice parameter a = 5.4721(1) Å.

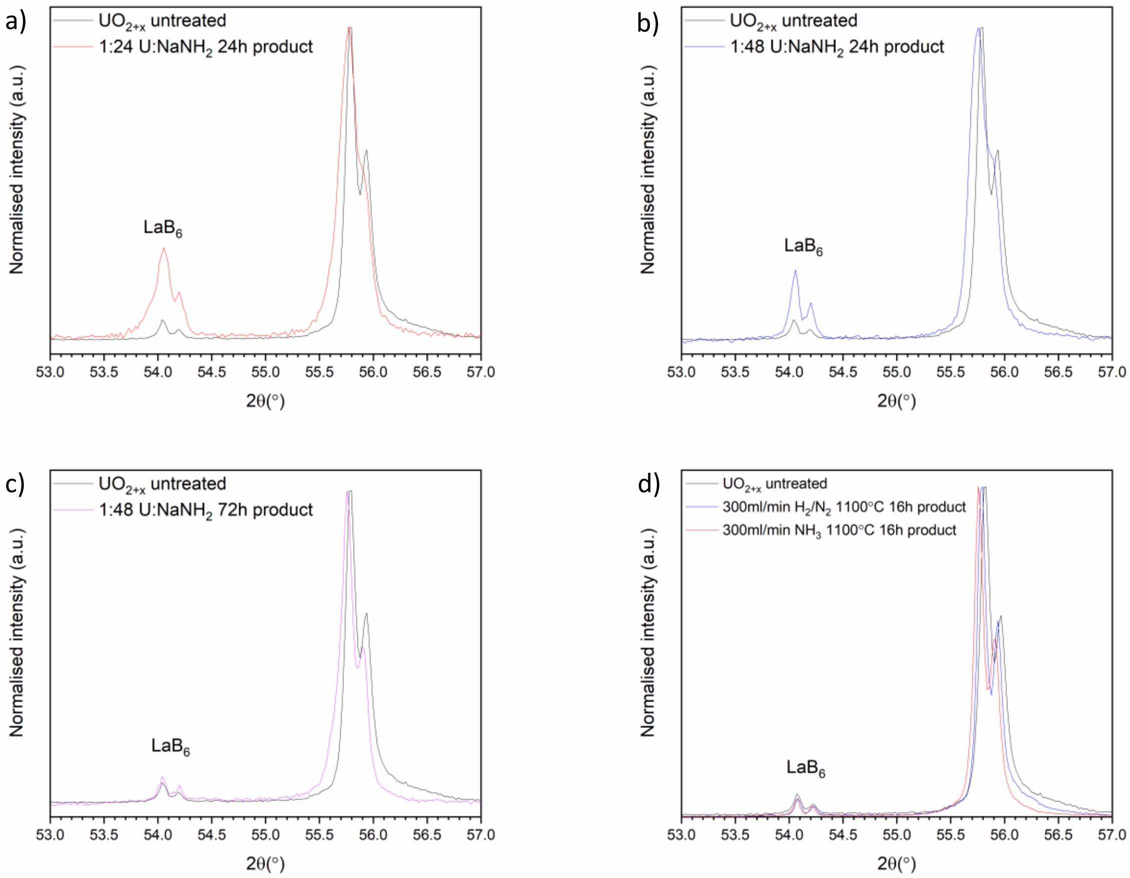

Figure S2. Comparison of XRD patterns of untreated UO_{2+x} reagent and reduced products showing the shift to lower 2θ indicative of unit cell expansion and the loss of the high angle asymmetry to the peak profile indicative of reduction of UO_{2+x} towards $UO_{2.00}$. a) UO_{2+x} and product of $NaNH_2$ reaction in 1:24 molar ratio at 200 °C for 24h. b) UO_{2+x} and product of $NaNH_2$ reaction in 1:48 molar ratio at 200 °C for 24h. c) UO_{2+x} and product of $NaNH_2$ reaction in 1:48 molar ratio at 200 °C for 72h. d) UO_{2+x} and product of gaseous reduction with 300 ml/min H_2/N_2 (blue) or NH_3 (red) at 1100 °C for 16h.

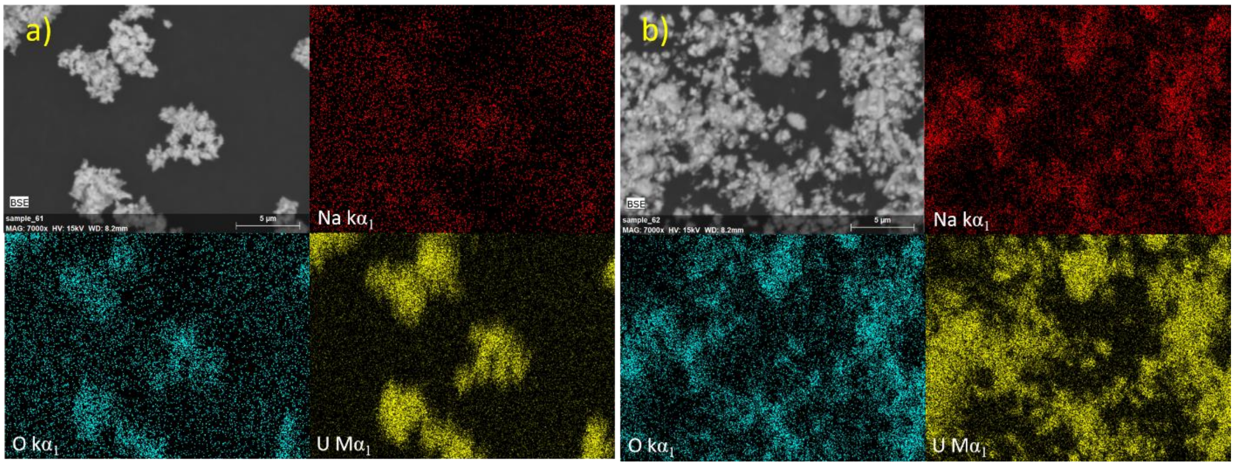

Figure S3. SEM images and EDX mapping (Na, O and U) for a) untreated UO_{2+x} reagent and b) UO_{2+x} product from reaction with 1:48 molar ratio with $NaNH_2$ at 200 °C for 72h (right).

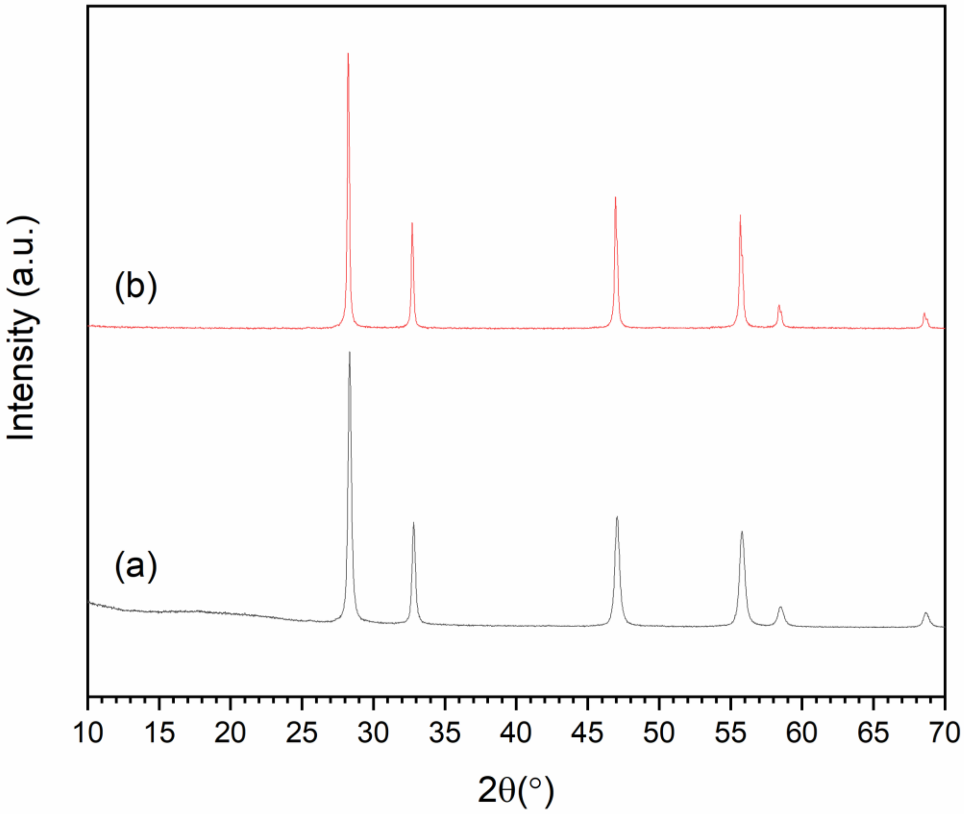

Figure S4. XRD patterns of products of α-UO_3 after gaseous reductions. (a) 300ml/min NH_3 at 1100 °C for 16h, refined UO_2 lattice parameter a = 5.4714(1) Å. (b) 300ml/min H_2/N_2 at 1100 °C for 16h, refined UO_2 lattice parameter a = 5.4697(1) Å.

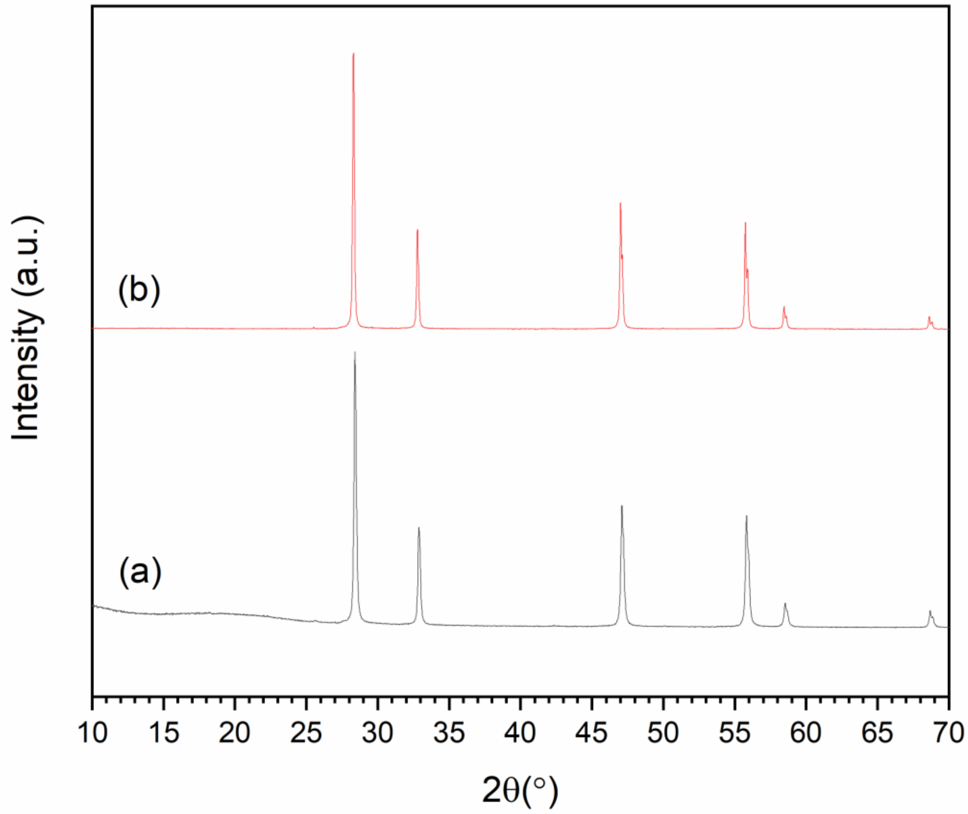

Figure S5. XRD patterns of products of U_3O_8 after gaseous reductions. (a) 300ml/min NH_3 at 1100 °C for 16h, refined UO_2 lattice parameter a = 5.4752(1) Å. (b) 300ml/min H_2/N_2 at 1100 °C for 16h, refined UO_2 lattice parameter a = 5.4692(1) Å.

Chapter 7

An investigation of the ammonolysis of β-SrUO$_4$ and CaUO$_4$ for ternary uranium oxynitride synthesis

An investigation of the ammonolysis of β-$SrUO_4$ and $CaUO_4$ for ternary uranium oxynitride synthesis

S.E. O'Sullivan[a], S.K. Sun[a], C.L. Corkhill[a], B.F. Spencer,[b] J. Buckley[c], M.C. Stennett[a] and N.C. Hyatt[a].

[a] Immobilisation Science Laboratory, Department of Materials Science and Engineering, The University of Sheffield, Mappin Street, Sheffield, S1 3JD.

[b] Sir Henry Royce Institute, Department of Materials, School of Natural Sciences, The University of Manchester, Manchester M13 9PL.

[c] Nuclear Fuel Centre of Excellence, Department of Mechanical, Aerospace and Civil Engineering, The University of Manchester, Sackville Street, Manchester, M13 9PL.

7.1 Abstract

Ammonolysis of β-$SrUO_4$ and $CaUO_4$ were explored for potential ternary uranium oxynitride synthesis in the context of accident tolerant nuclear fuels. Reaction of β-$SrUO_4$ under NH_3 produced mixtures of close to stoichiometric α-$SrUO_{4-x}$ (x ≈ 0) with unit cell dimensions a = 6.56(1), α = 34.90(1)° and V = 82.50(3) Å^3, and a volume expanded oxygen deficient α'-$SrUO_{4-x}$ (x ≈ 0.4) composition, with a = 6.57 Å, α = 35.39° V = 84.99 Å^3. The yield of α'-$SrUO_{4-x}$ was maximised when reacted under 75 ml/min NH_3 at 750 °C for 2h. Reaction of $CaUO_4$ under NH_3 produced mixtures of close to stoichiometric $CaUO_{4-x}$ (x ≈ 0) with unit cell dimensions a = 6.29, α = 35.88° and V = 76.6 Å^3, and a volume expanded oxygen deficient $CaUO_{4-x'}$ (x ≈ 0.5) composition, with a = 6.35 Å, α = 36.10° V = 79.7 Å^3. The yield of $CaUO_{4-x'}$ was maximised when reacted under 300ml/min NH_3 at 650 °C for 16h. Reduction of U^{6+} to U^{5+} in the oxygen deficient uranates was confirmed by analysis of U L_3 XANES and modelling of EXAFS data. XPS data provided no evidence for the incorporation of N within the oxygen deficient phases, based on the absence of detectable N 1s and Auger emission, which was also verified by coupled thermogravimetric mass spectroscopy analysis.

Ammonolysis of β-$SrUO_4$ and $CaUO_4$ did not, therefore, yield oxynitrides, but proved an efficient route to the synthesis of reduced α'-$SrUO_{4-x}$ and $CaUO_{4-x'}$ compositions.

7.2 Introduction

Accident tolerant nuclear fuels (ATF) are increasingly sought for the continued use of light water reactors (LWRs) in the legacy of the Fukushima Dai-ichi nuclear power plant accident of 2011. The standard Zircaloy clad UO_2 pellet assembly for LWRs shows problematic behaviour under loss of coolant accident conditions [1], with comparatively poor thermal conductivity resulting in fuel swelling and melt. Proposed ceramic ATFs include uranium nitrides, carbides and silicides [2]–[4], along with consideration of several cladding options [1], [5]–[7]. To enable the full implementation of ATF, a thorough safety case needs to be developed including consideration of design basis and beyond design basis accident scenarios. Ternary uranium oxynitrides are hypothesised products of nitride fuel corrosion, cladding failure or loss of coolant accidents. These are also of interest from a fundamental scientific perspective. Itinerant uranium 5f electrons combined with the overlap of O and N 2p orbitals have potential to exhibit interesting electronic and magnetic properties. This is similarly seen for the wider ternary oxynitride field, where tuneable manipulation of the electronic band structure gives rise to a diverse range of applications [8]–[14]. As uranium shows similar electropositive character to zirconium (relative electropositivity of the cation favouring oxynitride over nitride formation [15]) and ternary zirconium oxynitrides $LaZrO_2N$ [16] and $ZrTiON_2$ [17] exist, it is hypothesised that the ternary uranium oxynitrides should also stabilise.

The majority of uranium oxynitride literature considers binary uranium oxynitrides of the general form UO_xN_y, rather than ternary oxynitrides, the former being directly considered in the degradation of nitride nuclear fuels [18]. The first publication regarding uranium oxynitrides hails from 1895 [19], the derived composition of $U_{11}O_{25}N_5$ achieved by reaction of uranyl chloride UO_2Cl_2 with NH_3. This remains the only example of using ammonia in the synthesis of a uranium oxynitride, despite the effectiveness of this nitriding agent for the synthesis of other oxynitrides [14]. Solid solutions $UO_{2x}N_{1.5-x}$ ($0.5 < x < 1$) [20], [21] and

$UO_{2-x}N_{3x/4}$ ($0 < x < 0.5$) [22] are known , synthesised by high temperature reaction of the mixed oxide and UN or U_2N_3 nitride reagents or by carbothermal reduction of UO_2, both under an N_2 atmosphere. Reaction of UO_2 with carbon under a nitrogen atmosphere targeting a uranium carbonitride product proceeds via an intermediate oxynitride composition of $UO_{1.33}N_{0.45}$ [23]. Mixed UO_2-UN ceramic composites are also proposed as nuclear fuel options with oxynitride inclusions [24], [25]. Oxidation of uranium nitride forming an oxynitride composition is extensively explored in both experimental [18], [26]–[30] and modelling studies [31]–[33]. Examples of ternary U oxynitrides in the literature are focused on uranium-plutonium compounds of the form $(U,Pu)O_xN_y$, arising from oxygen impurities of mixed nitride fuels (U,Pu)N [34]–[36] or reaction of (U,Pu)N and $(U,Pu)O_2$ [37].

Given the paucity of ternary uranium oxynitride literature, this work sought to synthesise possible new families of such compounds. The choice of oxide precursors used for this ammonolysis synthesis investigation were the MUO_4 (M = Ca, Sr) alkali earth uranates. Strontium, particularly the ^{90}Sr isotope, is a high yield fission product of uranium, with $SrUO_4$ forming where fuel oxygen potential is high [38]. Additionally, Sr, along with Ba and Zr, were identified in the oxide "grey phase" fission product inclusions in irradiated UO_2 fuel [39]. In the MUO_4 compounds investigated, two polymorph structures are known: α-$CaUO_4$ adopts the rhombohedral α-polymorph structure in *R*-3*m* [40], whereas, $SrUO_4$ can adopt either the *R*-3*m* α-polymorph or the *Pbcm* β-polymorph, dependent on temperature [41]. The α to β transition of $SrUO_4$ occurs at 780 °C in air and is an irreversible reconstructive phase transition involving the breaking and reforming of chemical bonds [42]. Thus, appropriate synthesis approaches and conditions can be used to manipulate the choice of polymorph. α-$CaUO_4$ and α-$SrUO_4$ are characterised by U(VI) in 8 fold, body centred cubic coordination, as UO_8 polyhedra; whereas β-$SrUO_4$ is characterised by U(VI) in 6 fold coordinated UO_6 octahedra. In the former, the increased uranium coordination environment results in overbonding of the Sr cation which is compensated by anion vacancies, such that α-$SrUO_4$ stabilises as sub-stoichiometric α-$SrUO_{4-\delta}$ [41], [43]. In comparison, β-$SrUO_4$ is oxygen stoichiometric. α-$CaUO_4$ is also reported to exhibit oxygen non-stoichiometry, although with a propensity to readily oxidise [44].

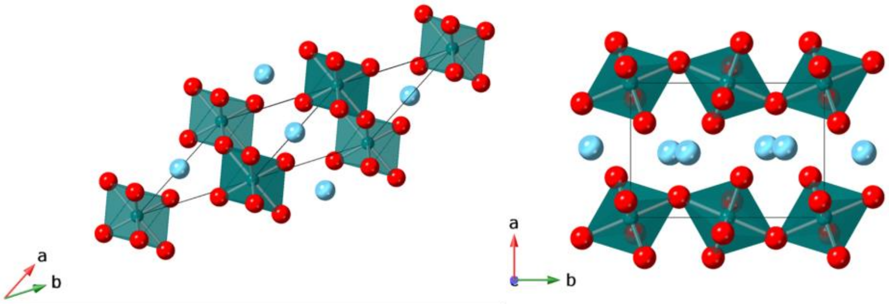

Figure 1. Structure models of α-$SrUO_4$ (left) in *R*-3*m* symmetry and β-$SrUO_4$ (right) in *Pbcm* symmetry. Light blue spheres indicate Sr cations, green polyhedral indicate U cation coordination, red spheres indicate oxygen anions. The unit cell is shown by the black line.

The sub-stoichiometric arrangements of α-$SrUO_4$ and α-$CaUO_4$ are of interest for ternary oxynitride formation. For nitrogen substitution into the oxide lattice, charge compensation must be achieved by positive defects, such as electron holes, amide defects or oxygen vacancies [45], with the latter being proven in both compounds. Additionally, Sr and Ca satisfy thermodynamic conditions that favour oxynitride over nitride formation, being sufficiently electropositive to prevent nitride stabilisation in favour of oxynitride formation [9], [15]. To this end, $CaUO_4$ and $SrUO_4$ were investigated for potential ternary uranium oxynitride synthesis.

7.3 Experimental

$SrUO_4$ and $CaUO_4$ were synthesised by milling of stoichiometric mixtures of UO_3 and metal carbonate, before repeated calcining in air at 950 °C for 8 hours with regrinding between calcines. Ammonolysis was performed in an Elite tube furnace consisting of an alumina process tube, Ar purge gas and anhydrous NH_3 reaction gas (BOC, 99.98% purity). Subsequent manipulations were performed in a positive pressure, dry Ar atmosphere glovebox to prevent oxidation of the materials. The phase assemblage was characterised by X-ray diffraction (XRD) using a Bruker D2 Phaser diffractometer with Cu Kα radiation of $\lambda = 1.5418$ Å. Determination of unit cell parameters was performed by Rietveld refinement of XRD data with an additional 10-20 wt% LaB_6 added to the prepared powder an internal standard. Rietveld refinement was performed in TOPAS [46].

U L_3 edge (17,166 eV) X-ray absorption spectroscopy (XAS) measurements were performed on beamline BL-27B, at The Photon Factory, High Energy Accelerator Research Organisation (KEK) for $SrUO_4$ compositions and beamline B18 at the Diamond Light Source STFC facility for $CaUO_4$ compositions. XAS data were acquired in transmission mode from 6 mm pressed PEG pellets of approximately 1 absorption length. XAS data were processed in ATHENA and ARTEMIS packages [47] and were compared to a suite of uranium oxide reference compounds also collected on B18. Bond valence sums of the form $V = \Sigma e^{(r0-r)/b}$ were calculated for U-O cation-anion pairs, using b = 0.37 for oxides and a reference U-O bond length r_0 of 2.075 Å [48].

Thermogravimetric analysis mass spectrometry (TG-MS) measurements were made using a Netzsch STA 449 F3 *Jupiter* thermal analyser coupled with a Netzsch QMS 403 *Aelos Quadro* quadrupole mass spectrometer and using an argon carrier gas. X-ray Photoelectron Spectroscopy (XPS) measurements were undertaken at the Photon Science Institute, University of Manchester using an ESCA2SR spectrometer (ScientaOmicron GmbH) using monochromated Al Kα radiation (1486.6 eV, 20 mA emission at 300 W, 1 mm spot size) with a base vacuum pressure of circa 1 x 10^{-9} mbar. Charge neutralisation was achieved using a low energy electron flood source (FS40A, PreVac). Binding energy scale was calibrated to the C 1s photoelectron peak at 285 eV. Analysis and component fitting was performed using Voigt-approximation peaks using CasaXPS [49] using Shirley background functions.

Colour measurement was achieved from images taken using a Canon 4000D camera with 18mm lens. Images were taken within a white LED light box containing a calibration grey card (R,G,B) (128,128,128). Colour attribution was determined by processing these images to the calibration card and extracting average (R,G,B) values as per methodology tested previously [50].

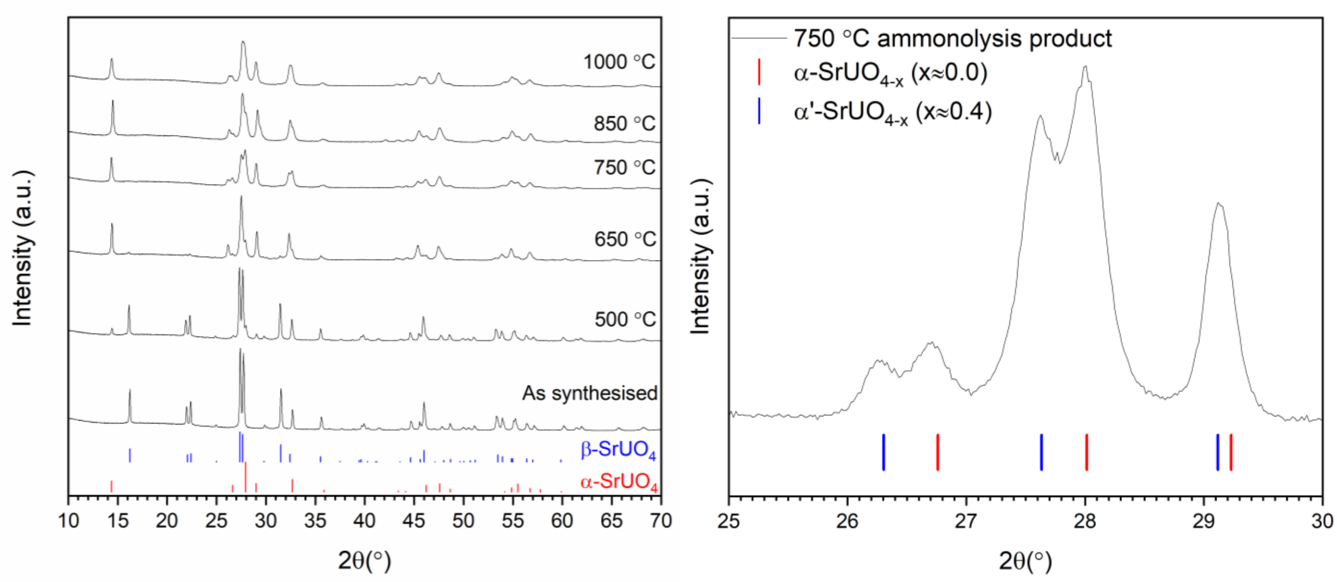

Figure 2. Left: XRD patterns of $SrUO_4$ reacted with 75 ml/min NH_3 for 2 h at 500, 650, 750, 850 and 1000 °C. Blue and red tickmarks indicate allowed reflections for β-$SrUO_4$ (PDF 01-086-3775) and α-$SrUO_4$ (PDF 01-086-3774), respectively, with the most significant reflections indexed. Right: Zoomed section of 750 °C product showing reflection splitting from presence of α-$SrUO_4$ (red) and α'-$SrUO_{4-x}$ (blue) phases of differing cell parameters.

7.4 Results and Discussion

Single phase specimens of β-$SrUO_4$ and α-$CaUO_4$ were successfully synthesised by reaction of respective carbonates with UO_3 at 950 °C in air, which was confirmed by XRD phase analysis (see Figure 2 and Figure 5). The determined unit cell parameters (Table 1 and 3) were in excellent agreement with those reported for oxygen stoichiometric β-$SrUO_4$ and α-$CaUO_4$ [42], [44], [51]. Initial ammonolysis investigations explored a temperature range of 500 to 1000 °C for β-$SrUO_4$ and 650 to 1000 °C for α-$CaUO_4$ with an applied NH_3 flow rate of 75 ml/min and reaction duration of 2h.

Figure 2 shows the XRD patterns of the as synthesised β-$SrUO_4$ regent and subsequent products of ammonolysis reactions. The XRD data of the product of ammonolysis at 500 °C, presented strong and sharp Bragg reflections characteristic of β-$SrUO_4$, together with weak reflections characteristic of α-$SrUO_{4-x}$, in particular the clearly identifiable (111) reflection at $2\theta = 14.4°$. In contrast, XRD data of the product of ammonolysis at 650 °C, evidenced almost compete conversion of the material to α-$SrUO_{4-x}$, as assessed by the relative

Sample	Phase	SG	a (Å)	b (Å)	c (Å)	α (°)	Volume (Å^3)	Phase% (±1%)
As synthesised	β	*Pbcm*	5.4982(4)	7.9825(6)	8.1288(5)	90		100
75 ml/min NH_3 500 °C 2h	β	*Pbcm*	5.4926(3)	7.9762(4)	8.1241(4)	90		92
	a	*R-3m*	6.55(1)			34.88(1)	82.04(3)	8
75 ml/min NH_3 650 °C 2h	β	*Pbcm*	5.488(3)	7.948(4)	8.113(4)	90		12
	a	*R-3m*	6.55(1)			34.91(1)	82.16(3)	13
	a'	*R-3m*	6.56(1)			35.50(1)	85.07(3)	75
75 ml/min NH_3 750 °C 2h	*a*	*R-3m*	6.56(1)			34.90(1)	82.50(3)	56
	a'	*R-3m*	6.57(1)			35.39(1)	84.99(3)	44
75 ml/min NH_3 850 °C 2h	*a*	*R-3m*	6.55(2)			35.00(2)	82.55(3)	35
	a'	*R-3m*	6.57(1)			35.45(1)	85.25(3)	65
75 ml/min NH_3 1000 °C 2h	*a*	*R-3m*	6.56(2)			34.89(3)	82.46(3)	100

Table 1. Phase analysis and refined unit cell parameters for as synthesised β-$SrUO_4$ and α-$SrUO_{4-x}$ products of reactions under 75 ml/min NH_3 at 500, 650, 750, 850 and 1000 °C. 1 e.s.d confidence intervals are given in parentheses. For *Pbcm* cell α = β = γ.

intensity of Bragg reflections, with only weak reflections of β-$SrUO_4$ present, for example the clearly identifiable (100) reflection at $2\theta = 16.1°$. The XRD data of the products from ammonolysis at 750 °C and 850 °C demonstrated the presence of two distinct phases of α-$SrUO_{4-x}$, giving rise to the obvious reflection splitting, due to the presence of a phase close to stoichiometric α-$SrUO_{4-x}$ ($x \approx 0$) with unit cell dimensions a = 6.56(1), α = 34.90(1)° and V = 82.50(3) Å^3, and a volume expanded oxygen deficient α'-$SrUO_{4-x}$ ($x \approx 0.4$) composition, with a = 6.57(1) Å, α = 35.39(1)° V = 84.99(3) Å^3 (see Table 1). The assigned stoichiometries are based on previously reported characterisation of α-$SrUO_{4-x}$, where values of $x = 0.00 \leq x \leq 0.06$ have reported cell parameters a = 6.55 Å, α = 34.8° and V = 82.0 Å^3 [42] [44] [51], while sub-stoichiometric compounds with x = 0.4 have a = 6.58 Å compounds with x = 0.4 have a = 6.58 Å, α = 35.3° and V = 85.3 Å^3 [44], [51]. This interpretation was verified from U L_3 XANES (X-ray Absorption Near Edge Spectroscopy) data, shown in Figure 3. The U

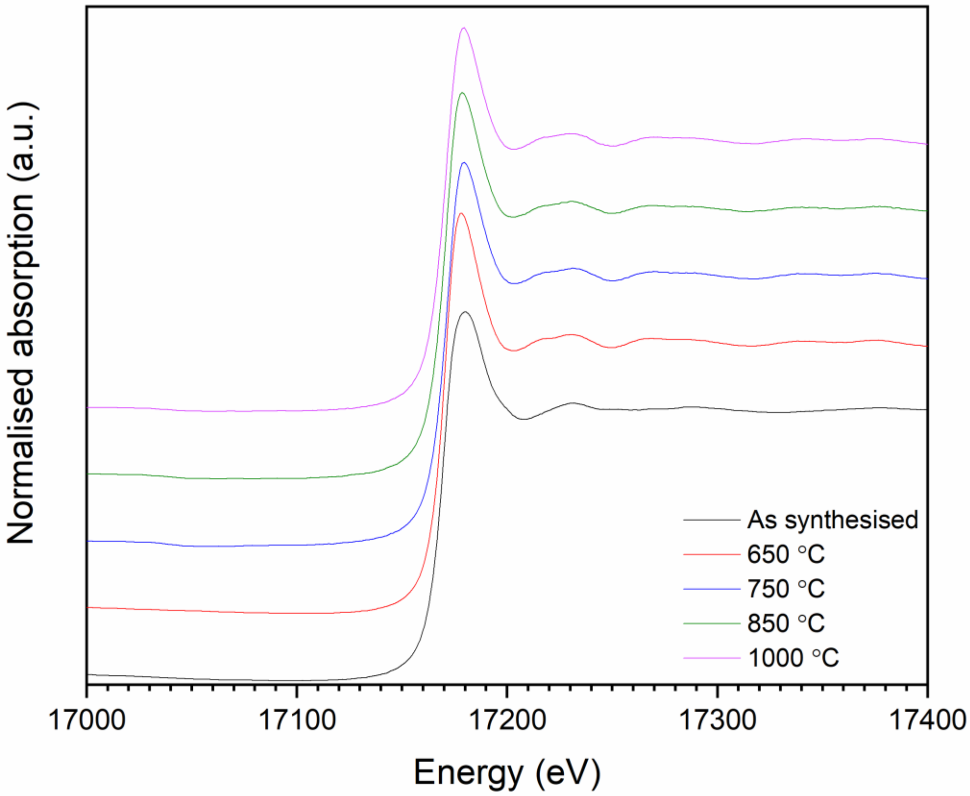

Figure 3. XANES spectra for as synthesised β-$SrUO_4$ and α-$SrUO_{4-x}$ products of reaction with 75 ml/min NH_3 for 2 h at 650, 750, 850 and 1000 °C.

L_3 XANES spectra of the α-$SrUO_{4-x}$ products of ammonolysis are all similar, implying a similar local co-ordination environment for U, and are clearly different to U L_3 XANES spectrum of the β-$SrUO_4$ starting material. Moreover, the absorption edge (E_0, determined at $\mu x(E) = 0.5$ and compared to calibration of reference compounds – see Figure S2) of the U L_3 XANES of the α-$SrUO_{4-x}$ products of ammonolysis all show small but discernible chemical shifts of 0.30 to 0.80 ± 0.05 eV, relative to the spectrum of β-$SrUO_4$ implying reduction of U^{6+} to U^{5+}. Estimated average uranium oxidation states are given in Table 2; these show reduction from 6.0(1) for the starting β-$SrUO_4$ to 5.5(1) for the most reduced composition produced at 750 °C which was determined by XRD to consist of two phases of α-$SrUO_{4-x}$ of differing stoichiometry in approximately equal proportion, thus an average uranium oxidation state of 5.5 corresponds to a 50:50 mixture of a stoichiometric α-$SrUO_{4-x}$ phase with U^{6+} ($x \approx 0.0$) and a reduced α'-$SrUO_{4-x}$ phase with U^{5+} ($x \approx 0.5$), consistent with analysis of XRD data.

Sample	U $4f_{7/2}$ binding energy (± 0.1 eV)	FWHM (± 0.1 eV)	XANES U oxidation state (v.u.)
β-$SrUO_4$	381.6	3.0	6.0(1)
75 ml/min NH_3 650 °C 2h	-	-	5.8(1)
75 ml/min NH_3 750 °C 2h	381.9	2.9	5.5(1)
75 ml/min NH_3 850 °C 2h	-	-	5.7(1)
75 ml/min NH_3 1000 °C 2h	-	-	5.8(1)

Table 2. U $4f_{7/2}$ binding energies and average U oxidation derived from XANES for as synthesised β-$SrUO_4$ and α-$SrUO_{4-x}$ products of 75 ml/min 2 h ammonolysis. 1 e.s.d confidence intervals are given in parentheses.

The products of ammonolysis exhibited a dark grey colour; the colour of the product from ammonolysis at 750 °C was determined to be (R,G,B) (71,66,58), in contrast to the cream colour (180,163,136) of the β-$SrUO_4$ reagent, as shown in Figure S1. The marked colour change was attributed to a more reduced compound, as established from U L_3 XANES data (Table 2). Tagawa and Fujino reported the synthesis of α-$SrUO_{4-x}$ by heating β-$SrUO_4$ under vacuum and under H_2 [41]. Heating under vacuum to 900 °C yielded a dark green compound of composition $SrUO_{3.6}$, whereas heating under 1 atm H_2 yielded a dark grey compound of composition $SrUO_{3.5}$, similar to observations reported above. Thus the colour of α-$SrUO_{4-x}$ is dependent on oxygen non-stoichiometry, which preferentially occurs on the O2 site [52], with concomitant reduction of U^{6+} to U^{5+}. Here, we achieved an estimated composition of α-$SrUO_{3.5}$ at a lower reaction temperature due both to the more potent NH_3 reducing agent used and flowing atmosphere, which facilitates removal of H_2O produced during the reduction [15].

XRD and U L_3 XANES evidenced the formation of oxygen deficient α-$SrUO_{4-x}$ under conditions of ammonolysis, charge compensated by reduction of U^{6+} to U^{5+}. However, N incorporation by substitution for oxygen could occur concurrently, forming anion vacancies, without the need for additional charge compensation (e.g. $3\ O \leftrightarrow 2\ N + \square$). To assess the potential for N incorporation, XPS data, shown in Figure 4, were acquired from the as synthesised β-$SrUO_4$ and α-$SrUO_{4-x}$ product resulting from ammonolysis under 75 ml/min NH_3 at 750 °C for 2 h. The high surface area of the material resulted in adsorption of adventitious carbon (as carbonate), which is reflected in the low signal to noise ratio of the

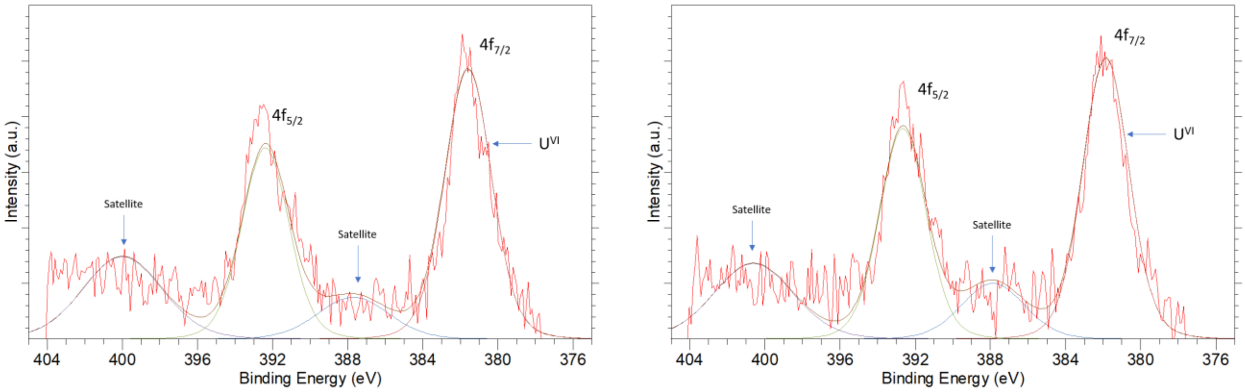

Figure 4. U 4f XPS spectra for as synthesised β-$SrUO_4$ (left) and α-$SrUO_4$ produced under 75 ml/min NH_3 at 750 °C for 2 h.

data. The XPS data present the expected U 4f doublets and were fitted with a single component consistent with U^{6+} speciation. The U $4f_{7/2}$ binding energy of 381.6(2) eV for β-$SrUO_4$ and 381.9(2) eV for α-$SrUO_{4-x}$ were in reasonable agreement with that reported for $SrUO_4$ (381.5 eV), polymorph unspecified [53]. The slightly higher binding energy of the α-$SrUO_{4-x}$ product is close to that of 382.1 eV reported for α-UO_{3-x}, which could imply surface decomposition, however, this interpretation is tentative, given the signal to noise quality of the data [54]. Significant N incorporation would be expected to yield measurable N 1s emission with a binding energy of ~400 eV and Auger peak near 1112 eV [55]. The N 1s emission overlaps the U $4f_{5/2}$ satellite which, together with the signal to noise quality of the data, complicates the analysis. Nevertheless, no discernible N 1s emission or Auger peak were observed in the XPS spectrum of α-$SrUO_{4-x}$ (or β-$SrUO_4$), from which it was concluded that no significant N incorporation was achieved. XPS data are highly surface sensitive and demonstrate surface oxidation of α-$SrUO_{4-x}$, relative to the more reduced bulk established by U L_3 XANES.

Figure 5 shows the XRD pattern for as synthesised $CaUO_4$ and products of ammonolysis at 650 – 1000 °C; the XRD data of the as synthesised material could be indexed in space group R-3m with unit cell parameters in good agreement with those of Takahashi *et al.* for stoichiometric $CaUO_4$ [44]. The XRD data of the product from ammonolysis at 650 °C, showed evidence of additional weak reflections which appear as discernible low angle “satellites” of the intense Bragg reflections (Figure 5). This was indicative of a second

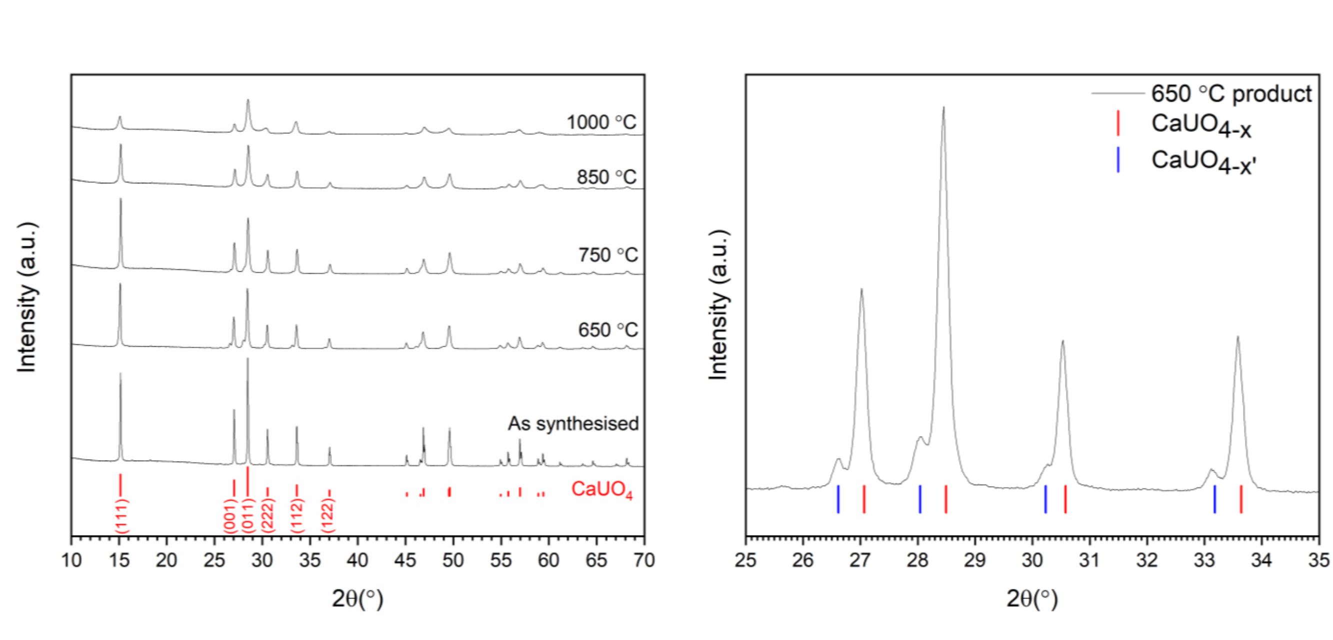

Figure 5. Left: XRD patterns of as synthesised $CaUO_4$ and $CaUO_{4-x}$ products from reaction with 75 ml/min NH_3 for 2 h at 650, 750, 850 and 1000 °C. Red tickmarks indicate allowed reflections for $CaUO_4$ (PDF 01-084-8399). Right: Zoomed section of 650 °C product showing $CaUO_{4-x}$ (red) and satellite $CaUO_{4-x'}$ (blue) reflections.

isostructural phase present at low concentration, with an expanded unit cell parameter (~79 Å^3) compared to the as synthesised material (~76 Å^3), as confirmed by the quantitative phase analysis shown in Table 3. This second phase was considered to be an oxygen deficient $CaUO_{4-x'}$ phase, based on the analysis of Takahashi *et al.* [44], who demonstrated reduction of $CaUO_4$ to yield two distinct phases with composition range $0.00 < x < 0.02$ and $0.3 < x' < 0.5$, the latter characterised by a ~4% expansion of unit cell volume compared to the former, consistent with determination of the unit cell dimensions presented in Table 3. The XRD data of the products from ammonolysis at 750-1000 °C, could also be interpreted in this way, but the additional weak reflections of the reduced $CaUO_{4-x'}$ phase appeared as low angle asymmetry on the intense Bragg reflections, rather than as distinctive "satellites". The products of $CaUO_4$ ammonolysis demonstrated a colour change from yellow-green (R,G,B) (164,143,70) to dark grey-black (49,45,41) (Figure S3), similar to that observed for oxygen deficient α-$SrUO_{4-x}$.

Gas	Flow rate (ml/min)	Dwell (h)	Phase	a (Å)	α (°)	Volume (Å^3)	XRD Phase% (±1%)
As synthesised	-	-	$CaUO_4$	6.2695(2)	36.029(1)	76.26(1)	100
NH_3	75	2	$CaUO_{4-x}$	6.283(2)	35.96(1)	76.47(8)	41
			$CaUO_{4-x'}$	6.340(1)	36.12(1)	79.24(3)	59
	75	16	$CaUO_{4-x}$	6.294(2)	35.89(2)	76.64(1)	19
			$CaUO_{4-x'}$	6.351(1)	36.13(1)	79.64(2)	81
	150	16	$CaUO_{4-x}$	6.296(2)	35.88(2)	76.6(1)	18
			$CaUO_{4-x'}$	6.355(1)	36.10(1)	79.70(2)	82
	300	16	$CaUO_{4-x}$	6.29(1)	36.0(3)	76.9(2)	12
			$CaUO_{4-x'}$	6.309(1)	36.22(1)	78.50(2)	88
5% H_2/N_2	300	16	$CaUO_{4-x}$	6.269(2)	36.03(2)	76.20(1)	18
			$CaUO_{4-x'}$	6.374(1)	35.97(1)	79.88(4)	82

Table 3. Refined unit cell parameters for as synthesised $CaUO_4$ and $CaUO_{4-x}$ products of reaction under NH_3 and 5% H_2/N_2 at 650 °C. 1 e.s.d. confidence intervals are given in parentheses.

Further optimisation of ammonolysis conditions was attempted, with the aim of increasing the yield of the reduced $CaUO_{4-x'}$ ($x' > 0.3$) product phase with an expanded unit cell volume. Ammonolysis of $CaUO_4$ under 75 ml/min NH_3 flow rate at 650 °C, but with longer reaction time of 4h or 16h, increased the yield of the $CaUO_{4-x'}$, as assessed from the relative intensity of reflections in the XRD data of Figure 6. The $CaUO_{4-x'}$ phase was evidently the major product after reaction for 16h, with a minor component of near stoichiometric $CaUO_{4-x}$ ($x < 0.02$), as shown in Table 3. Above 300 °C, NH_3 largely decomposes to H_2 and N_2; this is not an effective nitriding gas mixture due to the large enthalpy of the N-N triple bond [56]. Non-equilibrium conditions are required to limit H_2 and N_2 yield and maximise nitriding species (N, NH and NH_2), thus higher NH_3 flow rates are advantageous for ammonolysis at higher reaction temperature [14]. Therefore, ammonolysis of $CaUO_4$ under flow rates of 150 ml/min and 300 ml/min were also investigated at 650 °C for 16 h, with XRD patterns of these products presented in Figure 6. The 150 ml/min flow rate also yielded reduced $CaUO_{4-x'}$ with an expanded cell parameter as the major phase, as shown in Table 3. The yield of reduced $CaUO_{4-x'}$ was maximised for 300 ml/min flow rate, although the unit cell volume was slightly smaller compared to the other products. However, this should be interpreted with due caution since the XRD data of this product are noticeably broader, symptomatic

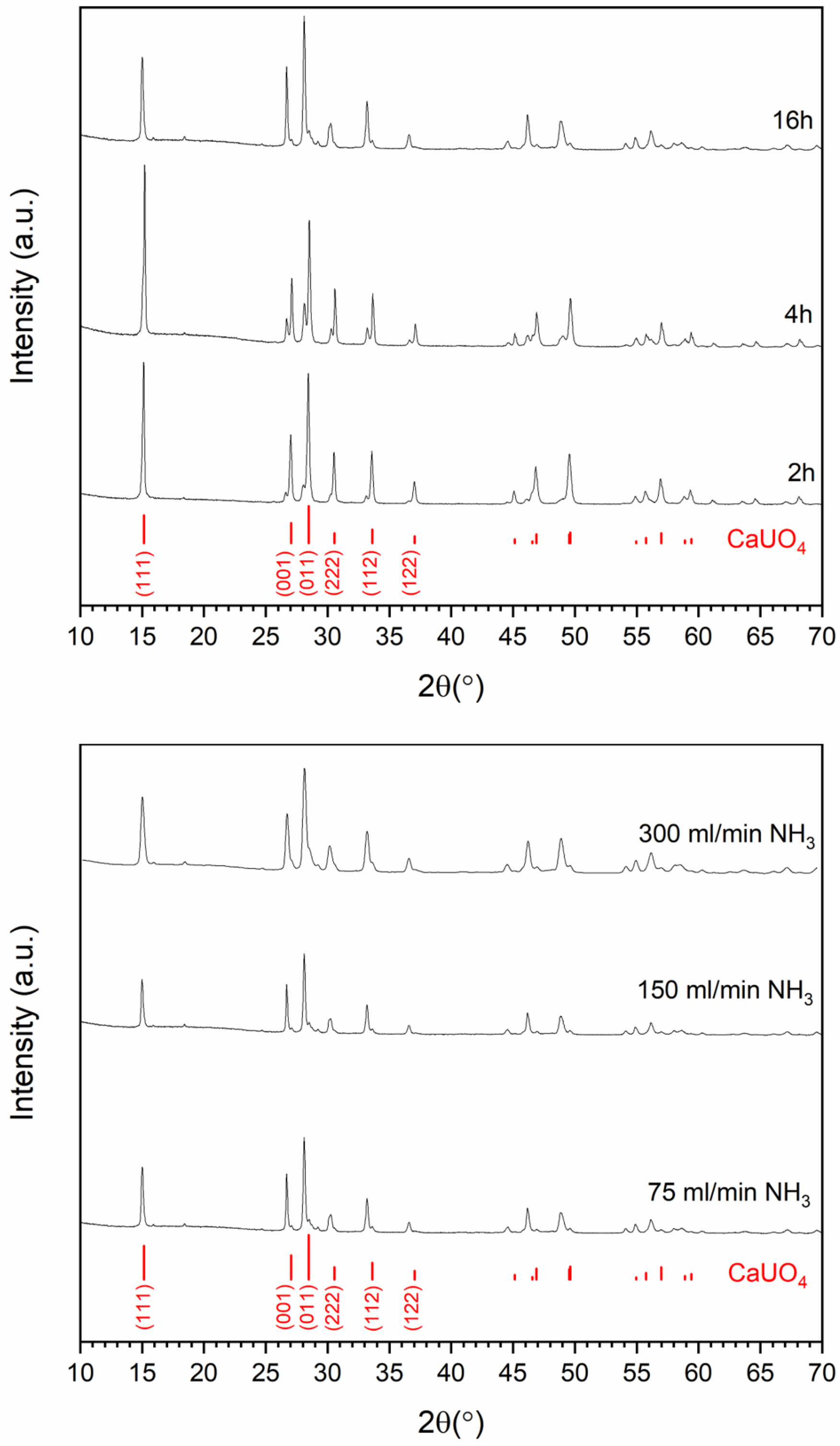

Figure 6. Investigation of reaction duration and flow rate variables for reactions of $CaUO_4$ with NH_3. Top: XRD patterns for $CaUO_{4-x}$ products of reactions with 75 ml/min NH_3 650 °C for 2, 4 and 16 h. Bottom: XRD patterns for $CaUO_{4-x}$ reactions at 650 °C for 16 h with 75, 150 and 300 ml/min NH_3 flow rates. Tickmarks indicate allowed reflections for $CaUO_4$ (PDF 01-084-8399).

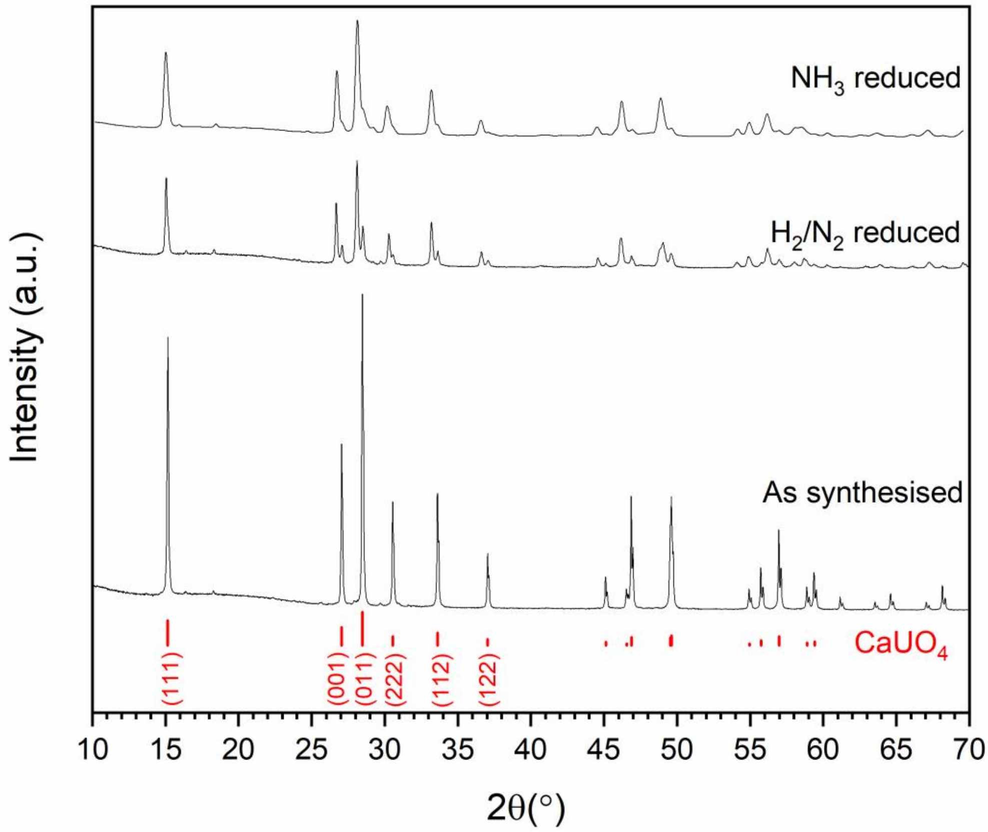

Figure 7. XRD patterns of as synthesised $CaUO_4$ (bottom) and $CaUO_{4-x'}$ produced by reaction under 300 ml/min H_2/N_2 (middle) and NH_3 (top) at 650 °C for 16 h. Tickmarks show allowed reflections for $CaUO_4$ (PDF 01-084-8399).

of reduced crystallite size, leading to greater uncertainty in the unit cell dimensions of the residual $CaUO_{4-x}$ phase.

For comparison, reduction of $CaUO_4$ was also investigated under conditions of 300 ml/min 5%H_2/N_2 for 16h. XRD analysis of the product (Figure 7) revealed a pattern consistent with formation of $CaUO_{4-x'}$ characterised by a similar expansion of unit cell volume, as shown in Table 3. As discussed above, in the context of β-$SrUO_4$, N incorporation by substitution for oxygen could occur concurrently with reduction of $CaUO_4$, forming anion vacancies, without the need for additional charge compensation. TGA-MS analysis of $CaUO_{4-x'}$ produced by reaction under 300 ml/min NH_3 at 650 °C for 16 h, was undertaken to investigate release of potentially incorporated N, by annealing under Ar flow up to 1500°C (Figure S4). TGA data showed four regions of mass loss with onset at approximately, 100 °C, 400 °C, 600 °C, and

Sample	U $4f_{7/2}$ binding energy (± 0.1 eV)	FWHM (± 0.1 eV)
As synthesised $CaUO_4$	381.7	2.3
300 ml/min H_2/N_2 650 °C 16h	382.0	1.9
300 ml/min NH_3 650 °C 16h	381.9	1.8

Table 4. U $4f_{7/2}$ binding energies for as synthesised $CaUO_4$ and $CaUO_{4-x}$ product from reaction with 300 ml/min NH_3 and 5%H_2/N_2 at 650 °C for 16 h.

1000 °C. Inspection of the coupled mass spectrometry data determined these mass losses to be associated with the release of: H_2O ($m/z = 18$), at 100 °C and 400 °C, with the latter the most significant; CO_2 ($m/z = 44$) at 650 °C, and O_2 ($m/z = 32$) at 1000 °C. The release of H_2O and CO_2 is consistent with their adsorption, and possible partial carbonation of the material, during storage. The release of O_2 above 1000 °C was associated with decomposition of $CaUO_{4-x'}$ to form perovskite type $CaUO_3$, as verified by XRD analysis. This is in broad agreement with the decomposition of $CaUO_{4-x'}$ to yield $CaUO_3$ above 1200 °C under vacuum, as reported by Pialoux and Touzelin [57]. MS channels for N ($m/z = 14$) and N_2 ($m/z = 28$) did not show any significant signal implicit of N incorporation.

Figure 8, was also undertaken to ascertain the potential for N incorporation within $CaUO_{4-x'}$ produced by ammonolysis under 300 ml/min NH_3 at 650 °C for 16 h. The U 4f doublets were fitted with a single component consistent with U^{6+} speciation, with extracted binding energies of 381.7(2) eV for the as synthesised $CaUO_4$, 382.0(2) eV for $CaUO_{4-x'}$ produced by 5% H_2/N_2 reduction, and 381.9(2) eV for $CaUO_{4-x'}$ produced by NH_3 reduction. Our data, presented in Table 4, are in reasonable agreement with the binding energy of 381.1 eV, previously reported for $CaUO_4$ [53]. The shift to higher binding energies could be consistent with surface decomposition to α-UO_3, with a binding energy of 382.1 eV [54], however, this is not conclusive. The signal to noise ratio of the XPS data were improved for the $CaUO_{4-x'}$ products when compared to the spectra of as synthesised $CaUO_4$ and β- $SrUO_4$ materials previously presented, however, no N 1s photopeak or N Auger peak were observed. Thus, consistent with TGA analysis, XPS data provided no evidence for significant N incorporation in $CaUO_{4-x'}$ produced by ammonolysis.

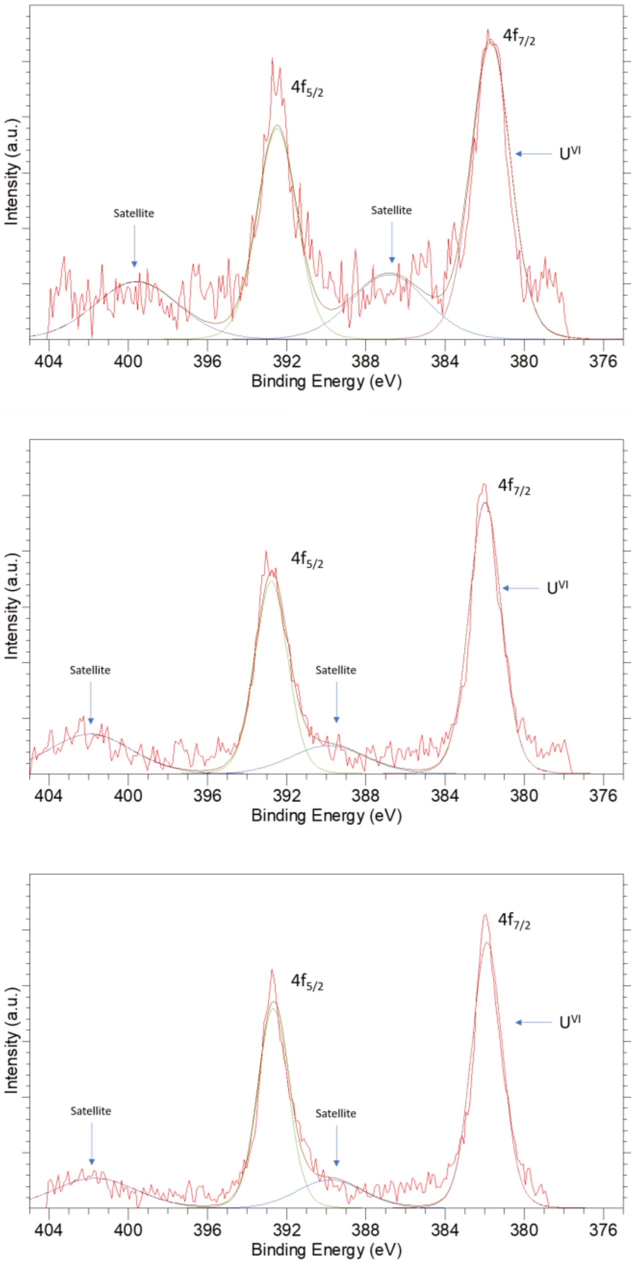

Figure 8. U 4f XPS spectra for as synthesised $CaUO_4$ (top) and $CaUO_{4\text{-}x}$ product from reaction with 300 ml/min H_2/N_2 (middle) and NH_3 (bottom) at 650 °C for 16h.

U L_3 edge XAS data were acquired from as synthesised $CaUO_4$ and reduced $CaUO_{4\text{-}x}$' produced by reduction at 650 °C for 16h, under 300 ml/min H_2/N_2 and NH_3. The U L_3 XANES shown in Figure 9 are all similar, implying a similar local co-ordination environment for U, consistent with retention of the $CaUO_4$ structure inferred by XRD. An estimation of the average uranium oxidation state was made from a linear calibration of the absorption edge E_0, defined for $\mu x(E) = 0.5$, from a suite of reference compounds (Figure S5). The estimated average uranium oxidation states were 6.0(1) v.u. for the as synthesised $CaUO_4$,

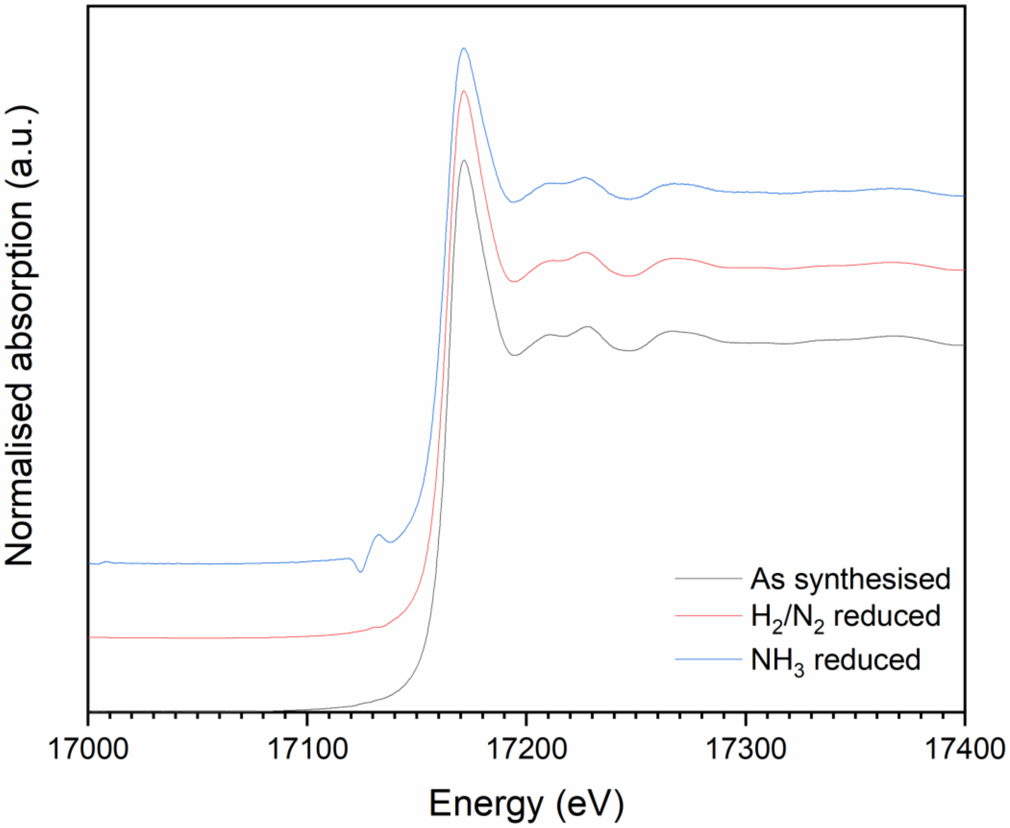

Figure 9. XANES spectra for as synthesised $CaUO_4$ and $CaUO_{4-x}$ produced from reaction under 300 ml/min H_2/N_2 and NH_3 at 650 °C for 16 h. The anomalous pre-edge feature in the data of the NH_3 reduced material is due to an insufficiently homogeneous specimen, such that the monochromator glitch at this energy is not adequately normalised.

5.5(1) v.u. for the $CaUO_{4-x'}$ product from of H_2/N_2 annealing (i.e. $x' \approx 0.25$), and 5.0(1) v.u. for the $CaUO_{4-x'}$ product of NH_3 annealing (i.e. $x' \approx 0.5$). In the present case, the reduced $CaUO_{4-x'}$ phase comprises the majority of the material, (>80% as estimated by XRD), but with a significant minor component of near stoichiometric $CaUO_{4-x}$ ($x < 0.02$). The determined oxygen stoichiometry is thus averaged over the material and, therefore, dominated by the contribution of the reduced $CaUO_{4-x'}$ phase.

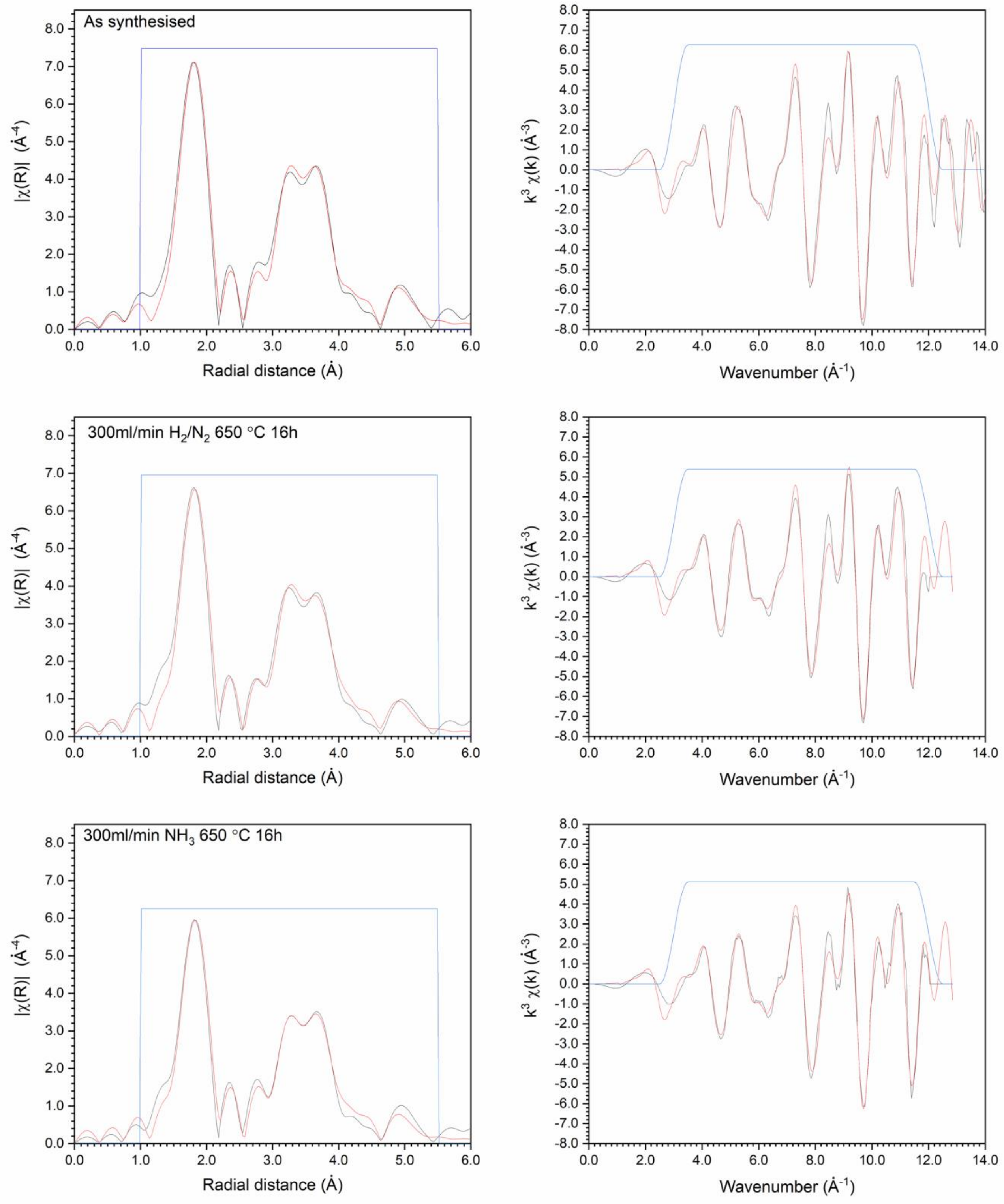

Figure 10. EXAFs fits for as synthesised $CaUO_4$ (top), $CaUO_{4-x}$ produced by reduction under 300 ml/min H_2/N_2 (middle) and NH_3 (bottom) at 650 °C for 16 h, showing the magnitude of the Fourier transforms (left) and k^3 weighted spectra (right). Black line indicates the measured spectra, red line indicates the applied model fit, blue line indicates the fitting window.

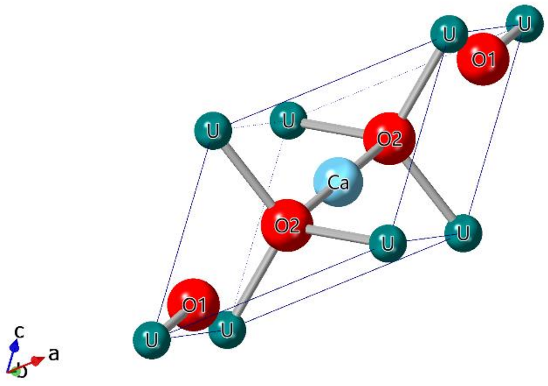

Figure 11. Unit cell of $CaUO_4$ (PDF 01-084-8399) with site labelling. Ca cations are shown in blue, U cations in green and O anions in red.

Figure 10 compares the Fourier transformed EXAFS data of as synthesised $CaUO_4$ with the $CaUO_{4-x'}$ products and shows that the amplitude of the first shell peak of the latter are reduced compared to the former. Additionally, the Fourier transformed data of $CaUO_{4-x'}$ show a subtle shoulder feature on the first shell peak at ~1.3 Å (uncorrected for phase shift) that was not observed to be present for as synthesised $CaUO_4$. The first shell peak in the Fourier Transform arises from scattering of the photoelectron by the O nearest neighbours to the U absorber and, therefore, these observations suggest a reduction in the average U co-ordination number, consistent with reduced oxygen stoichiometry. Data of as synthesised $CaUO_4$ were fitted using a local cluster model, based on the published crystal structure [43]; this afforded an excellent fit to the EXAFS data (R = 2.9%), with refined path lengths within 3 e.s.d. of values determined from crystallography. This enabled determination of the amplitude reduction factor $S_0^2 = 0.76(7)$; in general, it is assumed that the value of S_0^2 is transferrable between materials for a given element studied at the same beamline [58]. The S_0^2 parameter is correlated with refinement of path amplitudes, i.e., co-ordination number, and therefore to estimate the oxygen stoichiometry of reduced $CaUO_{4-x'}$ phases, we fixed $S_0^2 = 0.76$ as determined for as synthesised $CaUO_4$. Considering the unit cell of $CaUO_4$, shown in Figure 11, there are two O1 atoms and two O2 atoms. Oxygen non-stoichiometry in $CaUO_{4-x'}$ is known to arise from oxygen vacancies on the O2 site [44]. The oxygen stoichiometry can thus be expressed as the sum of the O1 and O2 sites, scaled to account for vacancies on the latter, that is, $CaUO_{2+2y}$. To model such vacancies, the local cluster

Sample	Estimated U valence from XANES (v.u.)	y scalar in EXAFS model (dimensionless)	Estimated composition $CaUO_{2+2y}$	BVS (v.u.)
As synthesised	6.0(1)	1.00	$CaUO_{4.00}$	6.24
300 ml/min H_2/N_2 650 °C 16 h	5.5(1)	0.86	$CaUO_{3.72}$	5.78
300 ml/min NH_3 650 °C 16h	5.0(1)	0.78	$CaUO_{3.56}$	5.45

Table 5. XANES analysis, EXAFS parameters and bond valence sums for as synthesised $CaUO_4$ and $CaUO_{4-x}$ produced by reduction under 300 ml/min H_2/N_2 and NH_3 at 650 °C for 16 h. Estimated U valence is derived from linear regression to uranium standards. y scalar applied to S_0^2 amplitude reduction factor in EXAFS models to account for oxygen non-stoichiometry. Full EXAFS outputs are given in Table S1. See text for details. 1 e.s.d confidence intervals are given in parentheses.

model was modified to include a refinable factor y applied to scale the contribution of U-O2 paths (labelled O11.1 in FEFF). This oxygen vacancy model afforded excellent fits to the data of $CaUO_{4-x'}$ produced by reduction at 650 °C for 16h, under 300 ml/min H_2/N_2 and NH_3, yielding estimated average oxygen stoichiometries of $x' = 2 - 2y = 0.28(3)$ and $x' = 0.44(4)$, and thus average U oxidation states of 5.44(6) and 5.12(8) v.u., respectively, in excellent agreement with the XANES determination. Bond valence sum calculations, $V = \Sigma e^{(r0-r)/b}$, where $b = 0.37$ and the U^{6+}-O bond length $r_0 = 2.075$ Å [48], assuming the refined oxygen stoichiometry, afforded average U oxidation states of 6.24 v.u. for near stoichiometric $CaUO_{4-x}$, 5.78 v.u. for $CaUO_{4-x'}$ produced by 5%H_2/N_2 annealing, and 5.45 v.u. for $CaUO_{4-x'}$ produced by NH_3 annealing, in broad agreement with the determined degree of non-stoichiometry. Results are summarised in Table 5, the refined model parameters are shown in Table S1. The inferred average stoichiometry of the product, $CaUO_{3.56}$, is in excellent agreement with that expected from the weighted contributions of 12 wt.% $CaUO_{4-x}$ ($x \approx 0.0$) and 88 wt.% $CaUO_{4-x'}$ ($x' \approx 0.5$) determined from quantitative phase analysis of XRD data (Table 3).

The mechanism of reduction of $CaUO_4$ and the limit of stoichiometry for the compound is not definitively established. Tagawa *et al.* propose a two stage reaction reducing $CaUO_4$ under H_2 to $CaUO_{3.55}$ above 550 °C and then $CaUO_{3.5}$ above 730 °C calculated from thermogravimetric analysis [59]. Prodan and Boswell propose an alternating arrangement of microdomains arising from an ordered oxygen defect structure [60] corresponding to compositions of $CaUO_{3.67}$ and $CaUO_{3.5}$. The apparent limit of stoichiometry indicated by more recent neutron diffraction studies is given in the range of α-$MUO_{3.6-3.7}$ (M = Sr, Ca) when reduced under H_2 [61]. Our reduced phase composition of $CaUO_{3.5}$, derived from EXAFS modelling, would suggest a greater concentration of oxygen vacancies has been achieved by use of NH_3 instead of H_2. These vacancies have been stabilised at room temperature given the subsequent characterisation performed at ambient temperatures. Neutron diffraction studies could provide better resolution of oxygen positions for structure determination and relative order or disorder of the stabilised vacancy structure. Previous work by Murphy *et al.* found reversible, first order phase transitions for both $CaUO_4$ and α-$SrUO_4$ when heated in a high purity H_2 atmosphere, providing a critical number of oxygen vacancies are generated [62], [63]. Above 450 °C, the respective delta polymorphs showed ordered oxygen vacancies and resultant lowered symmetry, indexed in the triclinic P-1 space group. The disordered R-3m symmetry is recovered upon cooling and the transition is purely thermodynamic in origin. For the proposed vacancy concentration in the ammonolysis samples discussed here, it would be interesting to identify whether this transition occurs in the same manner as previously reported given the differing, non-equilibrium thermodynamics required for NH_3 use. This may further build upon the proposed use of ordered vacancy structures for functional materials design [63]. While the intended synthesis of ternary oxynitrides was not achieved, this work demonstrates a careful and systematic optimisation of reduction of α-$SrUO_4$ and $CaUO_4$ under NH_3 to yield α-$SrUO_{3.5}$ and $CaUO_{3.5}$.

7.5 Conclusions

Ammonolysis reactions of $SrUO_4$ and $CaUO_4$ were explored for ternary uranium oxynitride synthesis. Although no evidence for oxynitride synthesis was found, reaction of β-$SrUO_4$ under 75ml/min NH_3 for 2h prompted a partial phase transition to α-$SrUO_{4-x}$ at 500 °C, with complete conversion achieved for reaction at 750 °C. Above this temperature, two phases of α-$SrUO_{4-x}$ were present in the product, evident as low angle “satellite” reflections in XRD data. This was most pronounced for the 750 °C product where quantitative phase analysis determined the two phases to be in approximately equal proportion. XRD and XANES analysis identified these as near stoichiometric α-$SrUO_{4-x}$ ($x \approx 0.0$) phase containing U^{6+} and a volume expanded, sub-stoichiometric α'-$SrUO_{3.5}$ phase ($x \approx 0.5$) containing U^{5+}. Similarly, reaction of $CaUO_4$ under 75 ml/min NH_3 for 2h resulted in the formation of a reduced isostructural $CaUO_{4-x}$ phase at 650 °C. The yield of this phase was optimised by systematic investigation of the ammonolysis variables, with the maximum yield of $CaUO_{4-x'}$ in the product of reaction at 650 °C under 300 ml/min NH_3 for 16h. Analysis by XPS and TGA-MS did not identify nitrogen doping in this product. EXAFS models were produced to estimate the stoichiometry of this product by refinement of the co-ordination number. The value of x' in $CaUO_{4-x'}$ was calculated at 0.44(4), corresponding to a reduced composition of $CaUO_{3.5}$, with an average uranium valence of 5.0(1) v.u.

7.6 Acknowledgements

Components of this research utilised the HADES/MIDAS facility at the University of Sheffield established with financial support from EPSRC and BEIS, under grant EP/T011424/1 [64]. The authors are grateful for financial support from EPSRC under grant numbers EP/L015390/1 and EP/S01019X/1. XPS measurement was supported by the Henry Royce Institute, funded through EPSRC grants EP/R00661X/1, EP/P025021/1 and EP/P025498/1.

7.7 References

[1] G. J. Youinou and R. S. Sen, "Impact of accident-tolerant fuels and claddings on the overall fuel cycle: A preliminary systems analysis," *Nucl. Technol.*, vol. 188, no. 2, pp. 123–138, 2014, doi: 10.13182/NT14-22.

[2] Y. Arai, "Nitride fuel," in *Comprehensive Nuclear Materials*, vol. 3, R. Konings, Ed. Oxford: Elsevier Inc., 2012, pp. 41–54.

[3] W. E. Lee, M. Gilbert, S. T. Murphy, and R. W. Grimes, "Opportunities for advanced ceramics and composites in the nuclear sector," *J. Am. Ceram. Soc.*, vol. 96, no. 7, pp. 2005–2030, 2013, doi: 10.1111/jace.12406.

[4] K. Johnson, V. Ström, J. Wallenius, and D. A. Lopes, "Oxidation of accident tolerant fuel candidates," *J. Nucl. Sci. Technol.*, vol. 54, no. 3, pp. 280–286, 2017, doi: 10.1080/00223131.2016.1262297.

[5] C. R. F. Azevedo, "Selection of fuel cladding material for nuclear fission reactors," *Eng. Fail. Anal.*, vol. 18, no. 8, pp. 1943–1962, 2011, doi: 10.1016/j.engfailanal.2011.06.010.

[6] L. J. Ott, K. R. Robb, and D. Wang, "Preliminary assessment of accident-tolerant fuels on LWR performance during normal operation and under DB and BDB accident conditions," *J. Nucl. Mater.*, vol. 448, no. 1–3, pp. 520–533, 2014, doi: 10.1016/j.jnucmat.2013.09.052.

[7] S. J. Zinkle, K. A. Terrani, J. C. Gehin, L. J. Ott, and L. L. Snead, "Accident tolerant fuels for LWRs: A perspective," *J. Nucl. Mater.*, vol. 448, no. 1–3, pp. 374–379, 2014, doi: 10.1016/j.jnucmat.2013.12.005.

[8] A. Fuertes, "Chemistry and applications of oxynitride perovskites," *J. Mater. Chem.*, vol. 22, no. 8, pp. 3293–3299, 2012, doi: 10.1039/C2JM13182J.

[9] A. Fuertes, "Metal oxynitrides as emerging materials with photocatalytic and electronic properties," *Mater. Horizons*, vol. 2, no. 5, pp. 453–461, 2015, doi: 10.1039/c5mh00046g.

[10] F. Tessier and R. Marchand, "Ternary and higher order rare-earth nitride materials: synthesis and characterization of ionic-covalent oxynitride powders," *J. Solid State Chem.*, vol. 171, no. 1–2, pp. 143–151, Feb. 2003, doi: 10.1016/S0022-4596(02)00201-3.

[11] À. R. Garcia, C. Clausell, and A. Barba, "Oxynitride glasses: a review," *Boletín la Soc. Española Cerámica y Vidr.*, vol. 55, no. 6, pp. 209–218, 2016, doi: https://doi.org/10.1016/j.bsecv.2016.09.004.

[12] R.-J. Xie and H. T. (Bert) Hintzen, "Optical Properties of (Oxy)Nitride Materials: A Review," *J. Am. Ceram. Soc.*, vol. 96, no. 3, pp. 665–687, 2013, doi: 10.1111/jace.12197.

[13] R. Aguiar, D. Logvinovich, A. Weidenkaff, A. Rachel, A. Reller, and S. G. Ebbinghaus, "The vast colour spectrum of ternary metal oxynitride pigments," *Dye. Pigment.*, vol. 76, no. 1, pp. 70–75, 2008, doi: 10.1016/j.dyepig.2006.08.029.

[14] S. G. Ebbinghaus *et al.*, "Perovskite-related oxynitrides - Recent developments in synthesis, characterisation and investigations of physical properties," *Prog. Solid State Chem.*, vol. 37, no. 2–3, pp. 173–205, 2009, doi: 10.1016/j.progsolidstchem.2009.11.003.

[15] S. H. Elder, F. J. DiSalvo, L. Topor, and A. Navrotsky, "Thermodynamics of Ternary Nitride Formation by Ammonolysis: Application to $LiMoN_2$, Na_3WN_3, and Na_3WO_3N," *Chem. Mater.*, vol. 5, no. 10, pp. 1545–1553, 1993, doi:

10.1021/cm00034a027.

[16] S. J. Clarke, B. P. Guinot, C. W. Michie, M. J. C. C. Calmont, and M. J. Rosseinsky, “Oxynitride perovskites: Synthesis and structures of $LaZrO_2N$, $NdTiO_2N$, and $LaTiO_2N$ and comparison with oxide perovskites,” *Chem. Mater.*, vol. 14, no. 1, pp. 288–294, 2002, doi: 10.1021/cm010577v.

[17] S. J. Clarke, C. W. Michie, and M. J. Rosseinsky, “New Zirconium Titanium Oxynitrides Obtained by Ammonolysis of Zirconium Titanate,” *Chem. Mater.*, vol. 12, no. 4, pp. 863–865, 2000, doi: 10.1021/cm990658f.

[18] A. F. Carley, P. Nevitt, and P. Roussel, “The interaction of uranium metal with nitrogen oxides: The formation of an oxynitride surface layer,” *J. Alloys Compd.*, vol. 448, no. 1–2, pp. 355–362, Jan. 2008, doi: 10.1016/j.jallcom.2007.05.028.

[19] E. F. Smith and J. M. Matthews, “Uranium Oxynitride and Uranium Dioxide.,” *J. Am. Chem. Soc.*, vol. 17, no. 9, pp. 686–688, 1895, doi: 10.1021/ja02164a003.

[20] P. L. Blum, J. Laugier, and J. M. Martin, “Section of ternary uranium-oxygen-nitrogen diagram,” *Comptes rendus hebdomadaires des sciences de l’Académie des sciences Série C*, vol. 268, no. 2. p. 148, 1969.

[21] P. Blum, J. Laugier, J. Martin, and J. Morlevat, “Existence and nature of the oxynitrides of uranium,” 1968, [Online]. Available: https://www.osti.gov/biblio/4526238.

[22] T. B. Lindemer, “Chemical thermodynamic representation of nonstoichiometry in UO2-xN3x/4,” *Calphad*, vol. 13, no. 2, pp. 109–113, 1989.

[23] T. B. Lindemer, “Kinetics of the UO_2-C-N_2 Reaction at 1700°C,” *J. Am. Ceram. Soc.*, vol. 55, no. 12, pp. 601–605, 1972, doi: 10.1111/j.1151-2916.1972.tb13452.x.

[24] B. J. Jaques *et al.*, “Synthesis and sintering of UN-UO_2 fuel composites,” *J. Nucl. Mater.*, vol. 466, pp. 745–754, 2015, doi: http://dx.doi.org/10.1016/j.jnucmat.2015.06.029.

[25] J. H. Yang, D. J. Kim, K. S. Kim, and Y. H. Koo, “UO_2 UN composites with enhanced uranium density and thermal conductivity,” *J. Nucl. Mater.*, vol. 465, pp. 509–515, 2015, doi: http://dx.doi.org/10.1016/j.jnucmat.2015.06.039.

[26] M. Eckle and T. Gouder, “Photoemission study of UN_xO_y and UC_xO_y in thin films,” *J. Alloys Compd.*, vol. 374, no. 1–2, pp. 261–264, Jul. 2004, doi: 10.1016/j.jallcom.2003.11.121.

[27] L. Luo *et al.*, “Extended study on oxidation behaviors of $UN_{0.68}$ and $UN_{1.66}$ by XPS,” *J. Nucl. Mater.*, vol. 501, pp. 371–380, 2018, doi: https://doi.org/10.1016/j.jnucmat.2018.01.020.

[28] L. Lu *et al.*, “The initial oxidation behaviors of uranium nitride UN_x (x = 0, 0.23, 0.68, 1.66) films,” *J. Nucl. Mater.*, vol. 480, pp. 189–194, 2016, doi: 10.1016/j.jnucmat.2016.08.025.

[29] K. Liu *et al.*, “Initial oxidation behaviors of nitride surfaces of uranium by XPS analysis,” *Appl. Surf. Sci.*, vol. 280, pp. 268–272, 2013, doi: https://doi.org/10.1016/j.apsusc.2013.04.147.

[30] L. Luo, L. Lu, D. Zhao, H. Zhang, T. Jing, and K. Liu, “Surface oxidation on $U_2N_{3+x}O_y$ films in oxygen atmosphere by XPS,” *J. Electron Spectros. Relat. Phenomena*, vol. 217, pp. 6–10, 2017, doi: https://doi.org/10.1016/j.elspec.2017.03.008.

[31] D. Bocharov, D. Gryaznov, Y. F. Zhukovskii, and E. A. Kotomin, “Ab initio modeling of oxygen impurity atom incorporation into uranium mononitride surface and sub-

surface vacancies," *J. Nucl. Mater.*, vol. 416, no. 1–2, pp. 200–204, 2011, doi: 10.1016/j.jnucmat.2010.11.090.

[32] D. Bocharov, D. Gryaznov, Y. F. Zhukovskii, and E. A. Kotomin, "Ab initio simulations of oxygen interaction with surfaces and interfaces in uranium mononitride," *J. Nucl. Mater.*, vol. 435, no. 1–3, pp. 102–106, 2013.

[33] X. Wang *et al.*, "Insight on the oxidation resistance of UO_xN_y layers: A density functional study," *Comput. Mater. Sci.*, vol. 123, pp. 224–231, 2016, doi: http://dx.doi.org/10.1016/j.commatsci.2016.06.029.

[34] K. Richter and C. Sari, "Investigation of the operational limits of uranium-plutonium nitride fuels," *J. Nucl. Mater.*, vol. 184, no. 3, pp. 167–176, 1991, doi: http://dx.doi.org/10.1016/0022-3115(91)90537-H.

[35] D. Y. Lyubimov, I. A. Deryabin, G. S. Bulatov, and K. N. Gedgovd, "Thermodynamic Modelling of the Phase Composition of Mixed Uranium-Plutonium Mononitride with Impurity Oxygen Under Irradiation to Burnup 140 GW·days/ton and Temperature 900-1400 K," *At. Energy*, vol. 118, no. 1, pp. 32–39, 2015, doi: 10.1007/s10512-015-9952-2.

[36] D. D. Sood, R. Agarwal, and V. Venugopal, "Phase diagram calculations of the U-Pu-N system with carbon and oxygen impurities," *J. Nucl. Mater.*, vol. 247, pp. 293–300, 1997, doi: https://doi.org/10.1016/S0022-3115(97)00077-9.

[37] F. Delvoye, "Investigation on uranium and plutonium nitrides with low oxygen and carbon contents," France, 1988. [Online]. Available: http://inis.iaea.org/search/search.aspx?orig_q=RN:19091999.

[38] K. Tokushima, K. Tanaka, K. Kurosaki, Y. Ohishi, H. Muta, and S. Yamanaka, "Thermophysical properties of $SrUO_4$," *J. Nucl. Mater.*, vol. 419, no. 1–3, pp. 353–356, 2011, doi: 10.1016/j.jnucmat.2011.06.022.

[39] H. Kleykamp, J. O. Paschoal, R. Pejsa, and F. Thümmler, "Composition and structure of fission product precipitates in irradiated oxide fuels: Correlation with phase studies in the Mo-Ru-Rh-Pd and BaO-UO_2-ZrO_2-MoO_2 Systems," *J. Nucl. Mater.*, vol. 130, pp. 426–433, 1985, doi: https://doi.org/10.1016/0022-3115(85)90329-0.

[40] W. H. Zachariasen, "Crystal chemical studies of the 5f-series of elements. I. New structure types," *Acta Crystallogr.*, vol. 1, no. 5, pp. 265–268, 1948, doi: 10.1107/s0365110x48000703.

[41] H. Tagawa and T. Fujino, "Phase transformation of strontium monouranate (VI)," *J. Inorg. Nucl. Chem.*, vol. 40, no. 12, pp. 2033–2036, 1978, doi: https://doi.org/10.1016/0022-1902(78)80197-3.

[42] G. L. Murphy *et al.*, "Nonstoichiometry in Strontium Uranium Oxide: Understanding the Rhombohedral–Orthorhombic Transition in $SrUO_4$," *Inorg. Chem.*, vol. 55, no. 18, pp. 9329–9334, 2016, doi: 10.1021/acs.inorgchem.6b01391.

[43] G. Murphy *et al.*, "Structural studies of the rhombohedral and orthorhombic monouranates: $CaUO_4$, α-$SrUO_4$, β-$SrUO_4$ and $BaUO_4$," *J. Solid State Chem.*, vol. 237, pp. 86–92, 2016, doi: 10.1016/j.jssc.2016.01.019.

[44] K. Takahashi, T. Fujino, and L. R. Morss, "Crystal chemical and thermodynamic study on $CaUO_{4-x}$, $(Ca_{0.5}Sr_{0.5})UO_{4-x}$, and α-$SrUO_{4-x}$ ($x = 0 \sim 0.5$)," *J. Solid State Chem.*, vol. 105, no. 1, pp. 234–246, 1993, doi: 10.1006/jssc.1993.1211.

[45] J. M. Polfus, T. Norby, and R. Haugsrud, "The defect chemistry of nitrogen in oxides: A review of experimental and theoretical studies," *J. Solid State Chem.*, vol. 198, pp.

65–76, 2013, doi: 10.1016/j.jssc.2012.09.010.

[46] TOPAS, *V4, General profile and structure analysis software for powder diffraction data- User's Manual.* Karlsruhe, Germany: Bruker AXS GmbH, 2008.

[47] B. Ravel and M. Newville, "ATHENA, ARTEMIS, HEPHAESTUS: data analysis for X-ray absorption sepctroscopy using IFEFFIT," *J. Synchrotron Radiat.*, vol. 12, pp. 537–541, 2005.

[48] I. D. Brown and D. Altermatt, "Bond-Valence Parameters Obtained from a Systematic Analysis of the Inorganic Crystal Structure Database," *Acta Crystallogr. Sect. B*, vol. 244, no. 2, pp. 244–247, 1985, doi: 10.1107/S0108768185002063.

[49] N. Fairley, "CasaXPS." Casa Software Ltd, 2020, [Online]. Available: http://www.casaxps.com/.

[50] N. B. A. Thompson, S. E. O'Sullivan, R. J. Howell, D. J. Bailey, M. R. Gilbert, and N. C. Hyatt, "Objective Colour Analysis from Digital Images as a Nuclear Forensic Tool," *Forensic Sci. Int.*, p. 110678, 2020, doi: https://doi.org/10.1016/j.forsciint.2020.110678.

[51] T. Fujino, N. Masaki, and H. Tagawa, "The crystal structures of α and γ $SrUO_4$," *Zeitschrift für Krist. - Cryst. Mater.*, vol. 145, no. 3–4, pp. 299–309, 1977, doi: doi:10.1524/zkri.1977.145.3-4.299.

[52] T. Fujino and L. R. Morss, "Oxygen nonstoichiometry in calcium and strontium uranates CaUO4-x and SrUO4-x: Lattice parameters and enthalpies of formation," *Inorganica Chim. Acta*, vol. 94, no. 1–3, p. 123, 1984, doi: 10.1016/s0020-1693(00)94589-4.

[53] G. C. Allen, A. J. Griffiths, and B. J. Lee, "X-ray photoelectron spectroscopy of alkaline earth metal uranate complexes," *Transit. Met. Chem.*, vol. 3, no. 1, pp. 229–233, 1978, doi: 10.1007/BF01393553.

[54] G. C. Allen and N. R. Holmes, "Surface characterisation of α-, β-, γ-, and δ-UO_3 using X-ray photoelectron spectroscopy," *J. Chem. Soc. Dalt. Trans.*, no. 12, pp. 3009–3015, 1987, doi: 10.1039/DT9870003009.

[55] "NIST X-ray Photoelectron Spectroscopy Database, NIST Standard Reference Database Number 20." National Institute of Standards and Technology, Gaithersburg, 2000, [Online]. Available: http://dx.doi.org/10.18434/T4T88K.

[56] R. Marchand, Y. Laurent, J. Guyader, P. L'Haridon, and P. Verdier, "Nitrides and oxynitrides: Preparation, crystal chemistry and properties," *J. Eur. Ceram. Soc.*, vol. 8, no. 4, pp. 197–213, 1991, doi: 10.1016/0955-2219(91)90096-I.

[57] A. Pialoux and B. Touzelin, "Étude du système U–Ca–O par diffractométrie de rayons X à haute température," *J. Nucl. Mater.*, vol. 255, no. 1, pp. 14–25, 1998, doi: https://doi.org/10.1016/S0022-3115(98)00015-4.

[58] S. D. Kelly, D. Hesterberg, and B. Ravel, "Analysis of Soils and Minerals Using X-ray Absorption Spectroscopy," *Methods of Soil Analysis Part 5—Mineralogical Methods.* pp. 387–463, Apr. 15, 2008, doi: https://doi.org/10.2136/sssabookser5.5.c14.

[59] H. Tagawa, T. Fujino, and T. Yamashita, "Formation and some chemical properties of of alkaline-earth metal monouranates," *J. Inorg. Nucl. Chem.*, vol. 41, no. 12, 1979, doi: 10.1016/0022-1902(79)80114-1.

[60] A. Prodan and F. W. Boswell, "The defect structure of reduced $CaUO_4$," *Acta Crystallogr. B.*, vol. 42, no. 2, pp. 141–146, 1986, doi: 10.1107/S0108768186098452.

[61] G. L. Murphy, Z. Zhang, and B. J. Kennedy, *The Solid-State Chemistry of AUO_4*

Ternary Uranium Oxides: A Review. Singapore: World Scientific Publishing Co. Pte. Ltd., 2019.

[62] G. L. Murphy *et al.*, “Controlling Oxygen Defect Formation and Its Effect on Reversible Symmetry Lowering and Disorder-to-Order Phase Transformations in Nonstoichiometric Ternary Uranium Oxides,” *Inorg. Chem.*, vol. 58, no. 9, pp. 6143–6154, 2019, doi: 10.1021/acs.inorgchem.9b00406.

[63] G. L. Murphy *et al.*, “Unexpected Crystallographic Phase Transformation in Nonstoichiometric $SrUO_{4-x}$: Reversible Oxygen Defect Ordering and Symmetry Lowering with Increasing Temperature,” *Inorg. Chem.*, vol. 57, no. 10, pp. 5948–5958, 2018, doi: 10.1021/acs.inorgchem.8b00463.

[64] N. C. Hyatt, C. L. Corkhill, M. C. Stennett, R. J. Hand, L. J. Gardner, and C. L. Thorpe, “The HADES Facility for High Activity Decommissioning Engineering & Science: part of the UK National Nuclear User Facility,” *IOP Conf. Ser. Mater. Sci. Eng.*, vol. 818, p. 12022, Apr. 2020, doi: 10.1088/1757-899x/818/1/012022.

7.8 Supporting information

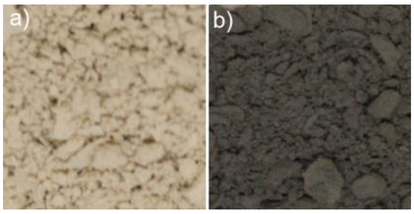

Figure S1. Colours of a) as synthesised $SrUO_4$ in *Pbcm* symmetry (R,G,B) (180,163,136) and b) after 75 ml/min NH_3 ammonolysis at 750 °C for 2h in the *R*-3*m* symmetry (R,G,B) (71,66,58).

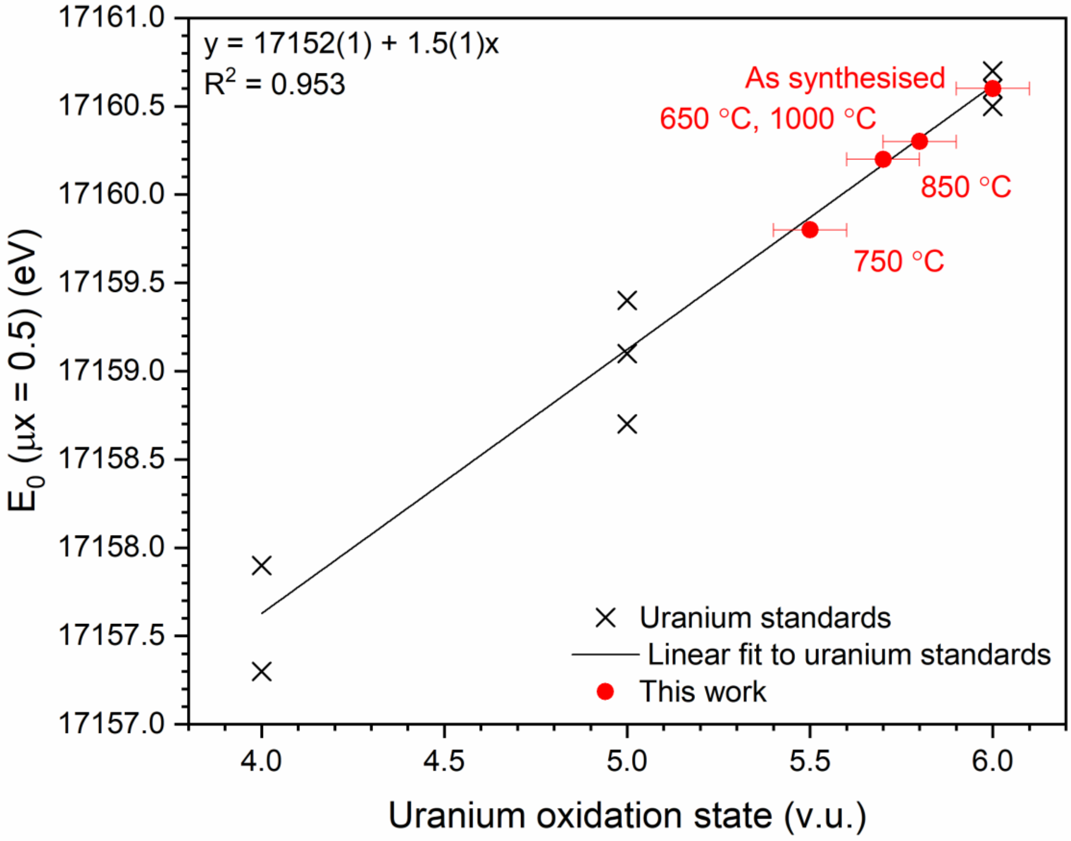

Figure S2. Linear calibration of absorption edge E_0, defined as $\mu x(E) = 0.5$, as a function of uranium oxidation state. Black crosses indicate measured reference compounds, black line indicates linear regression fit, red dots indicate α-$SrUO_4$ products from reaction under variable temperature 75 ml/min 2h ammonolysis measured in this work.

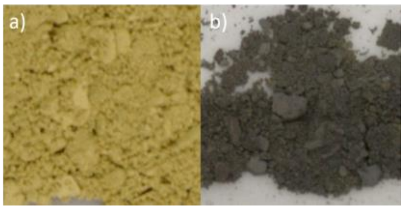

Figure S3. Colours of a) as synthesised $CaUO_4$ (R,G,B) (164,143,70) and b) after 75 ml/min NH_3 ammonolysis at 650 °C for 2 h (R,G,B) (49,45,41).

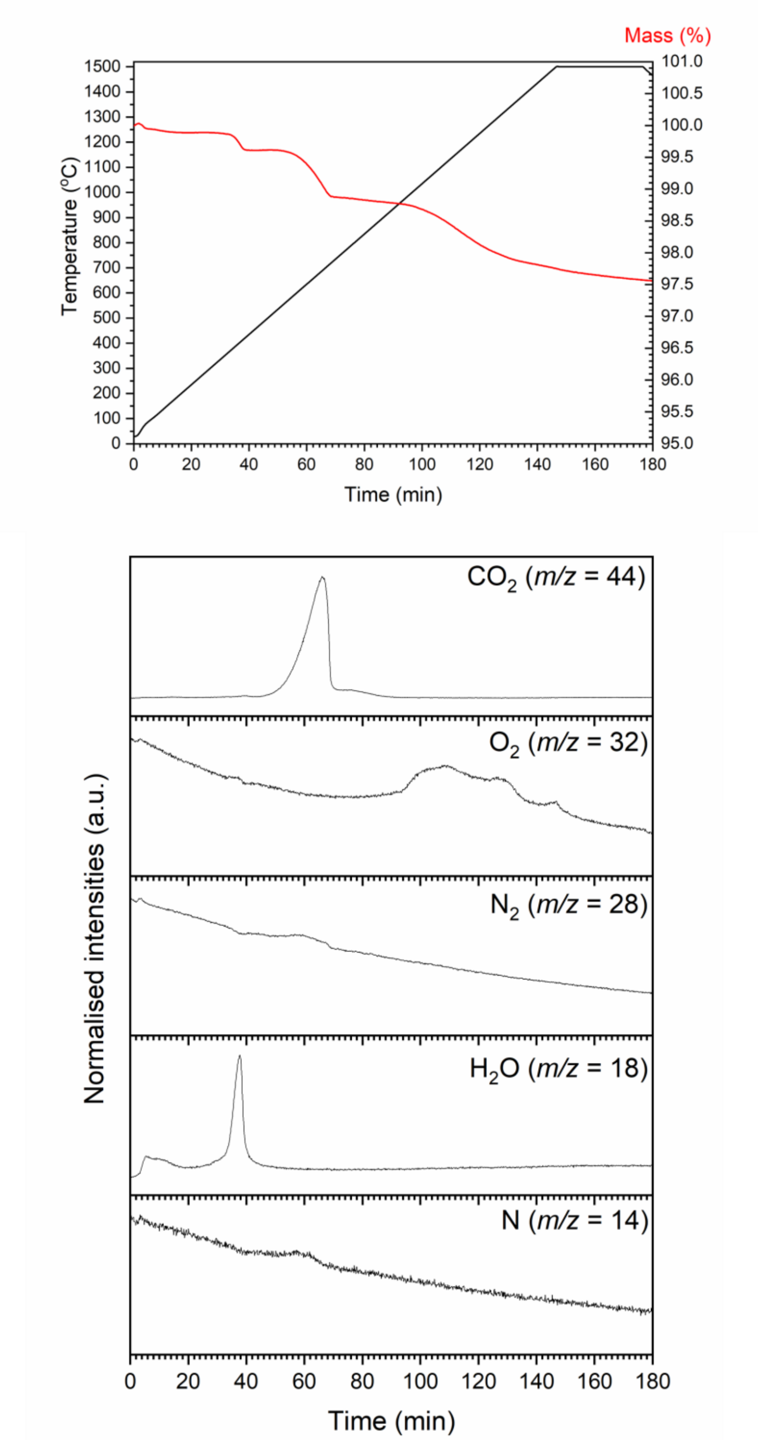

Figure S4. TGA-MS data for $CaUO_{4-x'}$ produced by reaction under 300 ml/min NH_3 at 650 °C for 16 h. Top: TGA analysis. Bottom: normalised intensities of m/z channels for N, H_2O, N_2, O_2 and CO_2.

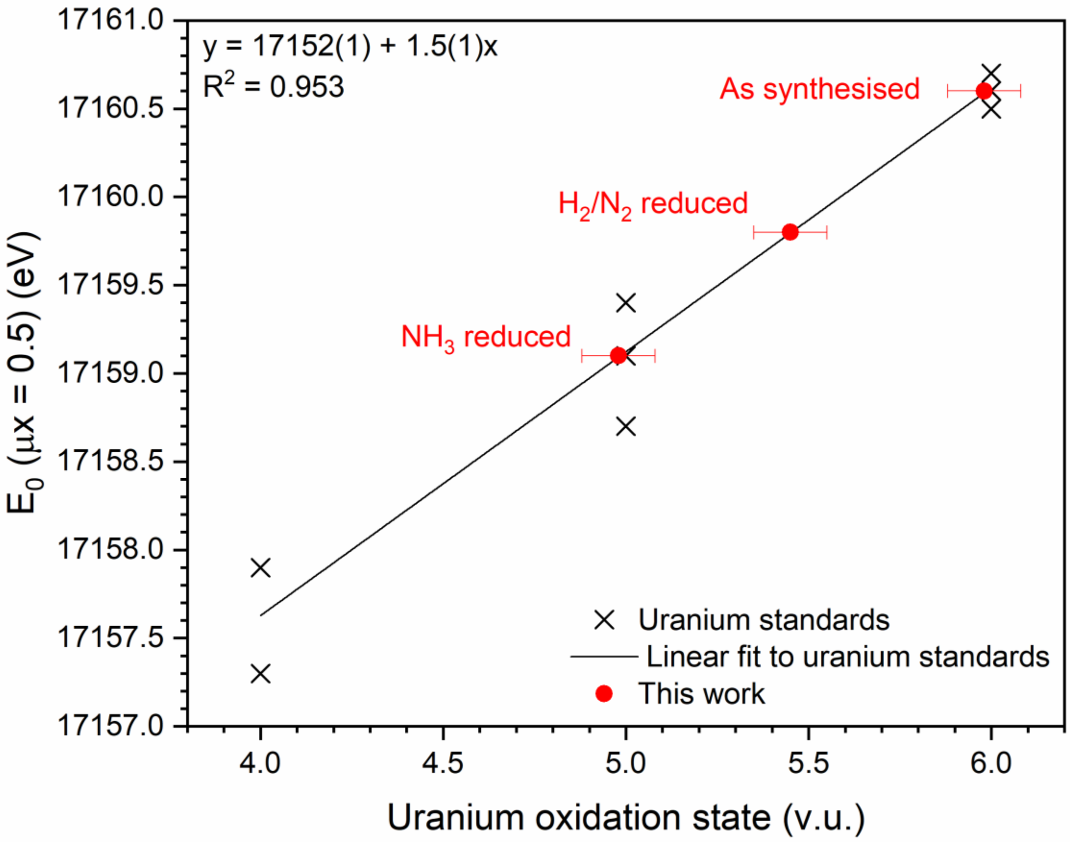

Figure S5. Linear calibration of absorption edge E_0, defined as $\mu x(E) = 0.5$, as a function of uranium oxidation state. Black crosses indicate measured reference compounds, black line indicates linear regression fit, red dots indicate $CaUO_4$ reaction products (as synthesised, 300 ml/min 5%H_2/N_2 reduced at 1100 °C for 16h and 300 ml/min NH_3 reduced at 1100 °C for 16h).

Sample	Path	R (Å)	σ^2 (Å^2)	$S_0{}^2$	y	E_0	R factor (%)
As synthesised	O12.1	1.948(8)	0.0035(9)				
	O11.1	2.283(6)	0.0035(9)				
	Ca1.1	3.69(1)	0.006(1)				
	U3.1	3.88(8)	0.0034(9)	0.76(7)	1	4.5(8)	0.029
	O12.2	4.334(8)	0.0035(9)				
	O13.1	4.47(2)	0.0035(9)				
	Ca1.2	5.35(1)	0.006(1)				
H_2/N_2 reduced	O12.1	1.956(8)	0.0029(9)				
	O11.1	2.273(7)	0.0029(9)				
	Ca1.1	3.69(1)	0.007(1)				
	U3.1	3.877(8)	0.0038(8)	0.76	0.86(9)	4.1(9)	0.032
	O12.2	4.343(8)	0.0029(9)				
	O13.1	4.49(2)	0.0029(9)				
	Ca1.2	5.35(1)	0.007(1)				
NH_3 reduced	O12.1	1.962(7)	0.0029(8)				
	O11.1	2.273(6)	0.0029(8)				
	Ca1.1	3.69(1)	0.009(1)				
	U3.1	3.877(6)	0.0038(7)	0.76	0.78(7)	4.2(8)	0.026
	O12.2	4.348(7)	0.0029(8)				
	O13.1	4.49(2)	0.0029(8)				
	Ca1.2	5.35(1)	0.009(1)				

Table S1. Outputted parameters from EXAFS fit for $CaUO_4$ and reduced samples. R is path length, σ^2 is Debye-Waller factor, $S_0{}^2$ is the amplitude reduction factor, y is the applied scalar to $S_0{}^2$, E_0 denotes shift from the calculated Fermi energy. Models assume the same Debye-Waller factor for all ions of the same type.

Chapter 8

Crystal and electronic structures of A_2NaIO_6 periodate double perovskites (A= Sr, Ca, Ba): Candidate wasteforms for I-129 immobilisation

Inorganic Chemistry

pubs.acs.org/IC Article

Crystal and Electronic Structures of A_2NaIO_6 Periodate Double Perovskites (A = Sr, Ca, Ba): Candidate Wasteforms for I-129 Immobilization

Sarah E. O’Sullivan, Eduardo Montoya, Shi-Kuan Sun,* Jonathan George, Cameron Kirk, Malin C. Dixon Wilkins, Philippe F. Weck, Eunja Kim,* Kevin S. Knight, and Neil C. Hyatt*

Cite This: *Inorg. Chem.* 2020, 59, 18407−18419 **Read Online**

ACCESS | Metrics & More | Article Recommendations | Supporting Information

ABSTRACT: The synthesis, structure, and thermal stability of the periodate double perovskites A_2NaIO_6 (A= Ba, Sr, Ca) were investigated in the context of potential application for the immobilization of radioiodine. A combination of X-ray diffraction and neutron diffraction, Raman spectroscopy, and DFT simulations were applied to determine accurate crystal structures of these compounds and understand their relative stability. The compounds were found to exhibit rock-salt ordering of Na and I on the perovskite B-site; Ba_2NaIO_6 was found to adopt the *Fm*-3*m* aristotype structure, whereas Sr_2NaIO_6 and Ca_2NaIO_6 adopt the $P2_1/n$ hettotype structure, characterized by cooperative octahedral tilting. DFT simulations determined the *Fm*-3*m* and $P2_1/n$ structures of Ba_2NaIO_6 to be energetically degenerate at room temperature, whereas diffraction and spectroscopy data evidence only the presence of the *Fm*-3*m* phase at room temperature, which may imply an incipient phase transition for this compound. The periodate double perovskites were found to exhibit remarkable thermal stability, with Ba_2NaIO_6 only decomposing above 1050 °C in air, which is apparently the highest recorded decomposition temperature so far recorded for any iodine bearing compound. As such, these compounds offer some potential for application in the immobilization of iodine-129, from nuclear fuel reprocessing, with an iodine incorporation rate of 25−40 wt%. The synthesis of these compounds, elaborated here, is also compatible with both current conventional and future advanced processes for iodine recovery from the dissolver off-gas.

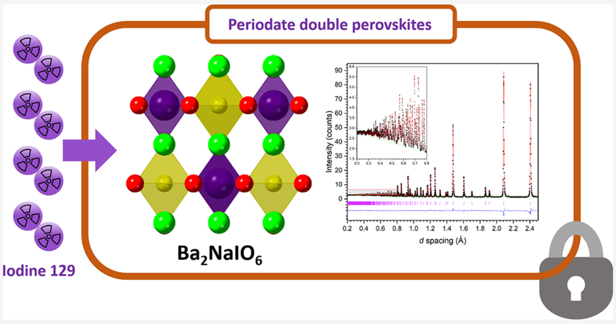

1. INTRODUCTION

The release of volatile iodine radionuclides, principally I-131 and I-129, arises from reprocessing of nuclear fuels, degradation of nuclear fuels during reactor accidents and storage, and nuclear weapons tests. I-129, with a half-life of 15.74 × 10^6 years, is an abundant fission product in used nuclear fuel with a fission yield of about 0.7%,[1] whereas the I-131 isotope has a half-life of 8.04 d. The iodide anion is highly soluble and weakly sorbed on mineral surfaces, over a range of geochemical conditions, and hence mobile in both environments,[2] and it is also known to bioaccumulate, being concentrated within the thyroid gland in the human body.[3] Therefore, I-129 is important as a key dose contributor in the safety case for geological disposal of radioactive wastes,[1] whereas I-131 is of critical importance for dose uptake in nuclear reactor accidents, given the *biological half-life* of 120 d.[4] I-129 is also of importance in population dose uptake in proximity to nuclear fuel reprocessing facilities; for example, data from the Savannah River site in 1989 showed that while I-129 composed only 0.00002% of the total radioactive assay released from the site, it contributed 13% of the offsite population dose.[5] The iodine biogeochemical cycle is known to be complex,[6] involving iodate (IO_3^-) and organo-iodine species, in addition to iodide (I^-), depending on the specific biogeochemical conditions, and hence there is high uncertainty in long-term predictions of iodine cycling and migration. Consequently, future regulatory practice may require immobilization and geological disposal of I-129, released from used fuel reprocessing, in contrast to the current practice of discharge and dilution in the marine environment.

A wide range of ceramic and glass wasteforms have been proposed as candidates for the immobilization and disposal of I-129, which can be categorized as follows: iodine or iodate salts (e.g., AgI or $Ba(IO_3)$[7]); tailored ceramic or glass

Received: October 13, 2020
Published: December 9, 2020

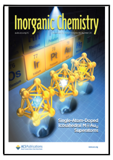

ACS Publications

https://dx.doi.org/10.1021/acs.inorgchem.0c03044
Inorg. Chem. 2020, 59, 18407−18419

compositions incorporating iodine at the atomic scale (e.g., $Pb_5(VO_4)_3I$ ceramic or $(Ag_2O{\cdot}nB_2O_3)_{1-x}(AgI)_x$ glasses[8,9]); or composites in which a discrete iodine bearing phase is encapsulated by a metal, ceramic, or glass matrix (e.g., Al_2O_3 ceramic and silicate glass encapsulated AgI;[10,11] see Riley et al. for a comprehensive review[1]). Within these waste forms, iodine is typically incorporated as the iodide anion, which is compatible with the speciation arising from the use of a sorbent to recover iodine from the dissolver off-gas (e.g., as AgI).[1] Thermodynamic considerations suggest that solubility limited iodide wasteforms should be broadly compatible with cool, nonreducing ground waters, of low dissolved solids concentration, to avoid reductive dissolution and anion displacement reactions.[7] This would require due consideration in the site selection for a geological disposal facility or emplacement at a shallower depth. In contrast, immobilization of iodine as the iodate anion has received considerably less attention, with the exception of iodate incorporated apatite ceramics $(Ca_{10}(PO_4)_6(OH_{1.6})(IO_3)_{0.4})$ and hydrotalcite Bi−O−I phases.[12,13] Iodate incorporation within tailored wasteforms offers the advantageous compatibility with the speciation afforded by simple caustic scrubbing of the dissolver off-gas, as well as the proposed Mercurex, Iodox, and Electrolytic scrubbing processes,[1] which would enable direct iodine incorporation, without conversion to, e.g., an iodide salt. However, although iodate salts of Hg, Ba, Sr, and Ca are resistant to hydrolysis and of moderately low solubility, the solubility of the most promising candidate, $Ba(IO_3)_2$, is 5 orders of magnitude greater than AgI.[7] Additionally, iodate wasteforms are expected to be stable under relatively oxidizing conditions, and it is suggested that in the presence of reducing ground waters, wasteform dissolution could be enhanced by reduction of IO_3^- to I^{-7}. Nevertheless, it is known that IO_3^- is significantly sorbed on mineral surfaces, in contrast to I^- [14,15] (in ref 7), which, combined with isotopic dissolution and slow dissolution kinetics, may be sufficient to mitigate comparatively higher solubility.

In considering potential candidate iodate ceramic wasteforms, our attention was drawn to a family of periodate double perovskites, formulated A_2MIO_6; with reference to the ideal perovskite structure, the large (12-coordinate) A-site is occupied by A = Ba^{2+}, Sr^{2+}, Ca^{2+}, whereas the small (6 coordinate) B-site is occupied by an ordered rock-salt arrangement of I^{7+} and M^+ = Na, K, and Ag cations. The periodate double perovskites offer an iodine incorporation rate of 25−40 wt%, comparable with that demonstrated for the most efficient iodide waste form counterparts.[1] Conceptually, such a waste form would be compatible with iodine recovery processes which afford iodate speciation, from which MIO_4 (M = Na, K) is easily prepared.[16] Although periodate compounds are known to be poorly or moderately soluble, the metaperiodate Ag_5IO_6, in contrast, is known to be highly insoluble.[17−19] Periodate compounds are relatively strong oxidizing agents and hence not obviously compatible with reducing conditions of geological disposal; nevertheless, redox reactions yield the iodate species,[18] which would offer some mitigation as described above. Therefore, it was considered worthwhile to investigate the synthesis, structure, and properties of the periodate double perovskites as potential ceramic waste forms for I-129.

The first periodate double perovskites, A_2MIO_6 (A = Ba, M = Ag, Na), were reported by Sleight and Ward in 1963, formed by the solid state reaction of BaO and $NaIO_4$ at 400 °C or precipitation from a solution of $NaIO_4$ or $AgIO_4$ by addition of $Ba(OH)_2$.[20] The compounds were reported to be cubic (a = 8.4 Å) and adopted rock-salt ordering of the B-site cations. Subsequently, De Hair et al. reported the compositions A_2MIO_6 (A = Ba, M = Ag, K, Na, Li and A = Sr, M = Na), using similar methods, and reported the Raman and infrared spectra.[21] Kubel et al. reported the first crystal structure determinations for the periodate double perovskites, A_2NaIO_6 (A = Ba, Sr, Ca, Pb), in 2013, synthesized by the following: the solid state reaction between AF_2 and an excess of NaI (A = Ba, Sr, Ca); the reaction of $A(OH)_2{\cdot}8H_2O$ and $NaIO_4$ (A = Ba, Sr), at 650 °C in air; or the precipitation from a solution of nitrates with NaOH and $NaIO_4$ (A = Ba, Sr, Ca, Pb).[22] From Rietveld analysis of powder X-ray diffraction data, Ba_2NaIO_6 was reported to adopt the undistorted Fm-$3m$ aristotype structure, whereas Sr_2NaIO_6, Ca_2NaIO_6, and Pb_2NaIO_6 were reported to adopt the $P2_1/c$ hettotype structure, with cooperative tilting of the rock-salt ordered B-site octahedra (Glazer notation, $a^+b^-b^-$).[22−24] However, our bond valence sum analysis,[25] using the reported crystal structure data, identified substantial deviations from formal valence states, as shown in Table S1, which may result from the limited accuracy and precision of locating the O positions. As highlighted by Howard et al., high resolution neutron or synchrotron X-ray diffraction data are preferable for structure determination of complex perovskites, to reveal subtle distortions of symmetry coupled with sensitivity to weak supercell reflections diagnostic of the octahedral tilt system,[24] which are not always apparent in laboratory X-ray diffraction data. Consequently, a reinvestigation of the synthesis and structure of the periodate perovskites, as reported herein, was considered a timely endeavor.

2. EXPERIMENTAL SECTION

Caution: sodium periodate, $NaIO_4$, is a strong oxidizing agent and should be handled with due caution and risk assessment.

Periodate double perovskites of general formula A_2NaIO_6 (A = Ca, Sr, Ba) were prepared by solid state synthesis. Stoichiometric quantities of the corresponding metal hydroxide ($Ca(OH)_2$, $Sr(OH)_2$, $Ba(OH)_2{\cdot}8H_2O$) and $NaIO_4$ (Sigma Aldrich, >99.8% purity) were hand ground using a pestle and mortar for 10 min under a dry nitrogen atmosphere to prevent carbonation of the hydroxide reagents. The powders were then consolidated into 10 mm pellets, pressed for 1 min under 2 tonnes pressure. The pressed pellets were packed into crucibles under a bedding of unconsolidated powder (~1 g), to prevent carbonation of the reagents during high temperature solid state reaction. All pellets were sintered in an air atmosphere muffle furnace, at 650 °C for 10 h, with a heating and cooling ramp rate of 5 °C min^{-1}. Once cooled, the pellets were recovered and gently brushed to remove any bedding material before regrinding for further analysis.

Initial X-ray diffraction (XRD) phase characterization was performed on a Bruker D2 Phaser diffractometer at room temperature in reflection mode, with Ni filtered Cu Kα radiation, λ = 1.5418 Å, and a Lynxeye position sensitive detector. High temperature X-ray diffraction (HT-XRD) was performed on a PANalytical XPert[3] diffractometer, using a parallel beam of Cu Kα radiation in reflection mode, with a PIXCel 1D position sensitive detector and Anton Parr 1200N high temperature stage. Scanning Electron Microscopy and Energy Dispersive X-ray (SEM EDX) analysis of product materials were performed using a Hitachi TM3030 SEM equipped with a Bruker Quantax 70 EDX system, operating at 15 kV and working distance of 8 mm. Specimens were prepared as a thin dusting of powder dispersed on adhesive carbon tabs. Thermogravimetric analysis mass spectrometry (TG-MS) measurements were made using a Netzsch STA 449 F3 *Jupiter* thermal analyzer coupled with a

Netzsch QMS 403 *Aelos Quadro* quadrupole mass spectrometer with synthetic air carrier gas. Raman spectra were collected on a Horiba X-ploRA Plus microscope with a 532 nm laser.

Neutron diffraction data were collected from Ba_2NaIO_6, Sr_2NaIO_6, and Ca_2NaIO_6 on the POLARIS time-of-flight powder diffractometer at the ISIS pulsed spallation neutron source, Rutherford Appleton Laboratory, UK.[26,27] Ba_2NaIO_6 (3.5 g), Sr_2NaIO_6 (2.9 g), and Ca_2NaIO_6 (2.5 g) respectively were each loaded into a 6 mm diameter thin-walled vanadium sample can, which were sealed using indium wire, inside a glovebox. The sample cans were mounted on an automatic sample changer in the diffractometer and data collected for a duration of 175 μAh integrated proton beam current to the ISIS neutron target (corresponding to 1 h total neutron beam exposure) from each sample. The diffraction data were normalized to the incident beam spectrum and corrected for detector efficiency (using a vanadium standard) and sample attenuation. Data reduction and generation of files suitable for profile refinement used the Mantid open source software.[28] Structure refinement was made by Rietveld analysis of neutron diffraction data, using the GSAS and EXPGUI suite of programs[29,30] and data from the high resolution back scattering detectors (Bank 5, 2θ range 134.6−167.4°, $\Delta d/d = 3 \times 10^{-3}$[27]).

Bond valence sums (BVS) of the form $V = \Sigma e^{(r_0 - r)/b}$ were calculated for each of the compounds across all cation−anion bonding pairs, using $b = 0.37$ for oxides.[25] Tabulated reference bond lengths of $r_0 = 2.285$ for Ba−O bonds, $r_0 = 2.118$ for Sr−O bonds, and $r_0 = 1.967$ for Ca−O bonds were used for the alkali earth cations.[25] For I−O bonds, $r_0 = 1.93$ was used,[31] and $r_0 = 1.661$ was used for Na−O bonds.[32] Observed bond lengths, r, were extracted from neutron refinement data. Additionally, the global instability index, $G^{II} = \left(\frac{1}{N}\sum_i d_i\right)^{0.5}$,[33] where d_i is the magnitude of difference between the BVS and the expected valence, and N is the number of atoms in the formula unit, was calculated to give the degree of failure of the BVS rule.

Density functional theory (DFT) was utilized in this study to investigate the crystal structures of the periodate double perovskites Ca_2NaIO_6, Sr_2NaIO_6, and Ba_2NaIO_6 synthesized experimentally. Total energy calculations were carried out using DFT implemented in the Vienna Ab initio Simulation Package (VASP).[34] In the Kohn−Sham (KS) equations, the interaction between valence electrons and ionic cores was described using the projector augmented wave (PAW) method[35,36] with Ca($3s^23p^64s^2$), Sr($4s^24p^65s^2$), Ba($5s^25p^66s^2$), Na($3s^1$), I($5s^25p^5$), and O($2s^22p^4$) electrons treated as valence electrons and the remaining core electrons, together with the nuclei, represented by PAW pseudopotentials. The exchange-correlation energy was calculated using the generalized gradient approximation (GGA) with the parametrization of Perdew-Burke-Ernzerhof (PBE).[37] The plane-wave energy cutoff was set to 500 eV, and a total-energy convergence criterion was fixed to 1 meV/atom. The Monkhorst-Pack scheme[38] was utilized to sample the Brillouin zone with a 3 × 3 × 3 k-point mesh. Simultaneous ionic and cell energy-relaxation calculations were carried out, without the symmetry constraint, until the Hellmann−Feynman forces acting on atoms were converged within 0.01 eV/Å.

Structures obtained from total-energy minimization with GGA/PBE were further relaxed with respect to Hellmann−Feynman forces until a convergence tolerance of 0.001 eV/Å was reached. Density functional perturbation theory (DFPT) linear response calculations were then carried out with VASP to determine the vibrational frequencies and associated intensities. The latter were computed based on the Born effective charges (BEC) tensor, which corresponds to the change in atom polarizabilities with respect to an external electric field. This computational approach was used in previous studies to successfully predict the vibrational/phonon properties of various crystalline materials.[39−41]

3. RESULTS AND DISCUSSION

3.1. Synthesis and X-ray Diffraction.

The powder X-ray diffraction data of the A_2NaIO_6 periodate double perovskites synthesized by solid state reaction at 650 °C are presented in Figure 1. Analysis of these data followed the methodology recommended by Howard et al.[24] for double perovskites and demonstrated synthesis of near single phase compounds. EDX analysis of powder specimens afforded elemental compositions consistent with the target stoichiometry: $Ba_{2.05(8)}Na_{0.98(2)}I_{0.95(5)}O_6$, $Sr_{2.00(3)}Na_{0.99(3)}I_{1.02(3)}O_6$, and $Ca_{2.1(1)}Na_{1.00(3)}I_{1.1(1)}O_6$ (Note: overlap of I Lα with Ba Lα and Ca Kα emission lines afforded greater uncertainty in determination of these elements; oxygen stoichiometry was assumed given the poor precision for EDX determination). All compounds presented as creamy white powders.

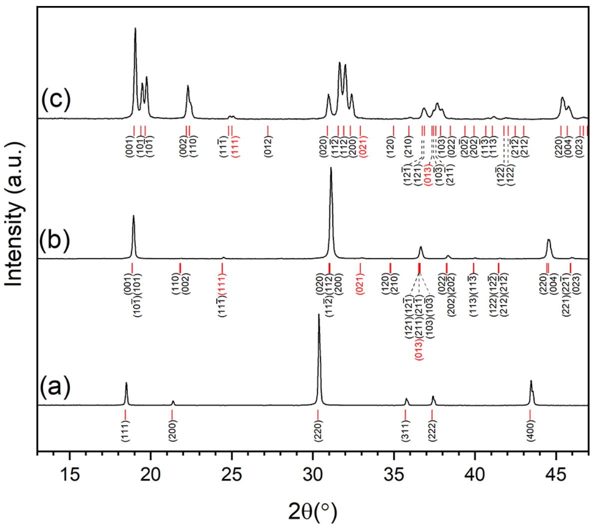

Figure 1. Indexed XRD patterns of prepared (a) Ba_2NaIO_6 (PDF 01-082-4575), (b) Sr_2NaIO_6 (PDF 04-018-9360), and (c) Ca_2NaIO_6 (PDF 04-018-9361). Tickmarks indicate allowed reflections. R-, M-, and X-point reflections are indexed in red.

The XRD pattern of Ba_2NaIO_6 was first indexed on the basis of a doubled perovskite unit cell (a = 8 Å), in space group *Fm*-3*m*. In this analysis, reflections of the type (*eee*) represent the fundamental reflections of the ideal cubic aristotype ABO_3 structure, in space group *Pm*-3*m* (where *e* or *o* denote *hkl* = *even* or *odd*, respectively). Rock-salt ordering of cations on the B-site gives rise to R-point reflections indexed as (*ooo*), which were clearly observed as a result of the high contrast in X-ray scattering factors of Na and I (in the language of group theory, this ordering corresponds to a symmetry breaking mode described by the irreducible representation R^+_1). Antiphase (−) tilting of B-site octahedra, i.e., rotation of the opposite sense in successive layers, also makes a small contribution to the intensity of R-point reflections (irreducible representation R^+_4), but this is masked by the dominant contribution of B-site ordering. Antiphase octahedral tilting would necessarily further lower the symmetry, resulting in obvious splitting of fundamental reflections, which was not observed. No additional reflections could be indexed, which implied an absence of in-phase octahedral tilting, although such reflections would be expected to be relatively weak in X-ray diffraction, due to the relatively small scattering factor of O. From this analysis, we deduce Ba_2NaIO_6 to be a rock-salt ordered double perovskite, adopting space group *Fm*-3*m* with the Glazer tilt system $a^0a^0a^0$.

Table 1. Ba$_2$NaIO$_6$ Structural Parameters Determined from Rietveld Analysis of Neutron Diffraction Data

space group: *Fm*-3*m*, Z = 4, a = 8.3335(2) Å, V = 578.731(4) Å^3					
formula weight: 520.542 u					
atom	site	x	y	z	U_{iso} × 100 (Å^2)
Ba	8c	0.25	0.25	0.25	0.497(8)
I	4a	0	0	0	0.14(1)
Na	4b	0.5	0.5	0.5	1.27(3)
O1	24e	0.22420(3)	0	0	0.937(6)
powder statistics:	χ^2 = 3.966	R_{wp} = 3.02%	R_p = 4.18%		

Considering Ca$_2$NaIO$_6$, reflections indexed as (400) and (220) in the *Fm*-3*m* cell were observed to be split and (with others) could be indexed on the basis of monoclinic symmetry (respectively, (220) (004) in intensity ratio 2:1 and (020) (112) (11-2) (200) in intensity ratio 1:2:2:1). Further inspection identified both M-point reflections of the type (*eoo*) diagnostic of in-phase (+) octahedral tilting (irreducible representation M$^+_3$), e.g., (013), and R-point reflections that are primarily a signature of B-site cation ordering, e.g., (111). Coupling of the B-site cation ordering and antiphase octahedral tilting (R-point reflections) and in-phase octahedral tilting (M-point reflections) is expected to afford additional X-point reflections, of the type (*eeo*), which were also apparent, e.g., (021). From this analysis, we deduce Ca$_2$NaIO$_6$ to be a double rock-salt ordered perovskite phase, adopting space group $P2_1/n$ with the Glazer tilt system $a^-a^-c^+$. This systematic analysis validates the previous assignment of space group $P2_1/c$ ($a^+b^-b^-$) which is the standard setting of $P2_1/n$; the latter is preferred in the perovskite literature, since it approximates an orthogonal cell with $\beta \approx 90°$.

The XRD data of Sr$_2$NaIO$_6$ also presented reflection profiles and splitting of fundamental reflections diagnostic of monoclinic symmetry. Additionally, R-point and X-point reflections (e.g., (111) and (021), respectively) were evident; however, reflection overlap did not allow unambiguous identification of the M-point reflections (e.g., (013)). Note, however, such reflections are implicit, since the associated in-phase octahedral tilting, coupled with rock-salt ordering and antiphase octahedral tilting, affords significant intensity at the X-point reflections, which are clearly observed. These observations are sufficient to deduce that Sr$_2$NaIO$_6$ is a rock-salt ordered double perovskite phase, isostructural with Ca$_2$NaIO$_6$, adopting space group $P2_1/n$ with the Glazer tilt system $a^-a^-c^+$; this systematic analysis validates the previous assignment of the standard setting $P2_1/c$ ($a^+b^-b^-$).

3.2. Structure Refinement.

Rietveld analysis of neutron powder diffraction data utilized an initial double perovskite model in *Fm*-3*m* or $P2_1/n$, according to prior analysis of X-ray powder diffraction data. Initial inspection of data identified diagnostic R-, M-, and X-point reflections, in agreement with analysis of powder X-ray diffraction data. The background was fitted using a fifth order shifted Chebyshev polynomial function, followed by systematic refinement of lattice structural parameters, and profile parameters. Rock-salt ordering of Na and I was initially assumed; in the final stage of the refinement, the potential for antisite disorder was examined but found to be insignificant, by refinement under constraint of full site occupancy. Additional reflections were observed in the data of Ca$_2$NaIO$_6$, which could not be indexed in space group $P2_1/n$, which were attributed to unidentified impurities.

3.2.1. Structure Refinement of Ba$_2$NaIO$_6$.

Structure refinement converged rapidly to a satisfactory fit with χ^2 = 2.49, R_{wp} = 2.40%, and R_p = 4.05%, for 17 variables including 6 structural parameters. The final structural parameters are summarized in Table 1, a schematic representation of the crystal structure is shown in Figure 2, and the profile fit is shown in Figure 3. The determined key bond lengths and bond valence sums are summarized in Table 2.

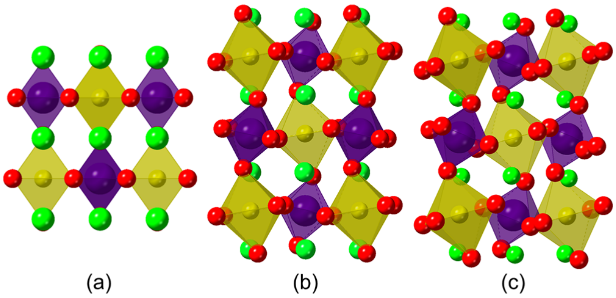

Figure 2. Structures of A$_2$NaIO$_6$ compounds modeled from neutron diffraction data. a) Ba$_2$NaIO$_6$ viewed down [110], and b) Sr$_2$NaIO$_6$ and c) Ca$_2$NaIO$_6$ viewed down [010]. Green spheres indicate respective alkali earth cations (Ba, Sr, or Ca), yellow octahedra indicate sodium cations, purple octahedra indicate iodine cations, and red spheres indicate oxygen anions.

The crystal structure of Ba$_2$NaIO$_6$ was thus determined to adopt cubic *Fm*-3*m* symmetry (tilt system $a^0a^0a^0$). Ba is 12-fold

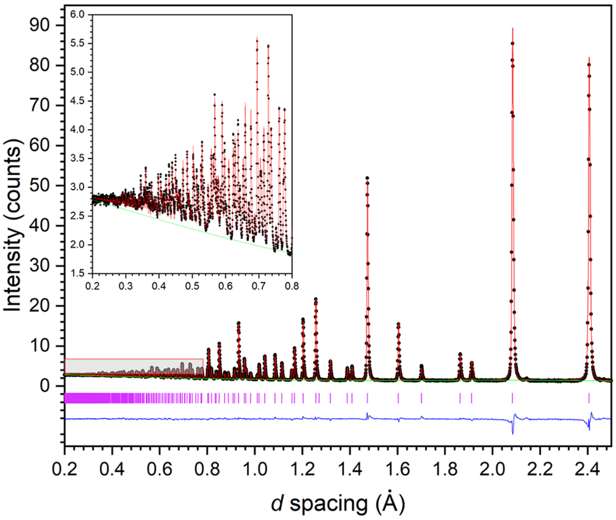

Figure 3. Rietveld refinement fit (red line) of powder neutron diffraction data (black dots) for Ba$_2$NaIO$_6$. Purple tick marks indicate allowed reflections in the *Fm*-3*m* space group. The blue line indicates difference profile.

Table 2. Bond Lengths and Calculated Bond Valence Sums for A_2NaIO_6 Perovskites

Ba_2NaIO_6			Sr_2NaIO_6			Ca_2NaIO_6		
bond	length (Å)	BVS	bond	length (Å)	BVS	bond	length (Å)	BVS
Ba−O1 (x12)	2.95420(2)	1.97	Sr−O1	3.186(2)	1.89	Ca−O1	3.617(2)	1.95
			Sr−O1	2.658(2)		Ca−O1	2.375(2)	
			Sr−O1	2.550(3)		Ca−O1	2.340(3)	
			Sr−O1	3.248(3)		Ca−O1	3.364(3)	
			Sr−O2	2.571(4)		Ca−O2	2.381(3)	
			Sr−O2	2.790(3)		Ca−O2	2.683(3)	
			Sr−O2	2.875(3)		Ca−O2	2.725(3)	
			Sr−O2	3.366(4)		Ca−O2	3.654(2)	
			Sr−O3	2.819(3)		Ca−O3	2.574(2)	
			Sr−O3	2.556(4)		Ca−O3	2.366(2)	
			Sr−O3	3.398(3)		Ca−O3	3.671(3)	
			Sr−O3	2.846(3)		Ca−O3	2.961(3)	
I−O1 (x6)	1.8684(3)	7.09	I−O1 (x2)	1.863(2)	7.08	I−O1 (x2)	1.861(2)	7.12
			I−O2 (x2)	1.870(2)		I−O2 (x2)	1.865(2)	
			I−O3 (x2)	1.874(2)		I−O3 (x2)	1.874(2)	
Na−O1 (x6)	2.2984(3)	1.07	Na−O1 (x2)	2.281(2)	1.12	Na−O1 (x2)	2.341(2)	0.98
			Na−O2 (x2)	2.275(2)		Na−O2 (x2)	2.297(2)	
			Na−O3 (x2)	2.286(2)		Na−O3 (x2)	2.368(2)	

Table 3. Sr_2NaIO_6 Structural Parameters Determined from Rietveld Analysis of Neutron Diffraction Data

space group: $P2_1/n$, $Z = 2$, $a = 5.7591\ (2)$ Å, $b = 5.7673(1)$ Å, $c = 8.1341(2)$ Å, $\beta = 89.934(3)°$, $V = 270.172(4)$ Å^3

formula weight: 421.128 u

atom	site	x	y	z	$U_{iso} \times 100$ (Å^2)
Na	2a	0	0	0	1.08(4)
I	2b	0	0	0.5	0.24(1)
Sr	4e	0.0057(3)	0.5287(2)	0.2499(3)	0.83(1)
O1	4e	−0.0665(4)	−0.0177(3)	0.2762(2)	0.72(2)
O2	4e	0.2433(4)	0.3071(4)	0.0331(3)	1.12(3)
O3	4e	0.3124(4)	0.7608(4)	0.0355(3)	1.24(3)
powder statistics:	$\chi^2 = 2.561$	$R_{wp} = 2.26\%$	$R_p = 3.05\%$		

coordinated by oxygen at the center of the cuboctahedral cavity defined by eight corner-sharing BO_6 octahedra, occupied alternately by Na and I. The Na and I cations are fully ordered in a rock-salt arrangement on the B site, as expected from the large difference in charge and ionic radius which affords a substantial contribution to the total Madelung energy, as shown by Rosenstein and Schor (i.e., the electrostatic contribution to the lattice energy).[42] The compound is thus isostructural with Ba_2NaBO_6 double perovskites, with an identical charge difference of six units between B and B′ cations (B = Re, Os).[43,44]

The Goldschmidt tolerance factor,[45] t, provides a metric by which to assess bond length mismatch and potential for structural distortion, with respect to the cubic aristotype structure. For double perovskites, t is expressed as

$$t = \frac{r_A + r_O}{\sqrt{2}\,(r_B + r_O)} \tag{1}$$

where r_A, r_B, and r_O denote the oxidation state and coordination specific (mean) ionic radii determined by Shannon and Prewitt[46] of the A and B cations and O anions. The tolerance factor, $t = 0.98$, within the stability field of $0.98 < t < 1.01$ was typically observed for adoption of the undistorted $Fm\text{-}3m$ structure.[47] Bond valence sums are commensurate with the expected valence of each of the cations, and the global instability index $G_{II} = 0.06$ v.u., indicating a stable structure.[33]

3.2.2. Structure Refinement of Sr_2NaIO_6. Structure refinement converged rapidly to an excellent fit with $\chi^2 = 2.26$, $R_{wp} = 2.55\%$, and $R_p = 3.05\%$, for 36 variables including 22 structural parameters. The final structural parameters are summarized in Table 3, the profile fit is shown in Figure 4, and a schematic representation of the crystal structure is shown in Figure 2. The determined key bond lengths and bond valence sums are summarized in Table 2. The crystal structure of Sr_2NaIO_6 was thus determined to adopt monoclinic $P2_1/n$ symmetry (tilt system $a^-a^-c^+$), with cooperative antiphase and in-phase tilting of slightly distorted BO_6 octahedra, occupied alternately by Na and I in a fully ordered rock-salt arrangement. Consequently, Sr adopts a distorted 12-fold coordination environment with 8 short and 4 long Sr−O bonds. As indicated by the Glazer tilt system, the NaO_6 and IO_6 octahedra show an in-phase tilt and an antiphase tilt. These were calculated using the mode decomposition formulism demonstrated for similar elpasolite structures, yielding an in-phase tilt of 7.8° about [001] and an antiphase tilt of 10.9° about [110].[48] Sr_2NaIO_6 is thus isostructural with the double perovskite Sr_2NaReO_6, although the Re counterpart exhibited considerable disorder of the oxygen sublattice which was not observed here.[44] The tolerance factor of Sr_2NaIO_6, $t = 0.92$, is outside the stability field of $0.98 < t < 1.01$ typically observed for adoption of the undistorted $Fm\text{-}3m$ structure[47] but within the range observed

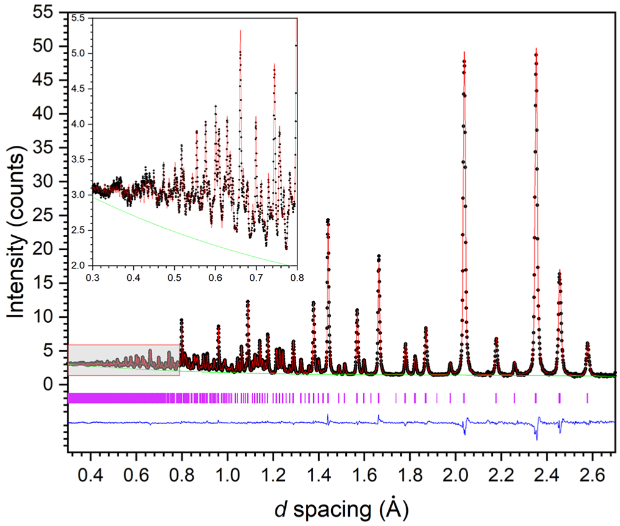

Figure 4. Rietveld refinement fit (red line) of powder neutron diffraction data (black dots) for Sr_2NaIO_6. Purple tick marks indicate allowed reflections in the $P2_1/n$ space group. The blue line indicates difference profile.

for isostructural $P2_1/n$ perovskites, $0.83 < t < 0.98$.[47] The Sr cation is evidently too small for the 12 coordinate cuboctahedral site, resulting in cooperative octahedral tilting as a result of bond length mismatch. Bond valence sums show the Sr cation to be underbonded, which is presumably a consequence of maintaining adequate Na−O and I−O bond lengths, while minimizing bond length mismatch. This is compensated by significant overbonding of the Na ion, although I ions remain within the acceptable tolerance of ±5% around the expected valence. The calculated global instability index arising from the BVS is $G_{II} = 0.09$ which is approaching the steric strain region $0.1 < G_{II} < 0.2$ v.u.; however, it still indicates a stable structure.[33]

3.2.3. Structure Refinement of Ca_2NaIO_6. Structure refinement converged rapidly to an excellent fit with $\chi^2 = 3.38$, $R_{wp} = 2.53\%$, and $R_p = 4.27\%$, for 34 variables including 22 structural parameters. The final structural parameters are summarized in Table 4, the profile fit is shown in Figure 5, and a schematic representation of the crystal structure is shown in Figure 2. The determined key bond lengths and bond valence sums are summarized in Table 2.

The crystal structure of Ca_2NaIO_6 was determined to be isostructural with Sr_2NaIO_6 adopting monoclinic $P2_1/n$ symmetry (tilt system $a^-a^-c^+$). The Ca site adopts a similarly distorted 12-fold coordination environment with 8 short and 4 long Ca−O bonds, arising from cooperative antiphase and in-phase tilting of slightly distorted BO_6 octahedra. Na and I adopt a fully ordered rock-salt arrangement in the B sites; the NaO_6 and IO_6 octahedra show an in-phase tilt angle of 11.7° about [001] and an antiphase tilt angle of 17.8° about [110].[48] The greater extent of octahedra tilting in comparison to Sr_2NaIO_6 arises due to the greater bond length mismatch. The tolerance factor of Ca_2NaIO_6, $t = 0.89$, is within the range $0.83 < t < 0.98$ observed for isostructural $P2_1/n$ perovskites. The low tolerance factor of Ca_2NaIO_6 implies considerable bond length mismatch and hence structural strain, since the Ca cation is too small for the 12 coordinate cuboctahedral site, resulting in cooperative octahedral tilting. Bond valence sums show the Ca cation to be slightly underbonded, which is presumably a consequence of maintaining adequate Na−O and I−O bond lengths. The global instability index is $G_{II} = 0.07$ v.u. indicating a stable and well determined structure.[33]

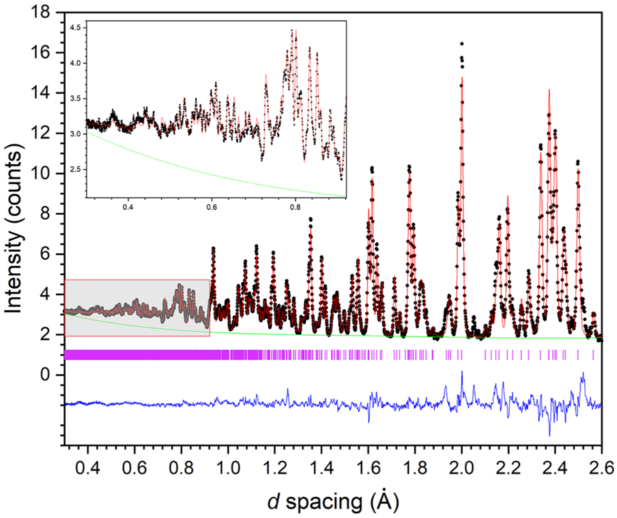

Figure 5. Rietveld refinement fit (red line) of powder neutron diffraction data (black dots) for Ca_2NaIO_6. Purple tick marks indicate allowed reflections in the $P2_1/n$ space group. The blue line indicates difference profile.

3.3. DFT Studies.

Total energy curves of each periodate double perovskite structure are provided in Figure 6, for model structures crystallizing in the cubic $Fm\text{-}3m$ and monoclinic $P2_1/n$ space groups. For both Ca_2NaIO_6 and Sr_2NaIO_6, the monoclinic phase was determined to be energetically favorable compared to the cubic phase, in agreement with diffraction and Raman spectroscopy data. The cubic and monoclinic structures of Sr_2NaIO_6 resulted in a relatively small difference

Table 4. Ca_2NaIO_6 Structural Parameters Determined from Rietveld Analysis of Neutron Diffraction Data

space group: $P2_1/n$, $Z = 2$, $a = 5.5365(1)$ Å, $b = 5.7845(1)$ Å, $c = 7.9352(2)$ Å, $\beta = 90.834(2)°$, $V = 254.103(8)$ Å^3

formula weight: 326.044 u

atom	site	x	y	z	$U_{iso} \times 100$ (Å^2)
Na	2a	0	0	0	0.62(5)
I	2b	0	0	0.5	0.041(9)
Ca	4e	0.0160(3)	0.5575(3)	0.2447(3)	0.68(3)
O1	4e	−0.1108(3)	−0.0537(3)	0.2809(2)	0.64(2)
O2	4e	0.2243(3)	0.3266(3)	0.0453(2)	0.79(2)
O3	4e	0.3381(3)	0.7666(3)	0.0705(2)	0.71(2)
powder statistics:	$\chi^2 = 3.381$	$R_{wp} = 2.53\%$	$R_p = 4.27\%$		

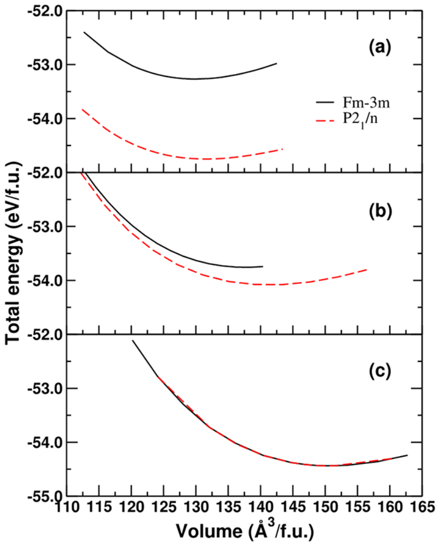

Figure 6. Total energy curves of (a) Ca_2NaIO_6, (b) Sr_2NaIO_6, and (c) Ba_2NaIO_6 as functions of volume per formula unit (f.u.) calculated at the GGA/PBE level of theory for structures crystallizing in the cubic *Fm*-3*m* (solid black curves) and monoclinic *P*2$_1$/*n* (dashed red curves) space groups.

in energetics, compared to Ca_2NaIO_6. The cubic phase is slightly less energetically favorable by 0.3 eV/f.u. in Sr_2NaIO_6 and 1.4 eV/f.u. in Ca_2NaIO_6. For Ba_2NaIO_6, the monoclinic *P*2$_1$/*n* and cubic *Fm*-3*m* structures were determined to be energetically degenerate. This suggests that a mixture of phases could coexist at room temperature or the presence of an incipient phase transition. Analysis of neutron diffraction data did not identify reflection asymmetry, weak supercell reflections, or unusual thermal parameters characteristic of a lower symmetry structure. Likewise, analysis of the Raman spectrum Ba_2NaIO_6 was consistent with *Fm*-3*m* symmetry. Future work will examine the possibility of a *Fm*-3*m* to *P*2$_1$/*n* phase transition in Ba_2NaIO_6 at low temperature.

The formation energies of Ca_2NaIO_6 (*P*2$_1$/*n*), Sr_2NaIO_6 (*P*2$_1$/*n*), and Ba_2NaIO_6 (*Fm*-3*m*) were calculated using eqs 2 and 3:

$$2M(OH)_2 + NaIO_4 \rightarrow M_2NaIO_6 + 2H_2O \tag{2}$$

$$E_f = [E(M_2NaIO_6) + E(2H_2O)] - [E(2M(OH)_2) + E(NaIO_4)] \tag{3}$$

The former describes the synthesis of the periodate double perovskites as applied in this study (where M = Ca, Sr, or Ba), while the latter is the formation energy (E_f) for that reaction.

The calculated formation energies of Ca_2NaIO_6 (*P*2$_1$/*n*), Sr_2NaIO_6 (*P*2$_1$/*n*), and Ba_2NaIO_6 (*Fm*-3*m*) were 5.518, 5.060, and 4.157 eV/f.u., respectively. Ba_2NaIO_6 has the lowest formation energy, followed by Sr_2NaIO_6 and Ca_2NaIO_6. A similar trend can be seen in the total energy difference between the cubic *Fm*-3*m* and monoclinic *P*2$_1$/*n* phases, which is the largest in Ca_2NaIO_6, followed by Sr_2NaIO_6 and the smallest in Ba_2NaIO_6.

The calculated lattice parameters of Ca_2NaIO_6 (*P*2$_1$/*n*), Sr_2NaIO_6 (*P*2$_1$/*n*), and Ba_2NaIO_6 (*Fm*-3*m*) are in excellent agreement with the experimentally determined values, as summarized in Table 5, with optimized structures also presented in Figure S1. Accordingly, the simulated XRD patterns from the DFT optimized structures, shown in Figure S2, match the experimentally determined patterns. The monoclinic *P*2$_1$/*n* and cubic *Fm*-3*m* structures for Ba_2NaIO_6 exhibit nearly identical XRD patterns; the converged atomic positions in the former structure are not significantly different from those in the latter.

Computed bond lengths and atomic positions are given in Tables S2 and S3, respectively, and show a good agreement with the experimentally derived values, across all three compositions. For Ca_2NaIO_6, bond lengths of Ca−O*X*, I−O*X*, and Na−O*X* (*X* = 1,2,3) are overestimated by 0.006 to 0.060 Å, the slight overestimation characteristic of the use of GGA functionals. The calculated bond lengths of Sr_2NaIO_6 are in very close agreement with the experimental measurements, with differences typically smaller than 0.001 Å. For example, the calculated bond lengths for Sr−O1 are 2.553, 2.658, 3.186, and 3.248 Å in excellent agreement with the experimentally derived values of 2.550, 3.248, 3.186, and 3.248 Å, respectively.

The atomic positions in the Ba_2NaIO_6 *Fm*-3*m* phase (Table S3) are essentially identical to the experimentally determined Rietveld refinement data, with a small difference of 0.002 Å for the *x* position of O1. The lattice constants are overestimated by about 0.1 Å. The bond lengths reported for the crystal appear to be in good agreement with the experimental results, albeit slightly overestimated for the Ba−O1 and I−O1 bonds. Na−O1 share similar values between the DFT and experimental values due to the effective DFT representation of the highly electropositive sodium core and its interaction with electronegative oxygens. Since no experimental data for the hypothetical *P*2$_1$/*n* Ba_2NaIO_6 crystal are available, only the DFT bond lengths are reported in Table S3. The Ba−O*X* bond lengths in the *P*2$_1$/*n* phase are predicted to differ by up to 0.01 Å. The bond lengths of I−O*X* in both phases are nearly identical, yet there is a relatively small difference of 0.008 Å between the Na−O*X* bonds.

3.4. Raman Spectra. Raman spectra were simulated using DFPT linear response calculations to obtain vibrational

Table 5. Calculated Lattice Parameters and Unit Cell Volumes of Ca_2NaIO_6, Sr_2NaIO_6, and Ba_2NaIO_6[a]

	Ba_2NaIO_6		Ba_2NaIO_6		Sr_2NaIO_6		Ca_2NaIO_6	
space group	*Fm*-3*m*, *Z* = 4		*P*2$_1$/*n*, *Z* = 2		*P*2$_1$/*n*, *Z* = 2		*P*2$_1$/*n*, *Z* = 2	
	DFT	exp	DFT	exp	DFT	exp	DFT	exp
a (Å)	8.444	8.3335	8.445		5.836	5.7591	5.575	5.5365
b (Å)			5.971		5.949	5.7673	5.844	5.7845
c (Å)			5.973		8.259	8.1341	8.046	7.9352
β (°)	90	90	89.97		90.06	89.93	91.03	90.83
V (Å^3)	602.090	578.731	301.358		286.708	270.172	261.752	254.103

[a] Experimental data from this study are also reported for comparison.

frequencies. These were assumed to have a natural line broadening of Lorentzian shape with FWHM of 5 cm^{-1}. These data were combined with experimental measurements in Figure 7, with Raman active frequencies and mode assignments given in Table 6. The modeled and experimental data are self-consistent within systematic calibration error and are consistent with those spectra previously reported.[22]

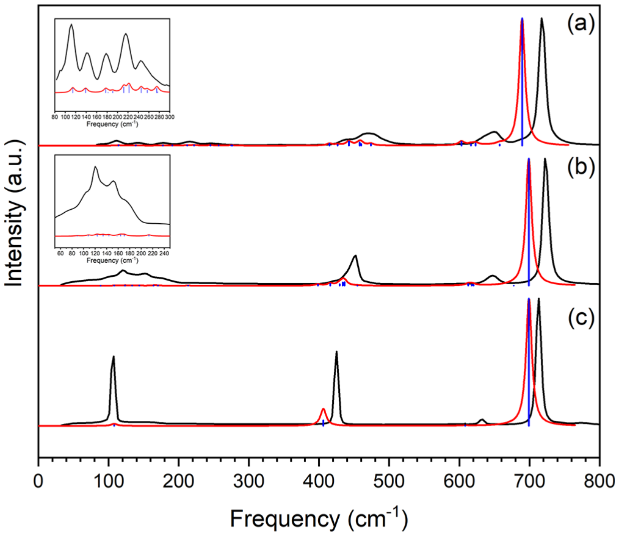

Figure 7. Raman spectra of (a) Ca_2NaIO_6 ($P2_1/n$), (b) Sr_2NaIO_6 ($P2_1/n$), and (c) Ba_2NaIO_6 (Fm-$3m$) simulated from DFPT at the GGA/PBE level (blue), with experimental measurement (black). Natural line broadening was simulated from DFPT eigenfrequencies using a Lorentzian line shape function with a full width at half-maximum (FWHM) of 5 cm^{-1} (red). Insets show the detail of low frequency regions for Ca_2NaIO_6 and Sr_2NaIO_6.

With N = 20 atoms (Z = 2) per monoclinic $P2_1/n$ cell, Ca_2NaIO_6 and Sr_2NaIO_6 possess $3N$ = 60 degrees of freedom. Among these modes of vibration of the C_{2h} point group,[49] there are three acoustic modes: $\Gamma_{acoustic}(3) = A_u + 2B_u$, which corresponds to zero-frequency modes of translation at the Γ-point, i.e., one longitudinal acoustic mode associated with the A_u irreducible representation (irrep), and two transverse acoustic modes with B_u irrep. The remaining 57 optical modes can be represented as $\Gamma_{optical}(57) = 12A_g + 17A_u + 12B_g + 16B_u$, where vibrational modes belonging to the A_g, A_u, B_g, and B_u irreps are nondegenerate.

According to selection rules for the C_{2h} point group, only the 24 optical modes belonging to the *gerade* (g) irreps, i.e., $12A_g + 12B_g$, are Raman active, while all 33 optical modes belonging to the *ungerade* (u) irreps, i.e., $17A_u + 16B_u$, are infrared (IR) active. However, coupling of the A_g and B_g modes typically occurs in $P2_1/n$ perovskite, thus significantly reducing the number of bands observed in Raman spectra. The 24 Raman-active modes can be decomposed as

$$\Gamma = 6T(3A_g + 3B_g) + 6L(3A_g + 3B_g) + 6\nu_5(3A_g + 3B_g) + 4\nu_2(2A_g + 2B_g) + 2\nu_1(A_g + B_g)$$

where low-intensity translational (T) lattice vibrational modes of Ca/Sr (4e sites) are usually observed in the region 80–240 cm^{-1}, low-intensity libration (L) lattice modes of Ca/Sr and internal oxygen bending modes (ν_5) of IO_6 octahedra appear in the ranges 100–280 cm^{-1} and 390–480 cm^{-1}, respectively, and broad low-intensity asymmetric oxygen stretches (ν_2) and intense symmetric oxygen stretches (ν_1) of IO_6 octahedra are present in the regions 600–680 cm^{-1} and 680–950 cm^{-1}, respectively.

Table 6. Raman-Active Frequencies (in cm^{-1}) and Mode Assignment of Ca_2NaIO_6 and Sr_2NaIO_6 ($P2_1/n$) and Ba_2NaIO_6 (Fm-$3m$) Simulated from DFPT at the GGA/PBE Level, along with Raman Band Centers Measured in This Study

	Ca_2NaIO_6		Sr_2NaIO_6		Ba_2NaIO_6	
assign.	DFPT	exp	DFPT	exp	DFPT	exp
ν_1	689.7	717	698.9	722	699.2	713
ν_1	689.4		695.7			
ν_2	657.3	650	677.5	647	608.2	633
ν_2	623.3		620.3			
ν_2	616.5		617.6			
ν_2	603.0		612.7			
ν_5	473.8	472	454.6	452	406.2	425
ν_5	460.1	437	436.5			
ν_5	457.7		433.8			
ν_5	442.6		429.5			
ν_5	426.7		415.9			
ν_5	415.0		398.3			
L	276.7	246	213.4	175	108.1	107
L	274.9	216	170.5	152		
L	256.9		164.1			
L	245.2		158.0			
L	222.0		143.8			
L	211.9		133.8			
T	190.8	177	230.1	175		
T	181.9	143	124.1	152		
T	177.4	111	123.4	120		
T	138.9		108.2			
T	114.4		93.9			
T	114.2		88.9			

The cubic Fm-$3m$ unit cell of Ba_2NaIO_6 is composed of 40 atoms (Z = 4), resulting in 120 in degrees of freedom. The vibration analysis was carried out using the corresponding 10-atom primitive cell (Z = 1). In the O_h point group,[49] the acoustic modes, $\Gamma_{acoustic}(3) = 3T_{1u}$, belong to the triply degenerate T_{1u} irrep, while the remaining 27 optical modes can be represented as $\Gamma_{optical}(27) = A_{1g} + E_g + T_{2u} + 2T_{2g} + 4T_{1u} + T_{1g}$, where vibrational modes of the A_{1g}, E_g, and T irreps are nondegenerate, doubly degenerate, and triply degenerate, respectively. Among optical modes, 12 modes belonging to the T_{1u} irrep are IR active. The 9 Raman-active modes belong to the $\Gamma = A_{1g} + E_g + 2T_{2g}$ irreps, which can be decomposed alternatively as $\Gamma = L(T_{2g}) + \nu_5(T_{2g}) + \nu_2(E_g) + \nu_1(A_{1g})$, where ν_5, ν_2, and ν_1 have a similar meaning as in the $P2_1/n$ case, while L corresponds here to libration lattice modes of IO_6 octahedra. For perovskites crystallizing in the Fm-$3m$ space group, libration lattice modes L of IO_6 octahedra typically appear in the 100–300 cm^{-1} range, the ν_5 mode from the oxygen bending motion in octahedra occurs in the 300–450 cm^{-1} range, and the strong ν_1 oxygen symmetric stretch in octahedra is usually seen in the region 650–900 cm^{-1}. The ν_2 asymmetric oxygen stretch band at a slightly lower frequency is either very weak or even nonexistent in high-symmetry Fm-$3m$ perovskites and appears as a much narrower peak compared to $P2_1/n$ perovskites.

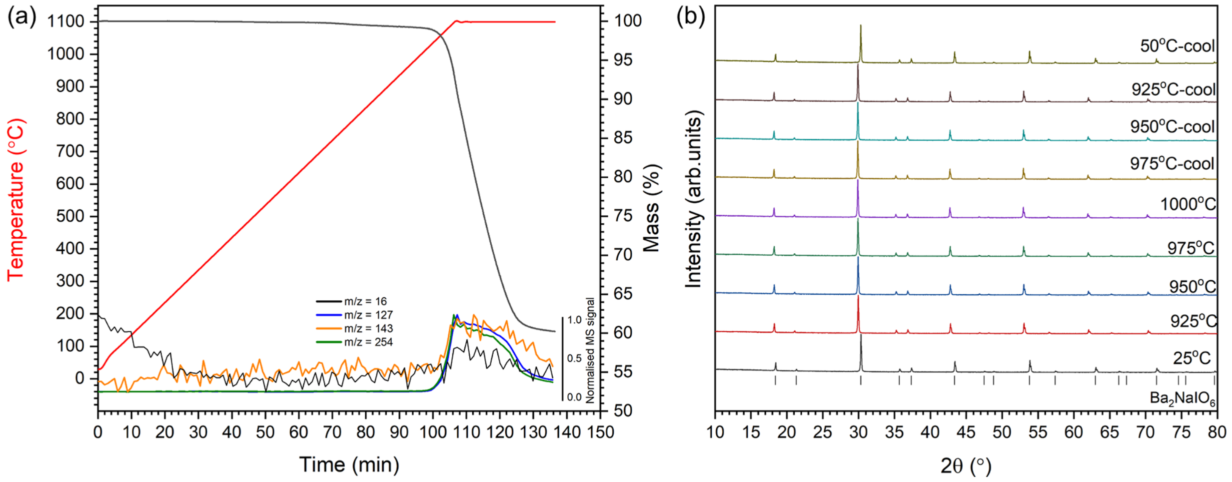

Figure 8. High temperature data for Ba_2NaIO_6. a) TGA-MS measurement with normalized m/z channels. b) HT-PXRD data for ramp to 1000 °C and subsequent cool. Tickmarks indicate allowed reflections.

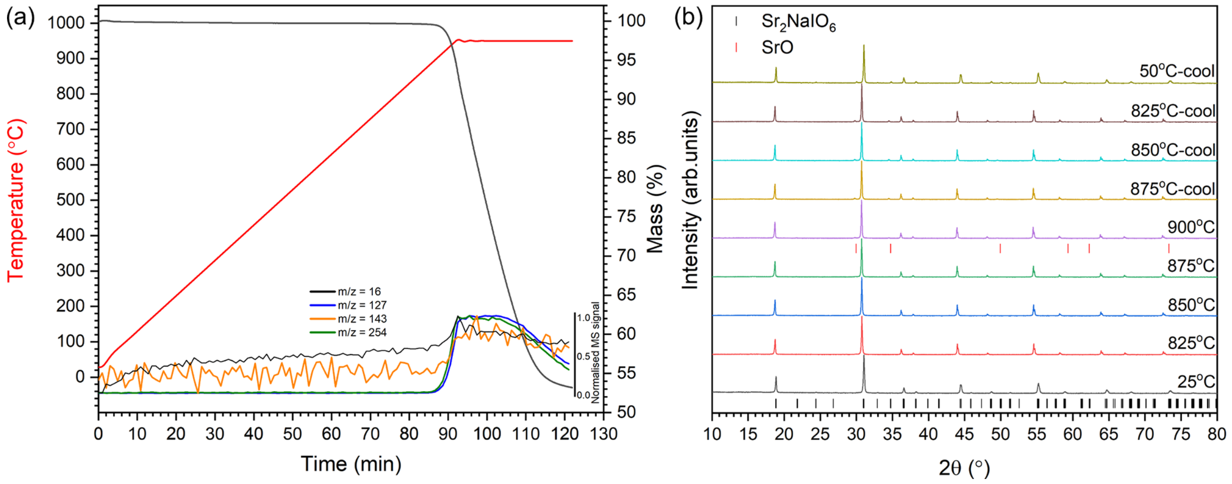

Figure 9. High temperature data for Sr_2NaIO_6. a) TGA-MS measurement with normalized m/z channels. b) HT-PXRD data for ramp to 900 °C and subsequent cool. Black tickmarks indicate allowed reflections for Sr_2NaIO_6, and red tickmarks indicate the onset of allowed reflections for SrO.

3.5. High Temperature Behavior.

The high temperature behavior of the periodate double perovskites was investigated by in situ high temperature X-ray powder diffraction (HT-PXRD) and thermogravimetric analysis (TGA-MS) coupled with mass spectroscopy.

TGA-MS analysis of Ba_2NaIO_6 (Figure 8) revealed this compound to remain stable up to a remarkably high temperature of 1050 °C, above which a sharp weight loss was observed. This was accompanied by signals at m/z = 127 and 254 (attributed to I^+ and I_2^+, respectively) and weaker signals at m/z = 16 and 143 (attributed to O_2^+ and IO^+). The final weight loss was determined to be 39.77 wt%, in good agreement with the expected weight loss of 41.1 wt% for the following decomposition reaction:

$$Ba_2NaIO_6(s) = 2BaO(s) + NaI(g) + 2O_2(g) \tag{4}$$

The sample was recovered from the TGA-MS analysis and confirmed to comprise BaO by XRD. Additionally, the material was characterized by SEM-EDX analysis (Figure S3) which evidenced the complete loss of NaI from the material, according to the absence of Na Kα and I Lα emission, consistent with the above decomposition reaction and XRD analysis. An additional strong signal arising from Al Kα emission was also evident, attributed to reaction between BaO and the Al_2O_3 crucible used for the measurement. Additionally, SEM images showed clear evidence for growth in particle size and development of faceting for the residual BaO which may be a result of a fluxing effect of NaI assisting diffusion (and reaction with the Al_2O_3 crucible). No MS signal was apparent at expected m/z = 23 or 150, attributable to Na or NaI, respectively, below or above 1050 °C. The melting point of NaI is 661 °C,[50] and therefore, it undoubtedly plated out in the gas transfer line between TGA and MS, which was maintained at 500 °C. The decomposition temperature of Ba_2NaIO_6 is higher than that reported for any periodate or metaperiodate reported in the most comprehensive tabulation available;[51] hitherto, the compound reported to have the highest thermal stability was $Ba_5(IO_6)_2$, which decomposes above 950 °C.

The high temperature behavior of Ba_2NaIO_6 was also investigated by in situ HT-PXRD but limited to a temperature of 1000 °C, as shown in Figure 8. The HT-PXRD data could

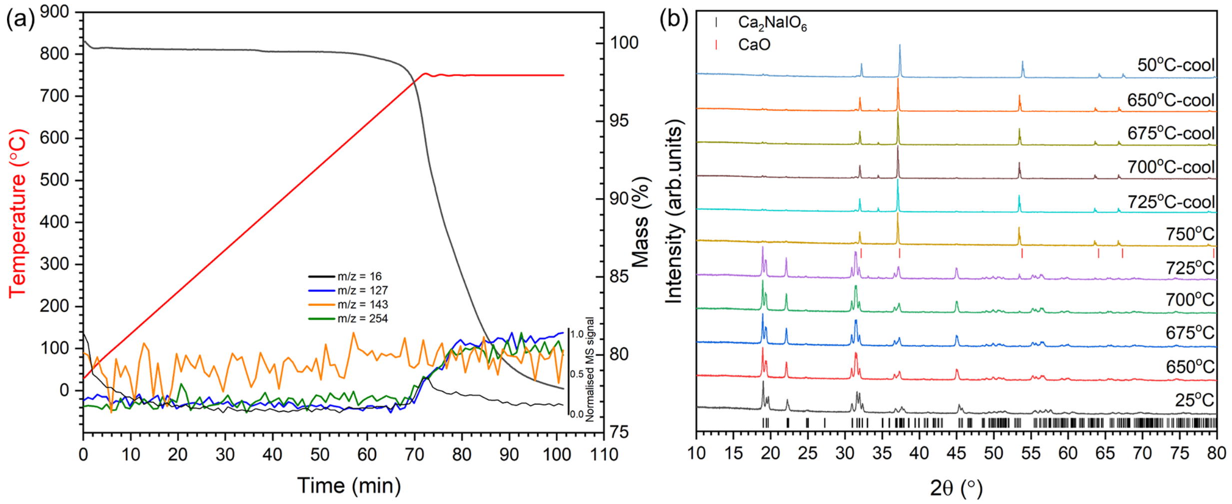

Figure 10. High temperature data for Ca_2NaIO_6. a) TGA-MS measurement with normalized m/z channels. b) HT-PXRD data for ramp to 750 °C and subsequent cool. Black tickmarks indicate allowed reflections for Ca_2NaIO_6, and red tickmarks indicate the onset of allowed reflections for CaO.

be indexed fully on the $Fm\text{-}3m$ structure of Ba_2NaIO_6, up to 1000 °C, and on subsequent cooling to 50 °C, demonstrating the thermal stability of the compound within this temperature window, consistent with TG-MS data. In particular, the R-point reflections, diagnostic of rock-salt ordering of Na and I on the B-site, remained clearly observable throughout. Thus, no order−disorder transition involving Na and I cations on the B-site is apparent up to 1000 °C.

TGA-MS analysis of Sr_2NaIO_6 (Figure 9) revealed this compound to remain stable up to 950 °C, accompanied by strong MS signals at $m/z = 127$ and 254 and weaker signals for $m/z = 16$ and 143, as observed for the Ba counterpart. The final weight loss was determined to be 46.8 wt%, in good agreement with the expected weight loss of 50.79 wt% for the following decomposition reaction:

$$Sr_2NaIO_{6(s)} = 2SrO_{(s)} + NaI_{(g)} + 2O_{2(g)} \tag{5}$$

The material recovered from TGA-MS analysis was characterized by SEM-EDX analysis (Figure S4) which showed the complete loss of NaI, and XRD analysis revealed the product to be SrO, in agreement with the above mechanism. SEM imaging showed evidence for some growth in particle size and development of faceting for the residual SrO, though to a less extent than observed in the case of Ba_2NaIO_6, likely due to reduced kinetics of diffusion at the lower temperature at which NaI is evolved.

Further investigation of the high temperature behavior of Sr_2NaIO_6 was made by *in situ* HT-PXRD, up to 900 °C, as shown in Figure 9. The HT-PXRD data could be indexed throughout with the $P2_1/n$ Sr_2NaIO_6 structure, with a secondary phase of SrO at 900 °C evident. R-point reflections indicative of rock-salt ordering on the B-site coupled with antiphase octahedral tilting (e.g., (111)) and X-point reflections (e.g., (021)) arising from the coupling of the aforementioned R- and implied M-point reflections were observed only in the room temperature and 50 °C data sets, prior to and after the heating regimen. Therefore, a reversible phase transition, involving relaxation of the coupled octahedral tilts, may occur between room temperature and 825 °C, though this must be understood as a tentative interpretation, given the weak nature of such reflections, and further investigation is warranted.

Finally, TGA-MS analysis of Ca_2NaIO_6 (Figure 10) revealed this compound to remain stable up to 730 °C, accompanied by MS signals at $m/z = 127$ and 254, as observed for the Ba and Sr counterparts. Unlike Ba and Sr, a stronger signal corresponding to $m/z = 16$ is seen and is not coupled to $m/z = 143$, which is not apparent in these data. The final weight loss obtained at 730 °C was determined to be 21.79 wt%; however, phase analysis of the post TGA product revealed this to be a mixture of majority CaO and residual Ca_2NaIO_6 and thus represents only a partial decomposition at 730 °C. Expected weight loss is 65.6 wt% for the following overall decomposition reaction:

$$Ca_2NaIO_{6(s)} = 2CaO_{(s)} + NaI_{(g)} + 2O_{2(g)} \tag{6}$$

The material recovered from TGA-MS analysis after ramping to 750 °C was characterized by SEM-EDX analysis (Figure S5) which showed the complete loss of I but some retention of Na, and XRD analysis revealed the product to be CaO together with an unidentified impurity phase. SEM imaging showed evidence for some evidence for sintering of the residual material but not the growth in particle size and development of faceting observed in the case of Ba_2NaIO_6 and Sr_2NaIO_6. These data suggest that thermal decomposition of Ca_2NaIO_6 proceeds via a different mechanism, compared to the Ba and Sr counterparts, involving the sequential loss of O_2 and I followed by volatilization of Na_2O.

Figure 11 shows the formation energy (E_f) and decomposition temperature of the A_2NaIO_6 compounds, as a function of the Goldschmidt tolerance factor, t. Ba_2NaIO_6 is the most thermally stable compound when heated in air, showing the onset of decomposition at 1050 °C, followed by Sr_2NaIO_6 at 950 °C and Ca_2NaIO_6 at 730 °C. As expected, this is inversely correlated to the formation energies previously discussed, which established Ba_2NaIO_6 to have the lowest formation energy at 4.517 eV/f.u., followed by Sr_2NaIO_6 at 5.060 eV/f.u. and Ca_2NaIO_6 at 5.518 eV/f.u. The formation energy indicates the thermodynamic driver for compound synthesis and, therefore, a comparatively large and positive E_f is

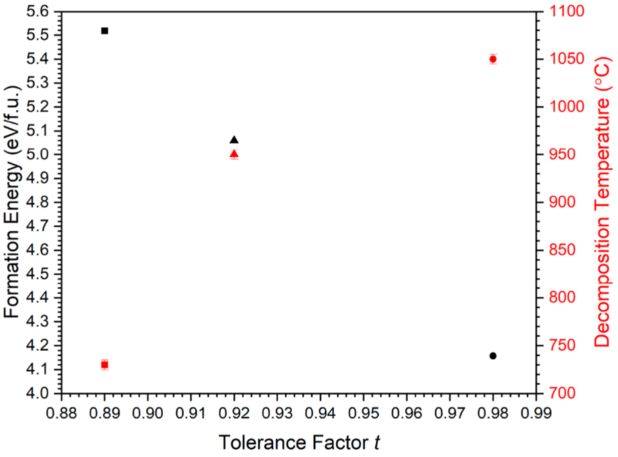

Figure 11. Formation energy and decomposition temperature as a function of tolerance factor for Ba_2NaIO_6 (circles), Sr_2NaIO_6 (triangles), and Ca_2NaIO_6(squares). Formation energies are plotted in black, and decomposition temperatures are plotted in red.

correlated with lower decomposition temperature. This can be further correlated with the structural stability of the compounds expressed as the tolerance factor. Ba_2NaIO_6, with a tolerance factor of $t = 0.98$, was shown to be an undistorted cubic *Fm*-3*m* symmetry, while the lower tolerance factors of the $P2_1/n$ compounds, $t \ll 1$, indicate bond length mismatch giving rise to structural distortion. For Ca_2NaIO_6, the tolerance factor is close to the lower limit observed for double perovskites with the tilt system $a^-a^-c^+$ ($P2_1/n$), $0.83 < t < 0.98$,[47] suggesting this compound is at the limit of structural stability; it therefore has the lowest decomposition temperature and highest formation energy, E_f.

4. CONCLUSIONS

The A_2NaIO_6 (A = Ba, Sr, Ca) double perovskite structures were determined from a combination of powder neutron and X-ray diffraction data, Raman spectroscopy, and DFT calculations. These perovskites are characterized by rock-salt ordering of I and Na on the B-site; Ba_2NaIO_6 adopts the *Fm*-3*m* aristotype structure without cooperative octahedral tilting, whereas Sr_2NaIO_6 and Ca_2NaIO_6 adopt the $P2_1/n$ hettotype structure with cooperative antiphase and in-phase octahedral tilting consistent with expectations of group theory. DFT calculations established the $P2_1/n$ structure to be energetically favorable, compared to *Fm*-3*m*, for Ca_2NaIO_6 and Sr_2NaIO_6, consistent with experimental data. In contrast, DFT calculations determined the $P2_1/n$ and *Fm*-3*m* structures of Ba_2NaIO_6 to be energetically degenerate, whereas diffraction and Raman spectroscopy data establish the structure to be cubic at room temperature. This may point to an incipient low temperature phase transition in Ba_2NaIO_6 involving the onset of cooperative octahedral tilting.

Ba_2NaIO_6 was found to exhibit remarkable thermal stability, decomposing only above 1050 °C (in air), and as far as we are able to ascertain, this compound exhibits the highest thermal stability of any iodine bearing substance so far documented. The decomposition temperatures of the A_2NaIO_6 perovskites follow the trend of formation energy determined from DFT, A = Ba > Sr > Ca, with Sr_2NaIO_6 decomposing above 950 °C and Ca_2NaIO_6 above 730 °C (in air). Ba_2NaIO_6 and Sr_2NaIO_6 thermal decompose by evaporation of NaI, whereas thermal decomposition of Ca_2NaIO_6 proceeds by loss of O_2 and I_2, followed by evaporation of Na_2O.

With regard to application of A_2NaIO_6 perovskites as an immobilization matrix for radioiodine, this investigation has demonstrated considerable potential. These compounds offer an iodine incorporation rate of 25−40 wt%, comparable with that demonstrated for the most efficient iodide waste form counterparts. The synthesis of A_2NaIO_6 phases is achieved in a quantitative yield, by reaction between $A(OH)_2{\cdot}nH_2O$ and $NaIO_4$, in one step at a relatively low temperature of 650 °C. This approach is compatible with conventional caustic and other advanced scrubbing processes for fuel dissolver off-gas which afford radioiodine speciated as iodate, which can easily be converted to $NaIO_4$. Thermal stability in the context of fire scenarios is one criterion of interest for selection of a waste immobilization matrix, and in this regard, Ba_2NaIO_6 surpasses the performance of alternate ceramic options. Future work will investigate the potential for forming sintered ceramic bodies of the periodate perovskites to facilitate examination of their dissolution behavior.

■ ASSOCIATED CONTENT

Supporting Information

The Supporting Information is available free of charge at https://pubs.acs.org/doi/10.1021/acs.inorgchem.0c03044.

> Comparison of BVS between this work and previous work, structures representation from DFT-optimization, simulated X-ray diffraction patterns, bond lengths and atomic positions comparison between DFT and experimental data, and SEM-EDS analysis of A_2NaIO_6 powder pre- and post-HT-XRD (PDF)

Accession Codes

CCDC 2036872−2036874 contains the supplementary crystallographic data for this structure. These data can be obtained free of charge via www.ccdc.cam.ac.uk/data_request/cif, or by emailing data_request@ccdc.cam.ac.uk, or by contacting The Cambridge Crystallographic Data Centre, 12 Union Road, Cambridge CB2 1EZ, UK; fax: +44 1223 336033.

■ AUTHOR INFORMATION

Corresponding Authors

Shi-Kuan Sun − *Department of Materials Science and Engineering, University of Sheffield, Sheffield S1 3JD, U.K.*; orcid.org/0000-0002-1688-5072; Email: shikuan.sun@sheffield.ac.uk

Eunja Kim − *Department of Physics and Astronomy, University of Nevada, Las Vegas, Nevada 89154, United States*; Email: kimej@physics.unlv.edu

Neil C. Hyatt − *Department of Materials Science and Engineering, University of Sheffield, Sheffield S1 3JD, U.K.*; orcid.org/0000-0002-2491-3897; Email: n.c.hyatt@sheffield.ac.uk

Authors

Sarah E. O'Sullivan − *Department of Materials Science and Engineering, University of Sheffield, Sheffield S1 3JD, U.K.*

Eduardo Montoya − *Department of Chemistry and Biochemistry, University of Nevada, Las Vegas, Nevada 89154, United States*

Jonathan George − *Department of Chemistry and Biochemistry, University of Nevada, Las Vegas, Nevada 89154, United States*

Cameron Kirk − *Department of Electrical and Computer Engineering, University of Nevada, Las Vegas, Nevada 89154, United States*

Malin C. Dixon Wilkins − *Department of Materials Science and Engineering, University of Sheffield, Sheffield S1 3JD, U.K.;* orcid.org/0000-0003-1520-7672

Philippe F. Weck − *Sandia National Laboratories, Albuquerque, New Mexico 87185, United States;* orcid.org/0000-0002-7610-2893

Kevin S. Knight − *Department of Materials Science and Engineering, University of Sheffield, Sheffield S1 3JD, U.K.; Department of Earth Sciences, University College London, London WC1E 6BT, U.K.*

Complete contact information is available at:
https://pubs.acs.org/10.1021/acs.inorgchem.0c03044

Notes

The views expressed in the article do not necessarily represent the views of the U.S. DOE or the United States Government. The authors declare no competing financial interest.

■ ACKNOWLEDGMENTS

Components of this research utilized the HADES/MIDAS facility at the University of Sheffield established with financial support from EPSRC and BEIS, under grant EP/T011424/1.[52] Experiments at the ISIS Neutron and Muon Source were supported by a beamtime allocation RB1920341 from the Science and Technology Facilities Council; we thank Dr. R. Smith for assistance with data acquisition.[26] S.O.S., S.K.S., and N.C.H. are grateful for financial support from EPSRC under grant numbers EP/L015390/1 and EP/S01019X/1. Components of this research was performed using funding received from the U.S. Department of Energy, Office of Nuclear Energy's Nuclear Energy University Program (NEUP). Sandia National Laboratories is a multimission laboratory managed and operated by National Technology and Engineering Solutions of Sandia, LLC., a wholly owned subsidiary of Honeywell International, Inc., for the U.S. Department of Energy's (DOE) National Nuclear Security Administration under contract DE-NA0003525. This work was performed, in part, at the Center for Integrated Nanotechnologies, an Office of Science User Facility operated for the U.S. Department of Energy (DOE) Office of Science.

■ REFERENCES

(1) Riley, B. J.; Vienna, J. D.; Strachan, D. M.; McCloy, J. S.; Jerden, J. L. Materials and Processes for the Effective Capture and Immobilization of Radioiodine: A Review. *J. Nucl. Mater.* **2016**, *470*, 307−326.

(2) Yeager, C. M.; Amachi, S.; Grandbois, R.; Kaplan, D. I.; Xu, C.; Schwehr, K. A.; Santschi, P. H. Microbial Transformation of Iodine: From Radioisotopes to Iodine Deficiency. *Adv. Appl. Microbiol.* **2017**, *101*, 83−136.

(3) Kaplan, D. I.; Denham, M. E.; Zhang, S.; Yeager, C.; Xu, C.; Schwehr, K. A.; Li, H. P.; Ho, Y. F.; Wellman, D.; Santschi, P. H. Radioiodine Biogeochemistry and Prevalence in Groundwater. *Crit. Rev. Environ. Sci. Technol.* **2014**, *44* (20), 2287−2335.

(4) Thomas, G. Radiation and Thyroid Cancer-an Overview. *Radiat. Prot. Dosim.* **2018**, *182* (1), 53−57.

(5) Kantelo, M. V.; Bauer, L. R.; Marter, W. L.; Murphy, J. C. E.; Zeigler, C. C. *Radioiodine in the Savannah River Site Environment*; Report WSRC-RP-90-424-2; Westinghouse Savannah River Co.: United States, 1993; DOI: 10.2172/10122501.

(6) Santschi, P. H.; Xu, C.; Zhang, S.; Schwehr, K. A.; Grandbois, R.; Kaplan, D. I.; Yeager, C. M. Iodine and Plutonium Association with Natural Organic Matter: A Review of Recent Advances. *Appl. Geochem.* **2017**, *85*, 121−127.

(7) Taylor, P. *A Review of Methods for Immobilizing Iodine-129 Arising from a Nuclear Fuel Recycle Plant, with Emphasis on Waste-Form Chemistry*; Canada, 1990.

(8) Dalba, G.; Fornasini, P.; Rocca, F. Short Range Order in AgI:Ag2O:B2O3 Glasses: Results from Exafs and Related Techniques. *J. Non-Cryst. Solids* **1990**, *123* (1), 310−314.

(9) Stennett, M. C.; Pinnock, I. J.; Hyatt, N. C. Rapid Synthesis of $Pb_5(VO_4)_3I$, for the Immobilisation of Iodine Radioisotopes, by Microwave Dielectric Heating. *J. Nucl. Mater.* **2011**, *414* (3), 352−359.

(10) Tanabe, H.; Sakuragi, T.; Yamaguchi, K.; Sato, T.; Owada, H. Development of New Waste Forms to Immobilize Iodine-129 Released from a Spent Fuel Reprocessing Plant. *Adv. Sci. Technol.* **2010**, *73*, 158−170.

(11) Garino, T. J.; Nenoff, T. M.; Krumhansl, J. L.; Rademacher, D. X. Low-Temperature Sintering Bi-Si-Zn-Oxide Glasses for Use in Either Glass Composite Materials or Core/Shell ^{129}I Waste Forms. *J. Am. Ceram. Soc.* **2011**, *94* (8), 2412−2419.

(12) Krumhansl, J. L.; Nenoff, T. M. Hydrotalcite-Like Layered Bismuth-Iodine-Oxides as Waste Forms. *Appl. Geochem.* **2011**, *26* (1), 57−64.

(13) Campayo, L.; Grandjean, A.; Coulon, A.; Delorme, R.; Vantelon, D.; Laurencin, D. Incorporation of Iodates into Hydroxyapatites: A New Approach for the Confinement of Radioactive Iodine. *J. Mater. Chem.* **2011**, *21* (44), 17609−17611.

(14) Couture, R. A.; Seitz, M. G. Sorption of Anions of Iodine by Iron Oxides and Kaolinite. *Nucl. Chem. Waste Manage.* **1983**, *4* (4), 301−306.

(15) Machesky, M. L.; Bischoff, B. L.; Anderson, M. A. Calorimetric Investigation of Anion Adsorption onto Goethite. *Environ. Sci. Technol.* **1989**, *23* (5), 580−587.

(16) Hill, A. E. Ternary Systems. VII. The Periodates of the Alkali Metals. *J. Am. Chem. Soc.* **1928**, *50* (10), 2678−2692.

(17) Thompson, N. R. In *The Chemistry of Copper, Silver and Gold*; Massey, A. G., Thompson, N. R., Johnson, B. F. G., Davis, R., Eds.; Pergamon: Oxford, UK, 1973; Chapter 28, pp 79−128, DOI: 10.1016/B978-0-08-018860-7.50007-4.

(18) Reimer, I.; Lister, M. W. The Compounds $KMnO_6$ and $NaMnIO_6$. *Can. J. Chem.* **1961**, *39* (12), 2431−2435.

(19) Levason, W. The Coordination Chemistry of Periodate and Tellurate Ligands. *Coord. Chem. Rev.* **1997**, *161*, 33−79.

(20) Sleight, A. W.; Ward, R. Compounds of Post-Transition Elements with the Ordered Perovskite Structure. *Inorg. Chem.* **1964**, *3* (2), 292−292.

(21) De Hair, J. T. W.; Corsmit, A. F.; Blasse, G. Vibrational Spectra and Force Constants of Periodates with Ordered Perovskite Structure. *J. Inorg. Nucl. Chem.* **1974**, *36* (2), 313−315.

(22) Kubel, F.; Wandl, N.; Pantazi, M.; D'Anna, V.; Hagemann, H. The Periodate-Based Double Perovskites M_2NaIO_6 (M = Ca, Sr, and Ba). *Z. Anorg. Allg. Chem.* **2013**, *639* (6), 892−898.

(23) Kubel, F.; Pantazi, M.; Wandl, N.; Hagemann, H. Synthesis and Crystal Structures of a Stable, a Metastable and a High Temperature Modification of Pb_2NaIO_6. *Z. Anorg. Allg. Chem.* **2014**, *640* (15), 3184−3189.

(24) Howard, C. J.; Kennedy, B. J.; Woodward, P. M. Ordered Double Perovskites - a Group-theoretical Analysis. *Acta Crystallogr., Sect. B: Struct. Sci.* **2003**, *59* (4), 463−471.

(25) Brown, I. D.; Altermatt, D. Bond-Valence Parameters Obtained from a Systematic Analysis of the Inorganic Crystal Structure Database. *Acta Crystallogr., Sect. B: Struct. Sci.* **1985**, *41* (4), 244−247.

(26) Hyatt, N. Crystal Structure of Ba_2NaIO_6, Sr_2NaIO_6m and Ca_2NaIO_6 *STFC ISIS Neutron and Muon Source* 2019; DOI: 10.5286/ISIS.E.RB1990180-1, DOI: 10.5286/ISIS.E.RB1990181-1, and DOI: 10.5286/ISIS.E.RB1990182-1.

(27) Smith, R. I.; Hull, S.; Tucker, M. G.; Playford, H. Y.; McPhail, D. J.; Waller, S. P.; Norberg, S. T. The Upgraded Polaris Powder Diffractometer at the Isis Neutron Source. *Rev. Sci. Instrum.* **2019**, *90* (11), 115101.

(28) Arnold, O.; Bilheux, J. C.; Borreguero, J. M.; Buts, A.; Campbell, S. I.; Chapon, L.; Doucet, M.; Draper, N.; Ferraz Leal, R.; Gigg, M. A.; Lynch, V. E.; Markvardsen, A.; Mikkelson, D. J.; Mikkelson, R. L.; Miller, R.; Palmen, K.; Parker, P.; Passos, G.; Perring, T. G.; Peterson, P. F.; Ren, S.; Reuter, M. A.; Savici, A. T.; Taylor, J. W.; Taylor, R. J.; Tolchenov, R.; Zhou, W.; Zikovsky, J. Mantid—Data Analysis and Visualization Package for Neutron Scattering and M Sr Experiments. *Nucl. Instrum. Methods Phys. Res., Sect. A* **2014**, *764*, 156−166.

(29) Larson, A. C.; Von Dreele, R. B. *General Structure Analysis System (GSAS)*; Los Alamos National Laboratory Report LAUR 86-748, United States, 2004.

(30) Toby, B. Expgui, a Graphical User Interface for GSAS. *J. Appl. Crystallogr.* **2001**, *34* (2), 210−213.

(31) Brese, N. E.; O'Keeffe, M. Bond-Valence Parameters for Solids. *Acta Crystallogr., Sect. B: Struct. Sci.* **1991**, *47* (2), 192−197.

(32) Allmann, R. Beziehungen Zwischen Bindungslängen Und Bindungsstärken in Oxidstrukturen. *Monatsh. Chem.* **1975**, *106* (3), 779−793.

(33) Brown, I. D. Recent Developments in the Methods and Applications of the Bond Valence Model. *Chem. Rev.* **2009**, *109* (12), 6858−6919.

(34) Kresse, G.; Furthmüller, J. Efficient Iterative Schemes for ab initio Total-Energy Calculations Using a Plane-Wave Basis Set. *Phys. Rev. B: Condens. Matter Mater. Phys.* **1996**, *54* (16), 11169−11186.

(35) Blöchl, P. E. Projector Augmented-Wave Method. *Phys. Rev. B: Condens. Matter Mater. Phys.* **1994**, *50* (24), 17953−17979.

(36) Kresse, G.; Joubert, D. From Ultrasoft Pseudopotentials to the Projector Augmented-Wave Method. *Phys. Rev. B: Condens. Matter Mater. Phys.* **1999**, *59* (3), 1758−1775.

(37) Perdew, J. P.; Burke, K.; Ernzerhof, M. Generalized Gradient Approximation Made Simple. *Phys. Rev. Lett.* **1996**, *77* (18), 3865−3868.

(38) Monkhorst, H. J.; Pack, J. D. Special Points for Brillouin-Zone Integrations. *Phys. Rev. B.* **1976**, *13* (12), 5188−5192.

(39) Weck, P. F.; Kim, E.; Buck, E. C. On the Mechanical Stability of Uranyl Peroxide Hydrates: Implications for Nuclear Fuel Degradation. *RSC Adv.* **2015**, *5* (96), 79090−79097.

(40) Weck, P. F.; Kim, E.; Jové-Colón, C. F. Relationship between Crystal Structure and Thermo-Mechanical Properties of Kaolinite Clay: Beyond Standard Density Functional Theory. *Dalton Trans.* **2015**, *44* (28), 12550−12560.

(41) Weck, P. F.; Kim, E. Thermodynamics of Technetium: Reconciling Theory and Experiment Using Density Functional Perturbation Analysis. *Dalton Trans.* **2015**, *44* (28), 12735−12742.

(42) Rosenstein, R. D.; Schor, R. Superlattice Madelung Energy of Idealized Ordered Cubic Perovskites. *J. Chem. Phys.* **1963**, *38* (7), 1789−1790.

(43) Stitzer, K. E.; Smith, M. D.; Zur Loye, H.-C. Crystal Growth of Ba_2MoSO_6 (M = Li, Na) from Reactive Hydroxide Fluxes. *Solid State Sci.* **2002**, *4* (3), 311−316.

(44) Bharathy, M.; Zur Loye, H. C. Crystal Growth and Structural Investigation of A_2BReO_6 (a = Sr, Ba; B = Li, Na). *J. Solid State Chem.* **2008**, *181* (10), 2789−2795.

(45) Goldschmidt, V. Geochemische verteilungsgesetze der elemente. *Skrifter der Norske Videnskaps-Akad* **1926**, *8* (3), 529−533.

(46) Shannon, R. D.; Prewitt, C. T. Effective Ionic Radii in Oxides and Fluorides. *Acta Crystallogr., Sect. B: Struct. Crystallogr. Cryst. Chem.* **1969**, *25* (5), 925−946.

(47) Lufaso, M. W.; Barnes, P. W.; Woodward, P. M. Structure Prediction of Ordered and Disordered Multiple Octahedral Cation Perovskites Using Spuds. *Acta Crystallogr., Sect. B: Struct. Sci.* **2006**, *62* (3), 397−410.

(48) Knight, K. S. Parameterization of Centrosymmetric Elpasolite-Type Crystal Structures in terms of Symmetry-Adapted Basis-Vectors of the Primitive Cubic Aristotype Phase. *Can. Mineral.* **2009**, *47* (2), 401−420.

(49) Dresselhaus, M. S.; Dresselhaus, G.; Jorio, A. *Group Theory*; Springer Berlin Heidelberg: Berlin, Heidelberg, 2008; DOI: 10.1007/978-3-540-32899-5.

(50) Galamba, N.; Costa Cabral, B. J. First Principles Molecular Dynamics of Molten NaI: Structure, Self-Diffusion, Polarization Effects, and Charge Transfer. *J. Chem. Phys.* **2007**, *127* (9), 094506.

(51) Stern, K. *High Temperature Properties and Thermal Decomposition of Inorganic Salts with Oxyanions*; Taylor & Francis: Boca Raton, FL, 2000; DOI: 10.1201/9781420042344.

(52) Hyatt, N. C.; Corkhill, C. L.; Stennett, M. C.; Hand, R. J.; Gardner, L. J.; Thorpe, C. L. The Hades Facility for High Activity Decommissioning Engineering & Science: Part of the UK National Nuclear User Facility. *IOP Conf. Ser.: Mater. Sci. Eng.* **2020**, *818*, 012022.

Supporting Information

The crystal and electronic structures of A_2NaIO_6 periodate double perovskites (A=Sr,Ca,Ba): Candidate wasteforms for I-129 immobilisation

Sarah E. O'Sullivan[a], Eduardo Montoya[b], Shi-Kuan Sun[a*], Jonathan George[b], Cameron Kirk[c], Malin C. Dixon Wilkins[a], Philippe F. Weck[d], Eunja Kim[e*], Kevin S. Knight[a], and Neil C. Hyatt[a*].

[a] Department of Materials Science and Engineering, University of Sheffield, Sheffield, S1 3JD, UK

[b] Department of Chemistry and Biochemistry, University of Nevada, Las Vegas, NV 89154, USA

[c] Department of Electrical and Computer Engineering, University of Nevada, Las Vegas, NV 89154, USA

[d] Sandia National Laboratories, Albuquerque, NM 87185, USA

[e] Department of Physics and Astronomy, University of Nevada, Las Vegas, NV 89154, USA

*Corresponding authors. E-mail address: shikuan.sun@sheffield.ac.uk; kimej@physics.unlv.edu; n.c.hyatt@sheffield.ac.uk. Here, Shi-Kuan Sun (shikuan.sun@sheffield.ac.uk) will handle correspondence at all stages

Table S1: Comparison of BVS as calculated in this work against calculations using bond length data from previous work [22].

Compound	**Bonds**	**Expected valence**	**BVS from previous work**	**BVS from this work**
Ba_2NaIO_6	Ba-O (CN=12)	2	1.980	1.967
	I-O (CN=6)	7	5.840	7.079
	Na-O (CN=6)	1	1.289	1.073
Sr_2NaIO_6	Sr-O (CN=12)	2	1.827	1.892
	I-O (CN=6)	7	5.854	7.077
	Na-O (CN=6)	1	1.341	1.125
Ca_2NaIO_6	Ca-O (CN=12)	2	2.008	1.876
	I-O (CN=6)	7	5.996	7.122
	Na-O (CN=6)	1	1.142	0.982

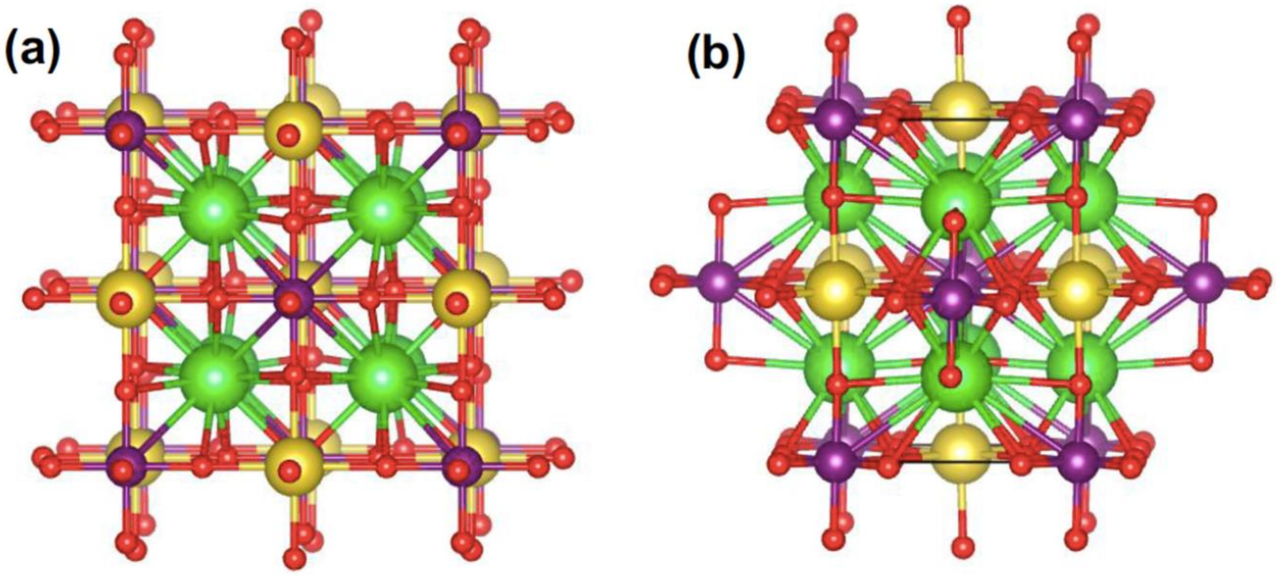

Figure S1: Ball-and-stick representation of the DFT-optimized (a) cubic *Fm*-3*m* phase (b) monoclinic *P*2₁/*n* phase. Colour legend: green, M = Ca, Sr, or Ba; yellow, Na; purple, I; red, O.

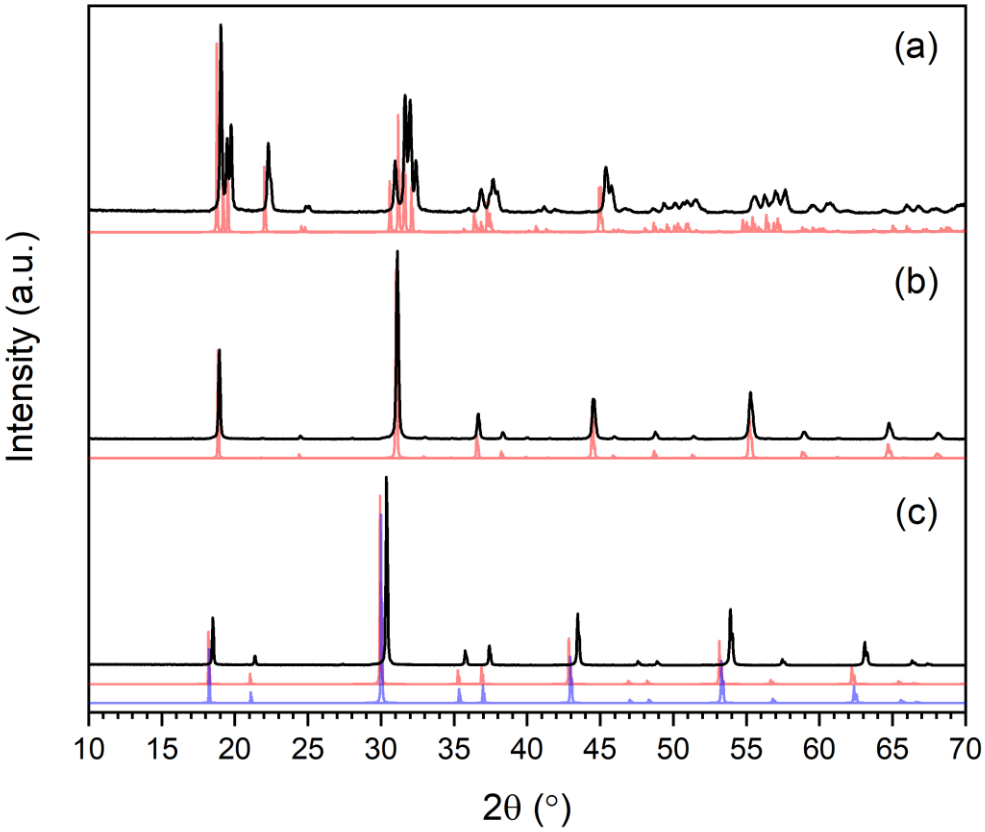

Figure S2: Simulated X-ray diffraction patterns of (a) Ca_2NaIO_6 in the monoclinic *P*2$_1$/*n* phase, (b) Sr_2NaIO_6 in the monoclinic *P*2$_1$/*n* phase, and (c) Ba_2NaIO_6 in the cubic *Fm*-3*m* (red) and monoclinic *P*2$_1$/*n* (blue) phases. Corresponding experimental XRD patterns collected in this study are displayed in black.

Table S2: Comparison of bond lengths obtained via DFT to experimental data acquired in this study (where applicable).

Ba_2NaIO_6 *Fm-3m*			**Ba_2NaIO_6 $P2_1/n$**			**Sr_2NaIO_6 $P2_1/n$**			**Ca_2NaIO_6 $P2_1/n$**		
Bond	**DFT (Å)**	**Exp (Å)**	**Bond**	**DFT (Å)**	**Exp (Å)**	**Bond**	**DFT (Å)**	**Exp (Å)**	**Bond**	**DFT (Å)**	**Exp (Å)**
Ba-O1 (x12)	2.992	2.954	Ba-O1	3.022	-	Sr-O1	3.186	3.186	Ca-O1	3.673	3.617
			Ba-O1	3.021	-	Sr-O1	2.658	2.658	Ca-O1	2.384	2.375
			Ba-O1	2.962	-	Sr-O1	2.553	2.550	Ca-O1	2.352	2.340
			Ba-O1	2.970	-	Sr-O1	3.248	3.248	Ca-O1	3.395	3.364
			Ba-O2	2.945	-	Sr-O2	2.571	2.571	Ca-O2	2.387	2.381
			Ba-O2	3.042	-	Sr-O2	2.790	2.790	Ca-O2	2.697	2.683
			Ba-O2	2.985	-	Sr-O2	2.875	2.875	Ca-O2	2.745	2.725
			Ba-O2	3.001	-	Sr-O2	3.366	3.366	Ca-O2	3.705	3.654
			Ba-O3	3.012	-	Sr-O3	2.820	2.819	Ca-O3	2.562	2.574
			Ba-O3	3.019	-	Sr-O3	2.556	2.556	Ca-O3	2.384	2.366
			Ba-O3	2.976	-	Sr-O3	3.398	3.398	Ca-O3	3.703	3.671
			Ba-O3	2.968	-	Sr-O3	2.846	2.846	Ca-O3	3.020	2.961
I-O1 (x6)	1.908	1.868	I-O1 (x2)	1.909	-	I-O1 (x2)	1.863	1.863	I-O1 (x2)	1.905	1.861
			I-O2 (x2)	1.909	-	I-O2 (x2)	1.869	1.870	I-O2 (x2)	1.900	1.865
			I-O3 (x2)	1.908	-	I-O3 (x2)	1.874	1.874	I-O3 (x2)	1.910	1.874
Na-O1 (x6)	2.314	2.298	Na-O1 (x2)	2.315	-	Na-O1 (x2)	2.281	2.281	Na-O1 (x2)	2.353	2.341
			Na-O2 (x2)	2.318	-	Na-O2 (x2)	2.275	2.275	Na-O2 (x2)	2.287	2.297
			Na-O3 (x2)	2.315	-	Na-O3 (x2)	2.286	2.286	Na-O3 (x2)	2.369	2.368

Table S3: Atomic positions obtained via DFT and compared to experimental values for Ca_2NaIO_6 ($P2_1/n$), Sr_2NaIO_6 ($P2_1/n$), and Ba_2NaIO_6 (Fm-3m and $P2_1/n$).

Ca_2NaIO_6 $P2_1/n$

		x		y		z	
Atom	Wyckoff position	DFT	Exp	DFT	Exp	DFT	Exp
Na	2a	0	0	0	0	0	0
I	2b	0	0	0	0	0.5	0.5
Ca	4e	0.018	0.0160	0.558	0.5575	0.243	0.2447
O1	4e	-0.114	-0.1108	-0.057	-0.0537	0.278	0.2809
O2	4e	0.222	0.2243	0.324	0.3266	0.046	0.0453
O3	4e	0.335	0.3381	0.768	0.7666	0.072	0.0705

Sr_2NaIO_6 $P2_1/n$

		x		y		z	
Atom	Wyckoff position	DFT	Exp	DFT	Exp	DFT	Exp
Na	2a	0	0	0	0	0	0
I	2b	0	0	0	0	0.5	0.5
Sr	4e	0.010	0.0057	0.544	0.5287	0.249	0.2499
O1	4e	-0.080	-0.0665	-0.028	-0.0177	0.278	0.2762
O2	4e	0.238	0.2433	0.315	0.3071	0.038	0.0331
O3	4e	0.320	0.3124	0.761	0.7608	0.047	0.0355

Ba_2NaIO_6 Fm-3m

		x		y		z	
Atom	Wyckoff position	DFT	Exp	DFT	Exp	DFT	Exp
I	4a	0	0	0	0	0	0
Na	4b	0.5	0.5	0.5	0.5	0.5	0.5
Ba	8c	0.25	0.25	0.25	0.25	0.25	0.25
O1	24e	0.226	0.224	0	0	0	0

Ba_2NaIO_6 $P2_1/n$

		x		y		z	
Atom	Wyckoff position	DFT	Exp	DFT	Exp	DFT	Exp
Na	2d	0.5	-	0.0	-	0.0	-
I	2a	0.0	-	0.0	-	0.0	-
Ba	4e	-0.25	-	0.5	-	0.0	-
O1	4e	-0.005	-	0.775	-	0.226	-
O2	4e	0.226	-	-0.001	-	0.008	-
O3	4e	-0.004	-	0.227	-	0.225	-

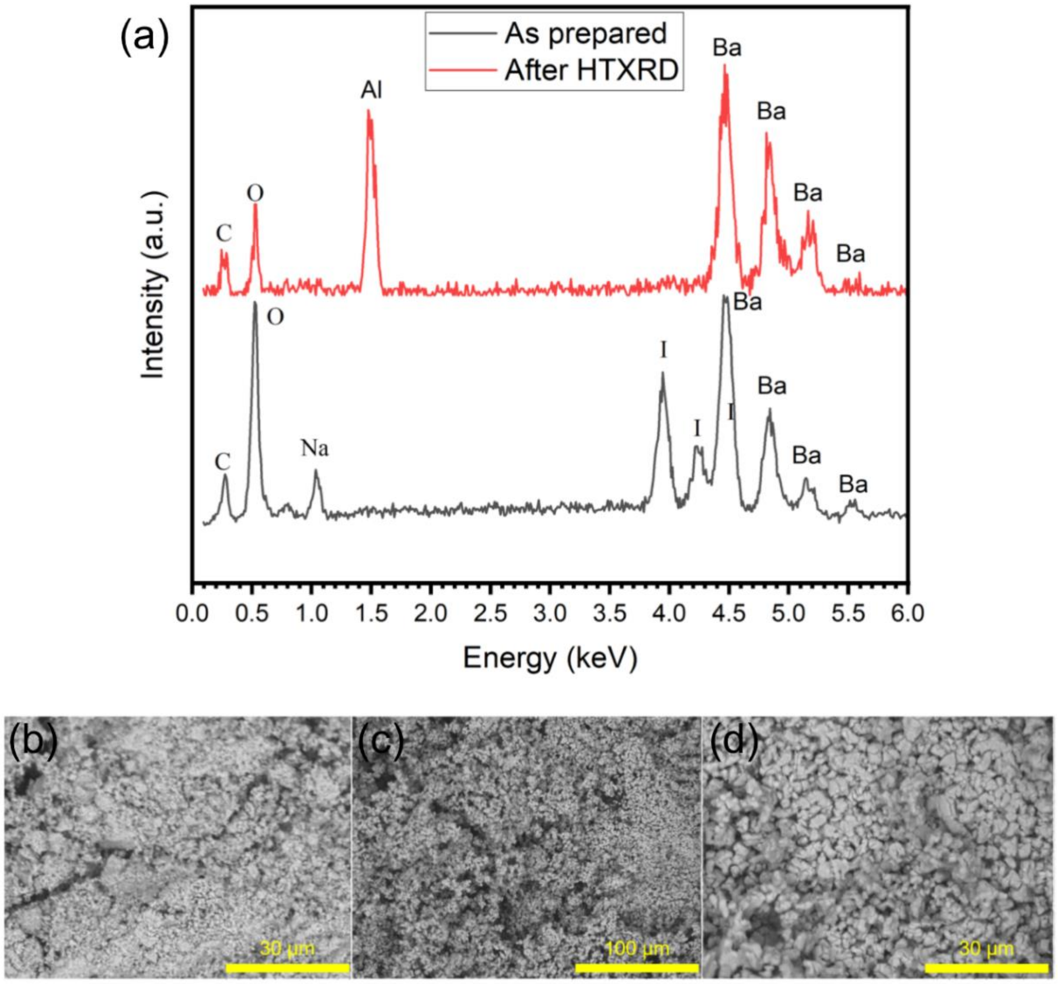

Figure S3: a) EDS analysis of Ba_2NaIO_6 powder pre- (black) and post- HT-XRD (red) showing the loss of Na and I after the heat treatment. The inclusion of Al is attributed to contamination arising from the Al_2O_3 crucible reacting under a combined heat treatment with a mild iodine flux. SEM images show as prepared Ba_2NaIO_6 (b) and after decomposition at 1030 °C to BaO ((c) and (d)).

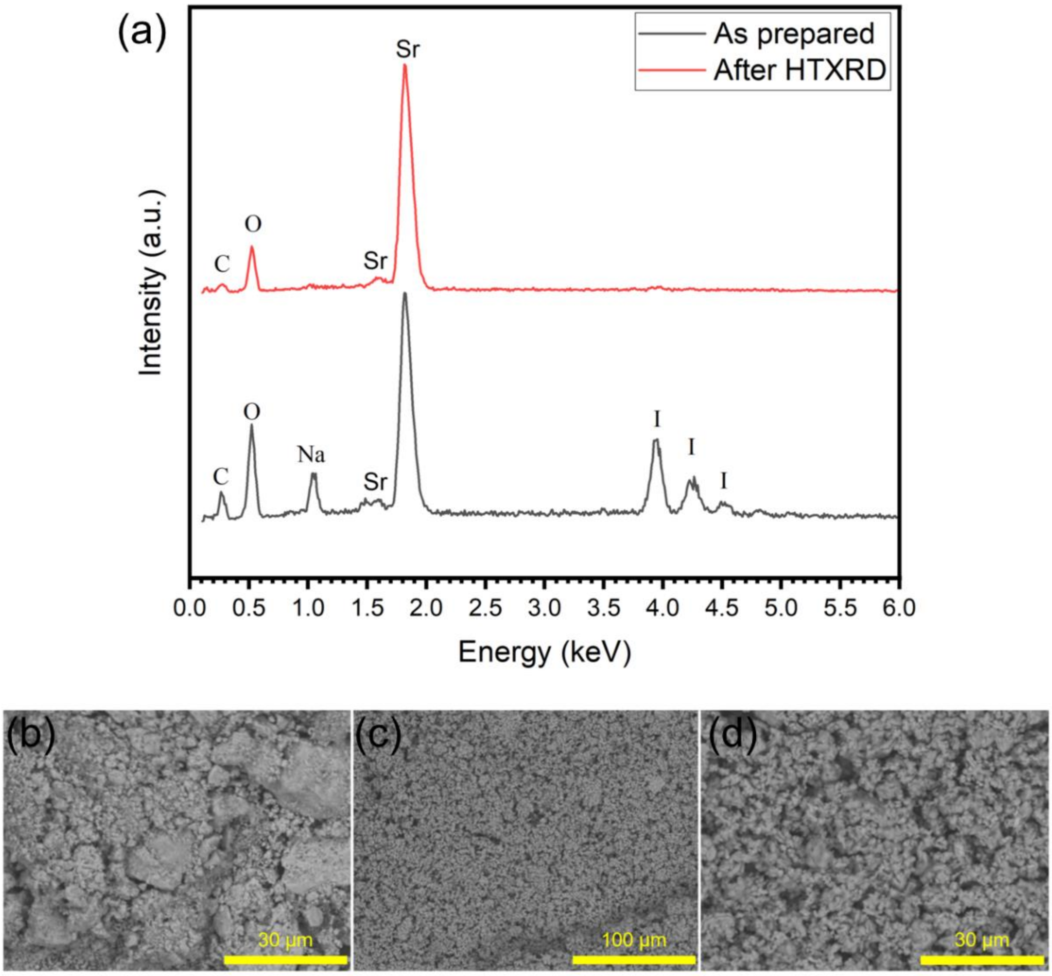

Figure S4 a) EDS analysis of Sr_2NaIO_6 powder pre- (black) and post- HT-XRD (red). SEM images show prepared Sr2NaIO6 (b) and after decomposition at 950 °C to SrO ((c) and (d)).

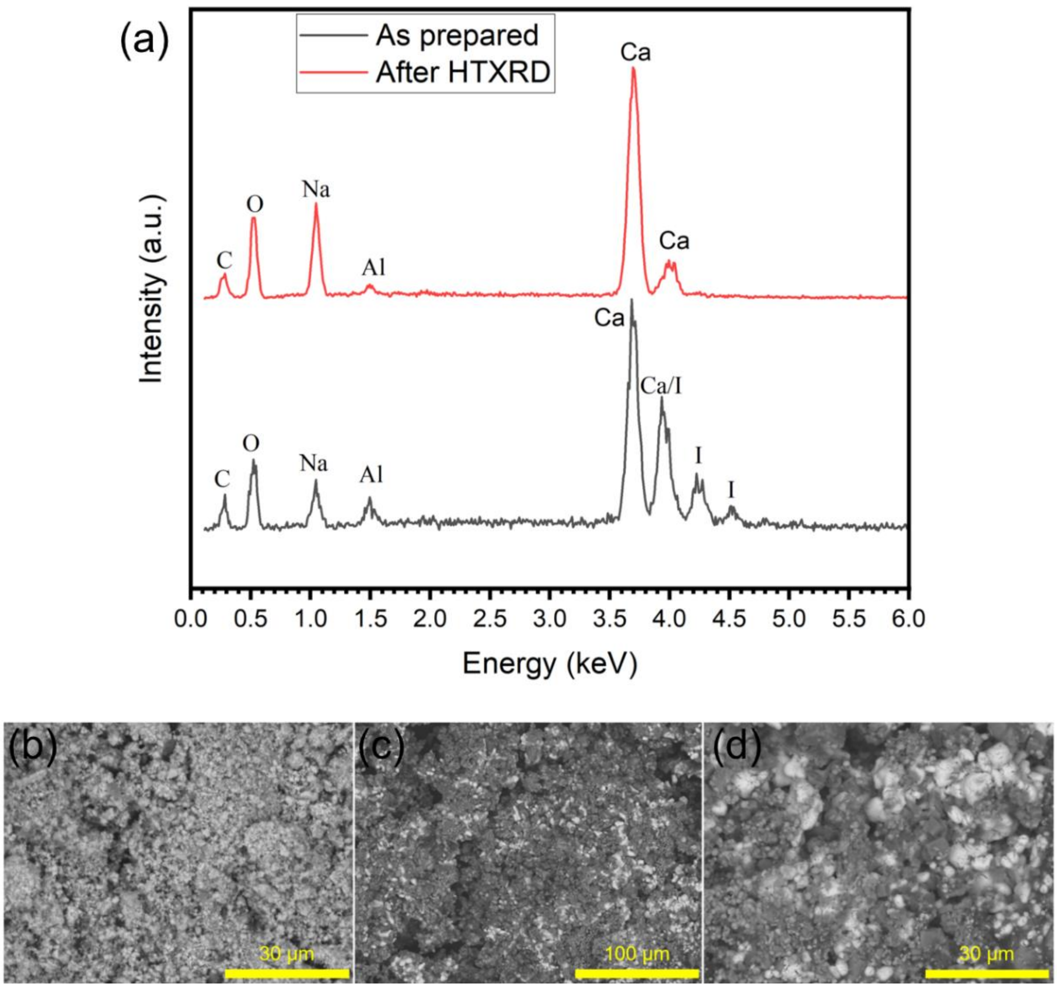

Figure S5: a) EDS analysis of Ca$_2$NaIO$_6$ powder pre- (black) and post- HT-XRD (red). A small amount of Sr contamination is visible both before and after HT-XRD. SEM images show as prepared Ca$_2$NaIO$_6$ (b) and after decomposition at 750 °C to CaO ((c) and (d)).

Chapter 9

The crystal and electronic structure of $Pb_2Tc_2O_{6.5}$: a vacancy ordered mixed valent pyrochlore

The crystal and electronic structure of $Pb_2Tc_2O_{6.5}$: a vacancy ordered mixed valent pyrochlore

Sarah E. O'Sullivan[a], Farnaz Kaboudvand,[b] Ram Seshadri[b], Shi-Kuan Sun[a], Martin C. Stennett[a], Claire L. Corkhill[a], Neil C. Hyatt[a], Daniel J. Bailey[a*]

[a] Department of Materials Science & Engineering, University of Sheffield, Sheffield, S1 3JD, UK

[b] Materials Department and Materials Research Laboratory, University of California, Santa Barbara, Santa Barbara, California 93106, United States

9.1 Abstract

We report the high temperature solid state synthesis, crystal structure, and electronic structure of the pyrochlore $Pb_2Tc_2O_{6.5}$, determined from neuron powder diffraction, X-ray absorption near edge spectroscopy (XANES), and DFT calculations. This compound adopts a vacancy ordered pyrochlore structure in space group F-43m with a = 10.3601(1) Å. Remarkably, this pyrochlore is the first example of a mixed valent Tc^{4+} / Tc^{5+}pyrochlore, with a mean oxidation state of $Tc^{4.5+}$ as determined from the refined oxygen stoichiometry and analysis of Tc K-edge XANES data, supported by bond valence sum calculations. Electronic structure calculations reveal a magnetically ordered half metallic ground state in $Pb_2Tc_2O_{6.5}$, which is discussed in the context of counterpart ruthenate and technetate pyrochlores. This investigation further develops the inorganic solid state chemistry of the Tc^{5+} oxidation state, which may be of importance in ceramic wasteforms designed for immobilisation and disposal of ^{99}Tc.

9.2 Introduction

In the 150th anniversary year of Mendeleev's prediction of eka-manganese [1], with atomic number 43 in the periodic table, the element now known as technetium since its discovery in 1937 [2], remains one of the most enigmatic elements, exhibiting a rich inorganic chemistry, with oxidation states -1 to +7 [3]–[5]. Technetium, so named from the Greek τεχνητός, meaning *artificial* [6], was the first element to be produced synthetically; all 22 known isotopes are radioactive with the longest half life of 4.2 x10^6 years observed for ^{97}Tc and ^{98}Tc; primordial technetium has long since decayed [7]. Whilst the metastable isotopes have short half lives and application in radiopharmaceuticals [8], the longer lived isotopes are problematic daughter products resulting from ^{235}U fission in nuclear power generation. The ^{99}Tc isotope, in particular, is produced in sizeable quantity with a thermal fission yield of 6%, equivalent to 2g per day per 100 MW_{th} in a Light Water Reactor (LWR); it has a half life of 2.1 x 10^5 years [9]. Tc shows complex behaviour in aqueous reprocessing of nuclear fuels by the conventional PUREX process and is concentrated in the high level waste raffinate [10], which is subsequently vitrified. However, modification of the PUREX process, and advanced aqueous reprocessing flow sheets, such as the UREX process, enable separation of Tc by co-extraction with uranium followed by ion exchange [11], [12].

Future regulatory practice, in the context of advanced nuclear fuels and fuel cycles, may require immobilization and geological disposal of ^{99}Tc in a tailored wasteform [11], [13]–[15], given its critical importance in the radiological risk assessment of geological disposal systems. Although the prevailing conditions in a geological disposal facility are likely to be reducing, a significant proportion of the Tc in the current UK radioactive waste inventory destined for geological disposal, is expected to be present as the Tc^{7+} pertechnetate species (TcO_4^-), which is considered to have unlimited solubility in ground waters [16]. Performance assessment models have shown that the radiological risk to future populations depends critically on Tc oxidation state, with the peak risk reduced by at least three orders of magnitude for the relatively insoluble and highly sorbing Tc^{4+} [16]. In this respect, expanding our limited understanding and knowledge of the fundamental materials chemistry of Tc^{4+} is of considerable importance.

Immobilisation of Tc in glass wasteforms has proved challenging due to the volatility of Tc_2O_7 under high temperature and oxidising process conditions [17], coupled with the low solubility of the pertechnetate species in borosilicate glass formations [18]–[20]. $TcO_3(OH)$ was observed as a volatile species as low as 600 °C, mediated by the presence of water during vitrification studies [21]. Moreover, the typical first-pass retention of Tc during vitrification of various Hanford waste simulants was 35% and requires significant additional infrastructure for further capture and recycling of the off gas collections [19]. It is posited that a best case scenario of Tc vitrification and recapture still results in 2% losses to the environment [17], which for the reasons discussed above, is unfavourable.

Several ceramic host materials have been proposed for Tc immobilisation as Tc^{4+}, Tc^{5+} and Tc^{7+}, including: spinel, sodalite, rutile, cassiterite, pyrochlore, perovskite, goethite and layered double hydroxides (as reviewed by Luksic *et. al.* [22]), as well as zirconolites and derivatives thereof [13], [23], [24]. A leading candidate for immobilisation of Tc^{4+} speciation is the pyrochlore structure, $A_2Tc_2O_7$, of which several variants have been reported, with A = Pr, Nd, Sm, Gd, Dy, Er, Lu, Bi, [24], [25], [25], [26] [27]. The pyrochlore $Cd_2Tc_2O_7$ was also reported and is one of only three known examples of a Tc^{5+} ternary oxide, in addition to Li_3TcO_4 and $NaTcO_3$ [28], [29]. The archetypal pyrochlore structure adopts the cubic *Fd*-3*m* space group, with general formula $A_2B_2X_6Y$, where A and B are cations, adopting 8-fold and 6-fold co-ordination, $X = O^{2-}$ and $Y = O^{2-}$, OH^- or F^- [30]. The pyrochlore structure type has been extensively studied for the immobilisation of U, Pu and minor actinides [31], due to its chemical flexibility, radiation tolerance, and low aqueous solubility. The pyrochlore structure comprises interpenetrating B_2X_6 and A_2Y networks, in which the B cations form corner sharing BX_6 octahedra, whereas the A cations form edge sharing 8-fold co-ordinated AX_6Y_2 scalenohedra. The BO_6 octahedra provide a preferential site for Tc^{4+} based on its [Kr]$4d^3$ electron configuration [25]. Typical synthesis involves high temperature reaction between TcO_2 and A_2O_3 (or other oxide) heated to 700 – 1230 °C, either under vacuum or argon to prevent oxidation of TcO_2 to the volatile Tc_2O_7.

Our interest was drawn to the unusual oxygen deficient pyrochlore formulated $PbTcO_3$, or $Pb_2Tc_2O_6$ on the conventional pyrochlore cell, first reported by Muller *et. al.* in 1964, synthesised by solid state reaction between TcO_2 and PbO, in a sealed tube, heated to 890 °C for 84 h [25]. This compound had not been extensively characterised, although from X-ray diffraction was reported to adopt a pyrochlore structure with a = 10.361 Å. The composition was described as close to $Pb_2Tc_2O_6$ stoichiometry due to the absence of residual PbO or TcO_2 reported in the diffraction pattern. Here, we report our investigation and synthesis and characterisation of $PbTcO_3$, which we show affords a vacancy ordered, mixed valent, pyrochlore $Pb_2Tc_2O_{6.5}$, from powder neutron diffraction data, Tc K-edge X-ray Absorption Near Edge Structure (XANES) spectroscopy, and electronic structure calculations.

9.3 Experimental

Caution: ^{99}*Tc is a weak beta emitter. Manipulations must be thoroughly risk assessed and carried out with appropriate contamination control and dose monitoring.*

Technetium was sourced from Oak Ridge National Laboratory in the form of NH_4TcO_4. The received polycrystalline material, being black in colour, was subsequently purified by aqueous oxidation of the NH_4TcO_4 in H_2O, with addition of NH_4OH and 30% H_2O_2. The solution was heated to 90 °C for 1h to fully decompose the H_2O_2 before evaporating the excess solution and washing with isopropanol to recover the white, pure NH_4TcO_4 precipitate. NH_4TcO_4 was then converted to TcO_2 by heat treatment at 700 °C for 2h under a flowing N_2 atmosphere (BOC, 99.98%).

$Pb_2Tc_2O_{6.5}$ was synthesised *via* solid state reaction of TcO_2 with PbO. The reagents were ground together with a small volume of isopropanol to yield a finely intermixed slurry. The isopropanol was allowed to evaporate before recovering the batch and transferring to an alumina boat. This boat was then placed into a larger, lidded crucible for secondary containment. The crucible assembly was positioned in the centre of the heated zone of an Elite tube furnace fitted with a quartz process tube. N_2 process gas (BOC, 99.98%) was flowed for 1 hour with the furnace at room temperature to purge the tube, before initiating the furnace programme. The furnace was ramped to the target temperature at a rate of 3 °C/min, and held at 850 °C for 12 hours before subsequent ramp down to room temperature at 3 °C/min. Heat treatment was repeated twice more at 850 °C and for a final iteration at 875 °C, each for 12 hours; after each heat treatment the powder was reground using a mortar and pestle.

Phase identification of the reaction product was undertaken by laboratory X-ray diffraction (XRD) performed on a Bruker D2 Phaser diffractometer Ni filtered Cu Kα radiation, $\lambda = 1.5418$ Å, and a Lynxeye position sensitive detector. The powder samples were placed onto a zero-background silicon wafer mounted within an airtight specimen holder with a hemispherical X-ray transparent cap. Scanning electron microscopy (SEM) was performed on a Hitachi TM3030 with 15 kV operating voltage using Bruker Quantax 70 Energy Dispersive X-ray Spectrophotometer software [32]. Specimens for SEM-EDX were prepared in Quantomix Q102 WETSEM capsules according to the method of Bailey *et al.* [32]. Briefly, a small mass of powder was suspended in isopropanol and pipetting onto the inner surface of the polyimide window of the Wet SEM ® capsule, and the solvent allowed to evaporate. The capsule was then cold sealed using the proprietary o-ring assembly and the specimen analysed by transmission through the polyimide window. With regard to EDX analysis, the Tc Lα_1 and Pb Mα_1 emission lines (2.42 and 2.34 keV, respectively) overlap; to minimise interference EDX maps we selected narrow energy discriminator windows and the Tc Lβ_1 and Pb M$_z$ lines for analysis; see Figure S1.

Tc K edge X-ray absorption spectroscopy data were acquired at beamline B18 of the STFC Diamond Light Source. Data were acquired in transmission mode using finely ground specimens dispersed in polyethylene glycol and formed as 3 mm pellets, to achieve a thickness of one absorption length. The beamline was configured with a fixed-exit double crystal Si (111) monochromator and a double toroidal focussing mirror, incident and transmitted beam intensities were measured using ionization chambers, operated in a stable region of their I/V curve. Data analysis was performed using the ATHENA program [33].

Powder neutron diffraction data were obtained on the POLARIS time-of-flight diffractometer at the STFC ISIS Neutron and Muon Source [34], [35]. 0.1753 g of $Pb_2Tc_2O_{6.5}$ was loaded into a 6 mm diameter, thin walled vanadium can which was cold sealed using malleable indium wire. The sample can was mounted on an automatic sample changer in the diffractometer and data collected for a duration of 2200 μAh integrated proton beam current to the ISIS neutron target (corresponding to 12 h total neutron beam exposure). The diffraction data were normalized to the incident beam spectrum and corrected for detector efficiency and sample attenuation using a vanadium reference. Data reduction and generation of files suitable for profile refinement used the Mantid open source software [36]. Structure refinement was performed using the GSAS and EXPGUI programs [37], [38] using Bank 4 data (2θ range 75.2 – 112.9°, $\Delta d/d = 5.1 \times 10^{-3}$ [35]). The neutron scattering length of ^{99}Tc was set as 6.00 fm, as previously determined [39] (by modification of the GSAS atmdat.dat file).

First-principles electronic structure calculations based on density functional theory (DFT) using the SCAN parametrization [40] were performed using the Vienna ab initio Simulation Package (VASP) [41], [42]. The projector augmented wave (PAW) method [43], [44] was employed with a plane wave energy cutoff of 520 eV and the following VASP PAWs: Pb_d, Tc_pv, and O. Reciprocal space k-point meshes were automatically generated at a density of 50 $Å^{-1}$ along each reciprocal lattice vector.

9.4 Results

9.4.1 Synthesis and characterisation of $Pb_2Tc_2O_{6.5}$

$Pb_2Tc_2O_{6.5}$ was successfully synthesised by solid state reaction between TcO_2 and PbO at 850 - 875 °C after 48 h. Figure 1, shows the powder X-ray Diffraction (XRD) data of the product, which were a good match to the published reference diffraction pattern of $PbTcO_3$ (PDF 00-016-0657). These XRD data were indexed satisfactorily in space group *Fd*-3*m*, with unit cell parameter a = 10.3627(3) Å, in good agreement with Muller *et al.* [25], and characteristic of the ideal pyrochlore structure, as shown in Figure 1. Additional weak reflections attributed to a trace TcO_2 impurity phase were just discernible. Note that the XRD data also present broad reflections and diffuse scattering which arise from the sealed sample containment

The composition and microstructure of the polycrystalline product was characterised by SEM-EDX. Back-scattered electron imaging, Figure S1, revealed a fine grained material (sub 1 μm dimension) with some larger, faceted particles (10 μm dimension). EDX element mapping showed a uniform and homogeneous distribution of Pb, Tc and O; semi quantitative EDX determined the ratio Pb / Tc = 1.0(1), consistent with stoichiometry (note EDX does not afford accurate oxygen determination). It was not possible to differentiate a separate TcO_2 phase, due to the low concentration (see below).

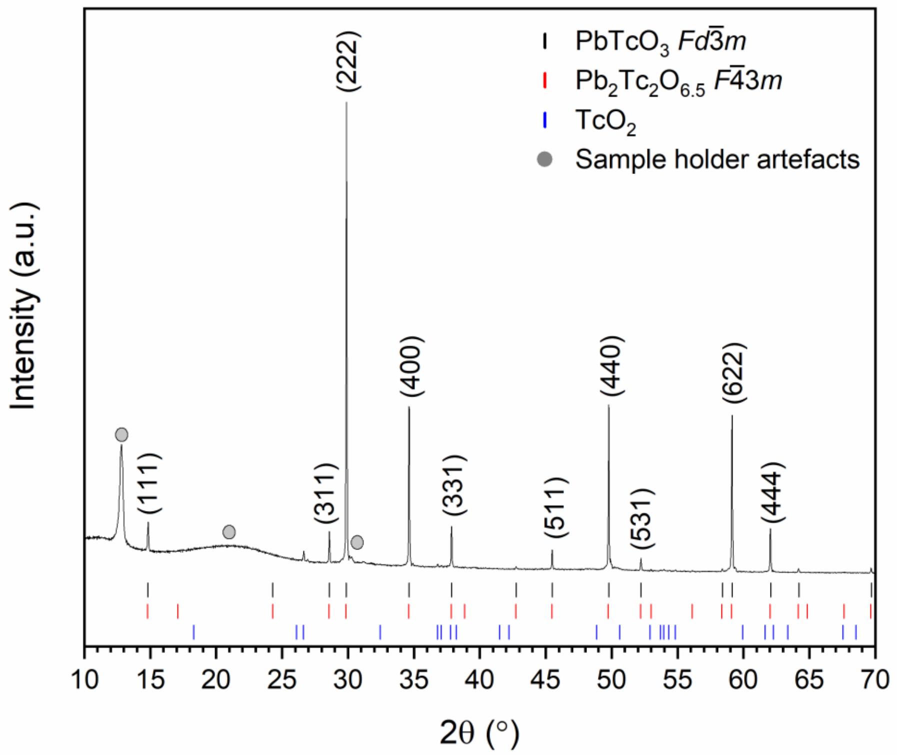

Figure 1. XRD pattern obtained for $Pb_2Tc_2O_{6.5}$ after 3x 850 °C 12h and 1x 875 °C heat treatments under Ar. Black tickmarks show allowed reflections for $PbTcO_3$ (PDF 00-016-0657, indexed) as a reference. Red tickmarks show reflections from TcO_2 (PDF 01-086-2944). Grey circles indicate features arising from the sample holder required for containment.

Figure 2 shows the Tc K edge XANES data for $Pb_2Tc_2O_{6.5}$ and also Tc, TcO_2 and NH_4TcO_4 reference compounds. The XANES data of $Pb_2Tc_2O_{6.5}$ were similar to those of TcO_2, with Tc^{4+} in octahedral co-ordination by oxygen, although shifted to slightly higher energy implying a higher average Tc oxidation state in $Pb_2Tc_2O_{6.5}$. The XANES data of NH_4TcO_4 present an intense pre-edge feature, characteristic of the TcO_4^- anion, associated with transition from Tc 1s to 4d states which are strongly hybridised with O 2p states; this is formally forbidden by the selection rule $\Delta l = \pm 1$, however, this rule is relaxed when Tc is located in such a non-centrosymmetric co-ordination environment and p–d mixing occurs. The absence of this distinctive pre-edge feature in the XANES data of $Pb_2Tc_2O_{6.5}$ rules out the possibility of pertechnetate speciation. Estimation of the average oxidation state of Tc in $Pb_2Tc_2O_{6.5}$ was made from a linear calibration of the absorption edge (E_0) against the known oxidation state of the reference compounds, taking both the conventional definition of $\mu x(E) = 0.5$ and also $\mu x(E) = 0.55$. These afford estimated average Tc oxidation states of 4.8 ± 0.2 and 4.6 ± 0.2,

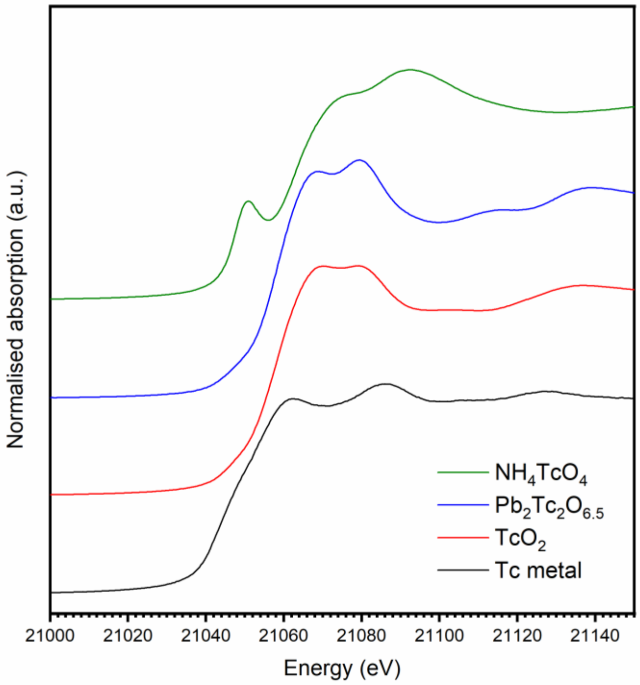

Figure 2. XANES comparison of $Pb_2Tc_2O_{6.5}$ (blue) with Tc metal (black), TcO_2 (red) and NH_4TcO_4 (green) standards.

respectively. The latter estimate is considered more accurate since defining E_0 as $\mu x = 0.55$, minimises the contribution of the intense pre-edge feature to the rising white line in the case of NH_4TcO_4 (see Figure S2) and is consistent with the oxidation state of 4.5+ determined from analysis of neutron diffraction data.

9.4.2 Crystal structure

Powder neutron diffraction data were first fitted assuming with a model of stoichiometric $Pb_2Tc_2O_7$ in an ideal pyrochlore structure, in space group *Fd*-3*m,* origin choice 2 (Pb at 16d (1/2, 1/2, 1/2); Tc at 16c (0, 0, 0); O at 48f (x, 1/8, 1/8); O′ at 8b (3/8, 3/8, 3/8)). Data were corrected for absorption and the background modelled using a 12 term shifted Chebyshev polynomial, before systematic refinement of structure and profile parameters. This model yielded a reasonable fit to the data and goodness of fit parameters, however, several reflections within the data were not accounted for. Further consideration identified reflections attributed to trace TcO_2 second phase and V (the latter attributed to the small sample size and hence significant contribution of the vanadium can to the overall scattering); the O′ occupancy at

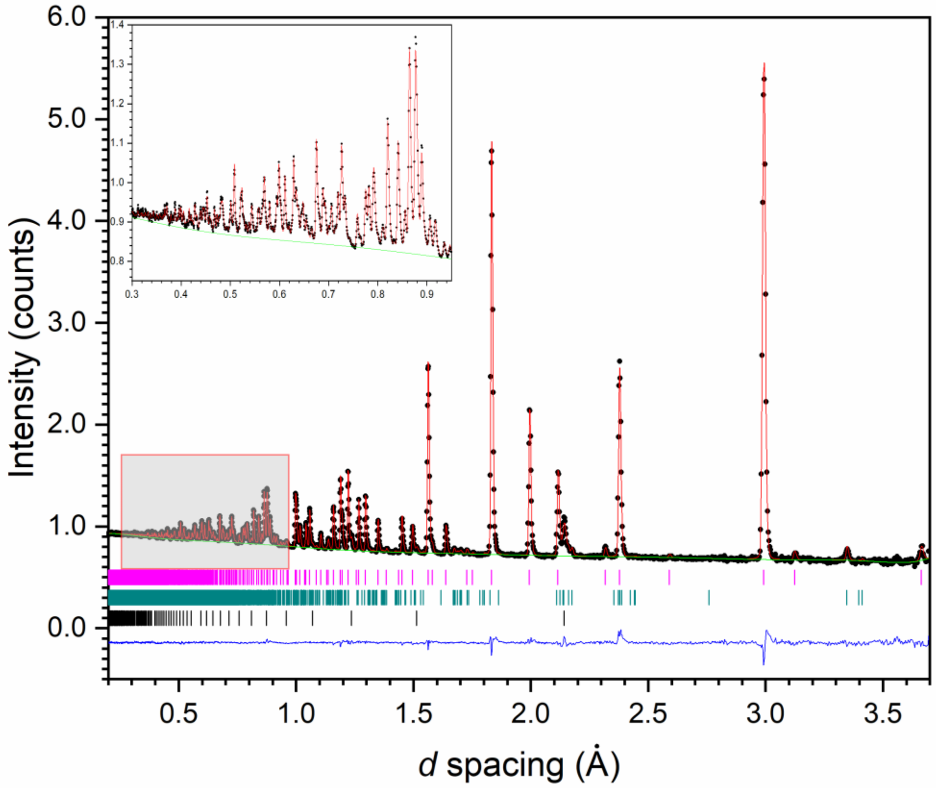

Figure 3. Rietveld refinement fit (red line) of powder neutron diffraction data (black dots) for $Pb_2Tc_2O_{6.5}$. Purple tickmarks indicate allowed reflections for *F*-43*m* $Pb_2Tc_2O_{6.5}$, green tickmarks indicate TcO_2, black tickmarks indicate vanadium. Inset shows a magnified view of the low *d* space region. Blue line indicates the difference profile.

the 8b site was also refined to account for possible oxygen non-stoichiometry. Addition of TcO_2 and V phases, and refinement of the O′ occupancy to 0.54(1), improved the fit considerably (R_{wp} = 1.44%, R_p = 1.64%, χ^2 = 3.36). However weak reflections at $d \approx 1.25$, 1.73, 2.31 Å within the Bank 4 data range (and $d = 5.18$ Å when inspecting Bank 5 data for verification) were not fitted by the ideal pyrochlore model (see Figure S3). Furthermore, the isotropic thermal parameters for the Pb atom at the 16d site and O′ atom at the 8b site were noted to be relatively large (U_{iso} = 0.0099(2) Å^2 and 0.0090(3) Å^2, respectively), which was interpreted as a signature of local static atomic displacements induced by the stereo-active $6s^2$ lone pair of the Pb^{2+} cation. Such displacements were previously reported in $Bi_2Tc_2O_{7-x}$ [26], and other closely related pyrochlores incorporating lone pair active Bi^{3+}, Pb^{2+}, Sn^{2+} and Tl^{+} species [45]–[49]. The model was therefore amended to allow for displacement of the Pb atom from the 16d to 96g site, and O′ atom from the 8b to 32e site, coupled with refinement of the 32e site

Space group: F-43m		a = 10.3601(1) Å, $\alpha/\beta/\gamma$ = 90°			Vol = 1111.98(4) Å^3	
Atom	Site	x	y	z	Fractional occupancy	U$_{iso}$ x 100 (Å^2)
Pb	16e	0.8766(6)	0.8766(6)	0.8766(6)	1.00	1.002(6)
Tc	16e	0.3745(7)	0.3745(7)	0.3745(7)	1.00	0.43(5)
O1	24f	0.3079(7)	0.00	0.00	1.00	0.59(11)
O2	24g	0.4475(7)	0.25	0.25	1.00	0.82(13)
O3	4d	0.75	0.75	0.75	1.00	0.45(12)
Powder statistics:		χ^2 = 3.030	R_{wp} = 0.79%		R_p = 1.18%	

Table 1. $Pb_2Tc_2O_{6.5}$ structural parameters determined from powder neutron diffraction data. Values for 1 e.s.d. are given in parentheses.

occupancy. Convergence was achieved with an improved fit (R_{wp} = 0.82%, R_p = 1.24%, χ^2 = 3.24), and the fractional occupancy of the O′ 32 site determined to be 0.48(1). However, the aforementioned reflections were not fitted by this optimised model. Further consideration of oxygen vacancy ordering, consistent with the refined occupancy of the O′ site, led to consideration of a model in space group F-43m, which provides for such oxygen vacancy ordering in the $Pb_2Ru_2O_{6.5}$ and a small family of other $Pb_2B_2O_{6.5}$ pyrochlore compounds [46], [50]–[53]. Further inspection of neutron diffraction data determined that this model indeed accounted for the additional reflections identified above (see Figure S3), which could be indexed as $hk0$ with $h + k \neq 4n$ or $h00$ with $h \neq 4n$, which are forbidden in Fd-3m ($d_{(820)} \approx 1.25$ Å, $d_{(600)} \approx 1.73$ Å, $d_{(420)} \approx 2.31$ Å, $d_{(200)} = 5.18$ Å). These reflections were not observable in our X-ray diffraction data (Figure 1), which was evidently not sufficiently sensitive to detect the oxygen vacancy ordering. The F-43m model provides two sites for the O′ atom, the nominally fully occupied 4d site and vacancy ordered 4a site, and cation displacement along the [111] direction to accommodate the Pb 6s^2 lone pair. Refinement of this model converged, with the aforementioned supercell reflections well fitted, yielding goodness of fit parameters R_{wp} = 0.79%, R_p = 1.18% and χ^2 = 3.03, for 32 variables including 15 structure parameters. The final structure parameters are detailed in Table 1, the profile fit is shown in Figure 3 and a structure model shown in Figure 4. The refined composition was determined to be $Pb_2Tc_2O_{6.5}$, with no evidence for partial occupancy of the O′/O3 4d site; the mean oxidation state of Tc$^{4.5+}$ is in agreement with that determined from Tc K-edge XANES data.

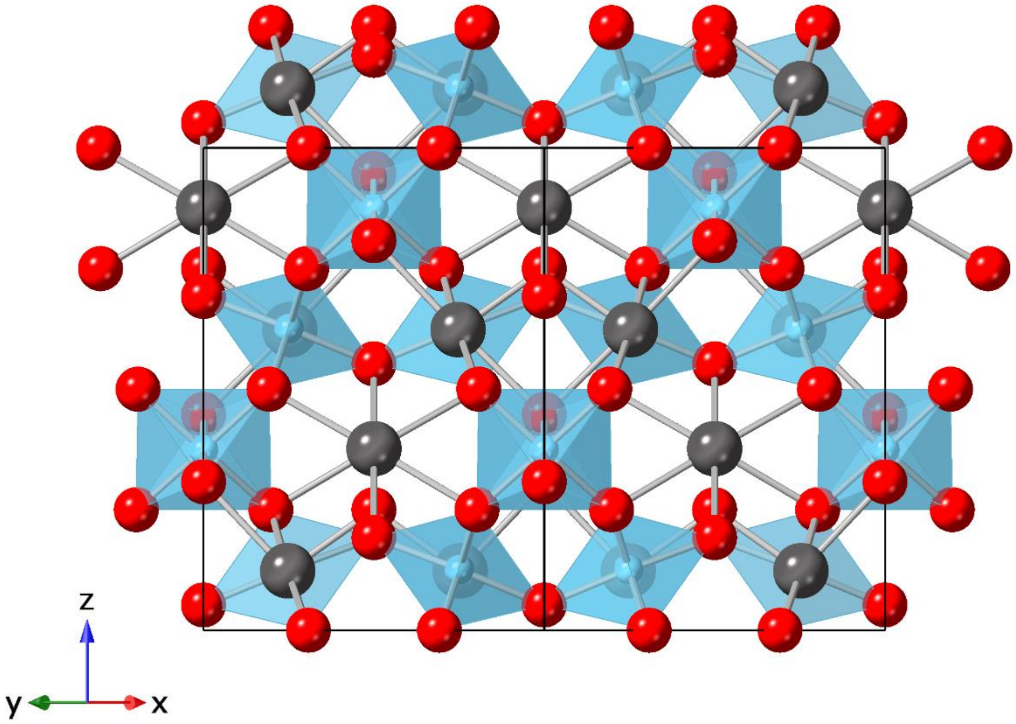

Figure 4. Unit cell structure of $Pb_2Tc_2O_{6.5}$ modelled from neutron diffraction data, viewed down the [110] plane. Light blue polyhedra indicate Tc cations, grey spheres indicate Pb cations and red spheres indicate O anions. Black line indicates the unit cell limits.

9.4.3 Electronic structure

Electronic structure calculations on $Pb_2Tc_2O_{6.5}$ were carried out using the SCAN parametrization in order to obtain a reliable description of the electronic structure. Calculations were carried out in the absence of spin polarization and with spin polarization. While an antiferromagnetic ground state could be expected, the complexities associated with creating tractable antiferromagnetically aligned spin arrangements on the frustrated pyrochlore arrangement of corner-connected Tc_4 tetrahedra have at this time obliged the use of a simpler ferromagnetic arrangement. No attempt was made to treat electronic correlation (that would normally be associated with an antiferromagnetic ground state and *vice-versa*). Magnetism is indeed stable, and seen from large Stoner enhanced densities of state in the calculations carried out in the absence of spin-polarization (labelled "non-magnetic), shown in panel (a) of Figure 5. Interestingly, switching on spin polarization in this ferromagnetic calculation yields a half-

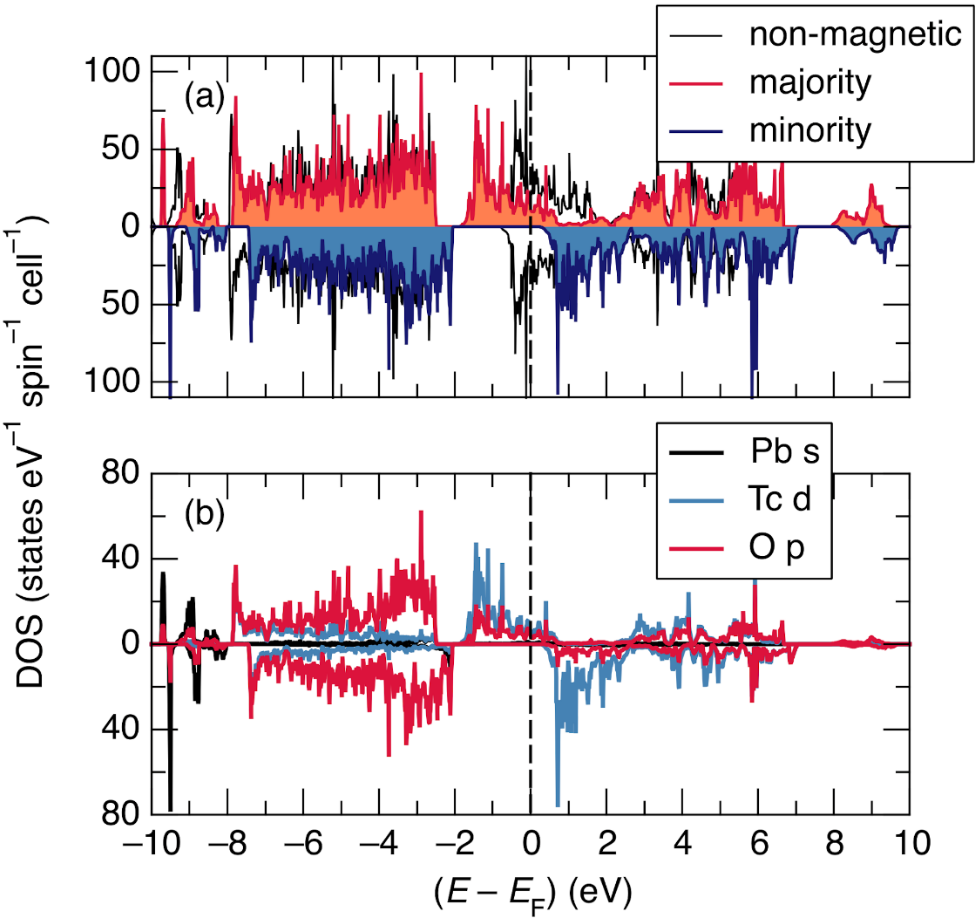

Figure 5: Calculated densities of states of $Pb_2Tc_2O_{6.5}$ with the Fermi energy indicated by the dashed line at 0 eV.

metallic ground state with a clean gap in the minority spin direction. The relaxed structure was found to be very close to the starting, experimental structure in terms of the unit cell and those positional parameters which could be relaxed. The magnetic moment from the calculations was 2.5 μ_B per Tc atom, which is consistent with fully spin-polarized $Tc^{4.5+}$. The atom-resolved densities of state displayed in panel (b) of this figure suggests the strong extent of Tc-O covalency which is expected for a 4d element in such a high oxidation state, which is known to result in the high magnetic ordering temperatures of perovskite oxides with Tc^{4+} [69]–[78].

9.5 Discussion

The structure of oxide pyrochlores, $A_2B_2O_6O'$, are comprised of interpenetrating B_2O_6 and A_2O' networks [54]. The B_2O_6 sub-lattice comprises corner sharing BO_6 octahedra which form a network of interconnecting cages, with the O' atom at the centre, whereas the A_2O' sub lattice comprises a network of corner-sharing O'_4A tetrahedra, forming a system of intersecting –A–O'–A– O'– zig-zag chains (similar to the Cu_2O cuprite structure). Oxygen non-stoichiometry in $A_2B_2O_{7-x}$ oxide pyrochlores arises from vacancies on the O' site, leading to $0 \leq x \leq 1$. According to Longo *et al.* [55], [56], when the A site cation has a polarisable $6s^2$ lone pair of electrons, the energy levels of the 6s and 6p states of the A site cation are comparable to the virtual energy levels of the O' vacancy. This is suggested to lead to the formation of a "trap mediated bond" between A cations, through the vacancy, as a result of hybridisation of 6s and 6p states of the A cation and their mixing with the virtual energy levels of the vacancy. When this interaction compensates for the reduced Madelung energy arising from oxygen vacancies, the pyrochlore structure is stabilised in preference to the alternate perovskite structure, for x = 1.0.

$Pb_2Tc_2O_{6.5}$ is isostructural with $Pb_2Ru_2O_{6.5}$ and a small family of plumbite; mixed valent vacancy ordered pyrochlores, $A_2B_2O_{6.5}$ (A = Pb, with B = Ir, $Ti_{0.75}W_{0.25}$, $Sn_{1.5}W_{0.5}$, $Sb_{0.75}Ga_{0.25}$, $Sb_{0.83}Ni_{0.17}$; and A = $Pb_{0.5}Tl_{0.5}$, with B = Nb, $Ti_{0.5}Sb_{0.5}$, $Sb_{0.75}Cr_{0.5}$) [46], [50]–[53]. The Tc environment within $Pb_2Tc_2O_{6.5}$ is defined by six oxygens at the vertices of a slightly distorted octahedron, typical of a pyrochlore compound, with three short and three long bonds of r = 1.964(6) Å and 1.975(6) Å, respectively. The Tc bond valence sum, in the form $v = \Sigma e^{(r0- r)/b}$ (b = 0.37) [57], was determined to be v = 4.24 v.u. or v = 4.45 v.u., taking r_0 (Tc^{4+}) = 1.841 Å and r_0 (Tc^{5+}) = 1.859 Å, respectively. This is in reasonable agreement with the mean oxidation state of $Tc^{4.5+}$ determined from the refined oxygen stoichiometry and Tc K-edge XANES data. The refined positional parameter of the Tc atom is within one standard deviation of the ideal position in the *Fd*-3*m* structure (x = 0.3745) and is therefore not significantly displaced within its octahedral environment. The Pb environment is defined by co-ordination to seven oxygens at the vertices of a scalenohedron, with one vertex unoccupied (with 3 x Pb–O1 at 2.630(1) Å, 3 x Pb–O2 at 2.599(1) Å, and 1 x Pb–O3 at 2.271(3) Å). The refined positional parameter shows that the Pb atom is slightly displaced from the ideal position in the *Fd*-3*m* structure (x = 0.875), moving 0.0285(3) A along the [111] direction toward the vacancy (□). The Pb–□ distance is 2.214(3) Å, forming $\square Pb_4$ tetrahedra, which alternate with $O3Pb_4$ tetrahedra along the [111] direction. Refinement of the Pb occupancy was tested but found to be within one standard deviation of full occupancy. The relatively large isotropic thermal parameter of the Pb atom may therefore be attributed to additional small uncorrelated static displacements of the Pb atom.

In comparison with $Pb_2Tc_2O_{6.5}$ and its counterpart $Pb_2Ru_2O_{6.5}$, the smaller degree of non-stoichiometry in the $Bi_2Tc_2O_{7-x}$ pyrochlore, $x = 0.14(1)$, is insufficient to give rise to long range vacancy ordering [26]. As an apparent consequence, the static displacement of the Bi cations from the 16d special position is disordered in $Bi_2Tc_2O_{7-x}$ and $Bi_2Ru_2O_{7-x}$ [26], [58]. The displacement of the Pb atom along the [111] direction toward the vacancy in $Pb_2Tc_2O_{6.5}$, 0.0285(3) Å is smaller than that of 0.040(4) Å reported for the counterpart $Pb_2Ru_2O_{6.5}$ pyrochlore [46]; however, the Pb–O3 bond in the latter, 2.260(2) Å, is comparably shorter by a similar margin. This supports the hypothesis of Beyerlein *et al.*, that A site displacement in these compounds are driven by optimisation of the Pb-O3 distance [46].

The ruthenate pyrochlores $Pb_2Ru_2O_{6.5}$ and $Bi_2Ru_2O_7$ demonstrate metallic conductivity and Pauli paramagnetism [47]. In contrast, the rare earth ruthenate pyrochlores $Ln_2Ru_2O_7$ are insulators with antiferromagnetic ordering [59]–[63]. This difference in behaviour, is believed to arise from the relatively small Ru-O-Ru bond angle in $Ln_2Ru_2O_7$ (~130°), which results in reduced overlap of Ru 4d and O 2p states in $Ln_2Ru_2O_7$, and a Mott – Hubbard gap opens in the Ru 4d states at the Fermi level [47], [59]. Whereas, the comparably greater Ru-O-Ru bond angle in $Pb_2Ru_2O_{6.5}$ (135°) and $Bi_2Ru_2O_7$ (133°) [46], [58], and shorter Ru-O distances, coupled with hybridisation of the Pb / Bi 6p and Ru 4d states, broadens the conduction band, giving rise to metallic conductivity in the Ru_2O_6 sublattice [47], [64]–[68]. In $Pb_2Tc_2O_{6.5}$, the Tc-O-Tc bond angle is 134.9(2)°, similar to that of the metallic ruthenate pyrochlores and $Bi_2Tc_2O_7$ (134.125(4)°), suggesting strongly hybridised Tc 4d and O 2p states, and the potential for metallic conductivity. This is confirmed by the electronic structure calculations which demonstrate a magnetically ordered half metallic ground state with a conduction band comprised of primarily Tc 4d states mixed with antibonding O 2p states, and thus strong Tc-O covalency, very similar to the electronic structure of $Bi_2Tc_2O_{7-x}$ [26]. Consistent with our electronic structure calculations of $Pb_2Tc_2O_{6.5}$, and those of $Bi_2Tc_2O_7$ [26], Rodriguez *et al.* reported antiferromagnetic ordering in "$Pb_2Tc_2O_6$" and $Bi_2Tc_2O_7$ pyrochlores below 140 K and 150 K, respectively [28]. Characterisation data of the "$Pb_2Tc_2O_6$" pyrochlore were not reported, although it was noted that the observed Curie behaviour at low temperature was most likely due to impurities; our data suggest that this material was likely $Pb_2Tc_2O_{6.5}$.

In the context of the motivation of this work, focused on the synthesis of oxides of Tc^{4+}, for the purpose of ^{99}Tc disposition in future nuclear fuel cycles, the results presented here provide some perspective of some interest. First, the synthesis of the first demonstrable mixed valent technetium oxide, $Pb_2Tc_2O_{6.5}$, suggests a more expansive solid state inorganic chemistry for the Tc^{5+} oxidation state than has previously been recognised. Therefore, it is reasonable to expect that the presence mixed valent Tc^{4+} / Tc^{5+} could be an important consideration in the design and performance assessment of ceramic or vitrified wasteforms targeting Tc^{4+}. In this regard, the stability of Tc^{5+} under the reducing and aqueous conditions of geological disposal may be recognised as a key knowledge gap. Secondly, the isostructural nature of the ruthenate and technetate pyrochlores offers a long term safeguard against the effects of ^{99}Tc transmutation to ^{99}Ru by β-decay, through potential solid solution formation. The capacity for oxygen non-stoichiometry may also be advantageous, buffering against changes in the redox characteristics of the local geochemical conditions. Thirdly, we have contributed to a growing body of evidence that demonstrates the potential for interesting and potentially useful magnetic and electronic properties to be realised in ternary Tc oxides. Given the significant fission yield of ^{99}Tc in LWRs this could conceivably justify recovery and utilisation of this element, in advanced reprocessing of nuclear fuels, rather than its consignment as a waste, given the relatively long half life and noting that the arising 0.29 MeV β particles are easily shielded by a thin layer of metal foil or plastic. Indeed, technetium alloys have attracted some attention for potential application in superconducting magnets [79].

9.6 Conclusions

The true composition of the previously reported pyrochlore phase “$PbTcO_3$” was shown to be $Pb_2Tc_2O_{6.5}$. This compound adopts a vacancy ordered pyrochlore structure, in space group $F\text{-}43m$, and is isostructural with $Pb_2Ru_2O_{6.5}$ and a small family of related plumbite pyrochlores. $Pb_2Tc_2O_{6.5}$ is the first example of a mixed valent ternary technetium oxide with an average oxidation state of $Tc^{4.5+}$ established from the neutron diffraction determined oxygen stoichiometry, bond valence sum analysis, and Tc K edge XANES. This may suggest a more extensive inorganic solid state chemistry of Tc^{5+} than hitherto considered, which could be important in the context of ceramic wasteforms designed for the immobilisation of ^{99}Tc. Electronic structure calculations reveal an antiferromagnetic half metallic ground state in $Pb_2Tc_2O_{6.5}$.

9.7 Acknowledgements

This research utilised the HADES/MIDAS facility at the University of Sheffield established with financial support from EPSRC and BEIS, under grant EP/T011424/1 [80]. The authors are grateful for financial support from EPSRC under grant numbers EP/L015390/1 EP/S011935/1 and EP/M026566/1. FK and RS are supported by National Science Foundation (NSF) under the DMREF Award DMR-1729489. We also acknowledge the use of the Center for Scientific Computing at UC Santa Barbara supported by the California NanoSystems Institute, the NSF MRSEC at UC Santa Barbara (DMR-1720256) and NSF CNS-1725797. Experiments at ISIS Neutron and Muon Source were supported by a beamtime allocation RB1920341 awarded by the Science and Technology Facilities Council; we thank Dr R. Smith for assistance with data acquisition. We are grateful to Prof. B. Toby and Prof. B. Von Dreele for helpful discussions regarding handling of neutron scattering lengths within GSAS to set the ^{99}Tc scattering length as 6.00 fm. The isotope(s) used in this research was supplied by the Isotope Program within the Office of Nuclear Physics in the Department of Energy's Office of Science.

9.8 References

[1] Mendeléeff, "LXIII.—The Periodic Law of the Chemical Elements," *J. Chem. Soc. Trans.*, vol. 55, no. 0, pp. 634–656, 1889, doi: 10.1039/CT8895500634.

[2] C. Perrier and E. Segrè, "Some Chemical Properties of Element 43," *J. Chem. Phys.*, vol. 5, no. 9, pp. 712–716, Sep. 1937, doi: 10.1063/1.1750105.

[3] F. A. A. De Jonge and E. K. J. Pauwels, "Technetium, the missing element," *Eur. J. Nucl. Med.*, vol. 23, no. 3, pp. 336–344, 1996, doi: 10.1007/BF00837634.

[4] G. E. Boyd, "Technetium and promethium," *J. Chem. Educ.*, vol. 36, no. 1, p. 3, Jan. 1959, doi: 10.1021/ed036p3.

[5] R. Zingales, "From masurium to trinacrium: The troubled story of element 43," *J. Chem. Educ.*, vol. 82, no. 2, pp. 221–227, 2005, doi: 10.1021/ed082p221.

[6] C. PERRIER and E. SEGRÈ, "Technetium : The Element of Atomic Number 43," *Nature*, vol. 159, no. 4027, p. 24, 1947, doi: 10.1038/159024a0.

[7] B. T. Kenna and P. K. Kuroda, "Technetium in nature," *J. Inorg. Nucl. Chem.*, vol. 26, no. 4, pp. 493–499, 1964, doi: https://doi.org/10.1016/0022-1902(64)80280-3.

[8] I. Zolle, "Technetium-99m Pharmaceuticals Preparation and Quality," pp. 173–337, 2007.

[9] K. Schwochau, *Technetium: Chemistry and Radiopharmaceutical Applications.* Wiley, 2008.

[10] D. D. Sood and S. K. Patil, "Chemistry of nuclear fuel reprocessing: Current status," *J. Radioanal. Nucl. Chem.*, vol. 203, no. 2, pp. 547–573, 1996, doi: 10.1007/BF02041529.

[11] F. Poineau, E. Mausolf, G. D. Jarvinen, A. P. Sattelberger, and K. R. Czerwinski, "Technetium Chemistry in the Fuel Cycle: Combining Basic and Applied Studies," *Inorg. Chem.*, vol. 52, no. 7, pp. 3573–3578, Apr. 2013, doi: 10.1021/ic3016468.

[12] F. Poineau *et al.*, "Uranium/technetium separation for the UREX process – synthesis and characterization of solid reprocessing forms," *Radiochim. Acta*, vol. 96, no. 9–11, pp. 527–533, 2008, doi: doi:10.1524/ract.2008.1533.

[13] D. J. Bailey *et al.*, "A new approach to the immobilisation of technetium and transuranics: Co-disposal in a zirconolite ceramic matrix," *J. Nucl. Mater.*, vol. 528, p. 151885, 2020, doi: 10.1016/j.jnucmat.2019.151885.

[14] K. L. Nash and M. Nilsson, "1 - Introduction to the reprocessing and recycling of spent nuclear fuels," in *Woodhead Publishing Series in Energy*, R. B. T.-R. and R. of S. N. F. Taylor, Ed. Oxford: Woodhead Publishing, 2015, pp. 3–25.

[15] L. G. Williams, "4 - Safety and security issues in the reprocessing and recycling of spent nuclear fuels for advanced fuel cycles," in *Woodhead Publishing Series in Energy*, R. B. T.-R. and R. of S. N. F. Taylor, Ed. Oxford: Woodhead Publishing, 2015, pp. 63–90.

[16] United Kingdom Nirex Limited, "Nirex Report Generic Repository Studies Generic post-closure Performance Assessment," 2003.

[17] J. G. Darab and P. A. Smith, "Chemistry of technetium and rhenium species during low-level radioactive waste vitrification," *Chem. Mater.*, vol. 8, no. 5, pp. 1004–1021, 1996, doi: 10.1021/cm950418+.

[18] C. Z. Soderquist, M. J. Schweiger, D.-S. Kim, W. W. Lukens, and J. S. McCloy, "Redox-dependent solubility of technetium in low activity waste glass," *J. Nucl. Mater.*, vol. 449, no. 1, pp. 173–180, 2014, doi: https://doi.org/10.1016/j.jnucmat.2014.03.008.

[19] I. L. Pegg, "Behavior of technetium in nuclear waste vitrification processes," *J. Radioanal. Nucl. Chem.*, vol. 305, no. 1, pp. 287–292, 2015, doi: 10.1007/s10967-014-3900-9.

[20] D. Kim and A. A. Kruger, “Volatile species of technetium and rhenium during waste vitrification,” *J. Non. Cryst. Solids*, vol. 481, pp. 41–50, 2018, doi: https://doi.org/10.1016/j.jnoncrysol.2017.10.013.

[21] B. C. Childs, F. Poineau, K. R. Czerwinski, and A. P. Sattelberger, “The nature of the volatile technetium species formed during vitrification of borosilicate glass,” *J. Radioanal. Nucl. Chem.*, vol. 306, no. 2, pp. 417–421, 2015, doi: 10.1007/s10967-015-4203-5.

[22] S. A. Luksic, B. J. Riley, M. Schweiger, and P. Hrma, “Incorporating technetium in minerals and other solids: A review,” *J. Nucl. Mater.*, vol. 466, pp. 526–538, 2015, doi: 10.1016/j.jnucmat.2015.08.052.

[23] M. C. Stennett, T.-H. Lee, D. J. Bailey, E. V Johnstone, J. Heo, and N. C. Hyatt, “Ceramic immobilization options for technetium,” in *MRS Advances*, 2017, vol. 2, no. 13, pp. 753–758, doi: 10.1557/adv.2017.268.

[24] N. P. Laverov, S. V. Yudintsev, and B. I. Omel’yanenko, “Isolation of long-lived technetium-99 in confinement matrices,” *Geol. Ore Depos.*, vol. 51, no. 4, pp. 259–274, 2009, doi: 10.1134/S1075701509040011.

[25] O. Muller, W. B. White, and R. Roy, “Crystal chemistry of some technetium-containing oxides,” *J. Inorg. Nucl. Chem.*, vol. 26, no. 12, pp. 2075–2086, 1964, doi: 10.1016/0022-1902(64)80152-4.

[26] E. E. Rodriguez, F. Poineau, A. Llobet, K. Czerwinski, R. Seshadri, and A. K. Cheetham, “Preparation and crystal structures of bismuth technetates: A new metal oxide system,” *Inorg. Chem.*, vol. 47, no. 14, pp. 6281–6288, 2008, doi: 10.1021/ic8003273.

[27] T. Hartmann *et al.*, “Structure studies on lanthanide technetium pyrochlores as prospective host phases to immobilize ^{99}technetium and fission lanthanides from effluents of reprocessed used nuclear fuels,” *J. Nucl. Mater.*, vol. 411, no. 1–3, pp. 60–71, 2011, doi: 10.1016/j.jnucmat.2011.01.033.

[28] E. E. Rodriguez, F. Poineau, A. Llobet, J. D. Thompson, R. Seshadri, and A. K. Cheetham, “Preparation, magnetism and electronic structures of cadmium technetates,” *J. Mater. Chem.*, vol. 21, no. 5, pp. 1496–1502, 2011, doi: 10.1039/c0jm02470h.

[29] C. Keller and B. Kanellakopulos, “Ternäre oxide des drei-bis siebenwertigen technetiums mit alkalien,” *J. Inorg. Nucl. Chem.*, vol. 27, no. 4, pp. 787–795, 1965, doi: https://doi.org/10.1016/0022-1902(65)80438-9.

[30] B. C. Chakoumakos, “Systematics of the pyrochlore structure type, ideal $A_2B_2X_6Y$,” *J. Solid State Chem.*, vol. 53, no. 1, pp. 120–129, 1984, doi: 10.1016/0022-4596(84)90234-2.

[31] R. C. Ewing, W. J. Weber, and J. Lian, “Nuclear waste disposal-pyrochlore ($A_2B_2O_7$): Nuclear waste form for the immobilization of plutonium and ‘minor’ actinides,” *J. Appl. Phys.*, vol. 95, no. 11 I, pp. 5949–5971, 2004, doi: 10.1063/1.1707213.

[32] D. J. Bailey, M. C. Stennett, J. Heo, and N. C. Hyatt, “Use of WetSEM ® capsules for convenient multimodal scanning electron microscopy, energy dispersive X-ray analysis, and micro Raman spectroscopy characterisation of technetium oxides (Submitted),” *J. Radioanal. Nucl. Chem.*, 2021.

[33] B. Ravel and M. Newville, “ATHENA, ARTEMIS, HEPHAESTUS: data analysis for X-ray absorption sepctroscopy using IFEFFIT,” *J. Synchrotron Radiat.*, vol. 12, pp. 537–541, 2005.

[34] N. C. Hyatt *et al.*, “Structure determination of compounds for the immobilisation of Iodine-129 and Technetium-99.” STFC ISIS Neutron and Muon Source, 2019, doi:

10.5286/ISIS.E.RB1920341.

[35] R. I. Smith *et al.*, “The upgraded Polaris powder diffractometer at the ISIS neutron source,” *Rev. Sci. Instrum.*, vol. 90, no. 11, p. 115101, 2019, doi: 10.1063/1.5099568.

[36] O. Arnold *et al.*, “Mantid—Data analysis and visualization package for neutron scattering and μSR experiments,” *Nucl. Instruments Methods Phys. Res. Sect. A Accel. Spectrometers, Detect. Assoc. Equip.*, vol. 764, pp. 156–166, Nov. 2014, doi: 10.1016/j.nima.2014.07.029.

[37] A. C. Larson and R. B. Von Dreele, “General Structure Analysis System (GSAS).” 2004.

[38] B. H. Toby, “EXPGUI, a graphical user interface for GSAS,” *J. Appl. Crystallogr.*, vol. 34, no. 2, pp. 210–213, Apr. 2001, doi: 10.1107/S0021889801002242.

[39] E. E. Rodriguez *et al.*, “Structural studies of TcO_2 by neutron powder diffraction and first-principles calculations,” *J. Am. Chem. Soc.*, vol. 129, no. 33, pp. 10244–10248, 2007, doi: 10.1021/ja0727363.

[40] J. Sun, A. Ruzsinszky, and J. P. Perdew, “Strongly Constrained and Appropriately Normed Semilocal Density Functional,” *Phys. Rev. Lett.*, vol. 115, no. 3, p. 36402, Jul. 2015, doi: 10.1103/PhysRevLett.115.036402.

[41] G. Kresse and J. Furthmüller, “Efficient iterative schemes for ab initio total-energy calculations using a plane-wave basis set,” *Phys. Rev. B*, vol. 54, no. 16, pp. 11169–11186, Oct. 1996, doi: 10.1103/PhysRevB.54.11169.

[42] G. Kresse and J. Furthmüller, “Efficiency of ab-initio total energy calculations for metals and semiconductors using a plane-wave basis set,” *Comput. Mater. Sci.*, vol. 6, no. 1, pp. 15–50, 1996, doi: https://doi.org/10.1016/0927-0256(96)00008-0.

[43] P. E. Blöchl, “Projector augmented-wave method,” *Phys. Rev. B*, vol. 50, no. 24, pp. 17953–17979, Dec. 1994, doi: 10.1103/PhysRevB.50.17953.

[44] G. Kresse and D. Joubert, “From ultrasoft pseudopotentials to the projector augmented-wave method,” *Phys. Rev. B*, vol. 59, no. 3, pp. 1758–1775, Jan. 1999, doi: 10.1103/PhysRevB.59.1758.

[45] R. Seshadri, “Lone pairs in insulating pyrochlores: Ice rules and high-k behavior,” *Solid State Sci.*, vol. 8, no. 3-4 SPEC. ISS., pp. 259–266, 2006, doi: 10.1016/j.solidstatesciences.2006.02.020.

[46] R. A. Beyerlein, H. S. Horowitz, J. M. Longo, M. E. Leonowicz, J. D. Jorgensen, and F. J. Rotella, “Neutron diffraction investigation of ordered oxygen vacancies in the defect pyrochlores, $Pb_2Ru_2O_{6.5}$ and $PbT1Nb_2O_{6.5}$,” *J. Solid State Chem.*, vol. 51, no. 2, pp. 253–265, 1984, doi: 10.1016/0022-4596(84)90341-4.

[47] M. Tachibana *et al.*, “Electronic properties of the metallic pyrochlore ruthenates $Pb_2Ru_2O_{6.5}$ and $Bi_2Ru_2O_7$,” *Phys. Rev. B*, vol. 73, no. 19, p. 193107, May 2006, doi: 10.1103/PhysRevB.73.193107.

[48] T. Birchall and A. W. Sleight, “Nonstoichiometric phases in the SnNbO and SnTaO systems having pyrochlore-related structures,” *J. Solid State Chem.*, vol. 13, no. 1–2, pp. 118–130, 1975, doi: 10.1016/0022-4596(75)90089-4.

[49] A. Walsh, D. J. Payne, R. G. Egdell, and G. W. Watson, “Stereochemistry of post-transition metal oxides: Revision of the classical lone pair model,” *Chem. Soc. Rev.*, vol. 40, no. 9, pp. 4455–4463, 2011, doi: 10.1039/c1cs15098g.

[50] B. J. Kennedy, “Oxygen Vacancies in Pyrochlore Oxides: Powder Neutron Diffraction Study of $Pb_2Ir_2O_{6.5}$and $Bi_2Ir_2O_{7-y}$,” *J. Solid State Chem.*, vol. 123, no. 1, pp. 14–20, 1996, doi: https://doi.org/10.1006/jssc.1996.0146.

[51] Ismunandar, B. J. Kennedy, and B. A. Hunter, “Surface Segregation and Oxygen Vacancy Ordering in Defect Pyrochlores,” *J. Solid State Chem.*, vol. 130, no. 1, pp. 81–

89, 1997, doi: https://doi.org/10.1006/jssc.1997.7271.

[52] Ismunandar, B. J. Kennedy, and B. A. Hunter, "Observations on pyrochlore oxide structures," *Mater. Res. Bull.*, vol. 34, no. 8, pp. 1263–1274, 1999, doi: https://doi.org/10.1016/S0025-5408(99)00122-1.

[53] J. A. Alonso, C. Cascales, I. Rasines, and J. Pannetier, "Oxygen-vacancy disordering revised in the defect pyrochlores $Pb_2(Cr_{0.5}Sb_{1.5})O_{6.5}$ and $Pb_2(TiSb)O_{6.5}$," *Phys. B Condens. Matter*, vol. 156–157, pp. 107–108, 1989, doi: https://doi.org/10.1016/0921-4526(89)90601-7.

[54] M. A. Subramanian, G. Aravamudan, and G. V Subba Rao, "Oxide pyrochlores — A review," *Prog. Solid State Chem.*, vol. 15, no. 2, pp. 55–143, 1983, doi: https://doi.org/10.1016/0079-6786(83)90001-8.

[55] J. M. Longo, P. M. Raccah, and J. B. Goodenough, "$Pb_2M_2O_{7-x}$ (M = Ru, Ir, Re) — Preparation and properties of oxygen deficient pyrochlores," *Mater. Res. Bull.*, vol. 4, no. 3, pp. 191–202, 1969, doi: https://doi.org/10.1016/0025-5408(69)90056-7.

[56] H. S. Horowitz, J. M. Longo, and J. T. Lewandowski, "New oxide pyrochlores: $A_2[B_{2-x}A_x]O_{7-y}$ (A = Pb, Bi; B = Ru, Ir)," *Mater. Res. Bull.*, vol. 16, no. 5, pp. 489–496, 1981, doi: https://doi.org/10.1016/0025-5408(81)90112-4.

[57] I. D. Brown and D. Altermatt, "Bond-Valence Parameters Obtained from a Systematic Analysis of the Inorganic Crystal Structure Database," *Acta Crystallogr. Sect. B*, vol. 244, no. 2, pp. 244–247, 1985, doi: 10.1107/S0108768185002063.

[58] M. Avdeev, M. K. Haas, J. D. Jorgensen, and R. J. Cava, "Static disorder from lone-pair electrons in $Bi_{2-x}M_xRu_2O_{7-y}$(M=Cu,Co;x=0,0.4) pyrochlores," *J. Solid State Chem.*, vol. 169, no. 1, pp. 24–34, 2002, doi: https://doi.org/10.1016/S0022-4596(02)00007-5.

[59] B. J. Kennedy, "Structural trends in pyrochlore-type oxides," *Phys. B Condens. Matter*, vol. 241–243, pp. 303–310, 1997, doi: https://doi.org/10.1016/S0921-4526(97)00570-X.

[60] M. Field, B. J. Kennedy, and B. A. Hunter, "Structural Studies of the Metal–Nonmetal Transition in Ru Pyrochlores," *J. Solid State Chem.*, vol. 151, no. 1, pp. 25–30, 2000, doi: https://doi.org/10.1006/jssc.1999.8608.

[61] B. J. Kennedy and T. Vogt, "Structural and Bonding Trends in Ruthenium Pyrochlores," *J. Solid State Chem.*, vol. 126, no. 2, pp. 261–270, 1996, doi: https://doi.org/10.1006/jssc.1996.0337.

[62] T. Yamamoto, R. Kanno, Y. Takeda, O. Yamamoto, Y. Kawamoto, and M. Takano, "Crystal Structure and Metal-Semiconductor Transition of the $Bi_{2-x}Ln_xRu_2O_7$ Pyrochlores (Ln = Pr-Lu)," *J. Solid State Chem.*, vol. 109, no. 2, pp. 372–383, 1994, doi: https://doi.org/10.1006/jssc.1994.1116.

[63] N. Taira, M. Wakeshima, and Y. Hinatsu, "Magnetic Properties of Ruthenium Pyrochlores $Y_2Ru_2O_7$ and $Lu_2Ru_2O_7$," *J. Solid State Chem.*, vol. 144, no. 1, pp. 216–219, 1999, doi: https://doi.org/10.1006/jssc.1998.8113.

[64] F. Ishii and T. Oguchi, "Electronic Band Structure of the Pyrochlore Ruthenium Oxides $A_2Ru_2O_7$ (A= Bi, Tl and Y)," *J. Phys. Soc. Japan*, vol. 69, no. 2, pp. 526–531, Feb. 2000, doi: 10.1143/JPSJ.69.526.

[65] W. Y. Hsu, R. V Kasowski, T. Miller, and T. Chiang, "Band structure of metallic pyrochlore ruthenates $Bi_2Ru_2O_7$ and $Pb_2Ru_2O_{6.5}$," *Appl. Phys. Lett.*, vol. 52, no. 10, pp. 792–794, Mar. 1988, doi: 10.1063/1.99286.

[66] R. Kanno, Y. Takeda, T. Yamamoto, Y. Kawamoto, and O. Yamamoto, "Crystal Structure and Electrical Properties of the Pyrochlore Ruthenate $Bi_{2-x}Y_xRu_2O_7$," *J. Solid State Chem.*, vol. 102, no. 1, pp. 106–114, 1993, doi: https://doi.org/10.1006/jssc.1993.1012.

[67] B. J. Kennedy, "Preparation and structure of $BiCaRu_2O_{7-y}$," *J. Solid State Chem.*, vol. 119, no. 2, pp. 254–259, 1995, doi: https://doi.org/10.1016/0022-4596(95)80039-R.

[68] K.-S. Lee, D.-K. Seo, and M.-H. Whangbo, "Structural and Electronic Factors Governing the Metallic and Nonmetallic Properties of the Pyrochlores $A_2Ru_2O_{7-y}$," *J. Solid State Chem.*, vol. 131, no. 2, pp. 405–408, 1997, doi: https://doi.org/10.1006/jssc.1997.7497.

[69] E. E. Rodriguez *et al.*, "High temperature magnetic ordering in the 4d perovskite $SrTcO_3$," *Phys. Rev. Lett.*, vol. 106, no. 6, pp. 1–4, 2011, doi: 10.1103/PhysRevLett.106.067201.

[70] J. Mravlje, M. Aichhorn, and A. Georges, "Origin of the High Neel Temperature in $SrTcO_3$," *Phys. Rev. Lett.*, vol. 108, no. 19, p. 197202, May 2012, doi: 10.1103/PhysRevLett.108.197202.

[71] E. M. Reynolds *et al.*, "Magneto-structural coupling in $SrTc_xRu_{1-x}O_3$ (x = 0.25,0.5) perovskites," *J. Solid State Chem.*, vol. 287, p. 121378, 2020, doi: https://doi.org/10.1016/j.jssc.2020.121378.

[72] E. Reynolds *et al.*, "Structure and magnetism in $Sr_{1-x}A_xTcO_3$ perovskites: Importance of the A-site cation," *Phys. Rev. B*, vol. 95, no. 5, p. 54430, Feb. 2017, doi: 10.1103/PhysRevB.95.054430.

[73] C.-M. Dai and C.-L. Ma, "Optical band gap of $SrTcO_3$ from first-principles calculations," *Mod. Phys. Lett. B*, vol. 28, no. 06, p. 1450049, Mar. 2014, doi: 10.1142/S0217984914500493.

[74] S. Calder *et al.*, "Magnetically Driven Metal-Insulator Transition in $NaOsO_3$," *Phys. Rev. Lett.*, vol. 108, no. 25, p. 257209, Jun. 2012, doi: 10.1103/PhysRevLett.108.257209.

[75] V. S. Borisov *et al.*, "Magnetic exchange interactions and antiferromagnetism of $ATcO_3$(A= Ca, Sr, Ba) studied from first principles," *Phys. Rev. B*, vol. 85, no. 13, p. 134410, Apr. 2012, doi: 10.1103/PhysRevB.85.134410.

[76] C.-L. Ma and T. Zhou, "Comparison of the structural and magnetic properties of ground-state $SrTcO_3$ and $CaTcO_3$ from first principles," *Phys. B Condens. Matter*, vol. 407, no. 2, pp. 218–221, 2012, doi: https://doi.org/10.1016/j.physb.2011.10.031.

[77] G. J. Thorogood, M. Avdeev, M. L. Carter, B. J. Kennedy, J. Ting, and K. S. Wallwork, "Structural phase transitions and magnetic order in $SrTcO_3$," *Dalt. Trans.*, vol. 40, no. 27, pp. 7228–7233, 2011, doi: 10.1039/C1DT10445D.

[78] C. Franchini, T. Archer, J. He, X.-Q. Chen, A. Filippetti, and S. Sanvito, "Exceptionally strong magnetism in the 4d perovskites $RTcO_3$ (R= Ca, Sr, Ba)," *Phys. Rev. B*, vol. 83, no. 22, p. 220402, Jun. 2011, doi: 10.1103/PhysRevB.83.220402.

[79] V. B. Compton, E. Corenzwit, J. P. Maita, B. T. Matthias, and F. J. Morin, "Superconductivity of Technetium Alloys and Compounds," *Phys. Rev.*, vol. 123, no. 5, pp. 1567–1568, Sep. 1961, doi: 10.1103/PhysRev.123.1567.

[80] N. C. Hyatt, C. L. Corkhill, M. C. Stennett, R. J. Hand, L. J. Gardner, and C. L. Thorpe, "The HADES Facility for High Activity Decommissioning Engineering & Science: part of the UK National Nuclear User Facility," *IOP Conf. Ser. Mater. Sci. Eng.*, vol. 818, p. 12022, Apr. 2020, doi: 10.1088/1757-899x/818/1/012022.

9.8 Supporting Information

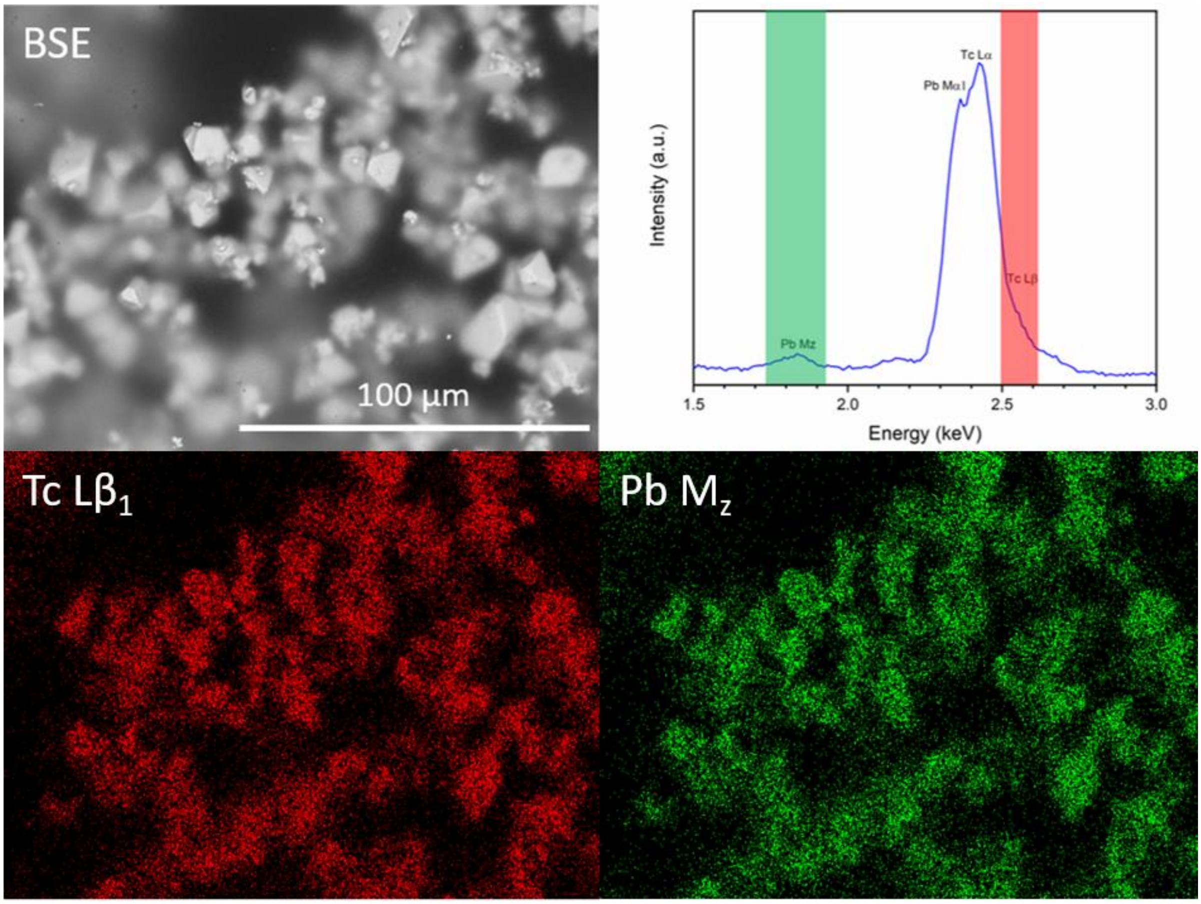

Figure S1. Backscatter electron SEM-EDX images for $Pb_2Tc_2O_{6.5}$. Top right image indicates the energy windows used to minimise interference between the emissions from Tc L and Pb M emission lines.

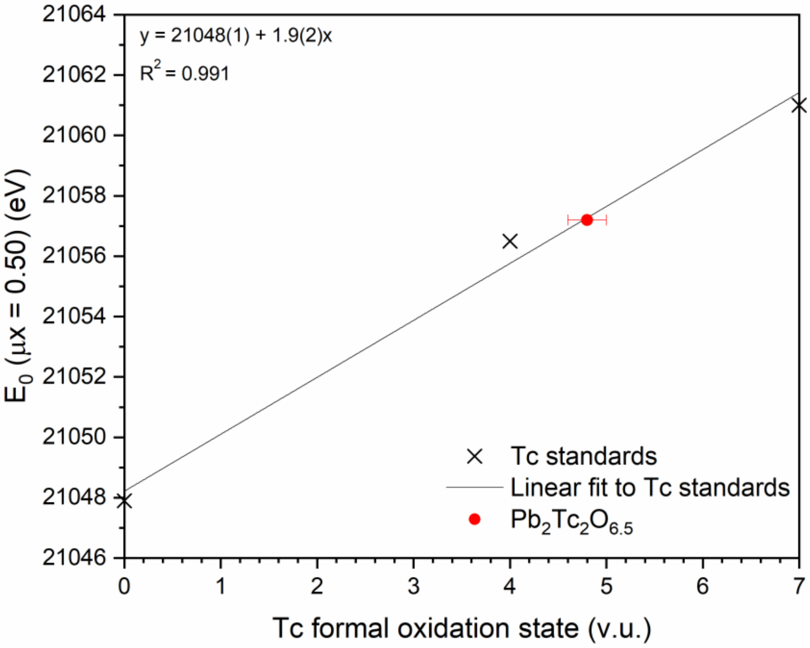

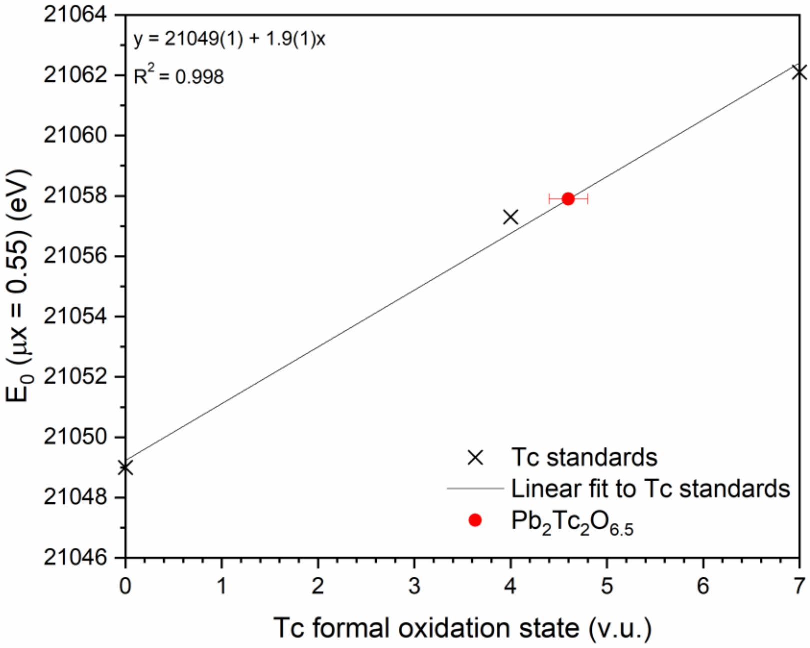

Figure S2. Calibration lines for estimation of Tc oxidation state from E_0 of reference compounds. Top: E_0 determined as µx = 0.5. Bottom: E_0 determined as µx = 0.55. Values for reference compounds, Tc metal (0), TcO_2 (+4) and NH_4TcO_4 (+7) are shown in black crosses. Values extrapolated for $Pb_2Tc_2O_{6.5}$ in this work shown in red.

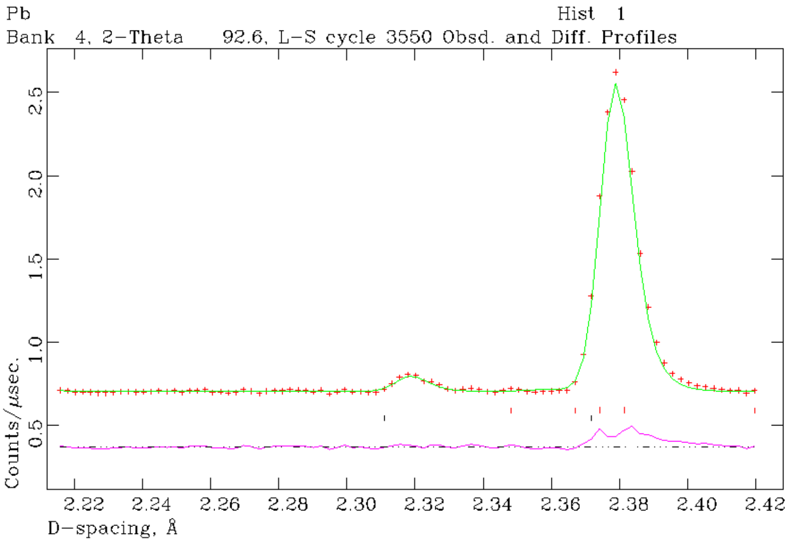

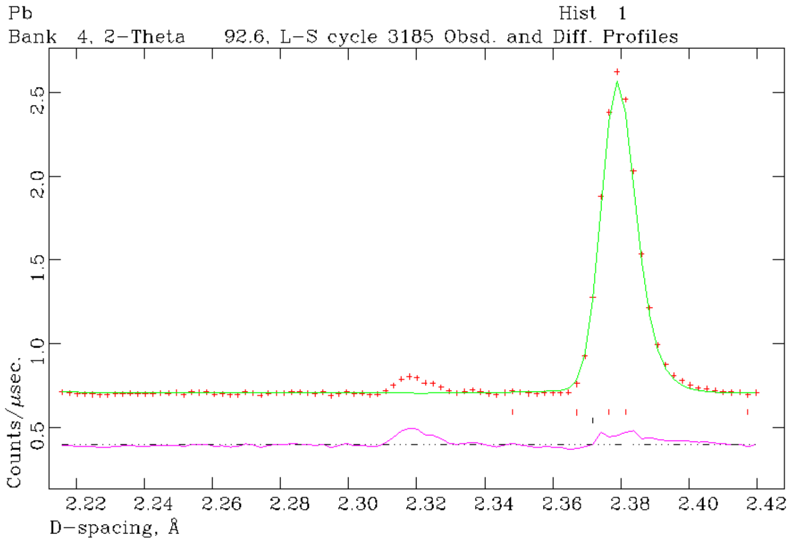

Figure S3. Top: Fit to powder neutron diffraction data of $Pb_2Tc_2O_{6.5}$, highlighting fit to (331) and (420) reflections located at 2.38 Å and 2.32 Å, respectively, based on model in space group *F*4-3*m*. Bottom: Fit to powder neutron diffraction data, based on model in space group *F*d-3*m*, which adequately models (331) reflection but does not account for (420) reflection.

Chapter 10

Conclusions

The aim of this thesis was to undertake a holistic investigation of the synthesis, structure and properties of novel nitrides, oxynitrides, and oxides of relevance to advanced nuclear fuel cycle, with a particular focus on uranium nitrides as accident tolerant fuel candidates and immobilisation host compounds for long lived ^{129}I and ^{99}Tc fission products.

In the considering uranium nitrides for accident tolerant fuels in the first half of this work, the first approach was to understand the use of sodium amide, $NaNH_2$, as a nitriding agent. This was achieved in Chapter 5, where reaction of Fe_3O_4 with $NaNH_2$ was investigated as a low temperature, solid state alternative to the typical ammonolysis reactions used in nitride synthesis. This expands upon the existing literature on an equivalent system using Fe_2O_3 and additionally explores lowered reaction temperatures.

Investigation of the reaction of Fe_3O_4 with excess $NaNH_2$ was performed in the range of 170 to 190 °C, for 24 or 96h. The phase assemblage was determined from a combination of XRD, ^{57}Fe Mössbauer spectroscopy and thermogravimetric analysis. ε-$Fe_{2+x}N$ was formed in 49 to 59 mol% yield, under exceptionally mild reaction conditions of 170 °C for 24h. The reaction was mediated by an $NaNH_2$-NaOH molten salt resulting in the dissolution of Fe_3O_4 and precipitation of the nanocrystalline nitride product. An amorphous contribution in the initial product phase assemblage was recrystallised and determined to be an oxynitride phase of $FeO_{1-x}N_x$, with a yield of 29 to 39 mol%. ^{57}Fe Mössbauer spectra could be fitted with components of ε-$Fe_{2+x}N$, $FeO_{1-x}N_x$ and γ''-FeN. Examination of TGA-MS data identified N_2 losses with thermal decomposition in good agreement to the assigned phase assemblage and proportions.

The mixed phase assemblage attained presents both a potential limitation to this method of nitride synthesis and a possible direction for future work. It has not been determined whether the oxynitride formed is part of the initial reaction products or as a result of the post reaction work up of the material causing hydrolysis of the targeted ε-$Fe_{2+x}N$ phase. Further investigation would need to identify the optimal conditions required to maximise yield of a well-defined, phase pure nitride product. Similarly, exploration of the exact mechanism of oxynitride formation may yield insight that can be refined for metastable oxynitride synthesis. Nevertheless, this work made three important advances in: i) demonstrating that the reaction mechanism is not topotactic in nature but proceeds by pseudomorphic dissolution-precipitation reaction; ii) since the $NaNH_2$ mediated nitridation is inherently reducing in nature, a more reduced oxide substrate enables the reaction to proceed at lower temperature; and, iii) the reaction may be effective in producing oxynitride phases, which, hitherto had not been recognised.

The $NaNH_2$ nitridation reaction was then applied to reactions with uranium oxides in Chapter 6, intending to investigate novel uranium nitride synthesis using this lower temperature, molten salt mediate nitridation method. Reactions between UO_{2+x}, UO_3 and U_3O_8 with $NaNH_2$ were modelled in the Materials Project Interface Reactions application, which predicted UN_2 and U_2N_{3+x} nitride as potential reaction products together with sodium uranyl phases. UO_{2+x} and UO_3 were reacted with variable excess of $NaNH_2$ in 1:12, 1:24 and 1:48 molar ratios at 200 °C for 24 or 72h. U_3O_8 was reacted in a 1:48 molar ratio with $NaNH_2$ for 24h at temperatures across the range of 120 to 240 °C. These reactions were complemented with reactions of the respective oxides under 300 ml/min NH_3 and 5%H_2/N_2.

Reaction of UO_{2+x} with $NaNH_2$ served to reduce the hyperstoichiometric oxide towards $UO_{2.00}$, with greater reduction achieved for increasing excess of $NaNH_2$. The estimated stoichiometries of the reaction products were derived from a calibration of the unit cell parameter against the value of x in UO_{2+x} according to Vegard's law. XRD and XPS measurement evidenced the presence of uranyl type secondary phases, identified as $Na_2U_2O_7$ and $Na_4(UO_2)(CO_3)_3$, which contributed to the remarkable colour change from the black starting UO_{2+x} to a deep yellow reaction product. The reactions are driven by decomposition of the $NaNH_2$ at 200 °C. Formation of nascent NH_3 reduces UO_{2+x}, with the H_2O by-product causing dissolution and precipitation of $Na_2U_2O_7$ and $Na_4(UO_2)(CO_3)_3$. No significant nitrogen doping was determined from XPS characterisation of the products. Similarly, gaseous reactions reduced the UO_{2+x}, with greater reduction achieved for the NH_3 than the 5%H_2/N_2, with no nitrogen doping in the products detected by XPS.

Reactions of UO_3 with $NaNH_2$ yielded reaction products comprised of $Na_2U_2O_7$ with retained

UO_3. The products were poorly crystalline, suggesting significant solubility of the oxide in $NaNH_2$. Both U L_3 edge XANES measurement and XPS measurement identified uranyl speciation in the product. The reaction products are consistent with known synthesis of $Na_2U_2O_7$ from $UO_3 \cdot 2.25H_2O$ and NaOH under hydrothermal conditions. No nitrogen incorporation in the product was detected by XPS.

U_3O_8 was reacted with $NaNH_2$ at a fixed 1:48 molar ratio between 120 and 240 °C. XRD characterisation showed these products to be poorly crystalline, with $NaUO_3$, Na_2UO_4 and $Na_2U_2O_7$ phases identified. Residual U_3O_8 could not be confidently ruled out of the phase assemblage. U L_3 edge XANES and XPS analyses of the reaction products were consistent with the presence of both U^{5+} and uranyl speciation, suggesting an oxidised product compared to the starting material.

The reactions of uranium oxides with $NaNH_2$ did not yield the intended nitride phases, however predicted sodium uranyl phases were attained. Future investigation should systematically explore reaction conditions to drive the thermodynamic conditions further in favour of nitride formation and improved crystallinity of the end products. However, it should be noted that the DFT calculated reaction energies obtained using the Materials Project Reaction Interfaces tool are relatively small and the thermodynamic driver for $NaNH_2$ mediated synthesis of uranium nitrides from uranium oxides is weak. As with the work in Chapter 5, the post reaction work up should also be examined to determine the effects of this on the phase assemblage. Although the majority of publications using $NaNH_2$ nitridation use oxide precursors, extension of this investigation to include UCl_4 is underway to continue efforts to synthesise uranium nitrides by this low temperature, solid state method. Nevertheless, this work did succeed in identifying a novel and unexpected low temperature reduction mechanism for UO_{2+x}, through abstraction of oxygen by nascent NH_3 in $NaNH_2$-NaOH molten salts.

In Chapter 7, the potential for ternary uranium oxynitride synthesis was explored. These compounds are proposed degradation products from UN as an accident tolerant fuel, hypothesised to occur during loss of coolant accidents or cladding failure. Systematic investigation of ammonolysis reactions of β-$SrUO_4$ and $CaUO_4$ were performed, with the reaction products characterised by XRD, XPS and XANES measurement.

Ammonolysis of β-$SrUO_4$, between 500 and 1000 °C with 75 ml/min applied NH_3 for 2h, resulted in an irreversible phase transition from β-$SrUO_4$ to α-$SrUO_4$, with full conversion to the α phase for the 750 °C reaction product. Products for reactions at 650 °C and above contained two phases of α-$SrUO_4$ and α-$SrUO_{4-x}$, evident as low angle "satellites" on the XRD patterns. The yield of the isostructural reduced phase was maximised for the 750 °C product, determined by quantitative phase analysis. XANES measurement of this product estimated a uranium oxidation state of 5.0(1) v.u. for this reduced phase, with a stoichiometry of α-$SrUO_{3.5}$. XPS analysis did not show any significant nitrogen doping for this product.

Reaction of $CaUO_4$ under NH_3 produced a reduced isostructural $CaUO_{4-x}$ phase. Optimisation of the ammonolysis parameters around this initial finding maximised the yield of the reduced phase for the product from reaction with 300 ml/min NH_3 at 650 °C for 16h. XANES analysis for this product estimated the uranium oxidation state of the reduced phase at 5.0(1) v.u. Stoichiometry was derived from fitting of the EXAFS spectra, refining for coordination number. This placed the average value of x in $CaUO_{4-x}$ at $x = 0.44$, yielding a weighted composition of $CaUO_{3.5}$ for the reduced phase. Possible nitrogen doping was examined by XPS and TGA-MS analyses, although no nitrogen was evident in these measurements.

While this work demonstrated reduction of the alkali earth uranates, oxynitride formation was not achieved. However, the highly reduced compounds show the limit of the composition allowable for the pentavalent uranium identified by XANES analyses. Further characterisation of these compounds should consider structural determination to evaluate the potential ordering of the oxygen vacancies and any associated lowering of symmetry that may have application as functional materials. Additionally, further investigation of ammonolysis reactions under relatively mild conditions may prove useful in facilitating the production of other U^{5+} compounds for characterisation.

The latter half of the work presented in this thesis focused on ceramic oxides proposed for the immobilisation of ^{129}I and ^{99}Tc. In Chapter 8, the A_2NaIO_6 (A = Ba, Sr, Ca) perovskite oxides were proposed for immobilisation of ^{129}I, which is a long lived, biologically active fission product.

The crystal structures of A_2NaIO_6 (A = Ba, Sr, Ca) perovskites were determined by careful analysis of XRD and neutron diffraction (ND) data along with Raman spectroscopy and DFT modelling. These compounds all adopt the perovskite structure with rock-salt ordering of Na^+ and I^{7+} cations on the octahedral site, as determined by Rietveld structure refinement. Ca_2NaIO_6 and Sr_2NaIO_6 were found to adopt the $P2_1/n$ hettotype, with co-operative octahedral tilting, which was confirmed as energetically favourable in the DFT analysis. For Ba_2NaIO_6, DFT analysis found the $Fm\text{-}3m$ and $P2_1/n$ to be energetically degenerate; however, XRD, ND and Raman spectroscopy determined the structure of Ba_2NaIO_6 to be $Fm\text{-}3m$ at room temperature, although the onset of a phase transition at this temperature may be possible.

The thermal stability of the A_2NaIO_6 perovskites was investigated by TGA-MS. The decomposition temperature of Ca_2NaIO_6 was 730 °C, which proceeded by loss of O_2 and I_2 followed by Na_2O evaporation at higher temperature. Sr_2NaIO_6 and Ba_2NaIO_6 decomposed by evaporation of NaI above 950 °C and 1050 °C, respectively. Ba_2NaIO_6 was shown to demonstrate remarkable thermal stability, and as far as can be ascertained, has the highest thermal stability of an iodine bearing compound hitherto reported. In the context of the objectives of this thesis, this work demonstrated synthesis of single phase periodate perovskites from $NaIO_4$, which could be isolated directly from advanced dissolver off gas scrubbing systems, or indirectly by oxidation of iodate species. The periodate perovskites are produced at relatively low temperature of 650 °C, which assures retention of the iodine inventory, which is normally problematic in the synthesis of iodine wasteforms, due to the thermal stability of $NaIO_4$. This work determined the first accurate crystal structures for these compounds, using ND data, verified by DFT modelling.

The structural data generated in this investigation is under consideration for deposit in the

International Centre for Diffraction Data repository. Further work on these compounds pertaining to their suitability as immobilisation compounds should consider manufacture of sintered ceramics in order to facilitate dissolution experiments.

In Chapter 9, immobilisation of the long lived ^{99}Tc isotope in a pyrochlore structure was considered, targeting the ostensibly Tc^{4+} pyrochlore "$PbTcO_3$", given the low solubility and strongly sorbing behaviour of Tc^{4+}. "$PbTcO_3$" was successfully synthesised by reaction between PbO and TcO_2 in air, however, careful structure determination from Rietveld analysis of powder neutron diffraction data established the true composition to be $Pb_2Tc_2O_{6.5}$. The compound was found to adopt a vacancy ordered pyrochlore structure in the $F\text{-}43m$ space group, evidenced by weak supercell reflections in ND data, which are a signature of vacancy ordering, that could not be indexed in the conventional $Fd\text{-}3m$ cell.

The average Tc valence from Tc K edge XANES measurement, along with bond valence sum analysis and the refined oxygen stoichiometry (from neutron diffraction data), was determined to be 4.5+. $Pb_2Tc_2O_{6.5}$ is therefore a mixed valent Tc^{4+}/Tc^{5+} oxide, the first example of such a technetium compound. Electronic structure calculations showed $Pb_2Tc_2O_{6.5}$ to demonstrate a half metallic magnetically ordered ground state, which is characteristic of the electronic structure of cuprate superconductors. This work is significant in demonstrating that the Tc^{5+} oxidation state may be stabilised under relatively low pO_2 conditions, since synthesis was performed under N_2 gas, if the host structure and chemical composition are conducive. This finding is arguably significant to wasteform design for Tc immobilisation, since the Tc^{5+} oxidation state has been overlooked, hitherto, but could be expected to be present if suitably charge compensated under neural to oxidising pO_2. The interesting electronic structure of this material and predicted magnetic ordering underline the potential for exploitable physical properties in Tc compounds, which could enable Tc to be utilised as a resource rather than treated as a waste product.

Further work on $Pb_2Tc_2O_{6.5}$ should consider assessment for suitability as an immobilisation host for ^{99}Tc, such as sintering and dissolution behaviour. Characterisation of magnetic and electronic properties to support the calculations presented here should also be acquired.